Area-dependent Resistive Switching in PCMO-based Memristive Devices

Von der Fakultät für Elektrotechnik und Informationstechnik der Rheinisch-Westfälischen Technischen Hochschule Aachen zur Erlangung des akademischen Grades eines

Doktors der Naturwissenschaften

genehmigte Dissertation vorgelegt von

Alexander Gutsche, M. Sc.

aus Grevenbroich

Berichter*innen: Universitätsprofessorin Dr. Regina Dittmann
Universitätsprofessor Dr. John Paul Strachan

Tag der mündlichen Prüfung: 05.05.2023

Diese Dissertation ist auf der Internetseite der Universitätsbibliothek online verfügbar.

Eidesstattliche Erklärung

Hiermit erkläre ich, Alexander Gutsche, dass ich die vorliegende Arbeit mit dem Thema

"Area-dependent Resistive Switching in PCMO-based Memristive Devices"

selbstständig und ohne Benutzung anderer als der angegebenen Quellen und Hilfsmittel angefertigt habe.
Alle Stellen, die wörtlich oder sinngemäß aus veröffentlichten oder nicht veröffentlichten Schriften entnommen wurden, sind als solche kenntlich gemacht. Die Arbeit ist in gleicher oder ähnlicher Form oder auszugsweise im Rahmen einer anderen Prüfung noch nicht vorgelegt worden.

(Ort, Datum)

(Unterschrift)

Bildungsgang Alexander Gutsche

2013	Abitur	Gymnasium Odenkirchen
2013 - 2016	Bachelorstudium Physik	RWTH Aachen University
2016 - 2018	Masterstudium Physik	RWTH Aachen University
2018 - 2023	Promotionsstudent Elektrotechnik	RWTH Aachen University/ Forschungzentrum Jülich

I. Abstract

Motivation, Goal and Task of the Dissertation:

In recent decades, the world has become increasingly connected. More and more devices are connected to each other and to the Internet. This development in the high-tech industry has been driven primarily by the Internet. The ever-increasing amounts of data being processed are pushing current technology to its limits. Not only physical limits stand in the way but also limits of today's computer architecture. Therefore, significant developments in storage and computer technology are necessary. A promising concept for this is resistive switching memory cells. Here, information is stored in a device by means of voltage-indicated resistance changes. These devices can be used in memories as well as in neuromorphic circuits. Different physical processes are responsible for the resistance change in these devices. Here one can also distinguish between so-called filamentary and area type switching devices. In filamentary type devices , the change in resistance happens by the formation of a conductive filament in the insulating layer. This results in an abrupt increase of the current during the SET process due to a strong heating of the devices. In area type resistive switching devices, on the other hand, the change in resistance is induced by ion migration over the entire surface of the devices. Here, both the switching on and the switching off occur without an abrupt change of the current. This happens gradually. This makes the area type resistvie switching devices interesting for storing multiple states in one device and also for use in neuromorphic circuits. However, the area type switching devices are less understood than the filamentary devices.

In this work, $Pr_{1-x}Ca_xMnO_3$ (PCMO) based area type resistive switching devices should be investigated for their applicability in such circuits. Here, in addition to electrical characterization, various analytical methods such as atomic force microscopy (AFM), X-ray photoelectron spectroscopy (XPS), and transmission electron microscopy (TEM) should be used to elucidate the physicochemical processes. These measurements should be used to establish a mathematical model to describe the switching behaviour in order to gain new insights into the switching mechanism in these devices and to be used for the simulation of neuromorphic circuits in the future.

Major Scientific Contributions:

One focus of the work was the development of the fabrication processes for PCMO-based memristive devices. First, the properties of the PCMO layers were investigated under different growth conditions. Here, it was shown that amorphous PCMO changes

its structure into a polycrystalline structure at a temperature of 650 °C. Furthermore, the switching behaviour of the PCMO layers in combination with different metals and oxides was investigated. Here, it was found by XPS that for the switching of the PCMO/metal combinations, the formation of a native oxide at the interface between PCMO and the metal is essential. For PCMO/metal combinations that did not form this oxide, no switching could be detected. However, switching could be observed for all PCMO/oxide combinations investigated. The combinations PCMO/Al, PCMO/Ta_2O_5 and PCMO/WO_3 were identified as promising and consequently characterised in detail. Measurement of the SET and RESET kinetics of the corresponding devices revealed that all area-switching devices are based on pure field-accelerated ionic motion and Joule heat plays no role. The PCMO/Al devices showed the lowest switching voltages and switching times, possibly due to the higher fields in the very thin Al_2O_3 interface.

The experimental results led to the implementation of a simple mathematical model consisting of two resistors to describe the switching curve of the devices. These two resistances could be assigned to the native oxide at the interface and to the oxygen and hole depletion zone in the PCMO. Then, the fit parameters were assigned to physical quantities corresponding to the transport mechanism in each material. The simple model could be used to describe ion movement within the devices during SET and RESET process. Therefore, the switching mechanism could be assigned to the exchange of oxygen between the PCMO and the oxide. This has provided new insight into the switching behaviour of area type switching memristors.

Due to the very gradual switching process, the implementation of the learning rule "spike-timing dependent plasticity" (STDP) could be demonstrated with the help of the PCMO-based devices. Furthermore, the applicability of the area type switching PCMO in artificial neural networks could be demonstrated. The devices could be used in simulations as weighted connections in a multidimensional perceptron network and achieved an accuracy of up to 82 % in pattern recognition.

II. Kurzfassung der Promotion

Motivation, Ziel und Aufgabenstellung:

In den letzten Jahrzehnten ist die Welt immer stärker vernetzt worden. Immer mehr Geräte sind untereinander und mit dem Internet verbunden. Diese Entwicklung der Hightech-Branche wurde vor allem durch das Internet vorangetrieben. Die immer größeren Datenmengen, die verarbeitet werden müssen bringen die aktuelle Technologie an ihre Grenzen. Nicht nur physikalische Grenzen stehen dabei im Weg sondern auch Grenzen der heutigen Computerarchitektur. Daher sind wesentliche Entwicklungen in der Speicher- und Computertechnologie notwendig. Ein erfolgsversprechendes Konzept hierfür sind resistiv schaltende Speicherzellen, auch Memristoren genannt. Hierbei werden durch spannungsindizierte Widerstandsänderungen in einem Bauelement Informationen gespeichert. Diese Bauelemente können sowohl zur Datenspeicherung, als auch als künstliche Synapsen in neuromorphen Schaltungen eingesetzt werden. Für die Widerstandsänderung in diesen Bauelementen sind verschiedene physikalische Prozesse zuständig. Hierbei kann man auch zwischen sogenannten filamentären und flächigen Systemen unterscheiden. Bei den weit verbreiteten filamentären Systemen wird die Widerstandsänderung durch ein leitendes Filament im Isolator herbeigeführt. Dabei kommt es durch ein starkes Aufheizen des Bauelements zu einem abrupten Anstieg des Stroms während des Einschaltprozesses. Bei den flächig schaltenden Systemen hingegen wird die Widerstandsänderung durch Ionenmigration über die gesamte Bauelementfläche induziert. Hierbei erfolgen sowohl das Ein- als auch das Ausschalten ohne eine abrupte Änderung des Stromes. Dies macht die flächigen Systeme interessant für das Speichern von mehreren Zuständen in einem Bauelement und auch für den Einsatz als Synapse in neuromorphen Schaltungen. Die flächig schaltenden Systeme sind jedoch im Vergleich zu den filamentären Systemen weniger gut verstanden.

In dieser Arbeit sollten $Pr_{1-x}Ca_xMnO_3$ (PCMO) basierte, flächig schaltende Bauelemente auf ihre Einsetzbarkeit in solchen Schaltungen untersucht werden. Hierbei sollten neben der elektrischen Charakterisierung auch verschiedene Analysemethoden wie Rasterkraftmikroskopie (AFM), Röntgenphotoelektronenspektroskopie (XPS) und Transmissionselektronenmikroskopie (TEM) verwendet werden, um die physikalisch-chemischen Prozesse aufzuklären. Mit Hilfe dieser Messungen sollte ein mathematisches Modell zur Beschreibung des Schaltverhaltens aufgestellt werden, um neue Erkenntnisse über den Schaltmechanismus innerhalb dieser Bauelemente zu gewinnen und um zukünftig für die Simulation neuromorpher Schaltungen eingesetzt werden zu können.

Wesentliche wissenschaftliche Beiträge der Arbeit:

Ein Schwerpunkt der Arbeit war die Entwicklung der Herstellungsprozesse für PCMO-basierte memristive Bauelemente. Zunächst wurden die Eigenschaften der PCMO Schichten bei verschiedenen Wachstumsbedingungen untersucht. Hierbei konnte gezeigt werden, dass amorphes PCMO bei einer Temperatur von 650 °C seine Struktur in eine polykristalline Struktur ändert. Darüber hinaus wurde das Schaltverhalten der PCMO Schichten in Kombination mit verschiedenen Metallen und Oxiden untersucht. Hierbei wurde mit Hilfe von XPS festgestellt, dass für das Schalten der PCMO/Metall Kombinationen die Formierung eines nativen Oxids an der Grenzfläche zwischen PCMO und dem Metall essentiell ist. Für PCMO/Metall Kombinationen die dieses Oxide nicht gebildet haben, konnte kein Schalten nachgewiesen werden. Für alle untersuchten PCMO/Oxid Kombinationen konnte hingegen Schalten beobachtet werden. Als erfolgsversprechend wurden die Kombinationen PCMO/Al, PCMO/Ta_2O_5 und PCMO/WO_3 identifiziert und demzufolge ausführlich charakterisiert. Die Messung der SET und RESET Kinetik der entsprechenden Bauelemente ergab, dass alle flächig schaltenden Zellen auf einer reinen Feld-beschleunigten Ionenbewegung basieren und Joule´sche Wärme keine Rolle spielt. Die PCMO/Al Bauelemente zeigten die geringsten Schaltspannungen und Schaltzeiten, was eventuell auf die höheren Felder in der sehr dünnen Al_2O_3 Grenzfläche zurückzuführen ist.

Die experimentellen Ergebnisse führten zu der Implementierung eines einfachen mathematischen Models bestehend aus zwei Widerständen zur Beschreiben der Schaltkurve der Bauelemente. Diese beiden Widerstände konnten dem nativen Oxid an der Grenzfläche und der Sauerstoff- und Lochverarmungszone im PCMO zugeordnet werden. Anschließend wurden die Fitparameter physikalischen Größen entsprechend dem Transportmechanismus in dem jeweiligen Material zugeordnet. Dieses einfache Model konnte dazu genutzt werden, die Ionenbewegung innerhalb der Bauelemente während des SET und RESET zu beschreiben. Dadurch konnte der Schaltmechanismus dem Austausch von Sauerstoff zwischen dem PCMO und dem Oxid zugeordnet werden. Dies hat neue Aufschlüsse über das Schaltverhalten der flächig schaltenden Memristoren ergeben.

Aufgrund des sehr graduellen Schaltprozesses konnten mit Hilfe der PCMO-basierten Zellen die Implementierung der Lernregel „Spike-timing dependend plasticity“ (STDP) demonstriert werden. Außerdem konnte die Einsetzbarkeit der flächig schaltenden PCMO in künstlichen neuronalen Netzen gezeigt werden. Die Bauelemente konnten in Simulationen als gewichtete Verbindungen in einem mehrdimensionalen Perzeptron Netzwerk eingesetzt werden und erreichten bei der Mustererkennung eine Genauigkeit von bis zu 82 %.

III. List of publications

Parts of this thesis have previously been published:

- Gutsche A, Siegel S, Zhang J, Hambsch S and Dittmann R (2021) "Exploring Area-Dependent $Pr_{0.7}Ca_{0.3}MnO_3$-Based Memristive Devices as Synapses in Spiking and Artificial Neural Networks." *Frontiers in Neuroscience.* 15:661261. [1]
- Gutsche, A., Hambsch, S., Branca, N. C., Dittmann, R., Scholz, S., & Knoch, J. (2022). "Disentangling ionic and electronic contributions to the switching dynamics of memristive $Pr_{0.7}Ca_{0.3}MnO_3$/Al devices by employing a two-resistor model." *Physical Review Materials*, 6(9), 095002. [2]

Other publications:

- Siegel, S., Baeumer, C., Gutsche, A., von Witzleben, M., Waser, R., Menzel, S., & Dittmann, R. (2021). Trade-Off Between Data Retention and Switching Speed in Resistive Switching ReRAM Devices. *Advanced Electronic Materials*, 7(1), 2000815. [3]
- Heisig, T., Lange, K., Gutsche, A., Goß, K. T., Hambsch, S., Locatelli, A., ... & Dittmann, R. (2022). Chemical Structure of Conductive Filaments in Tantalum Oxide Memristive Devices and Its Implications for the Formation Mechanism. *Advanced Electronic Materials*, 2100936 [4]
- Pries, J., Stenz, C., Schäfer, L., Gutsche, A., Wei, S., Lucas, P., & Wuttig, M. (2022). Resistance Drift Convergence and Inversion in Amorphous Phase Change Materials. *Advanced Functional Materials*, 32(48), 2207194.

Table of Contents

I. Abstract **v**

II. Kurzfassung der Promotion **vii**

III. List of publications **ix**

1. Introduction **3**

2. Fundamentals **7**

2.1. Resistive Switching 7

2.2. Praseodymium Calcium Manganate 10

2.3. Neuromorphic Computing 13

3. Experimental Methods **17**

3.1. Deposition Methods 17

3.1.1. Pulsed Laser Deposition 17

3.1.2. Electron-beam evaporation 18

3.1.3. Sputtering of metals and oxides 19

3.1.4. Atomic layer deposition of oxides 20

3.2. Sample Processing Methods 20

3.2.1. Rapid Thermal Annealing 20

3.2.2. Lithography 21

3.2.3. Reactive Ion Beam Etching 22

3.3. Thin Film Characterisation methods 22

3.3.1. Atomic Force Microscopy 23

3.3.2. X-Ray Diffraction 23

3.3.3. X-Ray Reflectometry 24
3.3.4. X-Ray Photo-electron Spectroscopy 25
3.3.5. Transmission Electron Microscopy 26
3.4. Electrical Characterisation 26
3.4.1. Keithley 2611 27
3.4.2. Keithley 4200-SCS 27
3.4.3. ArCONE 28

4. Growth **31**

4.1. General growth and properties of $Pr_{0.7}Ca_{0.3}MnO_3$ 31
4.2. Rapid Thermal Annealing 32
4.3. Variations of PCMO thin film growth 35
4.3.1. Impact of laser energy 35
4.3.2. Thickness variations of PCMO thin film 37
4.3.3. Impact of O_2 pressure 40
4.3.4. Growth of different PCMO stoichiometry 44
4.3.5. Impact of temperature during RTA 46
4.4. Conclusion of growth process 48

5. Deposition of interface layer **51**

5.1. PCMO in combination with oxidisable metals 51
5.1.1. PCMO/Al interface 52
5.1.2. PCMO/Ta interface 57
5.1.3. PCMO/W interface 59
5.2. PCMO in combination with Oxides 62
5.2.1. PCMO/Ta_2O_5 interface 62
5.2.2. PCMO/WO_3 interface 64
5.3. Conclusion of PCMO with different interface layer 64

6. Resistive Switching Properties of PCMO **67**

6.1. Impact of PCMO and Al thickness on resistive switching behaviour 67

6.1.1. Impact of PCMO thickness on resistive switching behaviour 67

6.1.2. Impact of Al thickness on resistive switching behaviour 72

6.2. Resistive switching of PCMO/metal devices 75

6.2.1. Discussion of PCMO/metal devices 79

6.3. Resistive switching of PCMO/oxide devices 81

6.3.1. Discussion of PCMO/oxide devices 90

6.4. Discussion of PCMO devices in combination with different interface layers 92

6.5. Switching properties of selected device stacks 94

6.6. Conclusion of switching properties of selected device stacks 103

7. Two Resistor Model **105**

7.1. Description of I-V measurement with two resistor model 105

7.2. Determination of R_1 and R_2. 106

7.3. Physical meaning of fit parameters of two resistor model 108

7.4. Description of resistive switching with two resistor model 110

7.5. Subloops 113

7.6. Conclusion of two resistor model 115

8. Switching Kinetics of PCMO **117**

8.1. PCMO/Al switching kinetics 118

8.2. PCMO/Ta_2O_5 switching kinetics 122

8.3. PCMO/WO_3 switching kinetics 124

8.4. Discussion of kinetics 126

8.4.1. Comparison of PCMO kinetics 126

8.4.2. PCMO kinetics in comparison with other systems 131

8.5. Conclusion of switching kinetics 133

9. Neuromorphic Applications **135**

9.1. Long Term Potentiation / Depression 135

9.1.1. Resistance-Time-Dependence 137

9.2. Spike Timing Dependent Plasticity 139

9.3. MNIST pattern recognition 141

9.3.1. Description of network and algorithm 141

9.3.2. Results of simulations 143

9.4. Conclusion of neuromorphic applications 145

10. Conclusion & Outlook **147**

10.1. Conclusion 147

10.2. Outlook 150

A. Appendix **153**

A.1. Additional information on PCMO thickness determination 153

A.2. Temperature during EBE process 155

List of Figures **156**

List of Tables **164**

References **165**

1. Introduction

In recent decades, the world has become increasingly interconnected. More and more devices are connected to each other and the internet. The evolution of high tech industries was driven by the internet in recent years [5]. Smartphones and computers are not the only decisive factor here; the Internet of Things (IoT) in particular is growing rapidly [6, 7]. IoT refers to the connection of physical objects with the internet. They can exchange data with their environment and the internet with minimal human interaction [8]. This exchange of data will transform the way everyone lives, plays and works [9]. Nevertheless, the amount of devices that exchange data within this framework not only solve problems but also places even higher demands on today's computer hardware like short access latency, high capacity, large bandwidth, low cost, and ability to execute artificial intelligence (AI) tasks [10]. Beside this, the energy consumption of these devices increased rapidly. 5 % to 15 % of the electrical energy generated worldwide is spent to process and manipulate data [11]. The other big challenge is to further increase the computing and memory speed in the computing architecture used today, the von-Neumann architecture. In this architecture the memory and processing unit are separated from each other and data has to be exchange between them frequently. This limits the computing speed and is therefore called the "von-Neumann-bottleneck" [12].

For today's computing architecture, Gordon E. Moore predicted already in 1965 that

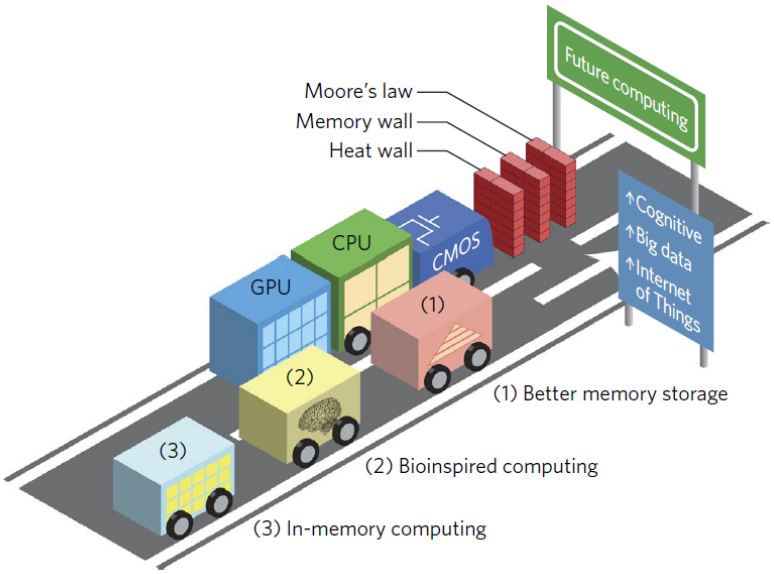

Figure 1.1.: Race to future solutions of today's computing architecture problems. Toady's computer architecture has to face challenges like the end of Moore's law, the memory and the heat wall. Different developments can overtake today's architecture like in-memory computing, bioinspired computing or better memory storage. Taken from [13]

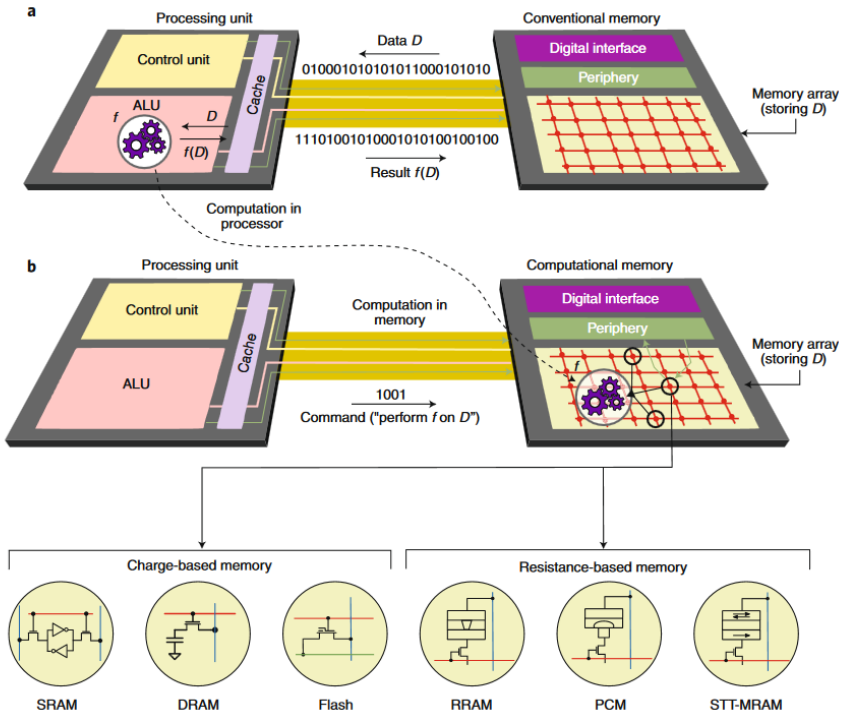

Figure 1.2.: a) Illustration of today's computing architecture with the exchange of date between the computing unit and data storage. b) Illustartion of in-memory computing without data exchange. Taken from [14]

the number of integrated circuits doubles every two years [15]. This enhancement of processing speed by further miniaturisation and increase of transistor density faces its physical limits in today's silicon based technology [16, 17], see figure 1.1. The FLASH memory as an example dominated the nonvolatile memory market the last decades due to its advantages like ultra-low costs or excellent reliability. Now, it is limited in its scaling possibilities due to the further reduction of the thickness of the tunnel oxide and the channel length [18–20]. This leads to quantum effects that affect the performance of these devices.

Therefore, research is being carried out on various solutions to the problems that today's computing architecture is facing. In-memory computing, bio-inspired, and neuromorphic computing is under investigation to overcome the problem of the data transmission and the "von-Neumann-bottleneck" [21–24]. Figure 1.2 shows a schematic drawing of today's computing architecture (a) and a possible solution for in-memory computing (b). One of the most promising techniques for novel memory application is the concept of resistive random-access memory (RRAM). It is based on the non volatile, reversible change of the resistance of a material stack by an external stimulus. Different mechanisms and material stacks have already been considered for resistive switching devices [22, 25, 26]. Furthermore, resistive switching has gained interest due to its fast switching and reading speed.

There is a common agreement in the scientific world that for one class of resistive switching devices the field driven movement of mobile donor type defects, for example oxygen

vacancies is the reason for the resistive change of the RRAM device. Within this movement, a valence change in the corresponding transition metal cations is happening [27–30]. Therefore, this mechanism is called valence change mechanism (VCM). For most of the investigated material stacks a formation of a conductive filament within an insulating layer is crucial for the resistive switching process [4, 30, 31]. Nevertheless, the degree of freedom in these types of devices is limited and material systems with a larger amount of degrees of freedom are indispensable, for example a homogeneous distributed switching effect over the whole device area, would be desirable. This homogeneous switching effects allows to tune device parameters with its area [1, 28, 29, 32]. A large drawback of the area type resistive switching devices is that in contrast to specific filamentary type switching devices, there are no advanced simulation models available for area type resistive switching devices that can describe the switching process. Therefore, the switching process of most of material stacks that show filamentary type resistive switching is better understood than the switching process of the area type resistive switching material stacks.

The transition metal oxide $Pr_{1-x}Ca_xMnO_3$ (PCMO) is known for its area type resistive switching properties. Previous work on PCMO has focused on single crystal PCMO as a model system for two-dimensional switching systems [33, 34]. In this work polycrystalline PCMO thin films in combination with different metals and oxides as candidates for future non-volatile memory and non "von-Neumann" computing architecture are investigated.

Starting with the growth of the PCMO thin film with PLD in chapter 4, variations of the thin film parameters due to variations of the growth parameters are investigated. Beside the impact of the growth, post processing steps are analysed and the impact on the thin film is presented.

In chapter 5, the interface between the PCMO and different metals/oxides is investigated by XPS. The focus here lies on the formation of an interface oxide for different metals in combination with PCMO due to the exchange of oxygen between the two films.

The resistive switching properties of the polycrystalline PCMO thin films are investigated in chapter 6. First, the impact of different PCMO growth parameters on the resistive switching properties in combination with Al as a model system are investigated. Afterwards, the impact of different metals and oxides on the resistive switching properties is analysed. The most promising combinations of PCMO and metals/oxides are used for further analysis of their properties with regard to use in data storage. Additionally, the switching kinetics for these devices are investigated in chapter 8.

Chapter 7 introduces a initial purely mathematical model to describe the switching of the PCMO based devices. With the results of chapter 5 and 6 and further impedance spectroscopy, the two resistors used in this model can be attributed to the interface oxide layer of the metal and an oxygen depletion zone in the PCMO layer. Furthermore, the fit parameters are assigned to physical values by analysing the conduction mechanism inside these two layer. The SET and RESET process is analysed with this two resistor model as well as a volatile part of the LRS that is presented in chapter 6.

This thesis will be completed by like Long Term Potentiation/Depression and Spike Timing Dependent Plasticity measurements. This measurements will be used as input for simulations of a perceptron network based on PCMO resistive switching devices, shown in chapter 9. A general conclusion and outlook is given in chapter 10.

2. Fundamentals

In this chapter the theoretical fundamentals of this work are presented. Here the most important classifications, aberrations and definitions are given. Starting with resistive switching (RS) in general, special attention will be drawn to the area type resistive switching. Afterwards, the properties of the used material $Pr_xCa_{1-x}MnO_3$ (PCMO) are presented. At the end a short introduction into neuromorphic computing is given.

2.1. Resistive Switching

Resistive switching (RS) can be defined as a reversible change in resistance of a given device or material stack, controlled by external stimuli, mostly an applied voltage. Most of the resistive switching devices are two-terminal devices with an active material between two electrodes. Nevertheless, resistive switching is also observed in three-terminal devices. Three-terminal devices are not part of this work and can be found elsewhere [35–37]. Two terminal devices often consist of a metal-insulator-metal structure (MIM). One of these metals forms an ohmic contact to the insulator, the ohmic electrode (OE) and the other one often a non-ohmic contact, the active electrode (AE). When we say positive/negative voltages in the following, the voltage is always applied at the active electrode.

The two resistive states of these devices are named after their relative resistance value, Low Resistive State (LRS) and High Resistive State (HRS), respectively. Typically these states will be defined as "0" (LRS) and "1" (HRS) to compare them with binary logic. It is also possible to write in more than two states into special resistive switching devices. Figure 2.1 shows a schematic of the current-voltage (I-V) curve of resistive switching devices. The transition from the LRS/HRS to the HRS/LRS is called SET/RESET, respectively. Depending on the position of the SET and the RESET one can distinguish between unipolar and bipolar switching. On the one hand if the SET and RESET

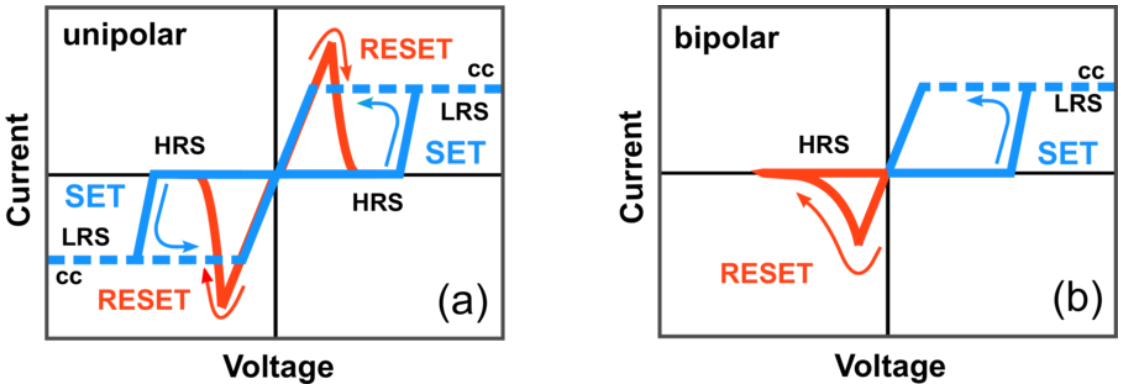

Figure 2.1.: Schematic I-V curves of resistive switching devices with the two basic operation principles unipolar (a) and bipolar (b) switching. Adapted from [27].

process occur within the same voltage polarity but different voltage values, the device shows unipolar switching, see Figure 2.1 (a). On the other hand if the SET and RESET process occur with different voltage polarity it is called bipolar switching, see Figure 2.1 (b).
In unipolar reistsive switching devices, SET and RESET are independent of the voltage polarity and occur within the same voltage polarity. In Bipolar switching devices, SET and RESET occur at different voltage polarities, can further classified by there switching direction, eight-wise (8w) and counter-eight-wise (c8w). In eight-wise switching devices, the SET process occurs at positive voltages and the RESET at negative voltages. It is the other way around for counter-eight-wise devices.

Another classification beside the switching polarity, is the switching mechanism. The main focus in this thesis is on redox-based resistive switching devices. Three different switching mechanisms are known for these type of devices: the thermochemical memory effect (TCM), the valence change mechanism (VCM) and the electrochemical metallisation (ECM) [27, 32]. In TCM cells, a controlled dielectric breakdown is used to change the resistance. TCM cells show an unipolar switching behaviour. Migrating cations are the underlying process of ECM cells. A conductive filament is formed by electrochemical metal deposition and dissolution inside an insulating electrolyte within the application of a voltage. The electrolyte is sandwiched between two metal electrodes. ECM cells show bipolar resistive switching.
The main focus in this work is on resistive switching devices that are based on the valence change mechanism (VCM). VCM is mostly observed in binary transition metals oxides or multinary oxides. Devices that are based on the VCM mostly show a bipolar switching as a of the active material and not electrode dominated as for the ECM devices. In this work the mixed valence manganate Praseodymium Calcium Manganate ($Pr_{1-x}Ca_xMnO_3$/PCMO) is used. The properties of the PCMO will be introduces in section 2.2. There are different models that try to explain the change of the resistance in VCM cells. These models are based on different effects like charge-trapping [38], interface traps [39], metal to insulator transitions [40], and others [25, 41]. Nevertheless, there is a common agreement in the scientific community that the main effect that leads to the resistance change is based on ion migration [27]. Oxygen vacancies act as mobile donors in the system and an enrichment or depletion of oxygen vacancies according to $O_O \longleftrightarrow \frac{1}{2} O_2(g) + V_O^{**} + 2\,e^{'}$ leads to change of the properties of the system.

In addition to the distinction with regard to the switching mechanism, resistive switching devices can also be distinguished based on their switching geometry. Here a distinction is made between filamentary and area type resistive switching [25, 27]. Figure 2.2 a) shows a scheme of a filamentary resistive switching device. In this type of devices, the resistance change is induced by the formation of a conductive filament in an insulating layer connecting the two electrodes. This leads to an abrupt increase of the current that has often be limited by an external current compliance. The resistive switching occurs by the formation and the partly rupture of the filament. Furthermore, during the formations of the filament, the device heats up [42]. The filament decouples the resistance of the LRS from the device size. Only the HRS changes with changing device size. This means that the ON/OFF-ratio increases with decreasing device size. This can only be generalised for single filament devices. Multi-filamentary devices are not covered here. Filamentary switching is observed in different oxide based devices, e.g. Ta_2O_5 , HfO_2 or

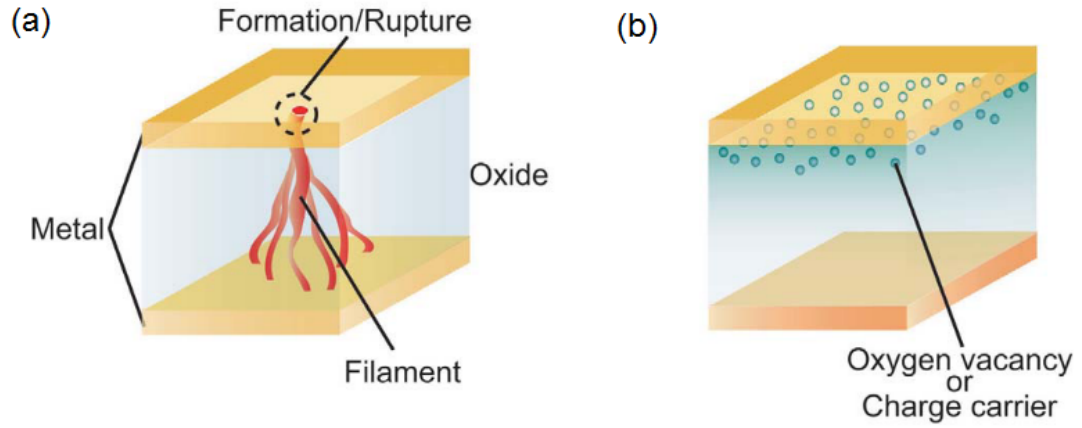

Figure 2.2.: a) Filamentary type resistive switching: A conductive filament is formed through the insulating oxide. (b) Homogeneous area type switching: The entire interface takes part in the switching process. Taken from [25]

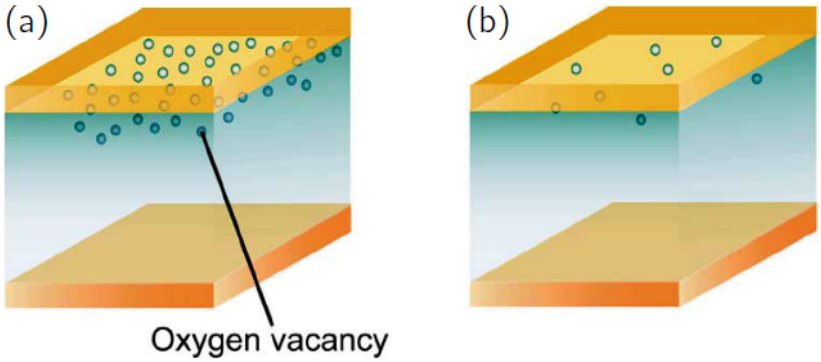

Figure 2.3.: Scheme of area type resistive switching devices. The amount of oxygen/oxygen vacancies inside the material determines the resistance state. The resistance is change by the exchange of oxygen/oxygen vacancies. Taken from [25]

$SrTiO_3$ [4, 30, 43–45]. The background behind the switching mechanism of filamentary switching devices is object of different scientific studies [4, 30].

The main focus of this work is on area type resistive switching due to the fact that PCMO is known for its area type resistive switching behaviour [25, 39, 46–49]. In contrast to the filamentary type resistive switching devices, the change of resistance in area type resistive switching devices is not induced by the formation and rupture of a filament but takes place over the whole device area, see figure 2.2 b). For ideal area type resistive switching devices, the resistance R of the LRS and the HRS scales with the device area A according to

$$R = \rho \frac{l}{A}. \tag{2.1}$$

ρ refers to the resistivity and l to the length.
The resistance change in these area type resistive switching devices can be attributed to

the motion of oxide ions between the material and an interface material, see figure 2.3. This can lead to a modulation of the resistance of the material itself, the band structure and the interface of between two materials. For PCMO a reduction of the oxygen content would lead to an increase of the resistance. Nevertheless, the underlying process is rather complex and no final explanations for the resistive switching in area type resistive switching devices is given in literature [25, 46, 50]. A special type of area type resistive switching is volume type resistive switching. Here the resistance is changed in the whole volume of the material. In this work, however, the name area type resistive switching is used for device stacks where the change in resistance occurs at the interface between two materials. These are also often referred to in the literature as interface type resistive switching devices.

Nevertheless, area type resistive switching devices have some advantages in comparison to filamentary switching devices. The area type resistive switching devices do not heat up during switching [42]. Furthermore, the area dependence of the LRS means that the resistance of the LRS in circuits is not determined by the periphery of the device, but the resistance of the device is decisive for the total resistance of the part of the circuit. This and the fact that the resistance can be adapted to the corresponding circuit characteristics make the flat-sounding components versatile. Additionally, the SET process as well as the RESET process of these devices show a gradual behaviour. This means that no external limitations of the current during the SET is necessary. This makes the area type resistive switching devices particularly interesting for use in multi-bit memories or for neuromorphic circuits in which different states have to be stored.

2.2. Praseodymium Calcium Manganate

$Pr_xCa_{1-x}MnO_3$ (PCMO) is part of the group of mixed-valence manganates. In general mixed-valence manganates form a distorted perovskite structure ABO_3. An ideal perovskite structure can be seen in figure 2.4 (a). It can be described by a cubic unit cell. In mixed-valance manganites the Mn is positioned on the B-site. The A-side is shared by a trivalent rare earth (R) cation, in this case Pr, and a divalent alkaline earth (A) cation, here Ca. The manganese ions are positioned at the corners of the cubic structure. Each manganese ion is surrounded by an octhahedral arrangement of oxygen ions. This leads to a splitting of the five 3d-orbitals of the Mn. The three axial 2p-orbitals of the oxygen ions are orientated in this arrangement along the same direction as the d_{z2} and d_{x2-y2} components of the d-orbitals of the manganese ion. Coulomb repulsion between the electrons of the Mn orbitals and the O^{2-} lifts the two orbitals up in energy to the e_g-level. The d_{xy}, d_{xz}, and d_{yz} components are orientated between the O_{2p} orbitals and only have a small overlap, they are energetically favourable. Therefore, they are energetically lowered and form the three t_{2g}-level. This crystal field splitting can be seen in figure 2.4 (b).

The composition $R_{1-x}A_xMnO_3$ can be seen as solid solution of $RMnO_3$ and $AMnO_3$. In this case A^{2+} acts as acceptor type dopant for the $RMnO_3$ host crystal due to the formal charges [33]. In the material used in this work calcium atoms replace the praseodymium atoms. The valence of Ca and Pr is different, Pr^{3+} and Ca^{2+} for this reason the Mn atoms have to change their valence to establish neutralisation, Mn^{3+} and Mn^{4+}. The

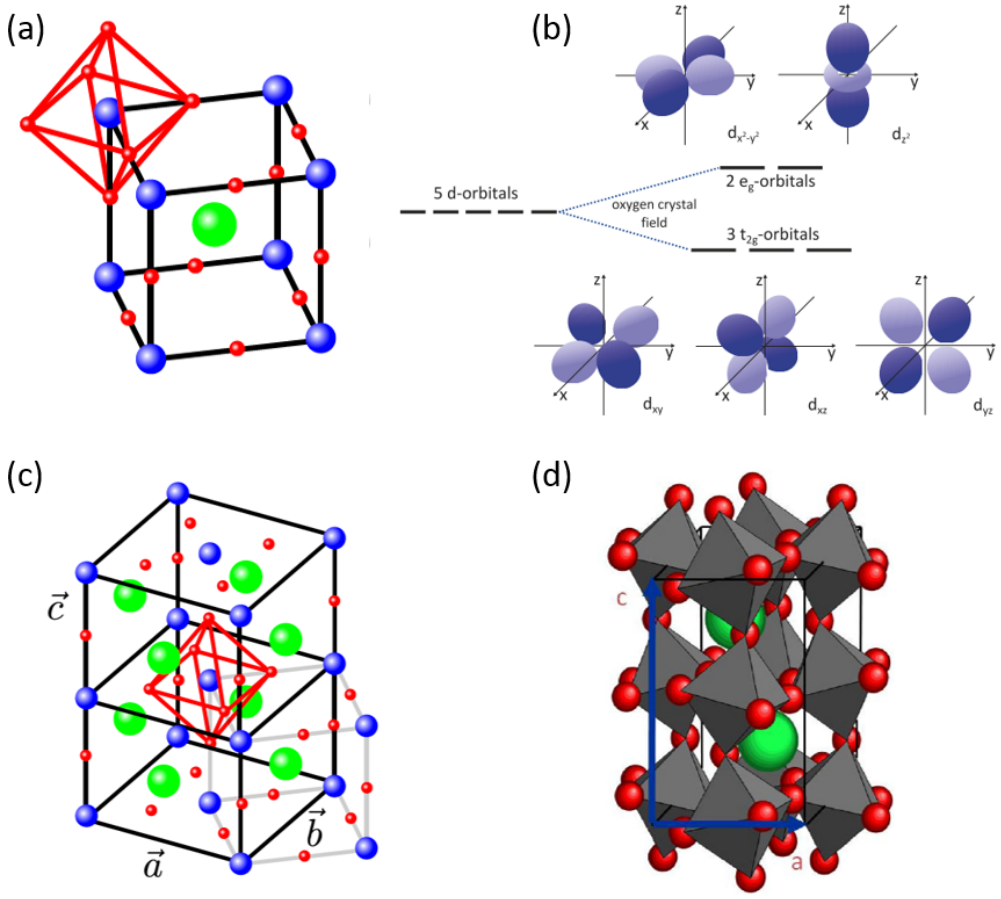

Figure 2.4.: (a) Schematic structure of a cubic perovskite structure with Goldschmitt factor of 1, taken from [51]. (b) Orbital splitting due to the electronic properties of the oxygen octahedran, taken from [33]. (c) Larger unit cell for perovskites with orthorhombic lattice structure and (d) tilted orthorhombic structure, taken from [51].

correct formula for PCMO is

$$Pr^{3+}_{1-x}Ca^{2+}_{x}[Mn^{3+}_{1-x}Mn^{4+}_{x}]O^{2-}_{3}. \tag{2.2}$$

The size of the different cations have a crucial impact on the stability of the structure and its cubic behaviour. The tolerance factor defined by Goldschmitt [52]

$$\Gamma = \frac{1}{\sqrt{2}} \frac{r_A + r_O}{r_B + r_O} \tag{2.3}$$

relates the radii of the ions to the lattice structure. If Γ would have a value of 1, PCMO would form a cubic structure. Hence the perovskite structure tolerates a misfit in ionic sizes which can go along with distortions of the unit cell leading typically to a larger unit cell of lower symmetry. Furthermore, in RMO with a factor of around 0.9 the oxygen octahedra are tilted.

The electrical properties of PCMO can be mainly described by Mn-O connections. To gain a deeper understanding of the electronic properties of the mixed valence state of PCMO, the two cases $PrMnO_3$ (PMO) and $CaMnO_3$ (CMO) will be discussed first. Afterwards, the PCMO will be discussed. In PMO, Mn only occurs in the Mn^{3+} state. The e_g orbital of each Mn ion is occupied and the Mn ions are coupled via the oxygen 2p-orbital. Due to the fact that the oxygen 2p-orbital is occupied by two electrons, the Mn electrons have to be aligned anti parallel due to the Pauli principle. This results in the so called "super-exchange". The antiferromagnetism is present in the co-planar layers and the different layers are coupled ferromagnetically in perpendicular direction. This is caused by the involvement of only one singly occupied d-orbital of the Mn atom. As a consequence, the Fermi level is positioned within the band gap, which forms due to the Jahn-Teller splitting of the e_g bands.
For the CMO case, the Mn ions would only occur in the Mn^{4+} state. No e_g orbital would be occupied and no Jahn-Teller distortion occurs. The t_{2g} orbitals are each filled with one electron. This leads to an octahedral hybridisation between the Mn^{4+} and the O^{2+} orbitals and a cubic structure of the CMO with G-type antiferromagnetism. Each Mn atom is antiparallel orientated to its neighbour. The PMO as well as the CMO are insulating due to the band gap and the lack of unbound charge carriers [33, 34, 53].

In PCMO both Mn states are present, namely Mn^{2+} and Mn^{3+}. This is due to the doping with Ca^{2+}. Therefore, the change of the manganese valence state $Mn^{4+} \rightarrow Mn^{3+}$ can be seen as a formation of holes. In fact the Mn ions lose their e_g electron. This change of the valence state leads to the so called "double-exchange". Here, an electron is transferred between the Mn^{3+} and the oxygen. At the same time an electron is transferred from the oxygen to the Mn^{4+}. The hopping of the electrons is connected with a spin-polarized transfer. This is in contrast to metallic conduction. Here, electrons have both spin directions. Therefore, conductivity and magnetism are correlated in manganates [33, 34, 53].

Polarons carry the electric current in PCMO [33, 54]. Polarons are fermionic quasi particles which are generated out of the local polarisation of the crystal lattice by a

charged particle. While moving through the crystal lattice the polaron and the lattice distortion move together in a certain direction [55]. The current can be calculated with

$$j = \frac{aen\omega_o}{\pi} \sinh\left(\frac{eaE}{2k_BT}\right) \exp\left(-\frac{E_a}{k_BT}\right) \tag{2.4}$$

which relates the field strength E to the current density j [56]. The other parameters are the distance to the next neighbour a, charge of an electron e, carrier concentration n, optical phonon frequency ω_o and the forming energy of a polaron E_a. This equation assumes that no interaction with defects of the crystal and within polarons occur. It is limited for field strengths of $E < 10^7\,\mathrm{V/cm}$ [56].
PCMO forms an ohmic contact to noble metals like gold or platinum. [25]

2.3. Neuromorphic Computing

As already stated in the introduction the flexibility of computers based on the "von-Neumann" computing architecture has produced a multitude of innovations in recent decades. Besides excelling in complex numerical tasks, "von-Neumann" computers struggle with task like image recognition which are simple to the human brain. Image recognition is solved by highly parallelised network. These networks are modelled on the brain structure. Large amounts of data have to be exchanged in these networks. The energy spent during the data transport between the memory and processor, the so called "von-Neumann bottleneck", become critical. This massive task can be performed by the human brain with a power consumption of only 20 W due to his parallel architecture [57–59]. The power consumption of a "von-Neumann" computer for recognising only 1000 different objects expends about 250 W [58, 60]. The parallel architecture of the brain is built from synapses and neurons. In a rough picture, neurons are the computation elements and synapses the weights connecting them [59, 61]. A scheme of the brain and the synapses can be seen in figure 2.5 a). Every neuron inside the brain has around 10000 inputs from other neurons. It is shown that e.g. the visual system is organised as a hierarchical cascade of interconnected regions in the brain. These regions transform the representation of an object gradually into a permanent form, facilitating perception [58, 62].

Therefore, modern brain inspired computing structures are inspired by the brains hierarchical structure and the framework of connected synapses and neurons [63]. A schematic of such a network is shown in figure 2.5 b). These networks that model the way the brain works are for example artificial neural networks (ANN) [64]. These ANNs are connections of hundreds of artificial neurons connected to each other with different weights [65]. These weights can be represented by the resistance of a memristor. Every artificial neuron has weighted inputs of other neurons, a function that manipulates and balances the input and only one single output. Here the weights form the storage units. Networks that are build in a hierarchical structure and only allow the propagation into a next layer are called feed forward networks. Nevertheless, ANNs consist only of a few thousand of neurons while the brain consist out of several billions of neurons. Even if ANNs are quite accurate by making predictions they are not intelligent in the usual sense of the word, more accurate would be computer intelligence [64].

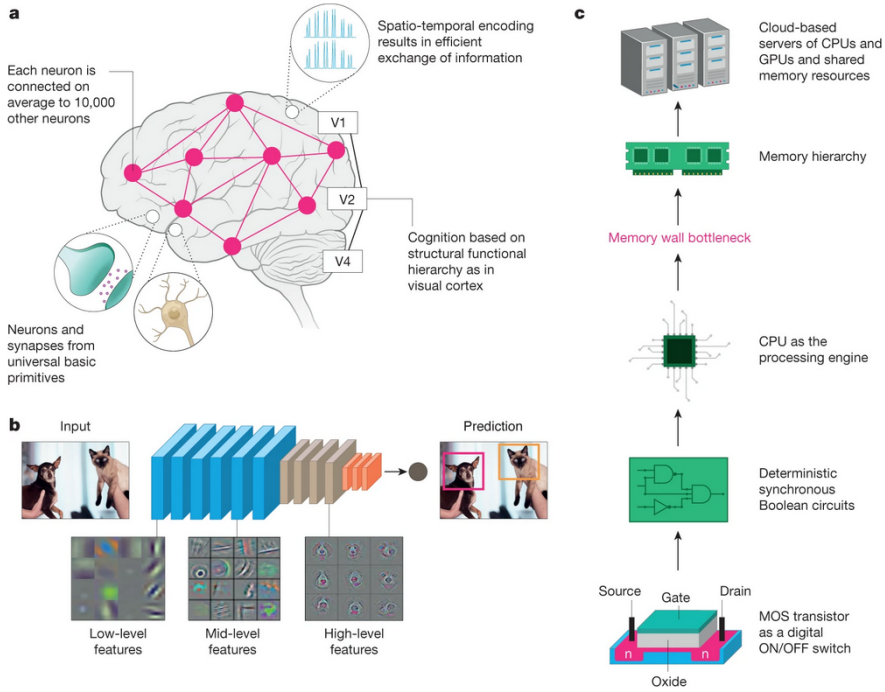

Figure 2.5.: a) A schematic of the organisational principles of the brain with its neurons and synapses. b) A schematic of a multi layer network performing object recognition. c) A schematic of a state-of-the-art silicon based computing system. Taken from [58].

A distinction can be made by the learning methods of the network, namely supervised learning, unsupervised learning, and reinforcement learning. In supervised learning the network is trained by providing input and correct output together [66, 67]. This can be done by an external teacher or the system itself. The latter is referred to as self-supervised. On the other hand, in unsupervised learning only the input signal is presented to the network. Additionally, there is no pre-defined set of categories that the inputs can be . Here, the network has to discover statistically salient features of the input population by itself [68, 69]. The third method, reinforced learning is intermediate form of supervised and unsupervised learning. Here, a feedback about the results, correct or false, is given to the network and adjusts the parameters according to the feedback given [70, 71].

Already in 1986 Rumelhart and McClelland introduced the learning by back-propagation algorithm [72, 73]. Back-propagation is used in layered feed-forward networks and can be classified as supervised learning. In these networks errors that are attributed to each weight by continous application of the chain rule of differentiation of the network formula. This leads to a change of the weights and the goal is to minimise this error [74, 75].

Beside ANNs, spiking neural networks (SNN) are of interest in neuromorphic computing. In SNNs the information is encoded in the timing and the frequency of spikes that are applied to the synapses. One update rule for SNNs is spike timing dependent plasticity (STDP). STDP is a biologically observed process to modify the strength of a synaptic connection in the brain [76]. The artificial implementation of STDP is using the time difference between a pre and a post-synaptic spike to modify the synaptic weight. The

post and pre-synaptic weight often have the same amplitude and duration. The synaptic weight plays a key role how the brain learns and memorises [77]. STDP can be considered as one implementation of the Hebbian learning rule [78]. The main concept of Hebbian learning can be summarised with: cells that fire together wire together [59]. Hebb's learning rule just provide a mechanism that strengthens the connection between two neurons and no active mechanism that weakens the connection. He proposed that unused synapses are weakened through a slow "synaptic decay" [78].

3. Experimental Methods

In this chapter, the growth methods and analysis techniques that were used in this work will be presented. Starting with the different deposition techniques, used to grow the thin films and structure the devices, we will move on to the analysis techniques. Here, a subdivision is made into thin film analysis and electrical characterisation techniques.

3.1. Deposition Methods

The different deposition methods used in this work, pulsed laser deposition (PLD), sputtering and electron-beam evaporation will be presented in the following. The PCMO thin films were grown by pulsed laser deposition. The Ta, Ta_2O_5, W, WO_3, Hf, HfO_2 and Al_2O_3 are grown by sputtering and atomic layer deposition (ALD). Pt, Ti and Al are grown by e-beam evaporation.

3.1.1. Pulsed Laser Deposition

Figure 3.1 shows a schematic drawing of the PLD chamber used for the PCMO growth. The PLD system used in this work was manufactured by *Twente Solid State Technology, B.V. (TSST)*. During the PLD process a pulsed laser is imaged on a moving target. During the time of this work, the movement of the target was changed from rotating target to scanning target (in y/z direction) by *TSST*. This change of the chamber did not change the growth process, only the area of the target that was ablated during the growth process and minimises the amount of unused target material. The used PLD system allows different deposition pressures and gases. In this work mostly O_2 is used as process gas. In one case Ar is used to modify the O_2 partial pressure. The pressure during the deposition is controlled by a massflow controller and a motorised valve, while the turbo pump is running at full capacity.

A *LPI 305 - Lambda Physik* laser with a wavelength of $\lambda = 248\,\text{nm}$, a pulse length between 10 ns to 50 ns and a maximum power of 50 W was used. An adjustable slit outside the vacuum chamber is used to select a homogeneous area of the laser beam and a lens is utilised to sharply focus the laser spot onto the installed target. The laser energy is measured between the slit and the lens. With this energy (E_L), the spot size (A) and the transmission factors of the lens and the window (τ), the fluence (F_L) can be calculated.

$$F_L = \frac{E_L \times \tau}{A} \tag{3.1}$$

Unless otherwise stated the growth parameters that are used for the PCMO can be found in Table 3.1

The main working principle of PLD is that the laser hits the target material. In this process, the target material is converted into a plasma plume[79]. This plasma plume

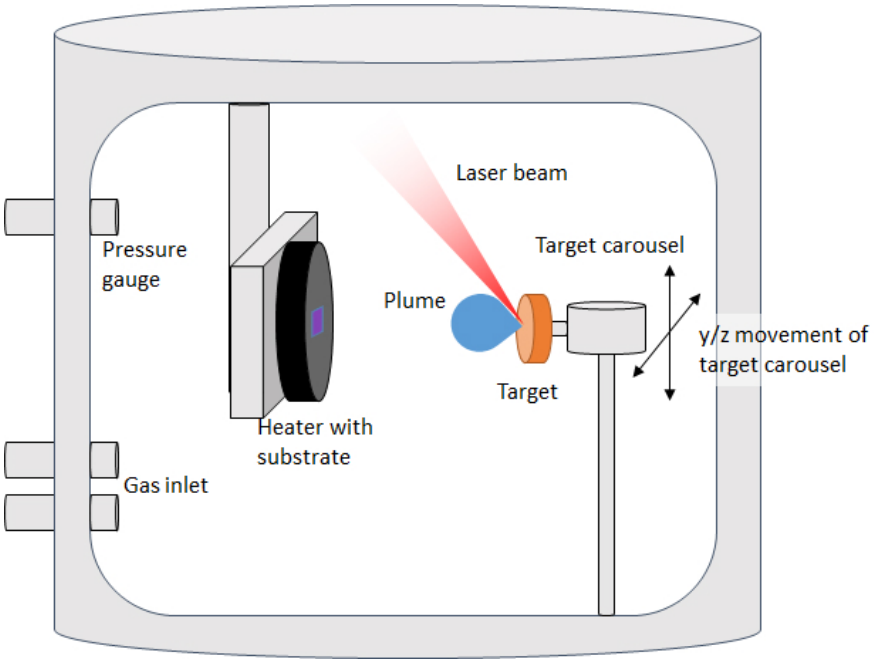

Figure 3.1.: Schematic of PLD chamber manufactured by *TSST*. Laser hitting the target material and creates the plasma plume onto the heated substrate. Different gas inlets and pressure gauges control the growth environment.

Energy	O_2-pressure	frequency	Temperature	Thin film thickness
28 mJ	0.133 mBar	5 Hz	RT	20 nm

Table 3.1.: General PLD parameters of PCMO growth. These parameters are used unless otherwise stated.

is directed into the substrate direction and interacts with the gas inside the chamber. When the plume reaches the substrate, the thin film is deposited.
Due to its larger number of adjustable parameters, PLD is a widely used technique to fabricate complex thin films of multiple elements in science. Parameters that can be adjusted include: the spot size of the laser, fluence and the repetition rate. Furthermore, the interaction between the plume and the substrate is important and can be tuned by the target substrate distance and the background gas. All these parameters are important for the kinetics of the plume and influences the ionisation as well as the oxidation of the plume particles. These influences the growth rate, stoichiometry and crystallinity of the deposited thin film. Small changes of the oxygen partial pressure

Typically, the thin film growth is monitored during the growth with RHEED. Due to the fact, that the growth in this work is performed on Pt covered Si chips, RHEED is not used in this work and will not be explained here.
Further information about PLD and RHEED can be found in references [80–85].

3.1.2. Electron-beam evaporation

Electron-beam evaporation (EBE) is part of the physical vapour deposition (PVD) methods. In this work a EBE chamber from *PST - Plasma & Semiconductor Technologies* is

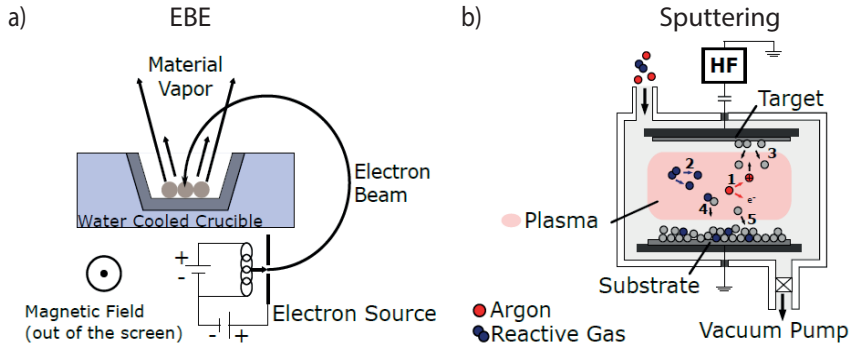

Figure 3.2.: a) Schematic drawing of the EBE process. b) Schematic drawing of a sputter chamber. Both drawings are taken from [34].

used. During EBE the material is evaporated by an electron beam that heats up a target. The material vapour is directed towards a substrate located at a defined distance from the target. The vapour condenses on the cold surface of the substrate and forms a thin film. The growth rate and the thickness of the deposited film is monitored by a quartz crystal oscillator. Figure 3.2 a) shows a schematic image of an electron-beam evaporator.

The EBE is used in this work to grow the Al and Ti inter-layer and Pt top electrode. The growth rate is set to $\approx 0.2\,\text{Å/s}$ for all materials.

Further information about electron beam evaporation can be found in references [86–88].

3.1.3. Sputtering of metals and oxides

Sputtering is a PVD technique to grow thin films. The used sputter tool in this work was build by *SURFACE systems+technology GmbH & Co. KG* and is part of the oxide cluster at *PGI-7, Forschungszentrum Jülich*. The base pressure of this sputter tool is $\approx 10^{-8}$ mbar.

A distinction is made between direct-current (DC) and radio frequency (RF) sputtering. Both techniques will be introduced in the following.

Dc sputtering is based on a glow discharge between two electrodes. The substrate is the anode and the target is the cathode. Additionally, a process gas to achieve the sputtering of the target material is necessary. This is usually Ar. After applying a voltage between the two electrodes a first random ionizing event creates an avalanche that results in the formation of a Plasma. The ions of the plasma are accelerated by the electric field and towards the target and bombard it. The material of the target is removed from the surface and propagates to the surface of the substrate, where it nucleates. Additional electrons are emitted during the ion bombardment that help to sustain the plasma. Adding an external magnetic field would increase the sputter yield and is called magnetron sputtering. The external magnetic field in the region of the target lead the electrons on spirals and increases the probability of the electrons to ionize the Ar atoms. A higher density of Ar^+ leads to a increase of the sputter yield. DC magnetron sputtering is often used for sputtering metallic targets as Pt. Figure 3.2 b) shows a schematic image of a sputter tool.

Table 3.2.: Sputter parameters of the different materials used in this work.

Material	Power / W	pressure / mbar	gas-mixture	distance	growth rate / nm/min
Ta	30 (RF)	1×10^{-2}	Ar	min	3.80
Ta_2O_5	200 (RF)	5×10^{-2}	$3\,Ar\,/\,2\,O_2$	max	16.81
W	50 (RF)	1×10^{-2}	Ar	min	1.67
WO_3	200 (RF)	5×10^{-2}	$3\,Ar\,/\,2\,O_2$	max	0.57
HfO_2	200 (RF)	5×10^{-2}	$3\,Ar\,/\,2\,O_2$	max	1.80

Depositing oxide thin films requieres the introduction of oxygen into the sputtering chamber as additional reactive process gas. The mixture of the two process gasses Ar and O_2 allows to control the oxidation state of the deposited thin film. Nevertheless, the drawback of DC sputtering is the limited applicability to metallic materials. Insulating materials would charge up during bombardment. this charge would work against the applied field. The charging of the material can be circumvented by using a high voltage RF source. The alternating current hast such a high frequency that only electrons are light enough to follow it. This avoids the charging of the target material. Electrons are attracted to the target during the positive cycle giving it a negative bias. During the negative part of the cycle the ion bombardment of the target takes place.

The sputter parameters for the different materials used in this work, can be found in Table 3.2.

Further information about sputtering can be found in references [87, 89, 90].

3.1.4. Atomic layer deposition of oxides

Atomic layer deposition (ALD) is a chemical vapour deposition (CVD) deposition technique that allows to grow within atomic layer precision. During the deposition chemical precursors are sequentially introduced into the chamber and to the surface of the substrate. On the surface they chemically react directly with it to form sub-monolayers of film. The main advantages of ALD are a high uniformity of the film quality, precise thickness control, conformal growth on three-dimensional structures, etc.
In this work, some Al_2O_3 and Ta_2O_5 layers are grown by ALD. If these layers are used, it will be indicated.

Further information about ALD can be found in references [91, 92].

3.2. Sample Processing Methods

The deposited thin films are processed after the deposition in different ways. In the following the rapid thermal processing (RTA), the lithography process and the eactive ion beam etching (RIBE) will be introduced.

3.2.1. Rapid Thermal Annealing

Rapid thermal annealing (RTA) is a high temperature process to expose the sample to a certain temperature for a defined, short period of time. In this work, two different RTA

setups are used. The effects on the sample and the thin film are the same. One setup that is used for RTA is a *Centrotherm RTP 648*. Here, halogen lamps heat up the sample up to a temperature around 1000 °C with a heating rate up to 400 $^{K}/_{s}$. During the processing different gas environments can be set. Temperature overshoots are prevented by using a preheating step up to 200 °C.

The other annealing setup tha is used in this work is a normal tube furnace that allows to move the processed sample into the heated region and out of it. Here also different gas environments can be set.
Unless otherwise stated the used annealing parameters in this work are the following: T=650 °C, t=120 s, N_2 atmosphere.

Further information about RTA can be found in references [93, 94].

3.2.2. Lithography

Lithography is an easy, reproducible method to pattern structures within the micrometer the nanometer range. During the lithography a predefined pattern is written into a photoresist, afterwards the device is etched and the photoresist is removed. One distinguishes between optical and electron-beam lithography. Optical lithography uses ultraviolet light while e-bam lithography uses an electron beam to write in the structure into the photoresist as the names already indicates. In this work mainly optical lithography is used, due to the fact that the lateral resolution of around 1 µm is sufficient for the devices presented in this work. The minimal resolvable structure depends on the wavelength λ and the resist thickness d, given by:

$$\mathrm{CD} = \sqrt{d \cdot \lambda}. \tag{3.2}$$

With a wavelength of $\lambda = 356$ nm, the minimal achievable structure is approximately 740 nm. But an imperfect contact or other factors limit the minimal achievable size. *MicroChemicals GmbH AZ 5214E* image reversal photoresist is used for all devices. This photoresist can be used as positive and negative resist, which makes it versatile in use for various applications.

A scheme of the optical and e-beam lithography process can be seen in figure 3.3. The photoresist is applied to the surface with the help of spin coating. Spin coating the resist with 500 rpm for 5 s, followed by 4000 rpm for 30 s will lead to a thickness of 1.5 µm. Afterwards, the soft bake at 90 °C for 5 min on a hotplate is done. The dehydration of the photoresist happens within a few minutes after the softbake. The exposure of the device is done with a *Süss MicroTec* mask aligner. The sample is exposed to ultraviolet light through the mask, a glass plate with a patterned chromium layer. The exposure time is set to 25 s. The ultraviolet lamp has an intensity of 2.0 $\mathrm{mW/cm^2}$. In this work, contact lithography is used. This means that the mask is put directly on the sample. The disadvantage of the contact lithography is that the mask is exposed to a constant physical stress during exposure.
The development of the resist is done in *AZ 5214E* from *MicroChemicals* for 90 s. Afterwards the sample with the structured resist is cleaned in ultra pure water and dried with N_2.

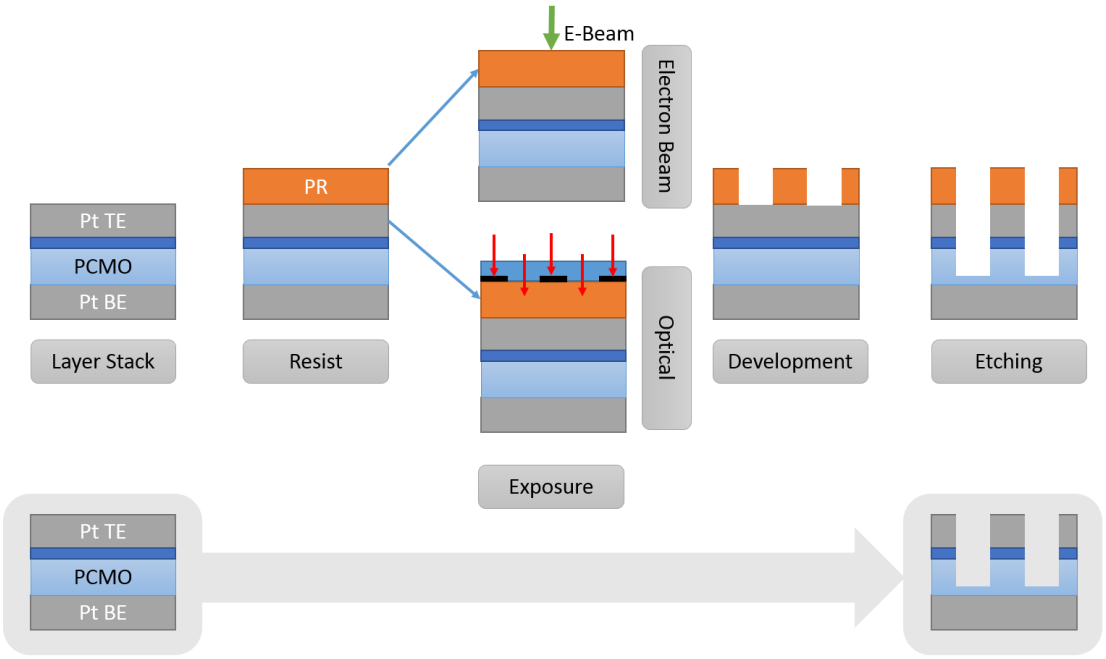

Figure 3.3.: Schematic drawing of the different steps that has to be performed during Lithography.

In this work the device stacks are structured into quadratic pads with 100 µm, 50 µm, 20 µm and 10 µm edge length. These pads are contacted with s-shaped tungsten needles. The bottom electrode is connected via wire-bonding onto a carrier wafer.

Further information about lithography can be found in references [95–99].

3.2.3. Reactive Ion Beam Etching

The etching in this work is done with an *Ionfab300plus* from *Oxford Instruments*, an reactive ion beam etcher (RIBE) with an inductively coupled plasma ion beam source. For the etching process Ar gas is used as process gas. Ar is a non-reactive gas. Therefore, the etching process is a sputter etching process. The Ar ions are accelerated towards the sample and hit its surface. This causes atoms to be knocked out of the material, as in sputtering. The etching based on sputtering is less selective than chemical etching.

Further information about RIBE can be found in references [100–102].

3.3. Thin Film Characterisation methods

Here the methods are presented that are used to determine the thin film properties. Starting with the Atomic Force and Scanning Electron Microscopy to determine the surface morphology of the film, moving forward to X-ray Diffraction (XRD) and X-Ray Photoelectron Spectroscopy (XPS) to analyse the thin film properties.

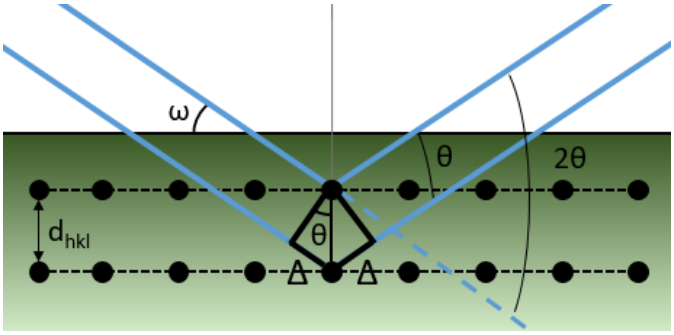

Figure 3.4.: Schmatic of Bragg-Brentano geometry for XRD measurement with reflection at the lattice planes. Redrawn from [34].

3.3.1. Atomic Force Microscopy

Atomic Force Microscopy (AFM) allows to determine the surface morphology of the prepared substrates and thin films. Two different AFMs are used in this work, a *Asylum Research Cypher AFM* and a *nanosurf FlexAFM*. The working principle of both AFMs are the same.

AFM is based on the inter-atomic force between a sharp tip and the sample. This atomically sharp tip is attached to an elastic cantilever and is scanning in lines over a predefined area of the surface if the substrate, mostly in the μm range. A laser is pointed on the backside of the cantilever and reflected on a multiple segment photo-diode. With this, small changes in the morphology of the can be detected. Additionally, an optical microscope is used to position the sample under the cantilever.

An AFM can be operated in different measurement modes. The mode used in this work is the AC tapping mode. Here, the cantilever oscillates with a given frequency close to the resonance frequency. The tip-sample interaction leads to a change in the oscillation frequency and the resonance frequency of the cantilever. This leads to a phase shift that can be measured. The tip-surface distance is enlarged or reduced regarding to the changes measured in the phase and frequency to reach the desired frequency again.

It is possible to image surfaces with a vertical resolution of 1 Å and a lateral solution below 100 nm. The scans are used to monitor the surface morphology between different samples and processing conditions.
Further information about AFM can be found in references [103–106].

3.3.2. X-Ray Diffraction

X-Ray diffraction (XRD) is performed *ex-situ* using a *Bruker D8* diffractometer with a *Cu-K_α* X-ray tube. In the Bragg-Brentano geometry, the X-ray intensity is measured as a function of the incident angle θ and plotted against the diffraction angle 2θ.

Figure 3.4 shows the working principle of the XRD measurement in Bragg–Brentano geometry. Bragg's law is

$$n\lambda = 2d_{hkl} \sin\theta \tag{3.3}$$

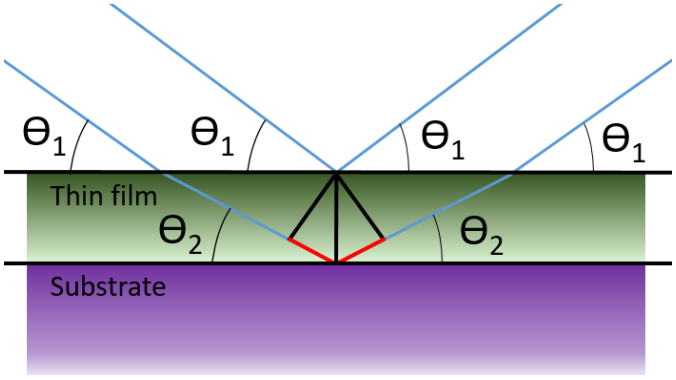

Figure 3.5.: Measurement scheme of the XRR geometry with reflection of at the interfaces. Redrawn from [34]

with λ is the wavelength of the X-ray tube, n is an integer and d_{hkl} corresponds to the distance between certain lattice planes specified by hkl. During measurement the X-ray source as well as the detector are moved, a so called $\theta - 2\theta$ scan. With this, the distance between two lattice planes for a given orientation of the lattice can be calculated.

Further informations about XRD can be found here: [107–110].

GIXRD

Grazing incident XRD (GIXRD) is performed for polycrystalline thin films without a fixed lattice orientation. During GIXRD the direction of the scattering vector and is no longer perpendicular to the sample surface due to the fact, that the incident angle is fixed and only the detector is moved. Therefore, the angle between the diffracting lattice planes and the sample surface changes during the GIXRD measurement.

Further information about GIXRD can be found in references [110, 111].

3.3.3. X-Ray Reflectometry

X-ray reflectometry (XRR) is a tool to measure the thickness of a thin film in a non-destructive way without patterning the thin film. XRR is independent on the crytalinity of the thin film. Beside the layer thickness, material composition, density and surface roughness can be measured.

Figure 3.5 shows a measurement scheme of the XRR measurement. The measurement is performed in the Bragg-Brentano geometry with angles between 0° and 10°. The incident X-ray is partly deflected at the surface and interface in he sample. Other than the XRD $\theta - 2\theta$ scan, the reflected intensity is not only dependent on th path difference but also on the difference in the refractive indices of X-ray beams of the included layers, depending on the electron density in the material. For different material densities the total reflection angle θ_C increases with increasing density of the material. The information of the layer thickness can be gained by the interference fringes. The distance of the of the interference fringes is anti proportional to the layer thickness. The roughness of the surface and the interface can be seen in the decay of the X-ray intensity. A higher roughness leads, due to the more diffuse scattering of the X-rays, to a quicker decay

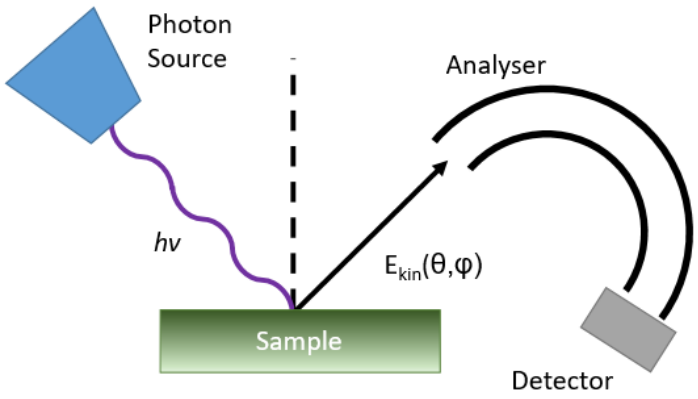

Figure 3.6.: Scheme of XPS measurement to determine the material. Redrawn from [34]

of the intensity with θ. Therefore, XRR can be used to determine interface roughness between two buried layers.

Further information about XRR can be found in references [112, 113].

3.3.4. X-Ray Photo-electron Spectroscopy

X-ray photo-electron spectroscopy (XPS) measurement were performed with a *PHI 5000 Versa Probe* that is part of the oxide cluster at *PGI-7*. Therefore, *in situ* and *ex situ* measurements are possible with this system. This setup consist of a monochromator with an X-ray source (Al K_α, $h\nu = 1486.7\,\text{eV}$) in an ultra high vacuum. The XPS spectra analysis were done using *Casa XPS* with a Shirley background and Gaussian line shapes for oxides and Lorentzian line shapes for metals.

XPS is a surface sensitive analysis technique to reveal the chemical state information of the elements in the sample [114, 115]. A schematic sketch of a XPS can be seen in figure 3.6. XPS is based on the photo ionisation of elements due to the photo-electrical effect. The energy of the incoming photon is absorbed by the sample and transferred to an electron which can leave the sample. The kinetic energy of this electron E_{kin} is measured in a electron spectrometer. From this kinetic energy, the binding energy E_{bin} can be calculated.

$$E_{\text{bin}} = h\nu - \Phi - E_{\text{kin}} \tag{3.4}$$

$h\nu$ is the energy of the incoming photon, Φ the work function of the detector material and E_{kin} is the measured kinetic energy of the electrons [115].

XPS is an element-sensitive technique, due to the fact that every element has a characteristic core level electron energy. The energy of the core level depends on the exact local chemical environment of the material. Chemical shifts are results of the changes of the binding energy. The photo-electrons that are leaving the samples after the excitation with a photon are analysed with a semi-spherical energy analyser. This allows to measure a spectrum of the photo-electron intensity as a function of the binding energy.

Table 3.3.: Intensity ratios of spin-orbit coupling [115].

Orbital	j	peak area ratio
s	$1/2$	-
p	$1/2$, $3/2$	1 : 2
d	$3/2$, $5/2$	2 : 3
...	...	...

An additional effect that can be measured with XPS is the spin orbit splitting. This will lead to two peaks within the XPS spectra, the so called doublet with two electronic states and two separated peaks in the spectrum, depending on the shell of the electron. The interaction of the spin magnetic momentum and the angular momentum of the electrons lead to this spin orbit splitting and the doublets. The spin orientation can either be parallel or anti-parallel to the orbital magnetic momentum which leads to different energetic states. The expected peak ratio and the splitting can be found in table 3.3

The intensity of the characteristic peaks of the materials are representations of the atomic concentration inside the sample. From these peaks the material composition and the valence states of the different materials can be extracted.

XPS is a surface sensitive technique due to the fact that the generated electrons move through the sample and scatter elastically and inelastically. Electrons generated near the surface have a higher probability of leaving the sample. The information depth t can be described as

$$t = 3\lambda \cos\theta \tag{3.5}$$

with λ the mean free path and θ the emission angle. t is typically in the order of a few nanometers.
Further information about XPS can be found in reference [116].

3.3.5. Transmission Electron Microscopy

The Transmission Electron Microscopy (TEM) measurements in this work are performed by *Central Facility for Electron Microscopy at RWTH Aachen.*. Information about the working principle of TEM and the measurements can be found here: [117, 118].

3.4. Electrical Characterisation

The electrical measurements in this work are performed with three different setups, *Keithley 2611, Keithley 4200* from *Keithley, a Tektronix company* and *ArcONE* from *ArC INSTRUMENTS*. The three setups are used in this work for different electrical measurements. The Keithley 2611 is used for voltage sweep measurements, the Keithley 4200 is used for voltage pulse measurements and the ArcONE ist used for Spike Timing Dependent Plasticity measurements. Nevertheless, all measurement setups can also be used for different measurements.

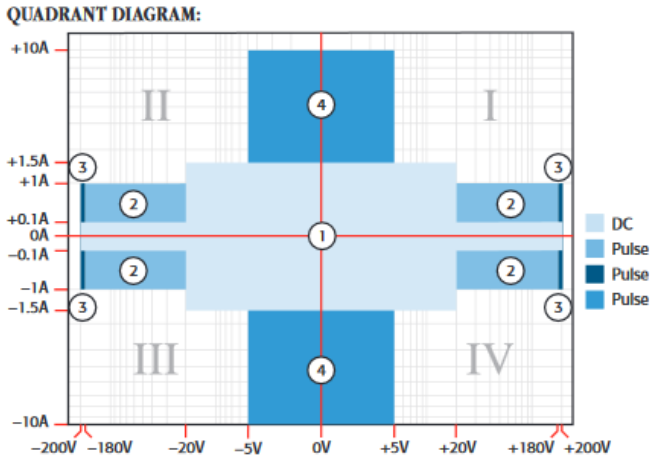

Figure 3.7.: Quadrant diagram of the Keithley 2611A with the different measurement regimes, taken from [119].

3.4.1. Keithley 2611

The Keithley 2611 is used for the voltage sweep measurements that are presented in this work. The samples are mounted in a probe station from *Cascade Mikrotech* and connected to the Keithley 2611 via two coaxial cables and two *7S Compliant S-Wire Shape Tungsten Fine Probe Tips* from *Micromanipulator*. The needles can be manipulated with *PH110* probe petitioners.

$\pm 200\,\mathrm{V}$ is the maximum voltage that can be applied. The used voltage range during the measurement is set to $\pm 20\,\mathrm{V}$ and the current range is set automatically by the Keithley 2611. The whole voltage and current range can be seen in the quadrant diagram in figure 3.7. The measurements in this work are done within the DC range of the quadrant diagram. The voltage sweeps are generated by applying a constant voltage that is increased by a defined voltage step after a defined hold time. After this hold time the current is measured. The voltage step in this work is defined to 20 mV and the hold time is set to 5 mV for all measurements.

Further information about the *Keithley 2611* can be found here: [119].

3.4.2. Keithley 4200-SCS

The used setup for pulse measurements is a *Keithley 4200-SCS* with two *4225-Pulse Measurement Units* (PMUs) with additional *4225-RPM Remote Amplifier/Switch* modules. Therefore, correntd down to the nA level can be measured. The used probe station, *Cascade Microtech MPS150*, that is part of the measurement setup have an *Motic PSM-100* microscope, two *DPP220* probe positioners. Additionally, the PMUs as well as the RPMs are positioned on top of the probe station.

Voltage pulses up to $\pm 40\,\mathrm{V}$ can be generated with the Keithley 4200-SCS with pulse lengths down to 70 ns with ramps of 20 ns. The measurement current range can be set between 100 nA and 200 mA. This wide current range allows a good current resolution for a broad range of device resistances. In table 3.4 and overview of the different pro-

Table 3.4.: Measurements ranges of the Keithley 4200-SCS. Taken from [120].

Used module	Current range	Min. Pulse width	Min. rise and fall time
RPM	100 nA	134 µs	1 µs
	1 µA	20.4 µs	360 ns
	10 µA	8.36 µs	360 ns
	100 µA	1.04 µs	40 ns
	1 mA	370 ns	30 ns
	10 mA	70 ns	20 ns
PMU	10 mA	160 ns	20 ns
	200 mA	70 ns	20 ns

grammable ranges of the current and pulse requirements in the 10 V measurement range can be seen. Depending on the pulse length, different current ranges can be used. For example if the expected current range is between 10 µA and 90 µA, the shortest pulse length that can be chosen is around 1 µs.

Furthermore, it is possible to apply abitrary pulse shapes with this measurement setup and it is possible to perform calculations during the measurements. This gives the opportunity to perform automatic measurements with control sequences.

Further information about the *Keithley 4200-SCS* can be found here: [120].

3.4.3. ArCONE

In this work, the *ArCOne* is only used for STDP measurement. The *ArCONE* is a measurement setup designed by *Arc Instruments* to measure crossbar arrays of non-volatile memory technology. Beside the measurement of device arrays also single devices can be analysed. Beside the possibility to programm own measurement routines within python, the measurement interface *ArCONE* includes some *ArC Beta* functionalities, like I-V measurements, pulse measurements, kinetic measurement, STDP measurements and more. The current cut-off during the I-V measurement happens in maximum 20 ns. Pulse width and inter pulse timing are accurate within 10 ns. Furthermore, the maximum pulse amplitude is $\pm$ 12 V with a raise and fall time down to 30 ns and a pulse width of 90 ns. The minimum current range is 1 nA and the maximum 5 mA with an error lower than 5 % at 0.5 V

Further information about the *ArCONE* can be found here: [121].

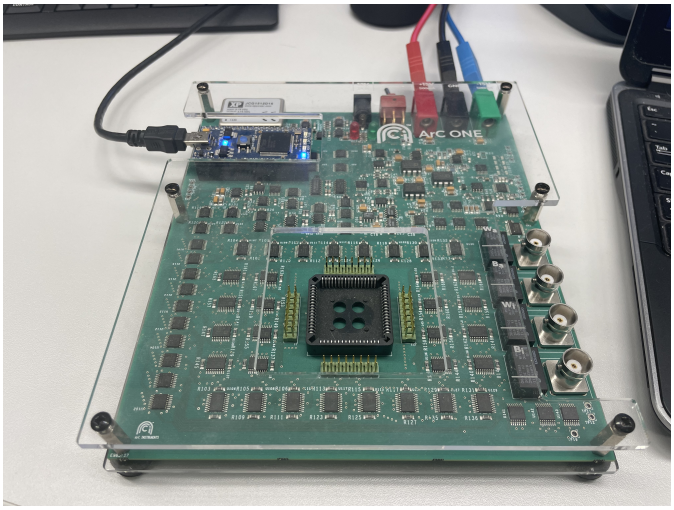

Figure 3.8.: Image of the ArcONE measurement system from *ArC Instruments*.

4. Growth

In this chapter the growth of the polycrystalline PCMO thin films will be discussed. Starting with the general PCMO growth and the Rapid Thermal Annealing process, which has turned out to be the standard growth process for the resistive switching thin films investigated later in this work, different thicknesses and oxygen partial pressures during the growth and the impact of the temperature during the RTA process will be investigated. At the end a short insight into the growth of different stoichiometries will be given.

4.1. General growth and properties of $Pr_{0.7}Ca_{0.3}MnO_3$

The $Pr_xCa_{1-x}MnO_3$ used in this work is grown by PLD at room temperature. The measurement that are used to determine the thin film thickness and growth rates during PLD can be found in Appendix A.

Unless otherwise stated the used PCMO thin films in this work have the properties that are described in this section and is grown with the PLD parameters given in table 3.1.

Figure 4.1 shows two $1 \times 1\,\mu m^2$ AFM scans of the used Pt bottom electrode grown on Si substrate and a 20 nm PCMO film grown with the standard growth parameter: 27 mJ laser energy, 0.133 mbar O_2 pressure, 5 Hz frequency. These parameters are also summarised in table 3.1. The root mean square (RMS) roughness of both scans are calculated 0.89 nm and 1.86 nm with a min-to-max difference of 8.83 nm and 12.82 nm for the Pt and the PCMO surface, respectively. This means that the roughness doubles after the PCMO whereby the min-to-max value increases by 50%.

ICPMS measurements determine the stoichiometry of a thin film grown with a $Pr_{0.7}Ca_{0.3}MnO_3$

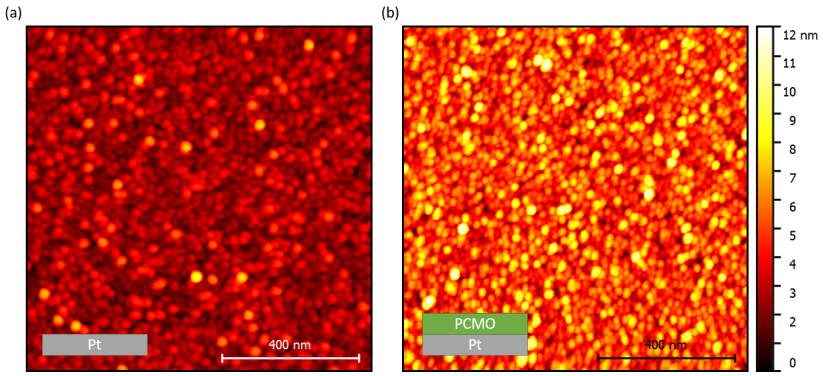

Figure 4.1.: AFM scans of (a) Pt grown on Si and (b) 20 nm PCMO thin film grown at room temperature with a energy of 27 mJ, a frequency of 5 Hz and a O_2-pressure of 0.133 mBar

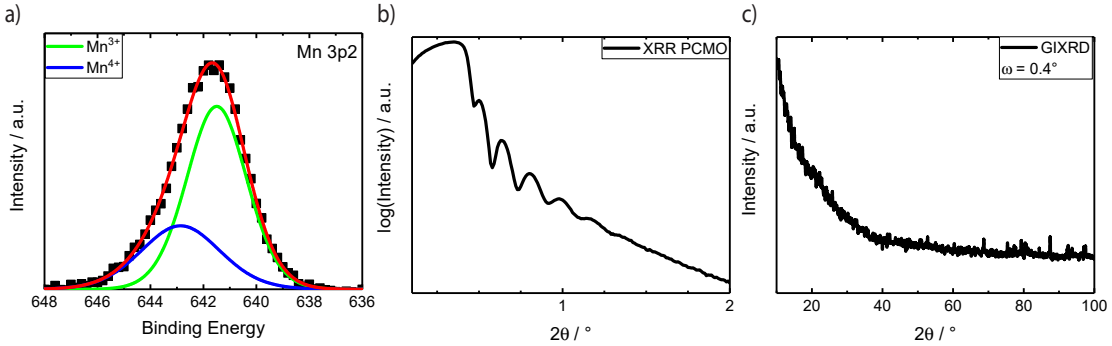

Figure 4.2.: XPS,XRR and GIXRD measurement of standard PCMO thin film. (a) XPS measurement of Mn $2p$ peak to determine the Pr/Ca-ratio of the thin film. The result is $Pr_{0.69\pm0.03}Ca_{0.31\pm0.02}MnO_3$. (b) XRR measurement of as grown PCMO thin film to determine the thickness to 20 nm. (c) GIXRD measurement of as grown PCMO thin film.

target and standard parameters to $Pr_{0.68\pm0.02}Ca_{0.318\pm0.012}MnO_3$. This stoichiometry could also be determined by the Mn oxidation states in the PCMO via XPS, see Figure 4.2 (a). Here the area comparison of Mn^{3+} and Mn^{4+} leads to an stoichiometry of $Pr_{0.69\pm0.03}Ca_{0.31\pm0.02}MnO_3$ that is in good agreement with the ICPMS measurement.

Furthermore, Figure 4.2 (b) shows XRR analysis of the grown thin film. The thin film thickness is determined with the XRR analysis to 20 nm. Due to the high roughness of the thin film, seen in Figure 4.1, the thickness determination can only be an approximation of the real thickness. Therefore, an thickness variation of ± 2 nm is assumed. The thickness of the PCMO thin film is regularly monitored during this work and the amount of pulses used during growth is adapted. Figure 4.2 (c) shows an GIXRD pattern of the as grown PCMO thin film in at an incident angle of $\omega = 0.4°$ in black. No PCMO peak can be seen for the thin film. Therefore one can conclude that the thin film is an amorphous state. The crystallisation into a polycrystalline state is done via a rapid thermal annealing step (RTA).

4.2. Rapid Thermal Annealing

Before going into detail of the PCMO growth with different PLD parameters, the impact of the Rapid Thermal Annealing (RTA) on the PCMO thin film will be described. Like mentioned before, the RTA step is used to crystallise the PCMO thin film. Unless otherwise stated the RT step is performed at 650 °C for 2 min in N_2-atmosphere.

Figure 4.3 shows the changes that occurs in the GIXRD pattern at an incident angle of 0.4°. The GIXRD pattern of the as grown PCMO thin film shows only the peak of the Si substrate underneath the PCMO thin film, see Figure 4.3 (a). After the annealing a wide range of different crystal orientations can be seen in Figure 4.3 (b). The most pronounced peak is the (1 2 1) peak. Beside this, the other peaks can be identified as (0 2 2), (2 0 2), (2 4 0), (2 4 2) and (2 0 4) [122]. In Table 4.1, the peak position, the height ratio of the most pronounced peaks and the full-width-half-maximum of the first four, most pronounced peaks is presented. The lattice planes that corresponds to this peak position are also given in the lower part of Figure 4.3 (b).

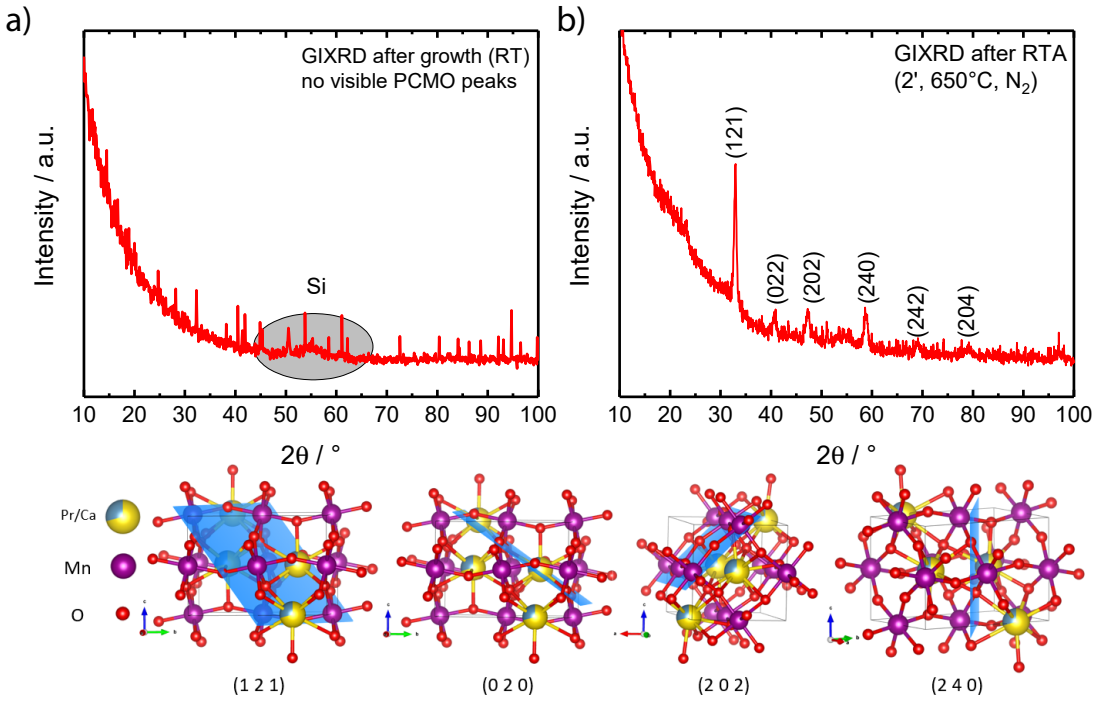

Figure 4.3.: GIXRD measurement of a 50 nm thick PCMO thin film before (a) and after (b) RTA at 650 °C for 2 minutes in N_2-atmosphere. The crystallization of the thin film in different crytsal phases can be seen. The lattice planes of the main diffraction peaks can be seen in the lower part of the figure.

Table 4.1.: Parameters of the highest peaks that are measured in Figure 4.3 (b).

Peak	**(1 2 1)**	**(0 2 2)**	**(2 0 2)**	**(2 4 0)**
Position (measured) / °	33	40.9	47.25	58.65
Position (theoretical) [122] / °	32.9	40.6	47.2	58.9
Height (normlaized on 121)	1	0.174	0.221	0.243
FWHM / °	0.51	0.80	0.76	0.78

ICPMS measurements shows a small change in the cation stoichiometry of the PCMO thin film before and after annealing.
The stoichiometry changes from $Pr_{0.68\pm0.02}Ca_{0.318\pm0.012}MnO_3$ to $Pr_{0.73\pm0.02}Ca_{0.27\pm0.03}MnO_3$. It seems that th amount of Ca^{2+} cations inside the thin film changes during the RTA. An explanation of what happens with the Ca atoms cannot be given here and is not yet fully understood. This behaviour could also be observed with XPS measurements of the Mn peak. The $^{Mn^{3+}}/_{Mn^{4+}}$ ratio changes accordingly.

The overall roughness of the PCMO thin film decreases after the RTA processing while the grain size of the measured grains increases. The calculated roughness is 1.33 nm with a max- value of 12.35 nm. While the max value at the first glance changes only slightly, the general roughness of the film decreases by around 25 %. Figure 4.4 shows the corresponding AFM images: a) $1 \times 1\,\mu m^2$ bare PCMO, b) $1 \times 1\,\mu m^2$ PCMO after RTA at 650 °C for 2 min and c) $5 \times 5\,\mu m^2$ PCMO after RTA at 650 °C fir 2 min. In a

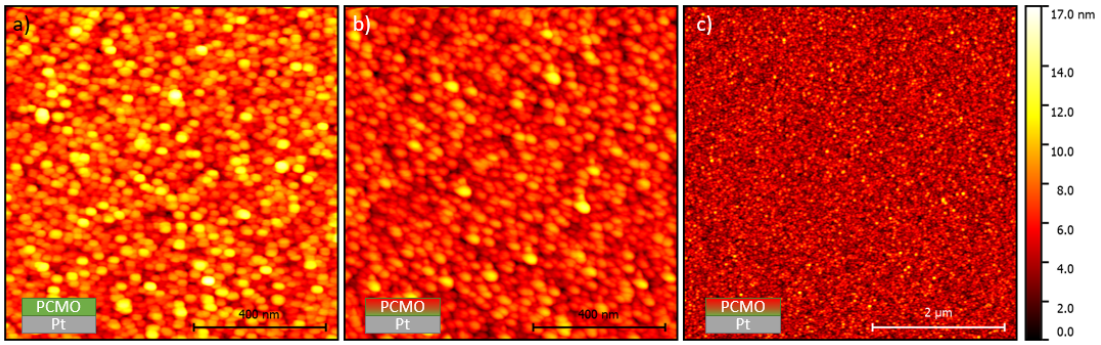

Figure 4.4.: AFM images of PCMO thin film before RTA a) and after RTA b)/c). A decrease of around 25 % in the overall roughness of the PCMO thin film can be observed after the RTA process at 650 °C for 2 min

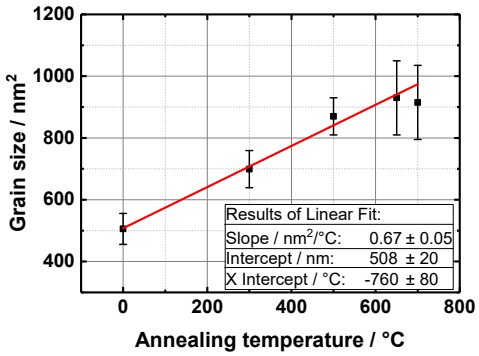

Figure 4.5.: Increase of grain size during the RTA process. Taken from [123]

pre-study it could be shown that beside the roughness, also the grain size changes during the annealing process, see Figure 4.5 [123].

Additionally to the changes in the thin film roughness, a overall change of the thin film thickness can be observed. The thickness is determined using AFM scanning over an predefined edge. Exemplary measurements can be found in Appendix A. Figure 4.6 shows the change of the thin film thickness for 2000 and 3000 laser pulses in absolute and relative values. A clear decrease of thickness by around 42 % can be seen. This change seems to be independent from the initial thin film thickness. For increasing laser energy also no clear trend could be observed, see figure 4.6.
The change in thickness could also be observed during XRR measurement, see Figure 4.7. Comparing the oscillations of the before and after RTA thin film, it can be seen that the thickness change is in the range of 40 % like it was estimated from the AFM measurements. Also a slight change in the total reflection angle could be observed. This gives a hint on changes in the electronic behaviour and the thin film density.

Unless otherwise emphasised, all thicknesses in this work, unless explicitly stated, refer to the layer thickness after annealing.

In conclusion, the RTA process affects the following properties of the thin film: crys-

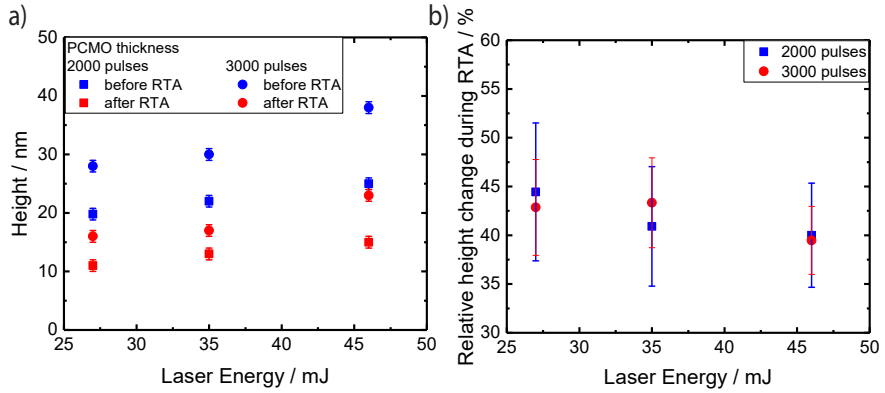

Figure 4.6.: Change of PCMO thickness during RTA process for 2000 and 3000 pulses for different laser energy in absolute and relative values. An overall change in thickness of around 42 % can be observed.

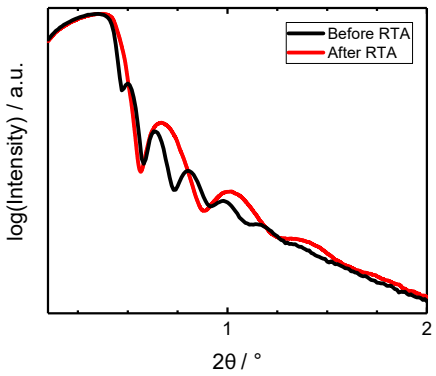

Figure 4.7.: XRR measurements before and after RTA process. Changes in oscillation can be seen.

tallinity, stoichiometry, morphology and thickness.

4.3. Variations of PCMO thin film growth

After describing the RTA process that is part of the standard sample processing in this work, changes in the growth parameters of the PCMO thin film will be described in the following. Unless otherwise indicated, the films shown later in the thesis are grown and processed as described in section 4.1 and 4.2. The following explanations serve only for further understanding of PCMO growth and lead to the general growth conditions. Of course, the order of presentation in this work does not reflect the order of the experiments and only serves to provide a better overview and separation of the additional characterised properties.

4.3.1. Impact of laser energy

To define the laser energy during growth, a series of PCMO thin films are grown at different laser energies at 0.133 mbar O_2-pressure with a laser frequency of 5 Hz. Due

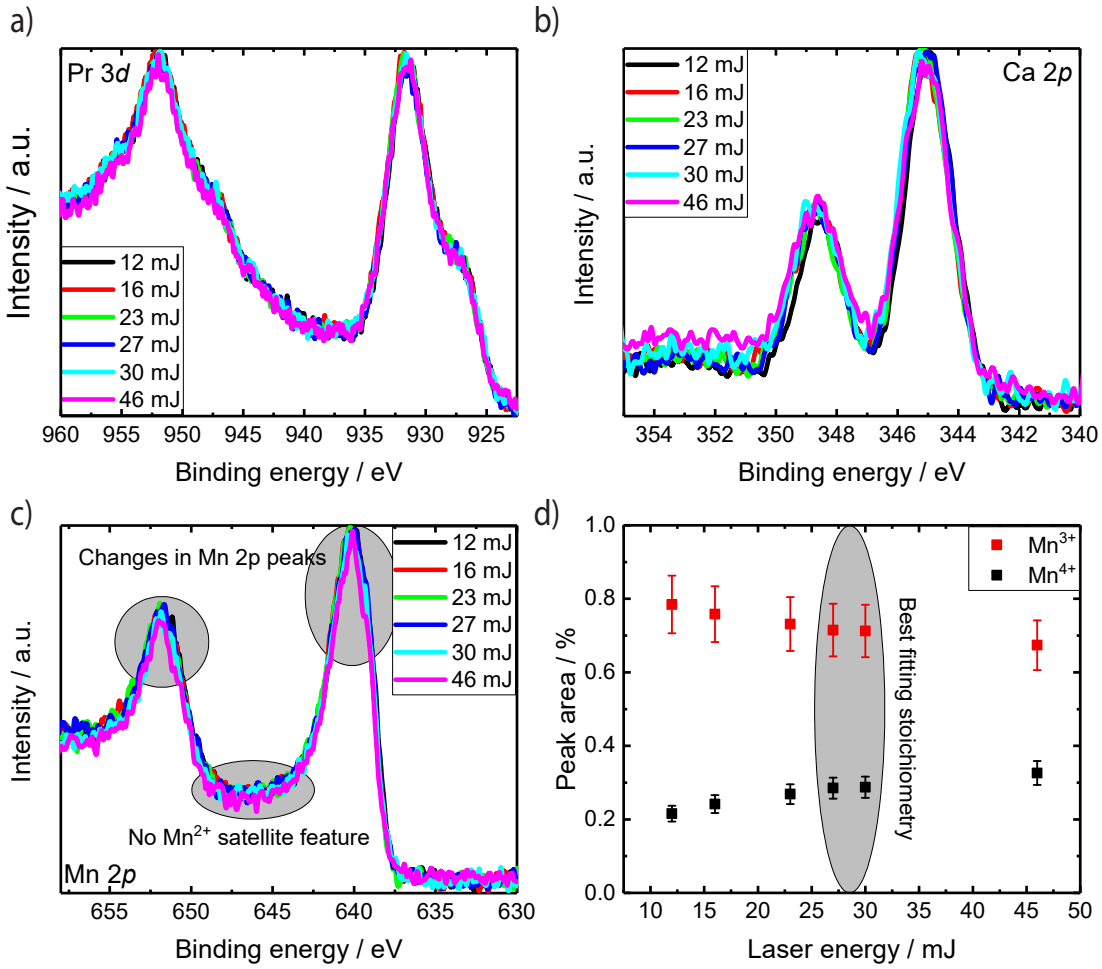

Figure 4.8.: XPS spectra and analysis of PCMO thin films grown at different laser energies. a) Pr $3d$ peaks of PCMO thin films grown with different laser energies. b) Ca $2p$ peaks of PCMO thin films grown with different laser energies. c) Mn $2p$ peaks of PMCO thin films grown with different laser energies. d) Analysis of $^{Mn^{3+}}/_{Mn^{4+}}$ ratio of PCMO thin films grown at different laser energies.

to the fact, that the PCMO thin films are grown polycrystalline at room temperature and no RHEED is used to monitor the thin film growth during growth, to analyse the thin film characteristics by different laser energies the $^{Mn^{3+}}/_{Mn^{4+}}$ behaviour is analysed. This is done with XPS measurements. The used laser energies are 12 mJ, 16 mJ, 23 mJ, 27 mJ, 30 mJ and 46 mJ.

Figure 4.8 shows the Pr $2d$, Ca $2p$ and the Mn $3p$ spectra of PCMO grown with different laser energies. Additionally the $^{Mn^{3+}}/_{Mn^{4+}}$ ratio, determined by the Mn $3p$ peak, is shown. The Pr $3d$ and Ca $2p$ spectra can be seen in figure 4.8 a) and b), respectively. Neither for the Pr nor for the Ca peak big changes can be seen at different energies. The Pr peaks shows a doublet that can be fitted with two peaks at 931.7 eV and 928.3 eV for the Pr $3d\,^5/_2$. In literature, this two doublets can be assigned to Pr_2O_3 [124–128]. This means that the Pr is present in the expected oxidation state, Pr^{3+}.
The Ca $2p$ peak, see figure 4.8 b) shows a doublet with binding energies at 345.6 eV and 348.9 eV. This doublet can be fitted with an single peak for each peak. The binding energies fit to the Ca^{2+} species [129–131]. Only slight changes of the peak position can be seen, this changes are within the measurement and calibration error of the XPS and the peak position control.

The Mn $2p$ peaks for the different laser energies are presented in figure 4.8 c). The Mn $2p$ doublet can be seen. The peaks of the doublet are each fitted two peaks. The binding energies of the fits for the Mn $2p\,^3/_3$ peak are 639.7 eV and 640.7 eV. The peak positions and the spacing of around 1.1 eV fits to the Mn^{3+} and Mn^{4+} oxidation state [132]. Furthermore, it can be seen, that the peak shape slightly differs for different oxidation states. Assuming that the film is completely oxidised, the stoichiometry of the film can be inferred from the ratio of the Mn states. The peak area of the different Mn oxidation states for PCMO thin films grown at different laser energies are shown in figure 4.8 c). It can be seen, that the relative peak area of the Mn^{3+} and Mn^{4+} peak changes with changing laser energy. The relative peak area of the Mn^{3+} peak , that can be referred to the Pr content of the thin film, decreases with increasing laser energy, the relative peak area of the Mn^{4+} peak , that can be referred to the Mn content of the thin film, increases with increasing laser energy. For a laser energy of 27 mJ and 30 mJ, the $^{Mn^{3+}}/_{Mn^{4+}}$ fits the best to the expected target stoichiometry. Beside this for all of the grown PCMO thin films, no Mn^{2+} satellite shake up can be seen. Therefore, one can conclude that no Mn^{2+} states are present in the as grown films. This means, that all of the films consist of Mn^{3+} and Mn^{4+} oxidation states. Therefore, the thin films in this work are grown with an laser energy of 27 mJ.

4.3.2. Thickness variations of PCMO thin film

In this section, the impact of the different PCMO thicknesses on the thin film properties will be shown. In particular, the surface properties of the PCMO layer at different layer thicknesses were investigated. Therefore, 10 nm, 15 nm, 20 nm, 25 nm, 30 nm and 50 nm thick PCMO thin films were grown. Figure 4.9 shows the XRR measurements of the different thicknesses. A clear increase in the oscillation frequency with increasing thickness could be seen. Furthermore it is visible that the 10 nm thin film does not match to the other thin films that are grown. The reason for this and will be explained later.

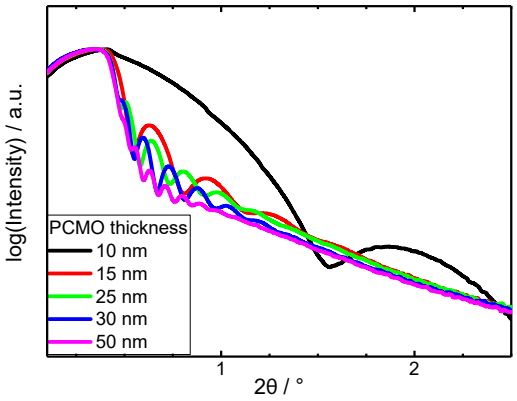

Figure 4.9.: XRR measurements of 10 nm, 15 nm, 25 nm, 30 nm and 50 nm thick PCMO thin films. It can be seen, that the oscillations of the 10 nm PCMO thin film do not match the oscillation of the thicker PCMO thin films.

Figure 4.10 shows $1 \times 1\,\mu m^2$ AFM scans of all different PCMO thicknesses except the 20 nm thin film, this is given in figure 4.4. For the 10 nm thin film an additional $5 \times 5\,\mu m^2$ AFM scan is given. It can be seen, that the 10 nm thin film forms islands. These islands are created during the RTA process and cover the whole substrate surface, like it can be seen in the $5 \times 5\,\mu m^2$ AFM scan. It can therefore be assumed that the PCMO contracts and form these grains. The islands have a size between $0.0025\,\mu m^2$ to $0.0150\,\mu m^2$ and cover 10 % of the whole sample surface. For all the other thicknesses, 15 nm, 25 nm, 30 nm and 50 nm, the PCMO thin film covers the whole sample surface and no clear formation of separated island can be seen.

Figure 4.11 compares different surface properties of the different PCMO thickness. Figure 4.11 a) shows the RMS value of the different thin films. It can be seen that the RMS value first decreases until a minimum is reached by 20 nm and afterwards increases with increasing thin film thickness. The decreasing RMS value for small PCMO thicknesses can be understood by the formation of island like described before. This can also be seen in figure 4.11 b) and c). They shows the highest measured value and the median value of the measurement, respectively. The highest value for the 10 nm thin film is measured to be around (19.3 ± 1.5) nm with the lowest value set to zero. This is twice as hight as the intended film thickness. The median height instead is only around (3.5 ± 0.3) nm for the 10 nm thin film. This is a clear indication for the above described formation of islands. By neglecting the island, the average thickness could be measured to (3.1 ± 0.2) nm. This 3.1 nm fits also to the XRR measurement, shown in figure 4.9.

The max. measured height value of the 15 nm thin film, figure 4.11 b), was determined to 11.8 ± 1.1 nm. This is equivalent to 80 % of the whole thin film. The median value is measured to 5.6 ± 0.3 nm. This corresponds to around 50 % of the max. measured height. This ratio decreases with increasing thin film height down to around 35 % for the 50 nm thin film. Furthermore, the median height value increases slightly with increasing thin film thickness. This is expected for increasing max. height values.

In conclusion it could be said, that the 20 nm PCMO thin film in terms of morphology

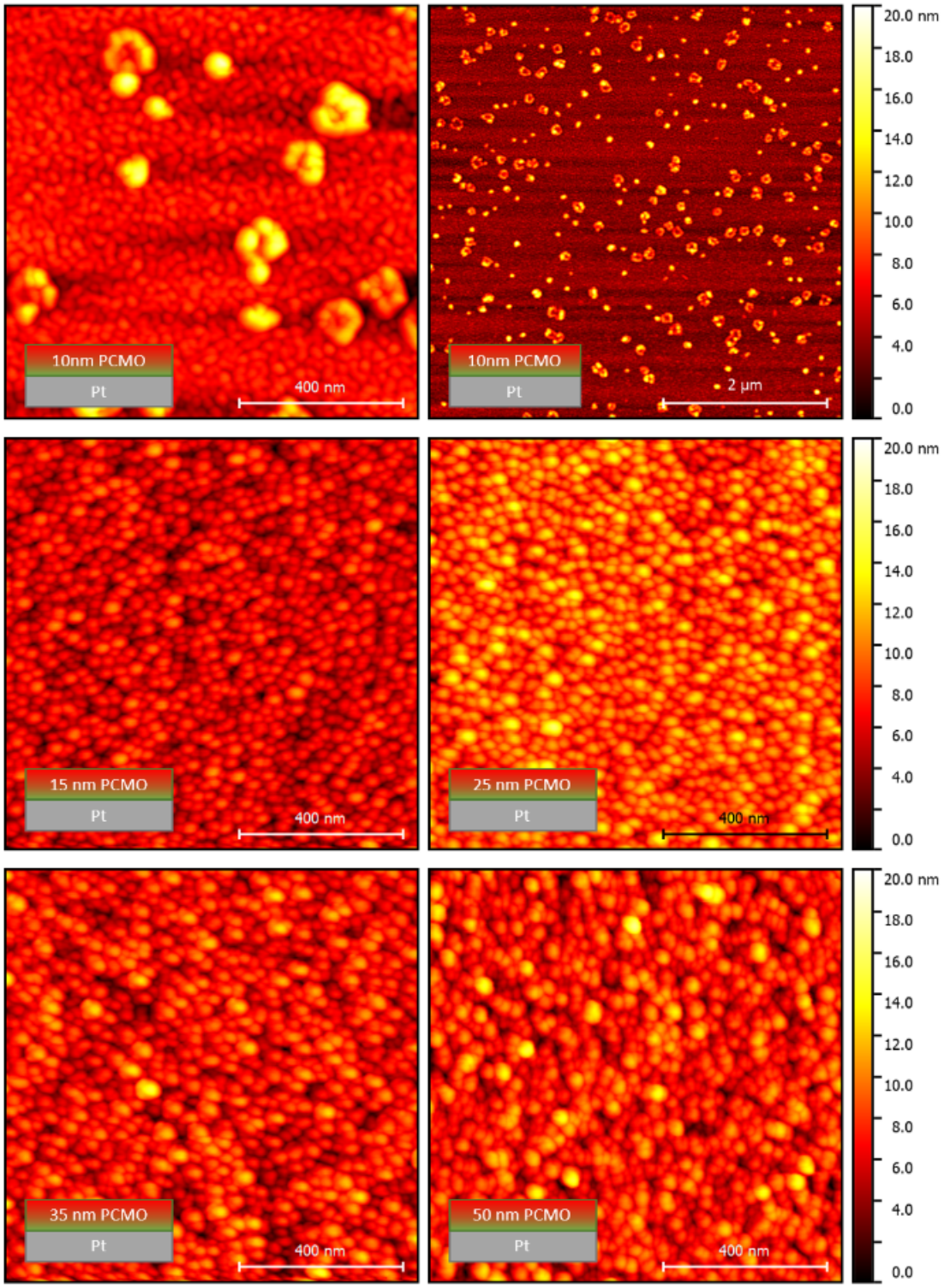

Figure 4.10.: $1 \times 1\,\mu m^2$ AFM scans of 10 nm, 15 nm, 25 nm, 30 nm and 50 nm thick PCMO thin films after RTA process. Additionally an $5 \times 5\,\mu m^2$ AFM scan of the 10 nm thin film is given, to show the island formation across the whole sample surface. The AFM image of the 20 nm can be found in figure 4.4.

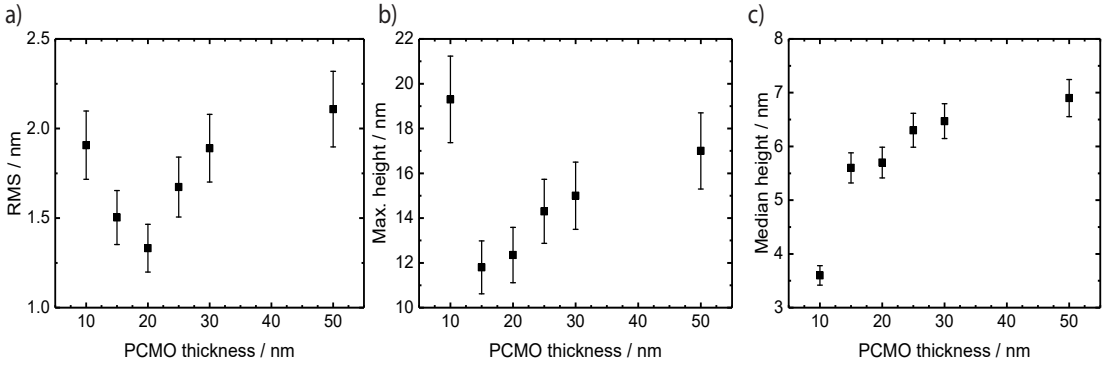

Figure 4.11.: Roughness parameters of the 10 nm, 15 nm, 25 nm, 30 nm and 50 nm PCMO thin film. a) RMS, b) max. height and c) median height values extracted from the AFM scans given in figure 4.10

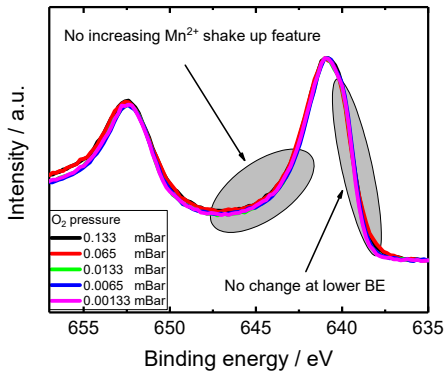

Figure 4.12.: XPS measurement of the Mn $2p3$ peak for different O_2 pressure during PCMO growth. No increase of the Mn^{2+} shake up and satelite feature can be seen. This means that the ambient pressure has no effect on the oxidation state of the PCMO layer.

with the given growth conditions, has the lowest roughness and is therefore the best suitable for the further device processing.

4.3.3. Impact of O_2 pressure

The O_2 pressure inside the PLD chamber effects the thin film growth properties. In this section, the changes in the thin film stoichiometry and the morphology will be shown. To investigate the impact of the gas pressure inside the chamber, 20 nm PCMO thin films are grown at 0.133 mbar, 0.065 mbar, 0.0133 mbar, 0.065 mbar and 0.001 33 mbar O_2 pressure. 0.133 mbar relates to the normal growth conditions.

Figure 4.12 shows the evolution of the Mn $2p3$ XPS peak with decreasing O_2 pressure inside the PLD chamber. No increase of the Mn^{2+} shake up and satellite feature and no change at lower binding energies could be seen, which would indicate a reduction of the thin film. Therefore, it would be possible to conclude, that all the films grown at different O_2 pressures are similarly oxidised. However, this conclusion cannot be considered as accurate, as the films were annealed in N2 and measured ex-situ. It only gives

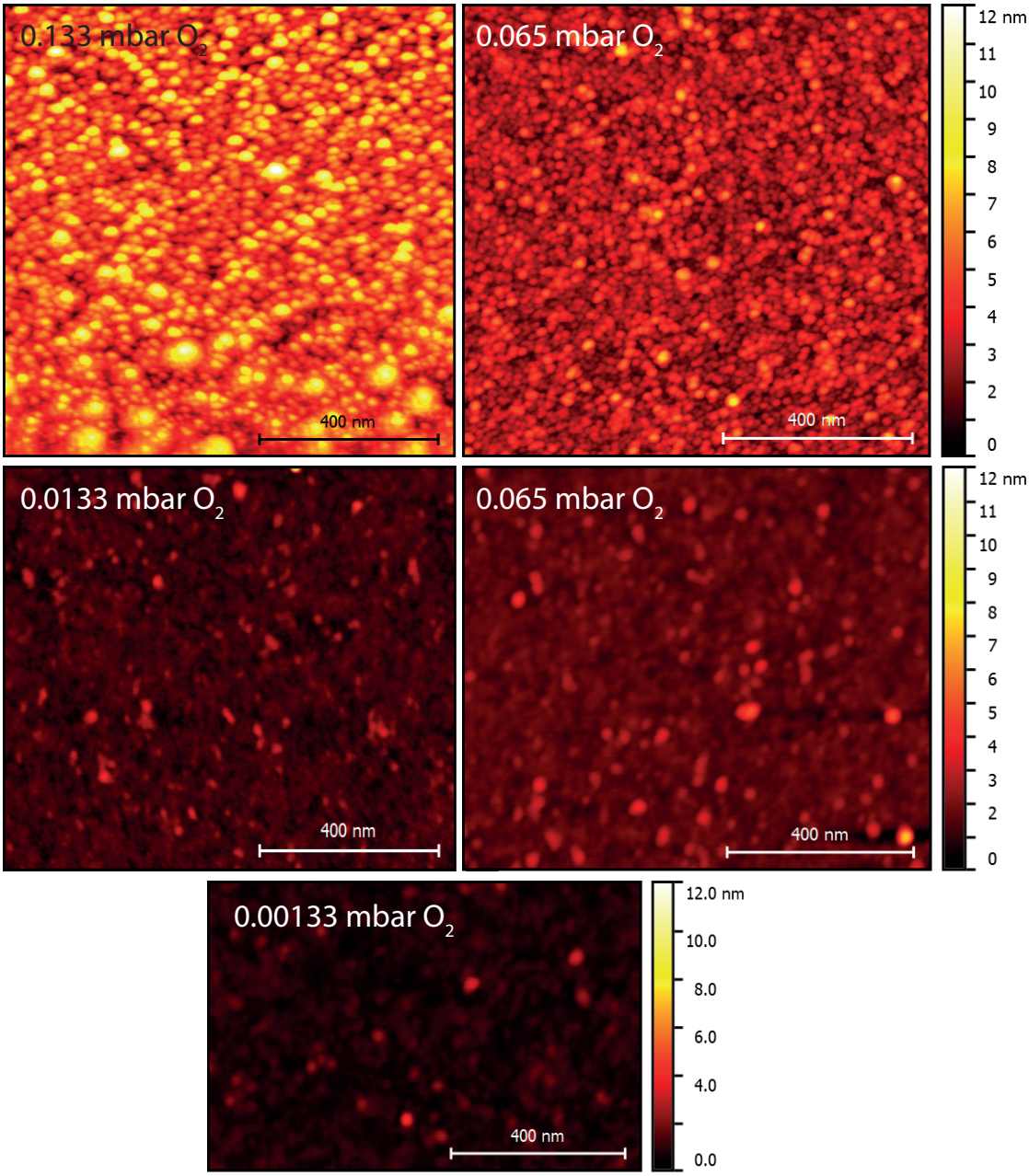

Figure 4.13.: $1 \times 1\,\mu m^2$ AFM images of 20 nm PCMO thin films grown 0.133 mbar, 0.065 mbar, 0.0133 mbar, 0.065 mbar and 0.001 33 mbar O_2 pressures after RTA process. The colour scales is fixed between zero and 12 for all images. A decrease of average height and roughness can be seen for decreasing O_2 pressure.

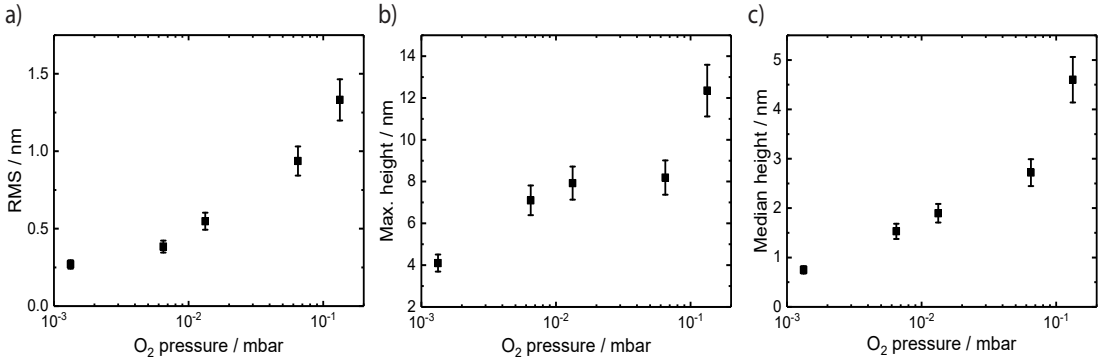

Figure 4.14.: Roughness parameters of 20 nm thick PCMO grown at 0.133 mbar, 0.065 mbar, 0.0133 mbar, 0.065 mbar and 0.001 33 mbar O_2 pressure in the chamber. a) RMS, b) max. height and c) median height values extracted from the AFM scans given in figure 4.13. The roughness of the sample decreases with decreasing O_2-pressure. An error of 10 % is assumed for all measuered values.

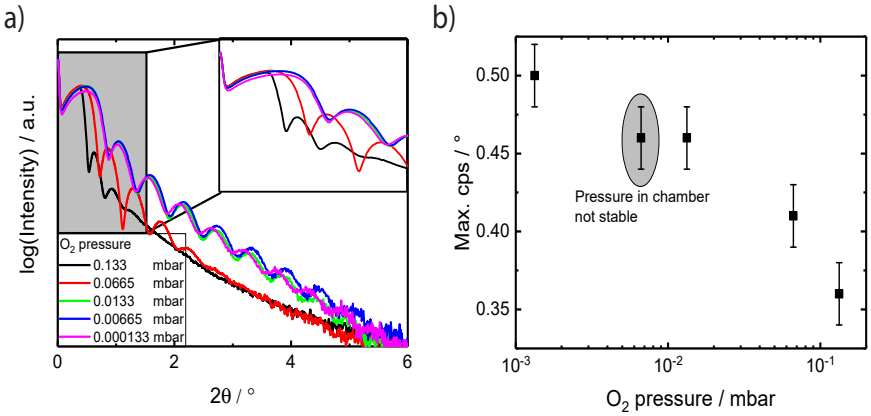

Figure 4.15.: a) XRR measurements of 20 nm PCMO thin films grown at different O_2 pressure inside the PLD chamber An increase of the total reflection angle of the XRR measurement with decreasing O_2 pressure can be seen. b) Angle with max. counts plotted against the O_2 pressure during growth. A clear increase of the max. cps / total reflection angle with decreasing pressure can be seen.

a small hint, that the oxygen pressure during growth does not affect the oxidation state in our PCMO thin film after annealing and transferring it in ambient air.

Figure 4.13 shows AFM scans of the 20 nm PCMO thin films grown at different O_2 pressure. The colour scale for all AFM images is fixed. It can be seen that the roughness and the average height of the PCMO thin film decreases with decreasing O_2 pressure. Also the amount of spikes decreases with decreasing O_2 pressure inside the chamber. This behaviour can also be seen in figure 4.14. The RMS value decreases with decreasing O_2 pressure, see figure 4.14 a). The max. height and the median height values also decrease with decreasing O_2 pressure inside the chamber, figure 4.14 b) and c).

Parallel to this decrease in roughness, the total reflection angle of the PCMO thin film during XRR measurements increases with decreasing O_2 pressure, see figure 4.15. This indicates an increase of the PCMO density with decreasing O_2 pressure during growth.

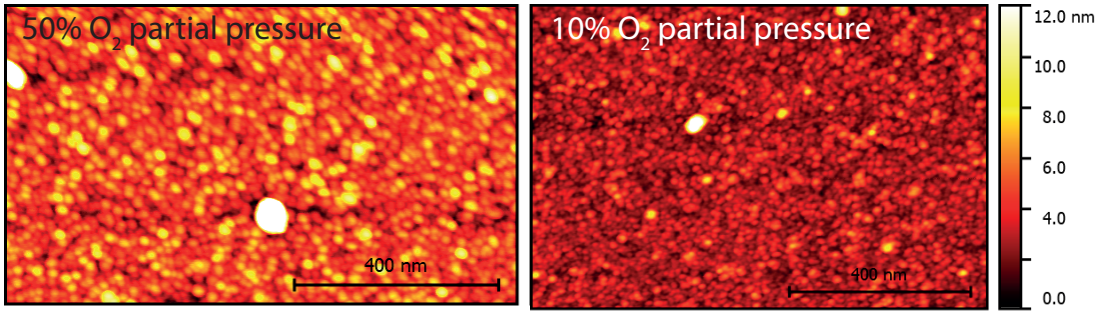

Figure 4.16.: AFM images of PCMO thin films grown at different 0.133 mbar with 50 % and 10 % O_2 partial pressure.

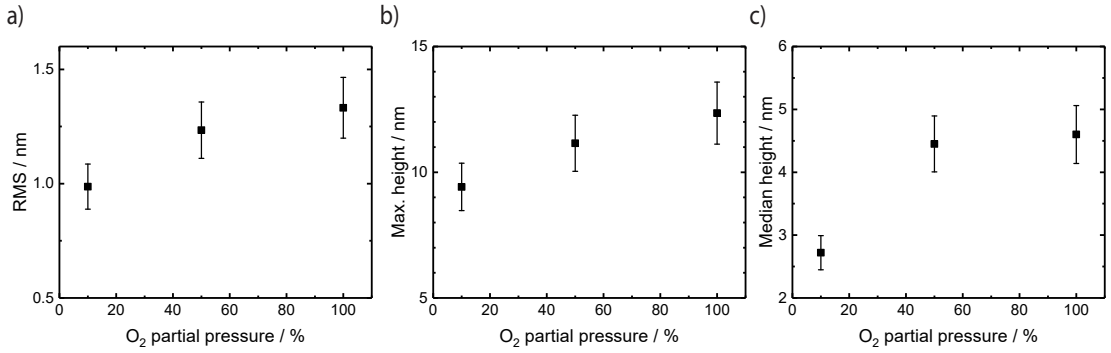

Figure 4.17.: Roughness parameters of 20 nm PCMO grown at 0.133 mbar with 50 % and 10 % O_2 partial pressure. a) RMS, b) max. height and c) median height values extracted from the AFM scans given in figure 4.16. The roughness of the sample decreases with decreasing O_2 partial pressure. An error of 10 % is assumed for all measured values.

Variation of O_2 partial pressure at 0.133 mbar pressure

Previously, the results of changing the pressure inside the PLD chamber during PCMO growth are presented. In this subsection only the O_2 partial pressure is changed during growth. The base pressure inside the PLD is kept at 0.133 mbar. As additional gas Ar is added inside the chamber. The O_2 partial pressure is given in percent. In this work, PCMO thin films grown at 100 %, 50 % and 10 % O_2 partial pressure are investigated.

Figure 4.16 shows the AFM scans of the PCMO thin films grown at 50 % and 10 % O_2 partial pressure at 0.133 mbar. It can be seen, that the roughness of the PCMO thin film decreases with decreasing O_2 partial pressure. This becomes more clear in figure 4.17 a). Here, the change in the RMS value with decreasing O_2 partial pressure can be seen. The RMS value decreases with decreasing oxygen partial pressure. This decrease is less pronounced than in figure 4.14 a) where the whole pressure inside the chamber is decreased. This decrease with decreasing O_2 partial pressure can also be seen in the max. height value and the median height value, see figure 4.17 b) and c). Even with these measurements, the decrease is not as pronounced as in figure 4.14 b) and c).

Figure 4.18 a) shows the change of the XRR measurement at different O_2 partial pressure. Unlike in figure 4.12, no change in the total reflection angle can be detected here.

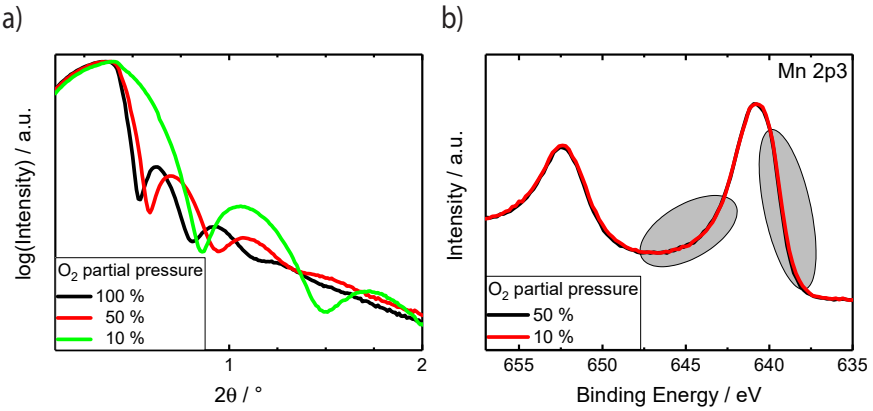

Figure 4.18.: XRR (a)) and XPS (b)) measurements of the PCMO thin film grown at different O_2 partial pressure. No change in the total reflection angle of the XRR measurement or the Mn oxidation state can be seen.

The oxidation state of the Mn $2p3$ peak does not change and no Mn^{2+} shake up or satellite feature occurs with decreasing oxygen partial pressure, see figure 4.18 b).

4.3.4. Growth of different PCMO stoichiometry

In literature, $Pr_{1-x}Ca_xMnO_3$ can be found in different stoichiometries [133–135]. Nevertheless, this work focuses on $Pr_{0.7}Ca_{0.3}MnO_3$. Therefore, the abbreviation PCMO used in this work always means the $Pr_{0.7}Ca_{0.3}MnO_3$ stoichiometry. In this section, the growth of different stoichiometries will be presented. The stochiometry will be indicated by a number added to the abbreviation. The number indicates the percentage of Pr in the thin film. For example $Pr_{0.6}Ca_{0.4}MnO_3$ will be PCMO60. All thin films presented in this section are grown with the standard deposition parameters that can be found in table 3.1 and are annealed at 650 °C for 2 min in N_2 atmosphere.

Figure 4.19 a)-d) shows the AFM images of PCMO thin films grown with PLD targets of different stoichiometry, $Pr_{0.6}Ca_{0.4}MnO_3$ (PCMO60), $Pr_{0.52}Ca_{0.48}MnO_3$ (PCMO52) and $Pr_{0.5}Ca_{0.5}MnO_3$ (PCMO50). Additionally $Pr_{0.7}Ca_{0.7}MnO_3$ is shown. Beside the fact, that the PCMO60 shows the largest grain size and the highest average value, indicated by color, no big difference between the AFM images can be seen.

Also the RMS, Max. height and Median height values are in the same order of magnitude for all different stochiometries, see figure 4.19 e)-g). Only the PCMO60 values differs from the other. Nevertheless, one could not conclude any stoichiometry depended surface characteristics from the AFM images. The growth parameters were also not adapted to the given stoichiometry.

This can also be seen in figure 4.20 a) and b). Figure 4.20 a) shows exemplary the fitting of the Mn $2p\,3/2$ peak of the PCMO60 thin film. The two peaks can be related to the Mn^{3+} and Mn^{4+} valence state of the Mn. These two valence states are expected in PCMO and are proportional to the Pr/Ca ratio due to the different valence states of Pr and Ca in PCMO, considering that the thin film is fully oxidised. Figure 4.20 b) shows

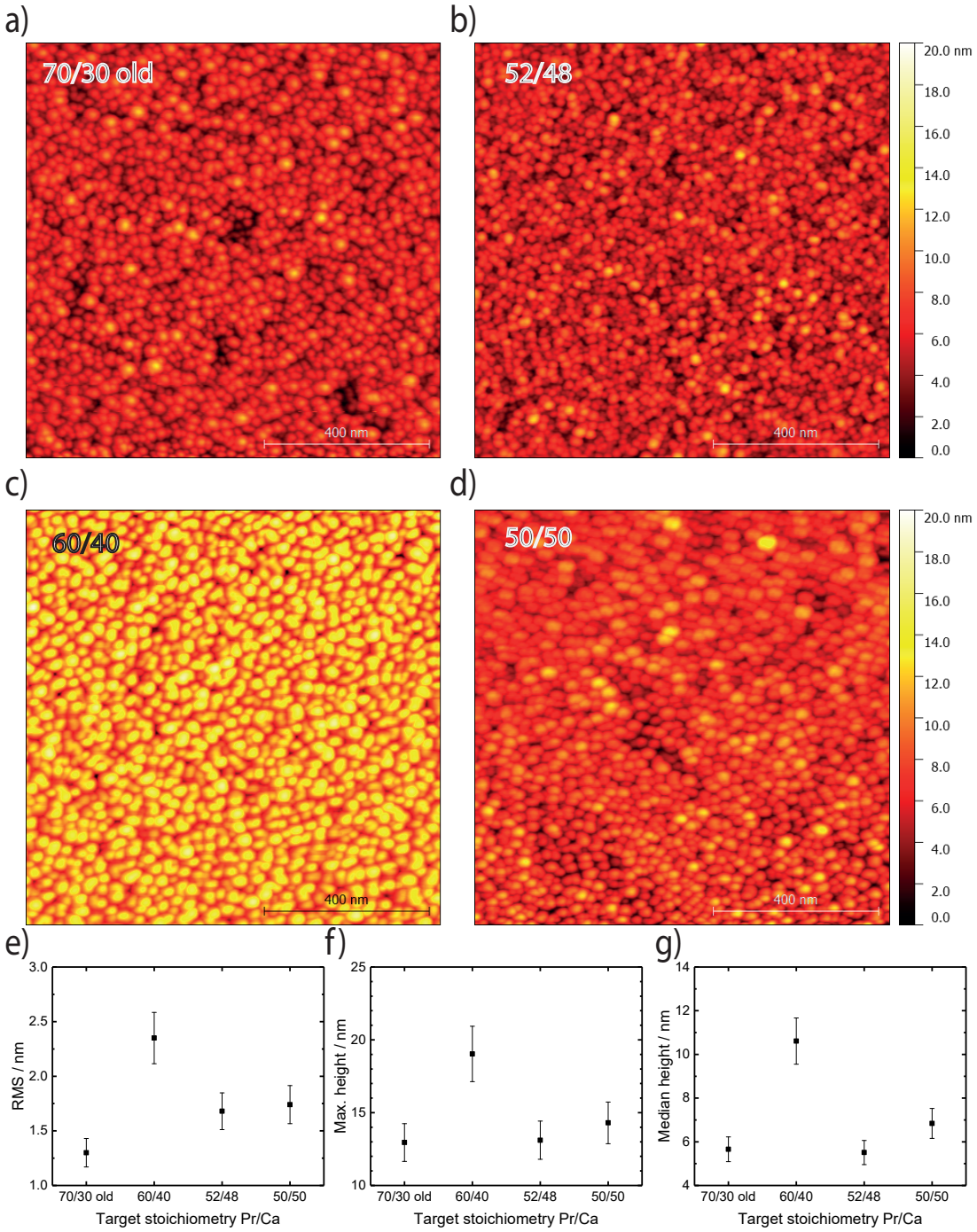

Figure 4.19.: a)-d) AFM images of PCMO grown with PLD targets of different stoichiometries. The stochiometry of the target is indicated by the inlet in the AFM images. e)-g) Height values extracted from the AFM images for the different stoichiometries. e) RMS, f) Max. height and g) Median height.

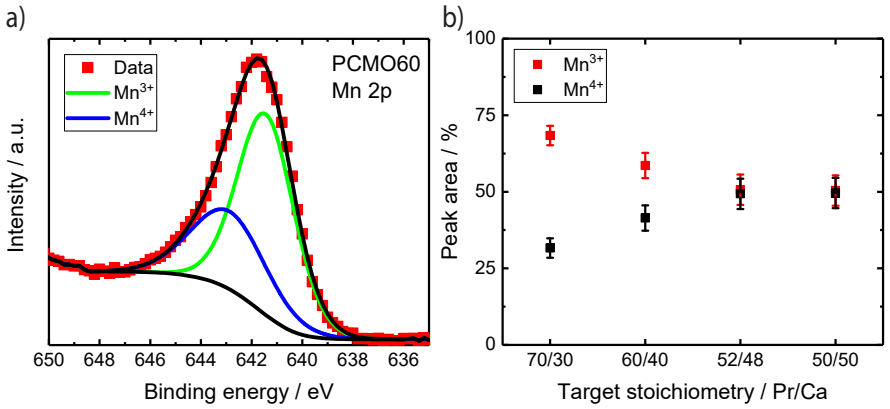

Figure 4.20.: a) Mn $2p$ peak of PCMO60 thin film with the fitted peaks, Mn^{3+} and Mn^{4+}. b) Percentage of Mn^{3+} and Mn^{4+} in the PCMO thin films grown with targets of different stoichiometry determined by the Mn $2p$ peak.

the Mn^{3+} and Mn^{4+} contribution to the Mn $2p$ peak of PCMO thin films grown with targets of different stoichiometry. It can be seen, that the $^{Mn^{3+}}/_{Mn^{4+}}$ ratio fits to the given target stoichiometries. The slight deviations are due to the fact, that the growth parameters for the $Pr_{0.7}Ca_{0.3}MnO_3$ thin film are used and the grwoth parameters are not adapted for every stoichiometry.

4.3.5. Impact of temperature during RTA

The disadvantage of the RTA at 650 °C is the incompatibility with today CMOS technology, since the highest temperature for these processes is around 450 °C. Therefore different annealing temperatures will be presented in a compressed way here. Further experiments concerning the RTA process, like different annealing times and atmospheres can be found here [123].

In Figure 4.21 a)-c), $1 \times 1\,\mu m^2$ AFM scans of PCMO thin films annealed for 2 minutes at 350 °C, 450 °C and 550 °C are shown, respectively. The colour scale for all AFM scans is set between 0 nm and 12 nm. No clear difference between the AFM scans is visible at first glance. The effect on the grain size is already shown in figure 4.5 [123]. Figure 4.21 d) shows the RMS value extracted from the AFM scans shown in figure 4.21 a)-c) and the standard RTA process at 650 °C. No trend of decreasing or increasing RMS with increasing or decreasing temperature during the RTA can be seen. Furthermore, no trend in the max. height of the thin film, figure 4.21 e), can be seen. Only the median height value increases slightly with increasing temperature. Nevertheless, within the error bars only a vague statement can be made.

Figure 4.22 shows the GIXRD scans of PCMO thin films annealed at 350 °C, 450 °C and 550 °C. Comparing this to the GIXRD scan of the PCMO thin film annealed at 650 °C, see figure 4.3 b), it can be seen, that for these lower temperatures, no peaks of a polycrystalline PCMO thin film can be seen for the samples that are annealed at lower temperatures. This means, that the PCMO thin film starts to crystallise between 550 °C and 650 °C.
Therefore, one can conclude that the main difference between the PCMO thin film an-

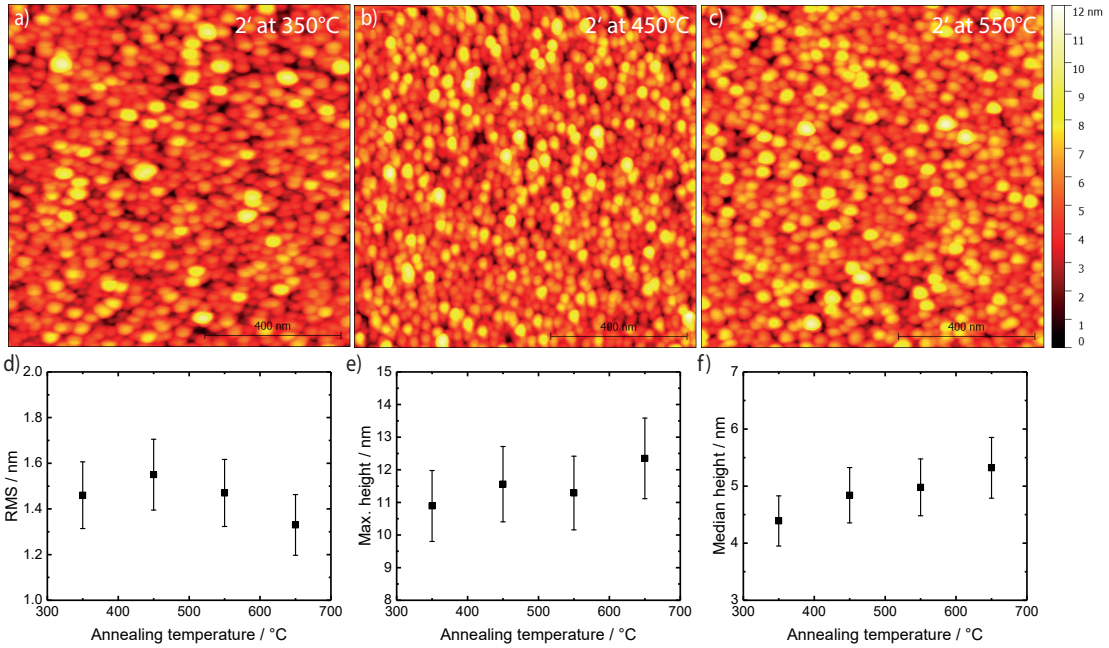

Figure 4.21.: a)-c) $1 \times 1\,\mu m^2$ AFM scans of PCMO thin films annealed at different temperature, 350 °C, 450 °C and 550 °C respectively. d) RMS values, e) max. height and f) median height of the AFM scans a)-c). Additionally the values of the 650 °C thin film are added to d)-f).

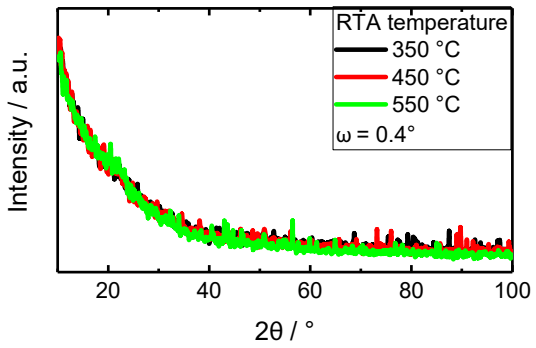

Figure 4.22.: GIXRD scans of PCMO thin films annealed for 2 min in N_2-atmosphere at 350 °C, 450 °C and 550 °C with an incident angle of 0.4°.

nealed at 650 °C and the PCMO thin films annealed at lower temperatures, 350 °C, 450 °C and 550 °C is the crystalline of the thin film.

4.4. Conclusion of growth process

First, the growth parameters were introduced, which will be used as a standard for the PCMO film in this work. This PLD parameters included a laser energy of 27 mJ, a free frequency of 5 Hz, and a growth pressure of 0.133 mbar in O_2 atmosphere. Furthermore, a RTA step was introduced. During this RTA process the PCMO thin film was heated up to 650 °C for 2 min in N_2 atmosphere. It was shown, that the stoichiometry changes slightly during the RTA. A general explanation for the stoichiometry change could not given. Furthermore, the crystallinity of the PCMO thin film changes from amorphous to polycrystalline. These changes are accompanied by a change in the thickness of the PCMO film. The thickness of the PCMO thin film decreased by 42 % on average. Of course, these growth and post-processing parameters were not simply recognised as such. Therefore, in the remainder of the chapter, properties of PCMO thin films grown under different conditions are presented.

First, growth was optimised with regard to laser energy. It was shown that the best stoichiometry transfer occurs at 27 mJ and 30 mJ. With decreasing energy, the Mn3+ content in the PCMO increases, which suggests a non-stoichiometric transfer of the target stoichiometry. The influence of the PCMO thickness on the roughness of the thin film was also investigated. It was found that thinner films have a lower roughness than thicker PCMO layers. However, it must be kept in mind that films that are too thin do not lead to flat film growth, but show island growth. This happened fir the 10 nm thin PCMO film. The 20 nm PCMO thin film had the lowest RMS roughness.

In addition to laser energy and PCMO thickness, the influence of the atmosphere during thin film growth was also investigated. Both lower pressures and lower oxygen partial pressures were used. For lower pressures during the growth, no big change in the stoichiometry could be observed. Furthermore it was shown, that lower pressures lead to a flatter thin film surface and also a denser thin film. The density change was observed by a change in the total reflection angle of XRR measurements that have been performed. For decreasing oxygen partial pressure a similar behaviour could be observed. Nevertheless, the decrease in roughness was considerably smaller as for the decreasing overall pressure. Neither the lower pressure nor the lower partial pressure led to a change in the Mn valence state. Also, no other $^{Mn^{3+}}/_{Mn^{4+}}$ ratio could be found compared to the standard growth pressure.

Furthermore, the growth was performed with targets of different stoichiometries. No trend could be detected with regard to any parameter. Du to the fact that the growth parameters have not been optimised, they only represent the possibility of growing different PCMO thin films.

Finally, the RTA process was investigated at different temperatures, as 650 °C is too high for CMOS integration of the components. No major differences in the roughness of the PCMO thin film after annealing at different temperatures were observed. The only

difference was that the PCMO layers annealed at lower temperatures showed no peaks in the GIXRD spectrum and are therefore probably amorphous.

If all these results are combined and compared with the switching curves introduced later, it can be concluded that the standard growth parameters introduced at the beginning, together with the annealing at 650 °C, lead to PCMO thin films that show the best switching behaviour. Nevertheless, in the long run, the annealing temperature must be reduced to a maximum of 450 °C. Of course, even lower temperatures would be better.

5. Deposition of interface layer

Parts of this chapter are published in [2]. Parts of the PCMO/Al measurement are performed by Sebastian Hambsch.

In this chapter, the effect of different deposited interface layer on top of a PCMO thin film will be presented and discussed. Starting with oxidisable metals, directly deposited oxides are also examined. The metals which are investigated are Al, Ta and W. The oxides which are investigated are Ta_2O_5 and WO_3. The PCMO thin film is grown with a thickness of 20 nm and annealed for 2 min at 650 °C in N_2.

The fits of the XPS peaks are all done with *CasaXPS*. A Shirley background was deducted for the background.

5.1. PCMO in combination with oxidisable metals

The metals used in this section are evaporated (Al) or sputtered (Ta and W). The heating of the sample during the evaporation of the Al as described in section 3.1.2 can be neglected. This is due to the fact that most of the heat is released during the Pt evaporation and no Pt is evaporated after the Al. For the sputtered metals, no heating of the material has to be considered either.

An Ellingham diagram, figure 5.1, presents the change of Gibbs free energy during the oxidation of different material for different temperatures. Here, the oxidation of the three used materials is represented. The change of Gibbs free energy is given by

$$\Delta G = \Delta H - T\Delta S. \tag{5.1}$$

ΔG is the change in Gibbs free energy, ΔH is the change in enthalpy , T is the temperature and ΔS is the change in entropy. Additionally, Hess's law provides an insight into the enthalpy change during a chemical reaction:

$$\Delta_r H = \underbrace{\sum \Delta_f H^0}_{products} - \underbrace{\sum \Delta_f H^0}_{reactants} \tag{5.2}$$

One can now expands Hess's law to the Gibbs free energy:

$$\Delta G = \underbrace{\sum \Delta G}_{products} - \underbrace{\sum \Delta G}_{reactants} \tag{5.3}$$

This means, as long as it is true for the sum of the reactions that $\Delta G < 0$, the reaction will be spontaneous. It can bee seen, that the Al is most likely to oxidise in combination with O_2, followed by the Ta. The W is the hardest one to oxidise, due to the change in

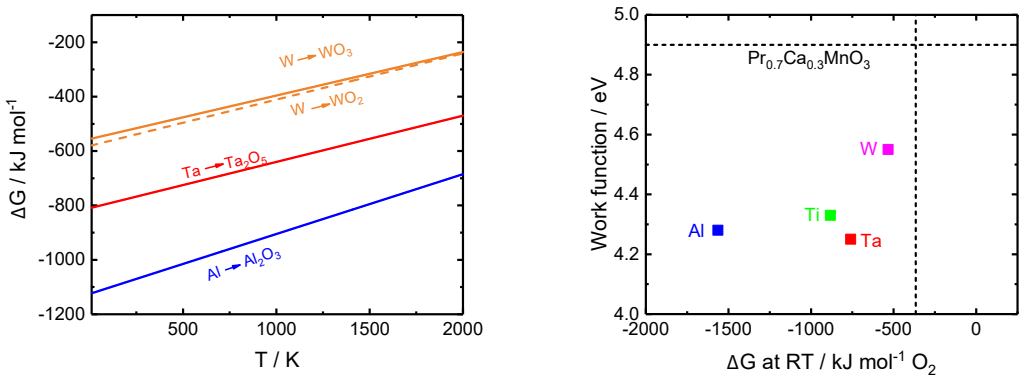

Figure 5.1.: Ellingham diagram of the oxidisable metals used in this chapter as interface materials: Al, Ta, and W. It shows the temperature dependence of the stability of the thermodynamically stable compounds likely to appear in the samples. It can be seen that the Al is more likely to form an oxide than Ta and W. Additionally, the work function and the change of Gibbs free energy is plotted for the different materials. [136, 137]

Gibbs free energy.

Figure 5.1 b) shows the change of the Gibbs free energy during oxidation and the work function of the different materials. Additionally, the work function and the change in Gibbs free energy of the PCMO is indicated. It can be seen, that the formation of an oxide at the interface would lead to a reduction of the Gibbs free energy and would therefore happen spontaneously.

Nevertheless, one has to mention, that the Ellingham diagram only represents thermodynamic stability and does not take difussion barriers and interface effects into account. The interface oxides will be investigated by XPS in the following. For every material, the bare PCMO film and the same PCMO film with the material deposited *in-situ* on top of the PCMO thin film are investigated. The measured XPS spectra are calibrated with Au foil on the Au peak.

5.1.1. PCMO/Al interface

This subsection is partly published in [2].

7 nm of Al metal are evaporated on top of a 20 nm PCMO thin film. Afterwards the PCM/Al stack is investigated in-situ by XPS. The measurements are done at take off angles of 30° and 80° to gain depth information of the Al film. Figure 5.2 a) shows the spectrum of the Al 2*p* region. The spectrum consist of two peaks at both angles, the main peak at 73 eV and a smaller shoulder at 75 eV. The main peak can be assigned to the Al metal and the smaller shoulder can be assigned to Al_2O_3 [116]. It can be seen that for higher take off angles the intensity of the oxide signal increases. This means that the oxidation state of the Al metal increases deeper inside the material and not on the surface, since XPS measurements at smaller take off angles are much more surface sensitive [114, 138].

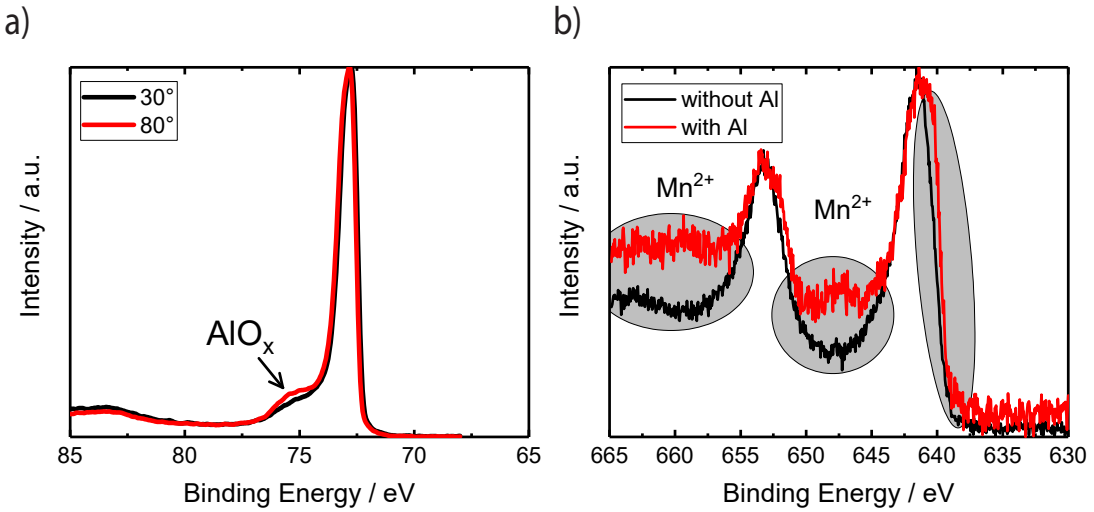

Figure 5.2.: XPS measurements of PCMO in combination with an Al interface layer. a) Al spectrum at different angles, 30° and 80°. A clear increase of the AlO_x feature at higher angles can be seen. This indicates an increase of the oxidation state deeper inside the PCMO. b) Mn $2p$ spectrum of PCMO without and with Al layer. A Mn^{2+} satellite feature can be seen for the PCMO thin film with the Al layer.

Figure 5.2 b) shows the spectrum of the Mn $2p$ region. A doublet at 641 eV and 653 eV can be seen. In black the Mn $2p$ spectra of the bare PCMO thin film is plotted. The red line belongs to the PCMO thin film with Al. In PCMO Mn is present in two different oxidation states: Mn^{3+} and Mn^{4+} [33]. In the Mn spectra of the PCMO in combination with Al metal, shake-up satellites appear. These shake up satellites appear when Mn^{2+} is present [139]. Furthermore, the Mn $2p\,3/2$ peak shifts slightly to lower binding energies, indicated in figure 5.2 b) with the grey region on the right. These Mn^{2+} features gives a hint, that the PCMO reduces during the Al deposition.

Both observations, the increase of the oxidation state of the Al deeper inside the material and the loss of oxygen inside the PCMO layer, lead to the conclusion that the Al pulls out the oxygen of the PCMO. This reduces the PCMO and oxidises the Al at the interface. This is also in good agreement with the theoretical considerations done before, see figure 5.1.

Figure 5.3 a) shows the measurement of the Pr $3d$ spectrum. Like before, the measurement presented in black shows the bare PCMO and the red one the measurement of PCMO with Al on top. The Pr $3d\,5/2$ peak shifts by 0.9 eV, from 932.9 eV to 933.8 eV after the Al deposition. Due to the fact that the binding energy is referenced to the Fermi energy of a system, the increase in binding energy indicates a downwards bending of the PCMO bands when Al is deposited.

The reconstructed band structure from the XPS measurement can be seen in figure 5.3 b). The amount of band bending shown in figure 5.3 a) is directly given by the peak shift of the Pr $3d\,5/2$ peak, 0.9 eV. This voltage drops over the AlO_x barrier. The band gap of PCMO is around 0.5 eV [140]. In literature, the AlO_x valence band position is calcu-

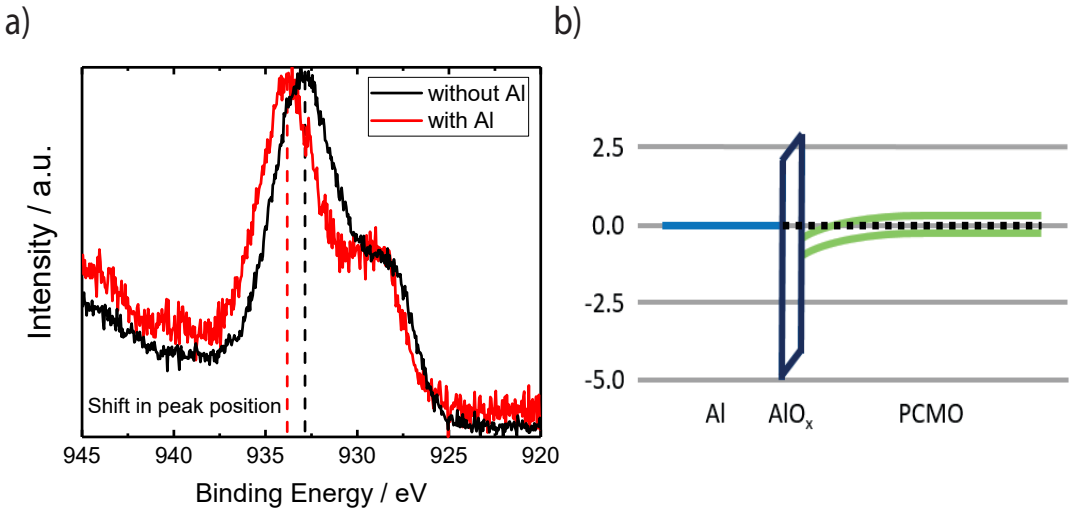

Figure 5.3.: a) XPS measurement of Pr $3d$ spectrum without (black) and with (red) Al layer. A slight shift to higher binding energies of the Pr $3d_{5/2}$ peak can be seen. b) Reconstructed band diagram of the PCMO, AlO_x, Al junction.

lated from the position of the Al $2p$ orbital of the oxidised part of the Al. The valence band edge for Al_2O_3 is at -4 eV and the $2p$ peak at -74.14 eV. In figure 5.2 a) the peak is at -75 eV. Therefore, the valence band edge lies at -4.9 eV. Adding the band gap of amorphous Al_2O_3 with 7 eV, the conduction band edge can be placed at 2.1 eV [141].

TEM investigation of PCMO/Al interface

The measurement presented in this section are performed by the Central Facility for Electron Microscopy at RWTH Aachen.

To investigate the interface oxide, TEM, STEM and EDX measurement of the PCMO, the interface, and the Al layer are performed. Two exemplary TEM measurements of the PCMO/Al device stack with a magnification of 300 k are shown in figure 5.4 a) and b). The Pt TE and BE are shown in black and the PCMO layer is bright in between. Despite the sharp demarcation of the Pt and PCMO layers, no clear Al layer can be identified between the PCMO and the Pt. Furthermore, it can be seen, that the interface between the Pt BE and the PCMO layer is well defined but the interface between the PCMO layer and the Pt TE is rough. At this position should be the Al/Al_2O_3 interface layer. It can be seen that in some places the PCMO has holes. Some of these holes is marked with the red box in figure 5.4 a) and b). Furthermore, it seems that the PCMO layer is fairly inhomogeneous with cavities in it. These cavities are the black regions inside the brighter PCMO layer that can be seen in the TEM images.

STEM images of the Pt/PCMO/Al/Pt stack can be seen in figure 5.4 c) and d). The Pt metal in this measurements is bright and the PCMO is darker. The holes, that can be seen on the interface between the PCMO and the Pt TE where also the Al/Al_2O_3 should be located, can also be seen in the STEM images, see figure 5.4 c) and d). It can be seen, that the Pt TE grows inside these holes. In figure 5.4 d) this is highlighted by

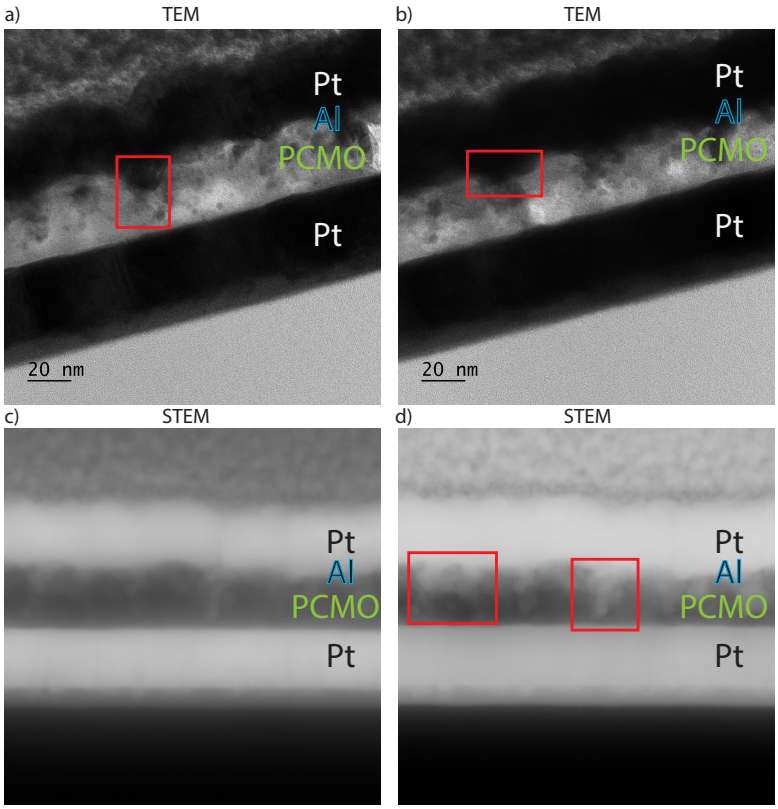

Figure 5.4.: a), b) TEM measurement of the PCMO/Al devices with a magnification of 300k. c), d) STEM measurement of the PCMO/Al devices.

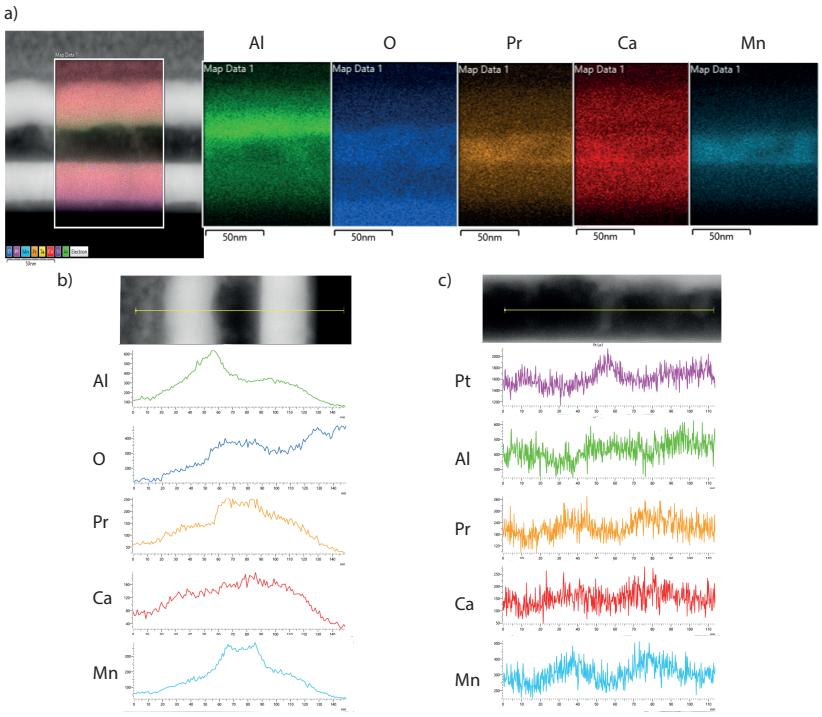

Figure 5.5.: EDX measurements of the PCMO/Al devices and interface. a) EDX map of the whole device stack with all investigated elements. b) EDX line scans across the device. c) EDX line scans along the PCMO layer.

the red boxes. Also in the STEM images no clear Al layer can be seen.

To show that the devices consist out of PCMO in combination with an Al/Al_2O_3 layer, EDX measurement are performed to prove the existence of the Al_2O_3 interface layer. Figure 5.5 a) shows the EDX mapping of the PCMO/Al devices. It can be seen, that the Al signal accumulates at the upper interface where one would expect the Al layer. This shows, that the Al is present at the interface, although it was not visible at the TEM and STEM images in figure 5.4. The O signal of the EDX map is equally spread across the cross section of the device and no oxygen accumulation or depletion at the interface can be seen. Figure 5.5 b) shows a EDX line scan across the PCMO/Al device. It can be seen, that the Al signal increases and shows a peak at the upper interface between the PCMO and Pt as expected. Nevertheless, the O signal is constant across the device area and no real increase or decrease can be seen at the beginning of the Al/Al_2O_3 layer. The O signal plateau that can be seen is wider than the Pr and the Mn plateau that reaches into the Al peak. Nevertheless, a clear indication for the Al_2O_3 layer that was measured with the XPS can not be seen here. A reason for this could be the resolution limit of the EDX spectra. Furthermore, EDX is a depth sensitive technique and therefore, the measured signal is an average of several atomic layers. Nevertheless, the inhomogeneity of the PCMO poses a major problem for this measurement.

To investigate the bright cavities inside the PCMO layer that could be seen in the STEM images in figure 5.4 c) and d), EDX line scans are performed inside the PCMO layer and across these bright regions. An exemplary measurement can be seen in figure 5.5 c). It can be seen, that the Pt signal of the EDX line scan increases in the area of the bright

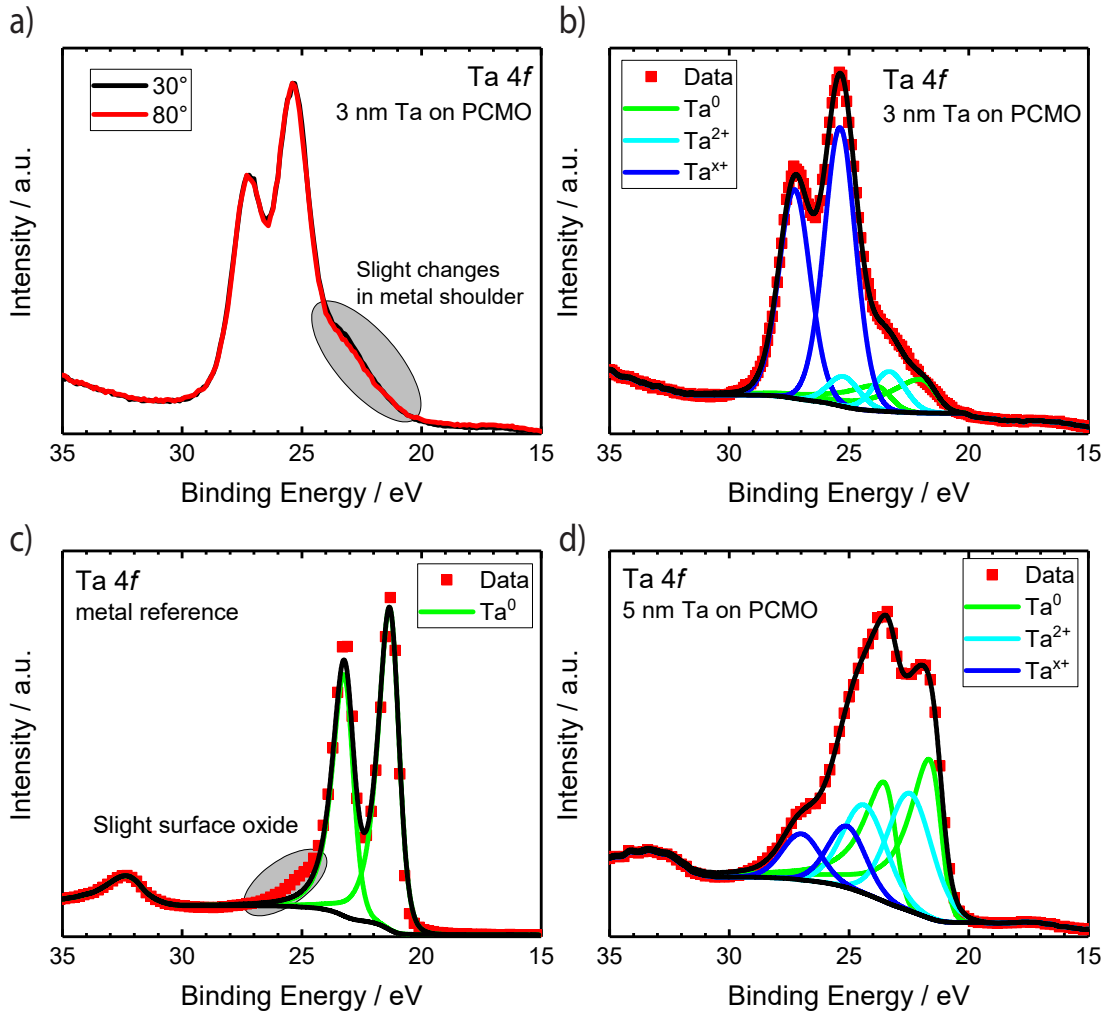

Figure 5.6.: Ta 4*f* spectra of Ta metal deposited on PCMO. a) Ta 4*f* spectrum of 3 nm Ta deposited on PCMO at different angles, 30° and 80°. b) Fitting of the Ta 4*f* spectrum of 3 nm Ta on PCMO. c) Ta metal reference spectrum. d) Fitting of Ta 4*f* spectrum of 5 nm Ta deposited on PCMO.

region and the Pr, Mn, and Ca signal decreases in this region. This means, that the bright spots that can be seen in the TEM and STEM images are cavities that are filled with the Al and the Pt that is deposited on top of the PCMO layer.

5.1.2. PCMO/Ta interface

The change of Gibbs free energy for Ta during the oxidation of the metal is lower than for the Al, see figure 5.1. Nevertheless, one would expect an interface oxide due to thermodynamics.

To investigate the interface layer, 3 nm and 5 nm Ta are deposited on top of the PCMO. Figure 5.6 a) shows the Ta 4*f* spectra of 3 nm Ta deposited on PCMO. The measurement at 30° is presented in black and the measurement at 80° is presented in red. Two peaks at 25.4 eV and 27.1 eV can be seen for both measurements. Additionally, a shoulder at

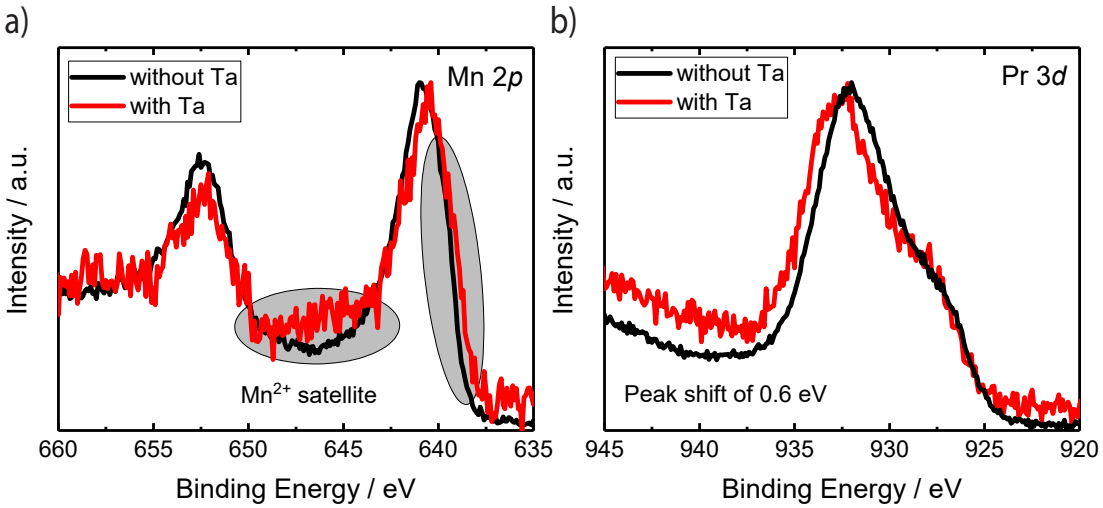

Figure 5.7.: a) Mn $2p$ spectrum of PCMO without (black) and with (red) 3 nm Ta on top. b) Pr $3d$ spectrum of PCMO without (black) and with (red) 3 nm Ta on top.

Table 5.1.: Proportion of the different fitted peak areas in the total area of the peak.

3 nm	Ta^0 / %	Ta^{2+} / %	Ta^{x+} / %
30°	17.7	11.1	71.1
80°	16.5	10.5	73.0
5 nm	Ta^0 / %	Ta^{2+} / %	Ta^{x+} / %
30°	46.3	37.0	16.6
80°	33.8	48.8	17.3

lower binding energies can be seen. This shoulder can be referred to less oxidised Ta or Ta metal. This shoulder is slightly more pronounced for smaller angles. This means, that the surface is less oxidised than the deeper part of the film. Nevertheless, the visible change is very small.

The fit of the measured peak is presented in figure 5.6 b). The peak is fitted with three doublets. The peak positions of the fitted doublets are 22.0 eV, 23.3 eV and 25.4 eV. The peaks at lower binding energies can be assigned to Ta metal and Ta^{2+} [142, 143]. The highest one, labelled with Ta^{x+} cannot be clearly assigned to a specific Ta oxidation state. In literature different oxidation states can be found, Ta^{3+} and Ta^{4+} [142, 143]. Nevertheless, Ta^{5+} can be excluded. The highest oxidation state also has the highest percentage of the whole peak area, see table 5.1. Furthermore, it can be seen in table 5.1 that the oxidation decreases slightly with decreasing measurement angle. Nevertheless, the film is still strongly oxidised.

A reference measurement of the deposited Ta thin film on SiO_2 can be seen in figure 5.6 c). Beside a slight surface oxide, the deposited film can be fitted only with the metal doublet. This means that the oxidation that can be seen in figures 5.6 a) and b) is caused by the PCMO.

The Ta $4f$ spectrum of a thicker Ta film, 5 nm, deposited on PCMO can be seen in fig-

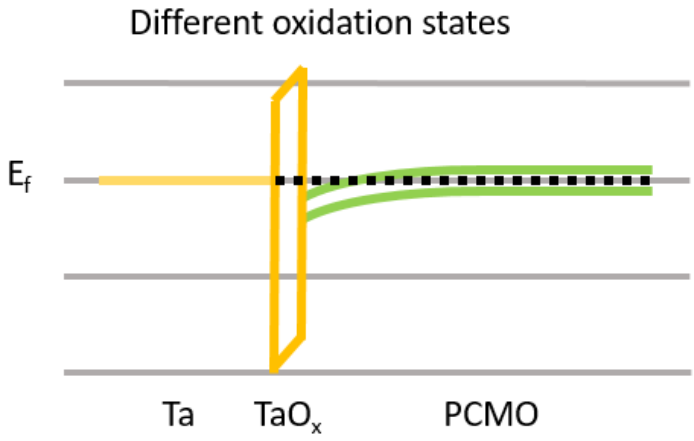

Figure 5.8.: Reconstructed band structure of the Ta/PCMO interface from the XPS measurements shown in figure 5.6 and figure 5.7.

ure 5.6 d). It can be seen, that the amount of metallic Ta, Ta^0, is enlarged. Table 5.1 also gives the percentage of the area for the different oxidation states for the 5 nm Ta measurement. Here, an increase of the metallic feature at the surface can be seen as well. This is an additional hint that the PCMO oxidizes the Ta metal at the interface.

The Mn $2p$ spectrum of PCMO with and without 3 nm Ta on top can be seen in figure 5.7 a). A Mn^{2+} satellite feature occurs after the deposition of Ta metal. Furthermore, the peak changes at lower binding energies, which indicates the change to lower valence states. Together with the results from the Ta $4f$ spectrum, one can conclude, that the Ta metal pulls oxygen out of the PCMO and oxidises at the interface, like in the case of Al.
Furthermore, a slight peak shift of around 0.6 eV of the Pr $3d$ is visible in figure 5.7 b). This indicates the expected downwards band bending of the PCMO bands at the interface.

A schematic of the PCMO/Ta band structure is shown in figure 5.8. The oxide that forms at the interface can be seen. As it was shown in figure 5.6, different oxidation states of the Ta occurs at the interface. For simplicity, however, only one oxide is shown in the schematic. Nevertheless, it is important to keep in mind that there are different oxidation states. There is also a band bending of the PCMO bands at the interface.

5.1.3. PCMO/W interface

W in combination with PCMO behaves differently than Al and Ta. Figure 5.9 shows the different XPS spectra, a) W $4f$ at different take off angles, b) the different oxidation peaks of the W fits into the W $4f$ spectrum, c) Mn $2p$ and d) Pr $3d$ measured of the PCMO thin film in combination with W metal. The W $4f$ spectrum shows the W metal peaks at 31 eV and 33.3 eV binding energy, as it is expected for the W metal [116, 144]. Furthermore, the peak shape has an asymmetric behaviour. This is a typical shape for metal spectra [116]. Beside this a shoulder at higher binding energies can be seen, see figure 5.9 a). This shoulder can be referred to an oxide. Furthermore, this shoulder is

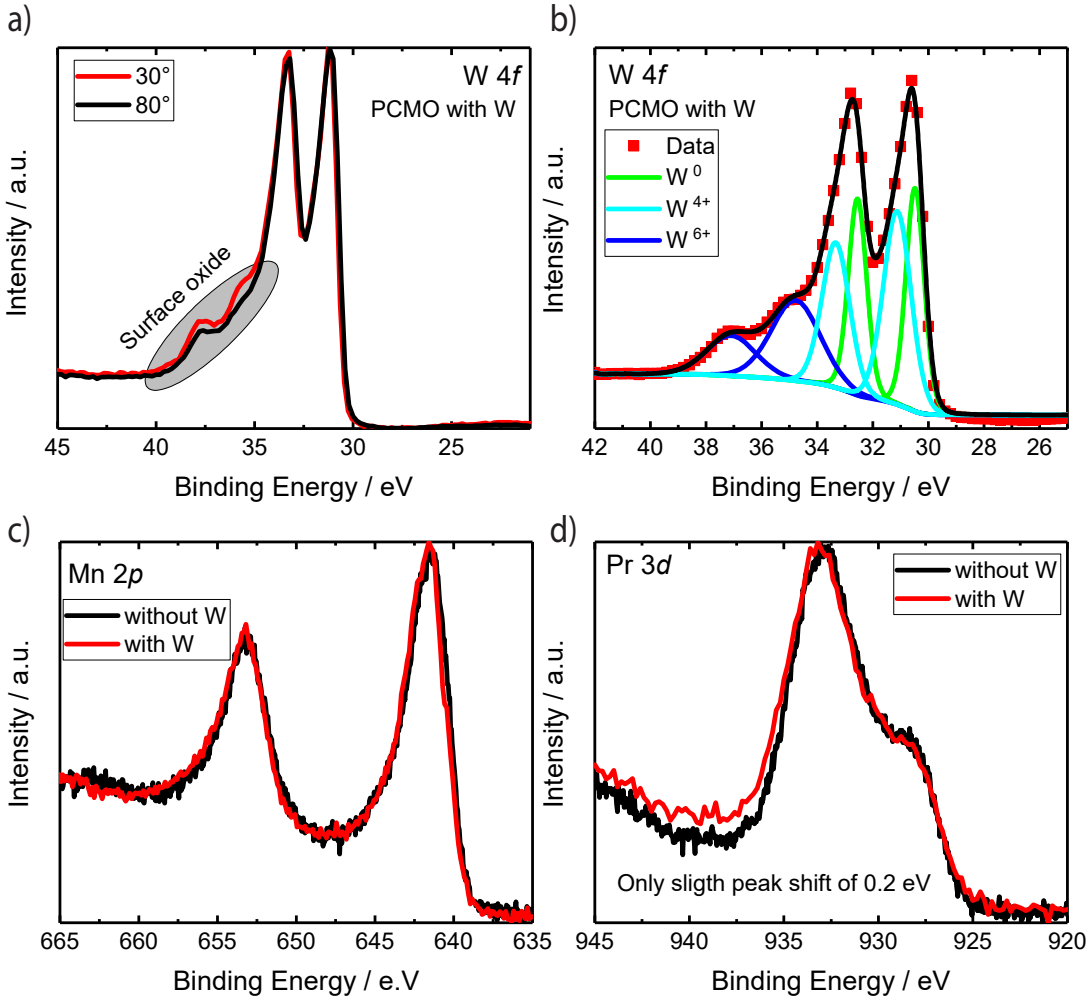

Figure 5.9.: XPS measurements of PCMO without and with W on top. a) Measurement of the W $4f$ spectrum at different take-off angles, 30° and 80°. b) Fitting of the W $4f$ XPS data with a metallic and two different oxidation states at 45° take off angle. c) Mn $2p$ spectrum of PCMO without and with W. Pr $3d$ spectrum of PCMO without and with W. d) Pr $3d$ spectrum of the PCMO with and without W metal on top.

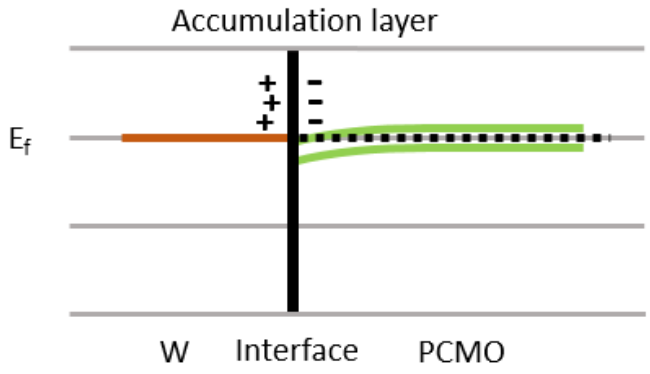

Figure 5.10.: Visualisation of the bands at the interface between W and PCMO without a WO_2/WO_3 layer at the interface. Only a slight band bending of the PCMO is expected due to figure 5.9 d).

more pronounced for 30°. This means that the oxidation is stronger at the surface than inside the W. The oxidation state can be determined as a mixture of WO_2 and WO_3, see figure 5.9 b). The W^0 peak is fitted at 30.8 eV and is fitted with an asymmetric lineshape, LA(1.3,2.5,11) . The W^{4+} is fitted at 31.9 ev and the W^{6+} is fitted at 35.2 eV, both with a symmetric lineshape (GL(30)). This fits quite well to the theoretical values of the W $4f$ spectra [116, 145]. The two different oxidation states are not astonishing due to the fact that the change of Gibbs free energy for WO_2 and WO_3 is in the same order of magnitude, see figure 5.1. Nevertheless, one can not conclude from the W $4f$ spectrum shown in figure 5.9 a) that no oxidation at the interface takes place. This is due to the fact, that for larger take off angles the oxide signal is only slightly reduced.

Figure 5.9 c) shows the Mn $2p$ spectrum of PCMO without and with W on top. In black the Mn $2p$ spectra of the bare PCMO thin film is plotted. The red line belongs to the PCMO thin film with W. A doublet at 641 eV and 653 eV can be seen. Unlike the Al and the Ta interface layer, no change in the oxidation state of the Mn can be seen. Also no Mn^{2+} shake up feature appears between the Mn $2p$ doublet. From this, one can conclude that the W deposited on top of the PCMO does not pull oxygen out of the PCMO and does not change its oxidation state. Together with the measurement of the W $4f$ spectra this is a second hint that the oxidation of the W layer happens at the surface of the W and not at the interface between W and PCMO.

Figure 5.9 d) shows the Pr $3d$ peak of the PCMO without and with W on top. In black the Pr $3d$ spectra of the bare PCMO thin film is plotted. The red line belongs to the PCMO thin film with W. Compared to the Al and the Ta interface layer, only a small shift of 0.2 eV of the Pr $3d$ can be seen. This shift is so small, that one cannot make clear prediction about the band bending of the PCMO at the interface. Nevertheless, a small downwards bend bending is expected due to the p-type semiconductor metal connection. Figure 5.10 shows a visualisation of the expected band structure at the interface between W and PCMO. Beside the fact that no WO_2/WO_3 layer is present at the interface, the small downwards band bending of the PCMO bands can be seen. This leads to an accumulation layer at the interface.

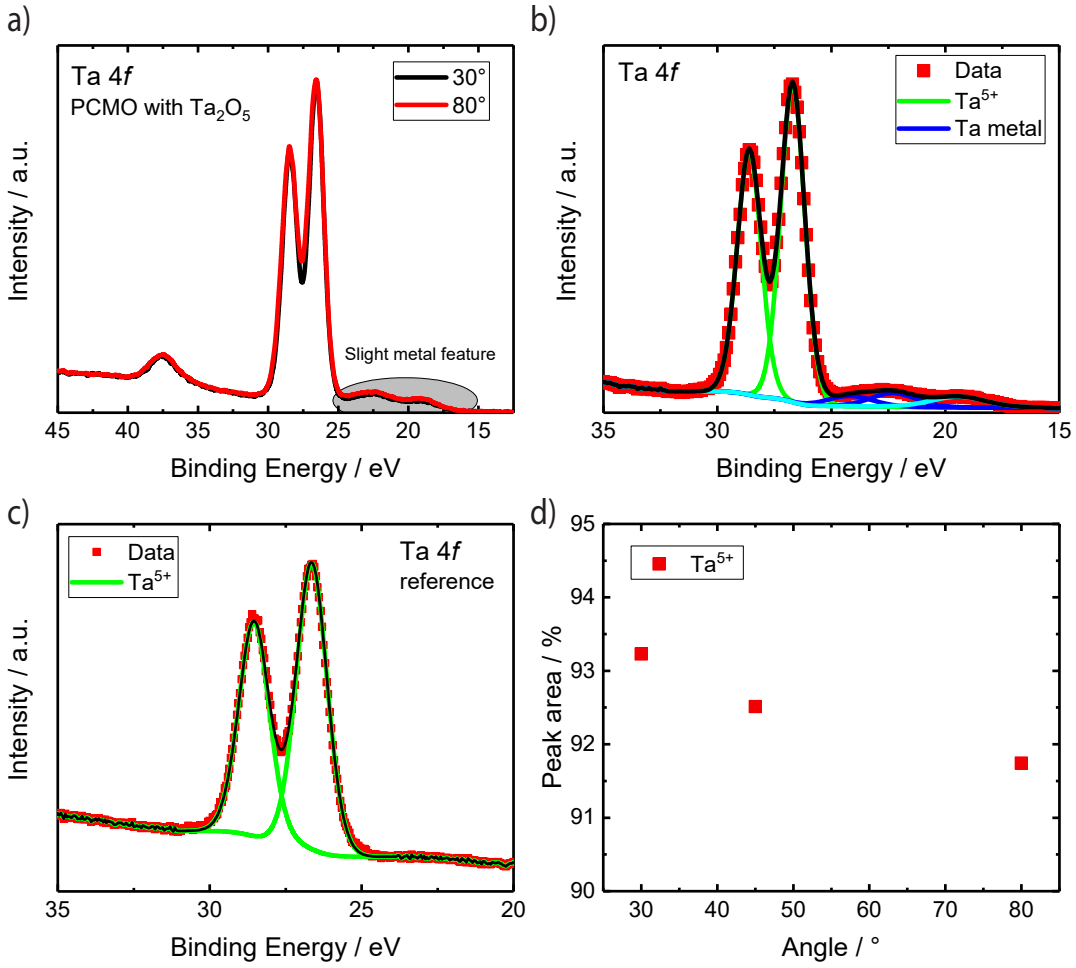

Figure 5.11.: Ta 4*f* spectra of Ta_2O_5 in combination with PCMO. a) Ta 4*f* spectrum of Ta_2O_5 in combination with PCMO at different angles, 30° (black) and 80° (red). A slight metal feature can be seen for both angles. b) Fitting of the Ta 4*f* with a Ta^{5+} and a Ta metal feature. c) Fitting of a Ta 4*f* reference spectrum grown on SiO_2 with the same growth parameters as for the growth on PCMO. d) Proportion of the Ta^{5+} area of the whole Ta 4*f* peak area. Decreasing Ta^{5+} proportion with increasing profiling depth.

5.2. PCMO in combination with Oxides

The investigation PCMO in combination with oxidisable metals shows that for some metals, i.e. Al and Ta, an interface oxide forms during deposition. For others metals, like W, no clear interface oxide can be identified. In this section the impact of a directly deposited oxide layer on top of the PCMO thin film will be investigated by spectroscopy. The studied oxides are Ta_2O_5 and WO_3

5.2.1. PCMO/Ta_2O_5 interface

In section 5.1.2, the impact of Ta metal on top of an PCMO thin film is presented. A clear formation of an interface oxide is visible. In this section the impact of an directly deposited Ta_2O_5 layer is presented.

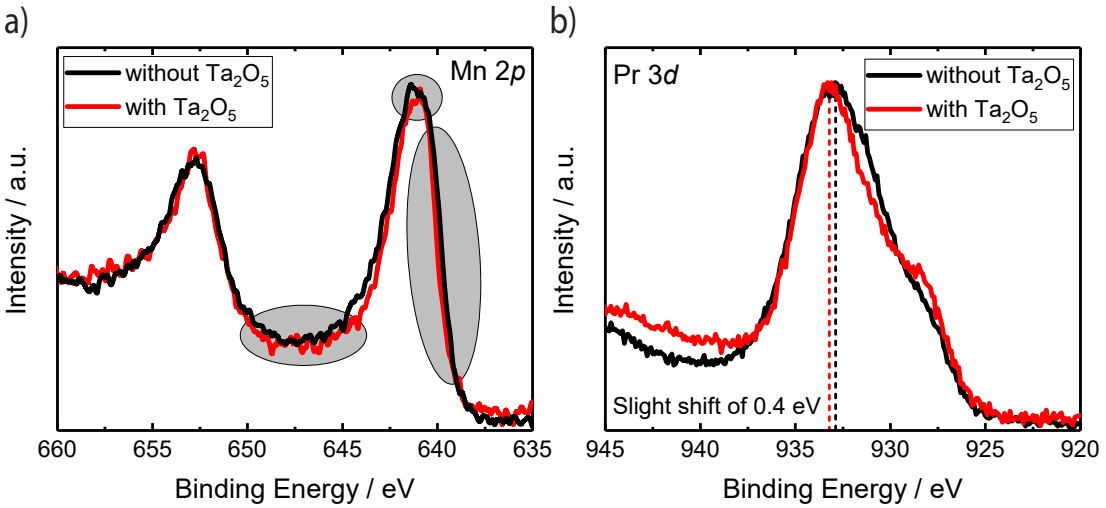

Figure 5.12.: XPS measurements of a) Mn $2p$ and b) Pr $3d$ peak without and with Ta_2O_5 on top of the PCMO thin film. a) No clear change of the Mn $2p$ spectrum can be seen. b) A slight shift of 0.4 eV of the Pr $3d$ peak can be seen.

Figure 5.11 a) shows the Ta $4f$ spectrum of the Ta_2O_5 in combination with PCMO. A clear peak doublet at 26.7 eV and 28.6 eV can be seen for both take of angles, 30° (black) and 80° (red). This is in good agreement with the theoretical value for Ta_2O_5, 26.3 eV and 27.2 eV [142, 143]. Beside the Ta_2O_5 doublet a shoulder at lower binding energies can be seen. This shoulder is often assigned to the O $2s$ peak [116]. Nevertheless, the given spectra show not a single peak, but also a doublet. This doublet can be assigned additionally to lower oxidation states of Ta. Furthermore, it can be seen for different angles.

Figure 5.11 b) shows the peak fitting of the Ta $4f$ spectrum with the Ta^{5+} peak and the fitted Ta^0 peak at 22.3 eV. This peak position fits to the literature peak position of Ta metal, 21.8 eV [143]. The Ta^{5+} peaks are fitted with a GL(30) and the Ta^0 peaks are fitted with an asymmetrical LA(1.1,7,25) line shape. With to these two Ta doublets and the O $2s$ peak, the data can be described quite well.

Figure 5.11 c) shows a Ta_2O_5 reference spectra grown on SiO_2 with the same growth parameters like the Ta_2O_5 thin film on PCMO, figure 5.11 a) and b). In this spectrum, no shoulder at lower binding energies can be seen. The data can be described with the Ta^{5+} doublet, no additional metal feature is needed. This means, that the deposited film is fully oxidised. The slight reduction of the thin film can not be explained by thermodynamics.

This reduction of the Ta_2O_5 layer is also indicated by different measurements angles. Figure 5.11 d) shows the percentage of the Ta^{5+} valence state on the whole Ta $4f$ peak. A slight decrease with increasing angle can be seen. This means, that the amount of reduced Ta_2O_5 increases with profiling depth. Therefore, one can conclude, that the Ta_2O_5 is reduced at the PCMO interface, even if this is thermodynamic not favourable, see figure 5.1 a). Nevertheless, the change of the amount of Ta^{5+} is only in the range of a few percent.

Beside this trend in the oxidation state of Ta, figure 5.12 a) shows the Mn $2p$ peak of the PCMO thin film without and with the Ta_2O_5 layer on top. No changes on the peak edges at lower binding energies can be seen. If a further oxidation of the PCMO thin film layer would takes place, one would expect an shift of the peak to higher binding energies and also a change in the overall peak shape. This is not visible here. Therefore, one can not conclude from figures 5.11 c)/d) and 5.12 a) that the PCMO oxidises further.

The Pr $3d\,5/2$ spectrum without and with Ta_2O_5 on top of the PCMO is plotted in figure 5.12 b). The peak position for the Pr $3d\,5/2$ peak without Ta_2O_5 is at 932.7 eV. The Pr $3d\,5/2$ peak with Ta_2O_5 shifts by 0.4 eV to slightly higher binding energies of 933.1 eV.

5.2.2. PCMO/WO_3 interface

In section 5.1.3, PCMO in combination with W metal was investigated. In contrast to the Al and Ta metal, no oxide at the interface between PCMO and W could be measured. Nevertheless, here the impact of WO_3 deposited directly on top of the PMCO layer will be presented.

Figure 5.13 a) shows the W $4f$ spectrum of WO_3 deposited on top of the PCMO film at different take of angles, 30° (black line) and 80° (red line). A peak doublet at 35.8 eV can be seen for both take off angles. No difference at different angles can be seen for this peak. This means, that the deposited thin film is fully oxidised throughout. The peak doublet can be related to the WO_3 or W^{6+} valence state. Figure 5.13 b) shows the fitting of the W $4f$ spectrum. It can be seen that the spectrum can be fitted quite well with only one doublet, blue lines. This doublet can be referred to WO_3. Additionally, a WO_3 loss feature can be seen. This means that even if there are two stable oxidation states for W, WO_2, and WO_3, only WO_3 was deposited with the used sputter parameters.

Figure 5.13 c) shows the Mn $2p$ spectrum without WO_3 (black) and with WO_3 (red) on top of the PCMO. A peak for both measurements can be seen at 641.9 eV and 653.3 eV. This peak is a combination of the Mn^{3+} and Mn^{4+} valence state, like it is expected for the PCMO thin film. No clear change of the Mn $2p$ spectrum between the PCMO thin film with and without WO_3 layer can be seen, no satellite feature and no change in the oxidation state can be seen. This means that the WO_3 does not pull oxygen out of the PCMO thin film, because WO_3 is already fully oxidised.

The Pr $3d$ spectrum of PCMO without (black) and with (red) WO_3 is shown in figure 5.13. A slight shift of the Pr $3d5/2$ peak of 0.6 eV can be seen.

5.3. Conclusion of PCMO with different interface layer

The interface between PCMO and different metals and oxides shows different behaviour. For Al and Ta an angle and depth dependent oxide layer is measured. Furthermore, a change of the Mn $2p$ spectrum could be observed for Al and Ta: Mn^{2+} has been formed. This is an indication that the PCMO layer is reduced at the interface and the metal pulls oxygen out of the PCMO. With these two aspects one can conclude that an oxide

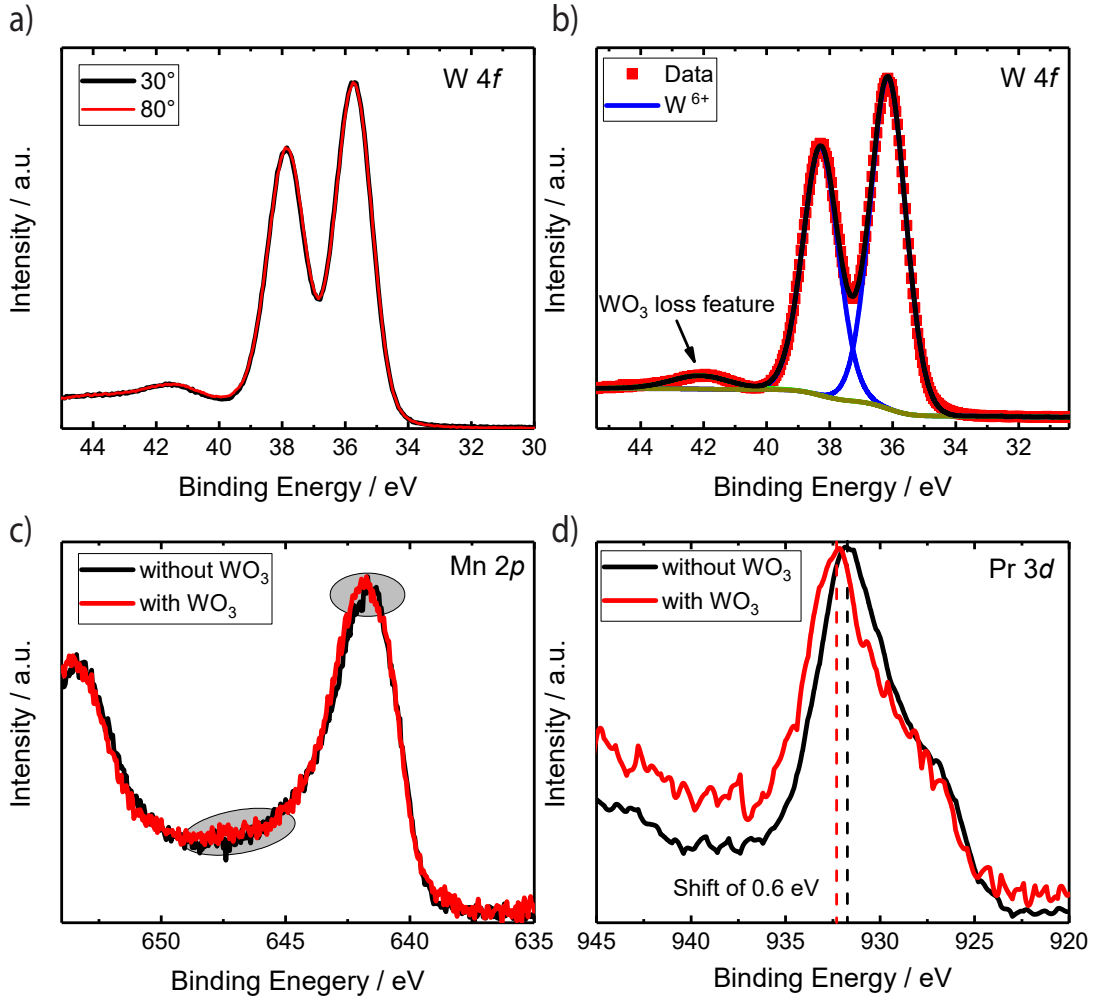

Figure 5.13.: XPS spectra of the PCMO in combination with WO_3. a) W $4f$ sepctra at different take of angles, 30° (black) and 80° (red). b) Fitting of the W $4f$ spectra with a W^{6+} doublet. Additionally a WO_3 loss feature can be seen. c) Mn $2p$ of PCMO without and with WO_3. No additional Mn^{2+} feature and also no change in peak shape. d) Pr $3d$ peak of PCMO without (black) and with (red) WO_3. A slight peak shift of 0.6 eV can be seen.

layer at the interface is formed.

For W, due to the fact that neither an oxide nor a change in the Mn $2p$ spectrum is measured, one can conclude that no oxide interface layer is formed. From thermodynamics, this is not surprising because the gain of energy by forming WO_2 or WO_3 is much lower than the energy gain of forming Al_2O_3 or Ta_2O_5.

A peak shift of the Pr $3d$ peak can be seen for all of three metals. The reason for this shift to higher binding energies is a downwards bending of the PCMO bands at the interface. This downwards bending is expected due to the different work functions of the PCMO and the used metals. Additionally the redox reaction that happens at the interface leads is curcial for the band bending.

For the deposition of oxides, the Ta_2O_5 seem to slightly change at the interface. This is not observed for the WO_3. The origin of the reduction of the Ta_2O_5 at the interface is not fully understood. Nevertheless, the amount of reduced Ta_2O_5 is so small that in the following, it will be regarded fully oxidised.

6. Resistive Switching Properties of PCMO

In this chapter, the resistive switching properties of PCMO grown and processed at different conditions in combination with different interface metals as standard system are shown. Here the impact of the PCMO thickness, the growth pressure, and the RTA process on the electrical properties of the devices are investigated. Furthermore, Al thickness variations are investigated. Afterwards, the resistive switching properties of PCMO grown and processed with the standard parameters introduced in section 4.1, in combination with different oxidisable metals and oxides will be presented.
For the most promising material combinations the retention, variability, subloops, and the multilevel switching behaviour will be investigated. At the end, a simple two resistor model to describe the switching behaviour of the area type resistive switching devices is introduced.

Unless otherwise stated the shown devices have the structure mentioned in section 3.2.2. The Pt bottom and top electrodes have a thickness of 20 nm for all devices. The top electrode is contacted via a tungsten needle and the bottom electrode is contacted via wire-bonding. The voltages are always applied to the top electrode. The bottom electrode is hold on ground.

6.1. Impact of PCMO and Al thickness on resistive switching behaviour

In a pre-study [123], 20 nm PCMO in combination with 7 nm Al showed good switching behaviour. Nevertheless, this pre-study did not focus on the impact of the PCMO growth conditions and Al thickness on the switching behaviour of the PCMO thin film. There was the focus on the impact of the RTA process. Therefore, the impact of the PCMO and Al layer thickness on the switching behaviour will be presented.

All PCMO thin films in the following are grown with the parameters presented in section 3.1.1, 4.1, and 4.2.

6.1.1. Impact of PCMO thickness on resistive switching behaviour

The impact of different PCMO thicknesses will be presented in this section. In figure 4.10 a) the AFM scan of a 10 nm PCMO thin film can be seen. Due to the fact that the AFM scan does not show a continuous thin film, no switching could be observed for these devices. Therefore, the 10 nm thick PCMO devices will be neglected in this chapter.

Figure 6.1 shows the switching curves and the area scaling of the resistance for PCMO thin films with different thicknesses, 15 nm, 20 nm, 30 nm and 50 nm, in combination with 7 nm Al. For each PCMO thickness switching curves of devices with different sizes,

100 µm, 50 µm and 20 µm edge length are measured.

The switching curves of 15 nm PCMO devices can be seen in figure 6.1 a). The switching voltage is −3 V for the SET and 2.2 V for the RESET process. The $100 \times 100\,\mu m^2$ devices (black) shows no resistive switching and only an ohmic behaviour with low resistance value. Beside this, the $50 \times 50\,\mu m^2$ devices and the $20 \times 20\,\mu m^2$ devices show resistive switching behaviour. The black arrows indicate the switching direction. It can be seen that for both devices, the difference between the HRS and the LRS is larger in the negative voltage range, compared to the difference between the HRS and the LRS in the positive voltage range. Additionally, it is noticeable that the LRS for the $50 \times 50\,\mu m^2$ devices and the $20 \times 20\,\mu m^2$ devices is partially at the same current value for the LRS. Furthermore, an abrupt increase in current can be seen. This is a hint that the device does not show area type resistive switching. Figure 6.1 b) shows the extracted resistance values at −0.3 V, black dashed line in figure 6.1 a), for the 15 nm thick PCMO devices of different sizes. In red, the HRS and in green the LRS is represented. The blue dots represent the initial state of the device. Due to the fact that only two HRS and two LRS are measured, it is not possible to make a general statement about the scaling of the resistance with the area. If one only considers the two points shown, the slope of the connecting line is $(-0.80 \pm 0.03)\,\Omega/\mu m^2$ and $(-0.49 \pm 0.04)\,\Omega/\mu m^2$ for the HRS and the LRS, respectively, see table 6.1. Beside the fact that the slope should be around $-1\,\Omega/\mu m^2$ due to ohms law

$$R = \rho \frac{L}{A}$$

with R the resistance, ρ the resistivity, L the wire length and A the size of the device, for area type resistive switching devices. Moreover, the abrupt SET process, which can be seen in figure 6.1 a), and the quite similar resistance values of the LRS for different device size are a hint that the switching mechanism of the 15 nm PCMO thin film is filamentary.

Figure 6.1 c) shows the switching curves of the 20 nm thick PCMO thin film in combination with 7 nm Al of $100 \times 100\,\mu m^2$, $50 \times 50\,\mu m^2$, $20 \times 20\,\mu m^2$, and $10 \times 10\,\mu m^2$ size and a SET/RESET voltage of −3.0 V/2.2 V, respectively. The black arrows indicate the switching direction of the I-V-curve. It can be seen, that both the SET and the RESET show a gradual change in resistance. Beside this, it can already be seen that the current decreases with decreasing device size. This trend can also also be seen in figure 6.1 d). Here, the resistance at −0.3 V (black dashed line in figure 6.1 c)) plotted against the different device sizes is shown. The values of the HRS are shown in red and the values of the LRS are shown in green. Additionally, the initial state of the device is shown in blue. A clear quasi linear trend in the double logarithmic plot can be seen. The slop of the linear trend is $-1.11 \pm 0.04\,\Omega/\mu m^2$ for the HRS and $-1.12 \pm 0.05\,\Omega/\mu m^2$ for the LRS, see table 6.1. This change in resistance is close to $-1\,\Omega/\mu m^2$ that is expected for area type resistive switching devices. Furthermore, the measured data points fit to the assumed linear behaviour. One can conclude from the linear behaviour in combination with the gradual SET and RESET process that the 20 nm thick PCMO devices in combination with 7 nm Al show area type resistive switching. Additionally, the switching curves do not change their shape or their switching characteristics for differently sized devices.

The switching curves of thicker PCMO thin films, 30 nm and 50 nm, can be seen in figure 6.1 e) and g). For both thicknesses, it can be seen that the switching curve (IV-

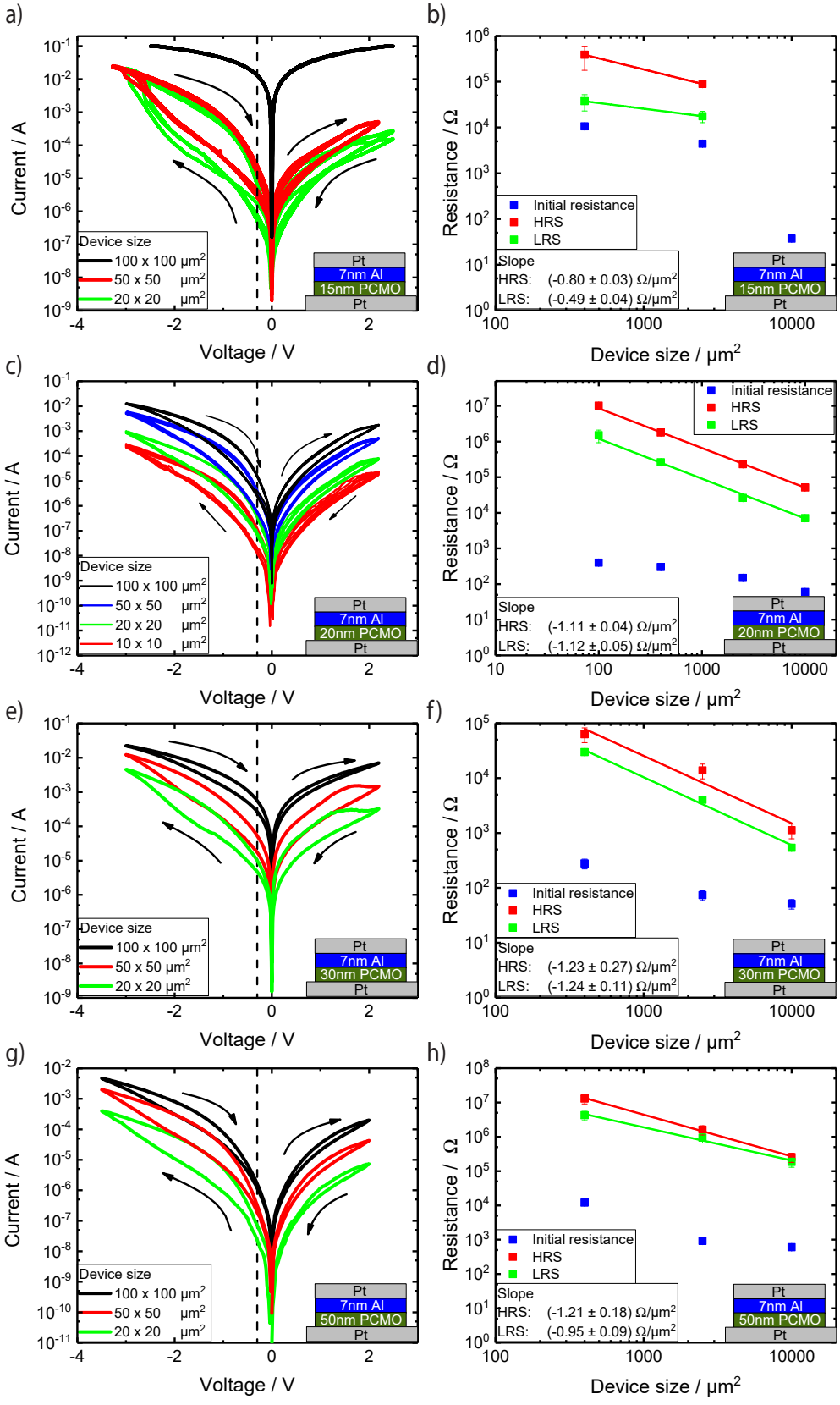

Figure 6.1.: Resistive switching curves and linear scaling of resistance with device size for devices with different PCMO thicknesses, 15 nm a) and b), 20 nm c) and d), 30 nm e) and f), 50 nm g) and h).

curve) of the $100 \times 100\,\mu m^2$ devices differ from the switching curves of the $50 \times 50\,\mu m^2$ and $20 \times 20\,\mu m^2$ devices. For the 30 nm devices, see figure 6.1 e), the switching curve of the $100 \times 100\,\mu m^2$ shows a smaller ON/OFF-ratio compared to the $50 \times 50\,\mu m^2$ and $20 \times 20\,\mu m^2$ devices. Additionally, for the smaller devices a change in slope of the switching curve during the SET process at $-2.0\,V$ and for the RESET process at $1.5\,V$ can be seen. This change is not visible for the $100 \times 100\,\mu m^2$ devices. This change in slope is the reason for the larger opening and a resulting higher ON/OFF-ratio of the switching curves of smaller devices. A possible explanation could be the more uniformity of the PCMO/Al interface for the smaller devices, resulting from the smaller area. The area scaling of the resistance with the device size can be seen in figure 6.1 f). It can be seen, that even if the switching curves looks quite different, for the different sizes, the fitted slope of the HRS (red) and LRS (green) is around -1 $\Omega/\mu m^2$, $(-1.23 \pm 0.27)\,\Omega/\mu m^2$ and $(-1.24 \pm 0.11)\,\Omega/\mu m^2$, respectively, see table 6.1. One can conclude from this fit, that the switching mechanism of the 30 nm thick PCMO in combination with 7 nm Al shows area type resistive switching.

For the 50 nm thick PCMO thin film devices in combination with 7 nm Al, the switching curves show the same behaviour as the switching curves of the 30 nm thick PCMO thin film devices, see figure 6.1 g). The switching curves of the $100 \times 100\,\mu m^2$ devices show a smaller difference between the HRS and the LRS compared to the smaller devices. Additionally, a similar change in the slope of the I-V curve at $-2.0\,V$ as for the 30 nm thick PCMO device can be seen. For the 50 nm thick PCMO devices a slight change in slope can also be guessed for the $100 \times 100\,\mu m^2$ devices. Nevertheless, at $-0.3\,V$ it seems that the HRS and the LRS have the same current value. With decreasing device size the measured ON/OFF-ratio at $-0.3\,V$ increases. The behaviour can also be seen in figure 6.1 h). The increase in resistance with decreasing device is larger for the HRS, $(-1.21 \pm 0.18)\,\Omega/\mu m^2$, than for the LRS $(-0.95 \pm 0.09)\,\Omega/\mu m^2$. Nevertheless, the slopes are still around $-1\,\Omega/\mu m^2$. Therefore, one can conclude that the devices still show area type resistive switching. The reason for the difference in slope is either a too high LRS or a too small HRS for larger devices. A reason for this could be an uneven interface oxide due to the higher roughness of the thin film compared to the thinner films, as shown in figure 4.10. These roughness can lead to unevenly thick Al and Al_2O_3 layers at the interface and thereby to an averaging over the barrier thickness over the device area and thereby in total to smaller differences between HRS and LRS. This impact of the unevenly thick layer is larger for larger devices and therefore, the resistive switching shows a smaller ON/OFF-ratio.

For a better comparison of the different PCMO thicknesses, table 6.1 shows the slopes of the different devices. These slopes are also presented in figure 6.2 a). It can be seen, that the 20 nm PCMO devices fits the best to the expected slope of $-1\,\Omega/\mu m^2$. Furthermore, the HRS and the LRS slope are the same. The 15 nm thick PCMO thin film device is the only one with a slope way lower than $-1\,\Omega/\mu m^2$. A possible reason for this difference is the thin PCMO film. It could be that the PCMO thin film does has not the same thickness all over the sample. Places with a small thickness of the PCMO thin film could be the main spots of interests of switching for these devices. These smaller PCMO thicknesses could already be seen in the TEM data shown for the 20 nm PCMO thin film in section 5.1.1. At these positions there may be a breakthrough which can explain the filamentary switching behaviour. Furthermore, this could also be a reason that the

Table 6.1.: Extracted change of resistance with devices size of PCMO/Al devices with different PCMO thicknesses from figure 6.

PCMO thickness / nm	HRS slope / $\Omega/\mu m^2$	LRS slope / $\Omega/\mu m^2$
10	no switching	no switching
15	-0.80 ± 0.03	-0.49 ± 0.04
20	-1.11 ± 0.04	-1.12 ± 0.05
30	-1.23 ± 0.27	-1.24 ± 0.11
50	-1.21 ± 0.18	-0.95 ± 0.09

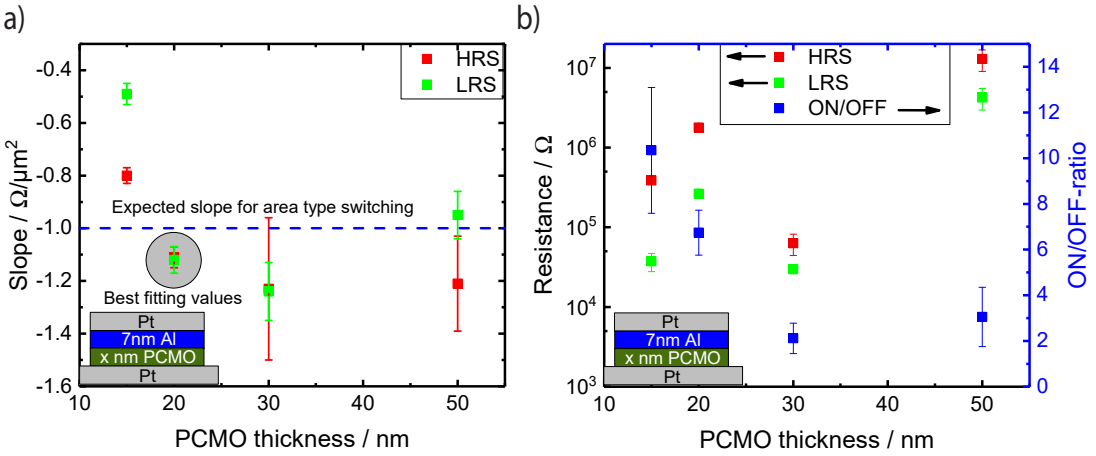

Figure 6.2.: a) Slope of the resistance change with changing device size for different PCMO thicknesses. b) HRS, LRS and ON/OFF-ratio value of the $20 \times 20\,\mu m^2$ devices for devices with different PCMO thickness.

$100 \times 100\,\mu m^2$ devices show no switching, due to the amount of these thin PCMO spots. For the 30 nm and 50 nm PCMO devices it can be seen that the values of the slope fit also quite well to the expected values. Nevertheless, the error of the slope is larger and at least for the 50 nm PCMO thin film device, the difference in slope between the HRS and LRS is large.

Figure 6.2 b) shows the resistance value of the HRS and the LRS and the ON/OFF-ratio of the $20 \times 20\,\mu m^2$ devices with different PCMO thicknesses. The ON/OFF-ratio of the switching curves decreases with increasing PCMO thickness. The 15 nm PCMO thin film shows the highest ON/OFF-ratio. Nevertheless, due to the fact that the switching shows filamentary switching behaviour and filamentary switching devices are known to show higher ON/OFF-ratios, the 15 nm PCMO device will be neglected here. The increase of the resistance could be hint for a thicker AlO_x layer. Furthermore, the microstructure of the PCMO thin film impacts the thickness the AlO_x layer. The 30 nm thick PCMO device does not follow this trend. On the contrary, the resistance value of the of the 30 nm thick PCMO thin film is the smallest. Unfortunately, no conclusive explanation for this behaviour can be given here. Various reasons can lead to these smaller resistance values: non uniform Al layer or PCMO layer, processing differences of the samples, etc..

To summarise, the 20 nm PCMO thin film shows the best switching properties in com-

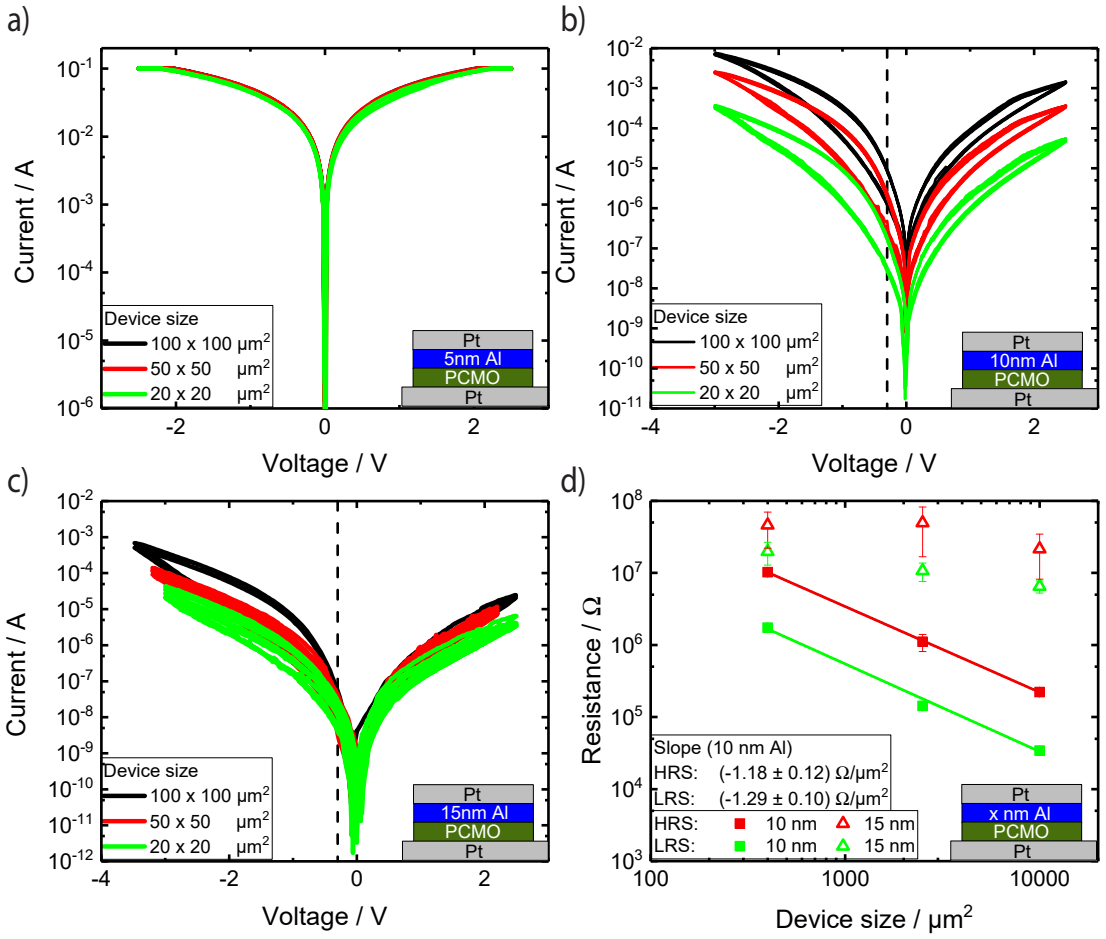

Figure 6.3.: a)-c) IV curves of PCMO based resistive switching devices with Al layers of different thicknesses, 5 nm a), 10 nm b), and 15 nm c). d) HRS and LRS dependence on the device size for the 10 nm and 15 nm thick Al layer.

bination with 7 nm Al. In the following, only 20 nm thick PCMO thin films will be used. They are therefore only referred to as PCMO.

6.1.2. Impact of Al thickness on resistive switching behaviour

20 nm PCMO showed the most reliable switching behaviour in combination with 7 nm Al interface layer. Nevertheless, different Al thicknesses in combination with 20 nm PCMO (PCMO) will be investigated in the following. Here 5 nm, 7 nm, 10 nm and 15 nm Al will be investigated. Due to the fact, that the switching curves of the 7 nm Al are already shown before, the focus will be on 5 nm, 10 nm and 15 nm Al. When comparing the individual thicknesses, the values for 7 nm Al from above are used in this section.

The switching curves of the 20 nm PCMO in combination with 5 nm, 10 nm and 15 nm Al can be seen in figure 6.3 a)-c). The 5 nm Al, see figure 6.3 a), only shows an ohmic behaviour and no resistive switching for the different device sizes can be seen. The resistance for all these devices is around 100 Ω. This low resistance might be explained by the thin Al layer. PCMO and Pt forms an ohmic contact. In section 5.1.1 it was shown by

Table 6.2.: Extracted resistance change of the LRS and HRS with device size for 20 nm PCMO in combination with different Al thicknesses from figure 6.3 and figure 6.1.

Al thickness / nm	HRS slope / $\Omega/\mu m^2$	LRS slope / $\Omega/\mu m^2$
5	no switching	no switching
7	-1.11 ± 0.04	-1.12 ± 0.05
10	-1.18 ± 0.12	-1.29 ± 0.10
15	-0.21 ± 0.14	-0.35 ± 0.03

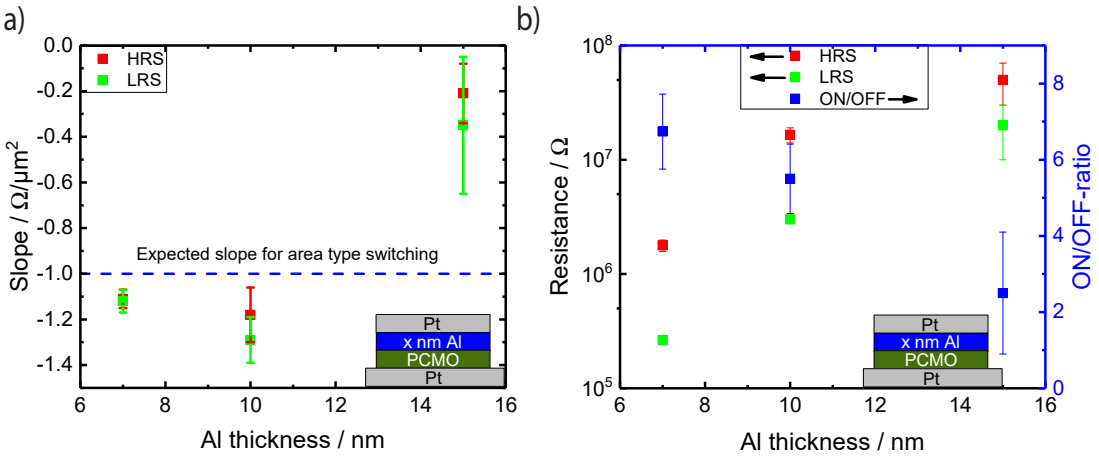

Figure 6.4.: a) Slope of the resistance change with changing device size for different Al thicknesses with 20 nm PCMO thickness. b) HRS, LRS and ON/OFF-ratio value of the $20 \times 20\,\mu m^2$ devices for devices with different Al thickness with 20 nm PCMO thickness.

TEM that the PCMO surface is quite rough and the Al layer has to have a certain thickness to cover the whole surface. Due to the fact that the 20 nm PCMO thin film is quite rough, 5 nm of Al might not cover the whole thin film or the thickness of the Al and the native oxide at the interface is imterrupted and can not be homogenised by the first cycle.

The switching curves of the devices with 10 nm Al layer can be seen in figure 6.3 b). They are comparable to the curves of the 7 nm Al layer devices. A gradual SET around −3 V and a gradual RESET around 2.2 V can be seen. Nevertheless, the current is around one order of magnitude lower compared to the 7 nm devices. This indicates an additional series resistance in the devices or a thicker Al_2O_3 layer at the interface. This thicker layer could be explained by the prolonged heating of the device during the longer evaporation of the Al layer, see section 3.1.2. Additionally, the thicker Al layer could suck more oxygen out of the PCMO thin film. This would also lead to a thicker or more oxidised AlO_x layer. Figure 6.3 d) shows the extracted HRS and LRS values at −0.3 V (black dashed line in figure 6.3 b)) for the different sized devices, $100 \times 100\,\mu m^2$, $50 \times 50\,\mu m^2$, and $20 \times 20\,\mu m^2$. The slope is $(-1.18 \pm 0.12)\,\Omega/\mu m^2$ and $(-1.29 \pm 0.10)\,\Omega/\mu m^2$ for the HRS and the LRS, respectively. The slopes can also be found in table 6.2. The slopes of the 10 nm layer fit quite well to the expected slope for area type resistive switching devices.

For the 15 nm Al layer devices, the switching curves are shown in figure 6.3 c). It can be seen, that the switching curve of the $100 \times 100\,\mu m^2$ devices are comparable to the switching curves of the 7 nm and 10 nm Al devices. Nevertheless, the current of the 15 nm Al devices is around one order of magnitude lower than the current of the 10 nm devices and even two orders of magnitude lower than the 7 nm Al devices. This also indicates an additional series resistance in the devices or a thicker Al_2O_3 layer at the interface like for the 10 nm Al layer. Nevertheless, all devices show a gradual SET and gradual RESET as expected for the area type resistive switching devices. It can be seen that the ON/OFF-ratio slightly decreases with decreasing device size. Furthermore, it can already be seen in the switching curves that the change of the resistance with the device area differs from the change observed for the 7 nm and 10 nm devices. The change of resistance with changing device size is shown in figure 6.3 d). The HRS and LRS values are extracted at −0.3 V, black dashed line in figure 6.3 c). It can be seen that the different sizes does not show a clear linear trend in the double logarithmic plot. If one nevertheless carries out a fit one gets $(-0.21 \pm 0.14)\,\Omega/\mu m^2$ and $(-0.35 \pm 0.03)\,\Omega/\mu m^2$ for the HRS and the LRS, respectively. The slopes can also be found in table 6.2.

For better comparison of the devices, the slopes of the 7 nm, 10 nm and 15 nm Al layer devices are shown in figure 6.4 a). It can be seen that the slope of the 7 nm Al and the 10 nm only show slight deviations from the expected value of -1 $\Omega/\mu m^2$. The slope of the 10 nm Al devices is slightly higher than the slope of the 7 nm Al devices and also the difference between the HRS and the LRS slope and the variance of the slope are larger compared to the 7 nm Al. The slope of the 15 nm Al devices is way lower compared to the 7 nm and 10 nm Al devices. One possible explanation for this could be the higher resistance of the 15 nm Al devices compared to the 7 nm and 10 nm Al devices. This higher resistance of the device can be achieved by a higher series resistance due to the a thicker AlO_x layer at the interface. This thicker native oxide at the interface cannot initially be explained by the thicker Al oxide, since, as described in chapter 5, the Al is

not completely oxidised. One possibility that the oxide of the interface is thicker for the 15 nm Al layer as for the 7 nm Al layer is the heat to which the sample is exposed during Al deposition, see section 3.1.2. An other possibility could be that the thicker Al sucks more oxygen out of the PCMO layer. This would lead to a thicker or more oxidised AlO_x layer. Furthermore, a reduced PCMO layer would also lead to an increase of the resistance of the device stack. This higher series resistance or thicker AlO_x leads to a smaller voltage drop over the interface between the PCMO and the Al/AlO_x. Therefore, the voltage needed to switch the device properly could be higher for the device with thicker Al layer. Nevertheless, higher voltages always lead to a breakdown into an ohmic state, therefore, higher voltages are not presented here.

The HRS and LRS of the $20 \times 20\,\mu m^2$ devices and the corresponding ON/OFF-ratio is shown in figure 6.4 b). It can be seen that the HRS and the LRS increase with increasing Al thickness. Furthermore, the ON/OFF-ratio decreases with increasing Al thickness as described before. These two behaviours suggest the previously described behaviour with a thicker AlO_x layer and a reduced PCMO layer, which may also cause the switching voltages to change with the thickness of the Al layer.

In summary, both the 7 nm and 10 nm Al show good switching properties for area type resistive switching devices. Nevertheless, the 7 nm devices are preferable due to their lower resistance, especially since the resistance would increase significantly if the device size would be decreased down to the 100 nm range. Further switching characteristics of the PCMO/7 nm Al devices will be presented later.

6.2. Resistive switching of PCMO/metal devices

In this section the impact of oxidisable metals beside Al on the resistive switching behaviour will be presented. Beside the metals that are investigated in chapter 5 Ta and W, that can also be found in literature [146, 147] in combination with PCMO, other metals that are commonly used are investigated, like Ti [33, 140, 146, 148] and Mo [149, 150].

PCMO/Ta

The switching curves of 20 nm PCMO in combination with 7 nm Ta for different device sizes, $100 \times 100\,\mu m^2$, $50 \times 50\,\mu m^2$, and $20 \times 20\,\mu m^2$, are shown in figure 6.5 a). The current decreases with the device size but no hysteresis can be seen for the devices. All devices show an ohmic behaviour. Figure 6.5 b) shows the switching curve of the $20 \times 20\,\mu m^2$ device with an adapted scale. The switching direction is indicated by the black arrows. In this presentation of the I-V-curve, a slight difference in the HRS and the LRS can be seen, even if it is quite small. The extracted HRS and LRS resistance values at $-0.3\,V$ (black dashed line) are shown in figure 6.5 c). It can be seen, that the HRS and the LRS can be clearly distinguished from each other. Nevertheless, the ON/Off-ratio is around 1.8 and quite low.

Figure 6.6 a) shows the switching curves of 20 nm PCMO in combination with 10 nm Ta. It can be seen, that the switching curves of the $100 \times 100\,\mu m^2$ and the $50 \times 50\,\mu m^2$ devices show only an ohmic behaviour and no resistive switching. The switching curve

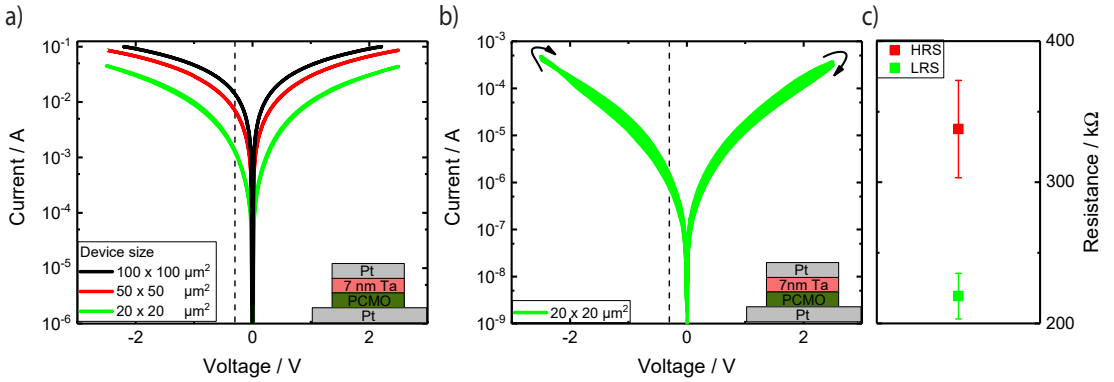

Figure 6.5.: a) Switching curves of PCMO in combination with 7 nm Ta metal of different device sizes. b) Switching curves of PCMO in combination with 7 nm Ta metal of $20 \times 20\,\mu m^2$ devices. c) Resistance value of $20 \times 20\,\mu m^2$ devices at $-0.3\,V$.

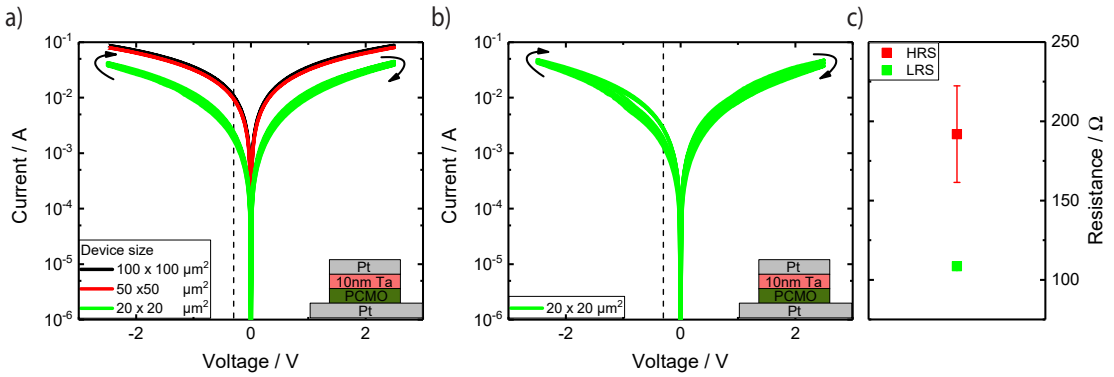

Figure 6.6.: a) Switching curves of PCMO in combination with 10 nm Ta metal of different device sizes. b) Switching curves of PCMO in combination with 10 nm Ta metal of $20 \times 20\,\mu m^2$ devices. c) Resistance value of $20 \times 20\,\mu m^2$ devices at $-0.3\,V$.

of the $20 \times 20\,\mu m^2$ shows a different current than the $100 \times 100\,\mu m^2$ and the $50 \times 50\,\mu m^2$ devices. The black arrows indicate the switching direction of the devices. Figure 6.6 b) shows an enlarged representation of the switching curve of the $20 \times 20\,\mu m^2$. For the negative voltage regime a clear change between the HRS and the LRS can be seen. In figure 6.6 c) the resistance values at $-0.3\,V$ (black dashed line in figure 6.6 a) and b)) for the $20 \times 20\,\mu m^2$ devices can be seen. It can be seen that the ON/OFF-ratio of the switching curves is around 1.5 and the resistance is in the $100\,k\Omega$ regime.

One can conclude that the PCMO in combination with 7 nm and 10 nm Ta metal shows resistive switching only for the $20 \times 20\,\mu m^2$ devices. The larger devices, $100 \times 100\,\mu m^2$ and $50 \times 50\,\mu m^2$, do not show any switching, neither for the 7 nm nor for the 10 nm thick Ta layer. Smaller devices could show better switching properties like a higher ON/OFF-ratio but this is not investigated in this work due to the higher homogeneity of the interface.

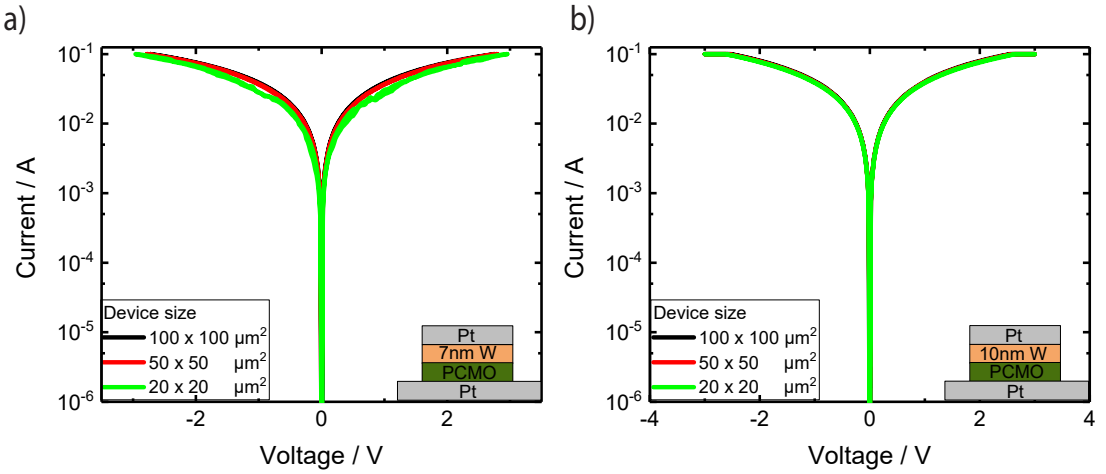

Figure 6.7.: Switching curves of PCMO in combination with a) 7 nm and b) 10 nm W of $100 \times 100\,\mu m^2$, $50 \times 50\,\mu m^2$, and $20 \times 20\,\mu m^2$ devices.

PCMO/W

Resistive switching devices consisting out of PCMO in combination with W can be found often in the literature [151–156]. Figure 6.7 shows the switching curves of PCMO in combination with a) 7 nm and b) 10 nm devices. For both devices it can be seen that the devices do not show any switching behaviour, neither for different W thicknesses, nor for different device sizes, $100 \times 100\,\mu m^2$, $50 \times 50\,\mu m^2$, and $20 \times 20\,\mu m^2$. For both different thicknesses the I-V curves only show a ohmic behaviour with a resistance of some hundreds of ohms. This behaviour can have different reasons. One possibility is the missing WO_3 layer that has been shown in chapter 5. Only a small band bending could be measured for these devices. Furthermore, a depletion zone is expected inside the PCMO, but the impact of the depletion zone inside the PCMO could be so small that only an ohmic behaviour can be measured. Furthermore, the exact thickness of the W layer on top can vary due to the roughness of the PCMO layer, which can lead to conducting paths through the W layer. The PCMO/W combination that have been shown in literature often consist out of a thicker PCMO layer, 100 nm, and a thicker W layer [157].

PCMO/Mo

Beside PCMO/W, PCMO/Mo is also reported in literature to exhibit resistive switching behaviour [149, 158]. Figure 6.8 a) shows the measured I-V characteristics of PCMO in combination with 7 nm Mo of devices with different sizes, $100 \times 100\,\mu m^2$, $50 \times 50\,\mu m^2$, and $20 \times 20\,\mu m^2$. For all different device sizes, no resistive switching can be seen. All devices show an ohmic behaviour, with a resistance of several ohms. I-V measurements of $20 \times 20\,\mu m^2$ devices with different Mo thicknesses, 7 nm and 10 nm, can be seen in figure 6.8 b). Neither for the 7 nm nor for the 10 nm devices any ressitive switching behaviour can be seen. This is also the case for devices of different sizes, $100 \times 100\,\mu m^2$ and $50 \times 50\,\mu m^2$, not shown here. This behaviour could also be due to the absence of an oxide layer at the interface. The PCMO/Mo is not measured in chapter 5 due to the fact, that the fabrication of the Mo happened in a different tool. Comparing the change in Gibbs free energy, no oxide layer formation is expected. The change of Gibbs

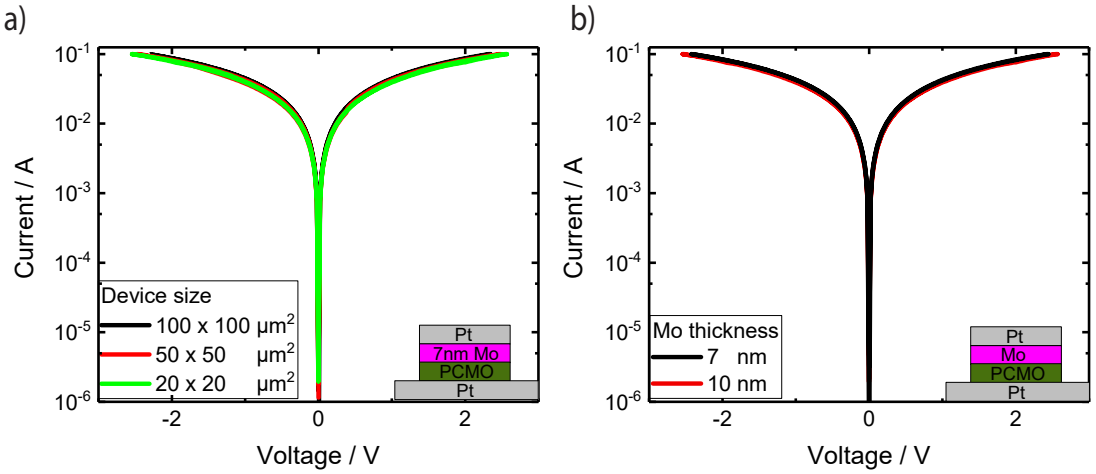

Figure 6.8.: a) I-V measurement of PCMO in combination with 7 nm Mo of devices with different sizes, $100 \times 100\,\mu m^2$, $50 \times 50\,\mu m^2$, and $20 \times 20\,\mu m^2$. b) I-V measurements of $20 \times 20\,\mu m^2$ PCMO devices in combination with 7 nm and 10 nm Mo.

free energy for the oxidation into MoO_2 or MoO_3 is $-533\,^{kJ}/_{mol}$ or $-668\,^{kJ}/_{mol}$ at room temperature, respectively [159]. This is in the same range as the WO_2 and WO_3 change in Gibbs free energy during oxidation. For the PCMO/W devices, it was shown, that no oxide at the interface was formed in chapter 5.

PCMO/Ti

Different studies have already investigated the switching behaviour of PCMO in combination with Ti [33, 146, 148, 160–162].

Figure 6.9 a) shows the IV measurement of a $100 \times 100\,\mu m^2$ PCMO/Ti device. It can be seen, that two different switching mechanisms are present, filamentary (red) and area type switching (blue). The two switching mechanisms can be distinguished by the switching direction and the switching characteristics. The filamentary switching (red) has the SET process at the positive voltage branch and the RESET process at the negative voltage branch, indicated by red arrows, and for the area type resistive switching (blue) it is the other way around, indicated by blue arrows. Furthermore, the filamentary switching and the area type resistive switching share one state, the HRS for the filamentary and the LRS for the area type resistive switching, respectively. This occurrence of different switching mechanisms for the PCMO/Ti system has also been observed in the literature [161]. The difference is that in [161] the different switching behaviour was voltage-dependent and influenced by the first switching cycle of the device. This is not the case for the devices shown here. The change between the filamentary and the area type resistive switching behaviour occurs spontaneously in the same cell and is not determined by the first switching cycle or the voltage. [161] explains the different switching mechanism, filamentary and area type resistive switching, with a reducing and oxidising interface oxide layer in the Ti layer for the area type resistive switching. The filamentary switching is explained by a filament of higher oxygen vacancy concentration inside the PCMO layer and only a slight oxidation of the Ti layer at the position of the filament. The exchange of oxygen vacancies between the filament and the Ti/TiO_x layer

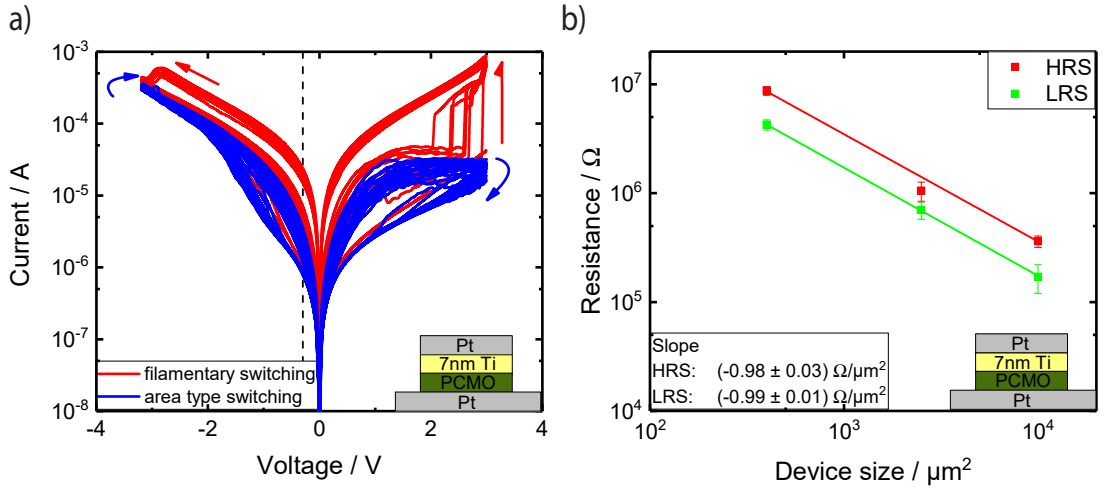

Figure 6.9.: a) I-V measurements of a $100 \times 100\,\mu m^2$ PCMO in combination with 7 nm Ti that shows filamentary switching (red) and area type resistive switching (blue). b) Area scaling of the area type resistive switching curve of the PCMO/Ti devices.

leads to a reduction or oxidation of a small part of the Ti layer only at the place of the filament [161]. This was concluded by the depth profiles of the chemical composition measured by SIMS [161]. One of the biggest differences between the devices, presented in [161] and the devices presented in this work, are the switching voltages. The switching voltages are way lower in this work, compared to other devices [161]. Therefore, the explanation would not fit properly to the devices shown here.

On the other hand, different studies have shown, that Ti metal in combination with PCMO forms a native interface oxide and changes in this interface oxide are the main reason for resistive switching [47, 163]. Also, the TiO_x/TiO_2 bilayer is well known in literature to show filamentary switching [164–168].
The change of Gibbs free energy for Ti being oxidised to TiO_2 is around $-900\,kJ/mol$ [169]. This means, that the change in Gibbs free energy is in the same range as for Al, see chapter 5. Therefore, one can expect the forming of an oxide interface layer between the PCMO and the Ti. The considerations regarding the interface and the switching curves shown before point more towards filamentary switching in the TiOx.
Analysing the area type resistive switching, it can be seen, that the current of the I-V measurements scales with the area, see figure 6.9 b). The change of resistance with device size is $-0.98 \pm 0.03\,\Omega/\mu m^2$ for the HRS and $-0.99 \pm 0.01\,\Omega/\mu m^2$ for the LRS. These values are close to -1 $\Omega/\mu m^2$, that is expected value for area type resistive switching devices.

6.2.1. Discussion of PCMO/metal devices

After showing all the different material combinations, one can cluster them into the ones who are switching (Al, Ta, Ti) and the ones who are not switching (Mo, W), regardless of the different thicknesses that were examined. Even if the PCMO/Ta combination only showed resistive switching for the smallest investigated device size, $20 \times 20\,\mu m^2$, the devices will be marked as generally switching. For the investigated materials that does not show switching, switching devices can be found in literature, PCMO/W [151, 153] and PCMO/Mo [150, 158]. Nonetheless, comparing the devices investigated in this work

to the one investigated in literature, multiple things differ, like the deposition of the PCMO, the thickness of the PCMO and the metal layer, the device size, etc.. Therefore, it could be possible that the devices investigated in this work also could be switched if some process parameters would be adapted.

If one now compares the devices that are investigated in this work with the study of the interface reaction of the PCMO layer presented in chapter 5, a connection can be drawn between the interface reaction and the switching behaviour. In chapter 5, it could be seen that the Al and the Ta metal form a native oxide at the interface between the PCMO and the metal. For the PCMO/W material combination no such interface oxide layer could be observed. This difference in the formation of a native oxide layer at the interface was attributed to the changes in Gibbs free energy during the oxidation for the different materials. The change of Gibbs free energy for W is the lowest compared to Al and Ta. Furthermore, the change in Gibbs free energy for Ti during oxidation is in the same range as Al or Ta and the change of Gibbs free energy for Mo is in the same order of magnitude as the change for W. Beside this, the existence of TiO_2 at the interface between PCMO and Ti has been shown in literature. For PCMO/Mo an interface oxide was also observed in literature for resistive switching devices [150]. Nevertheless, for the devices in this work, the existence of an interfacial oxide between the PCMO and the Mo is not assumed. The fact that no switching was observed for devices without an interface oxide is the fact that no incorporation of oxygen vacancies into the interface oxide, out of the PCMO and vice versa could happen during the switching. This would lead to a change of the resistance of the interface oxide as well as the resistance of the PCMO layer. Without the oxide layer, this exchange can not happen.

Beside the interface oxide and the transfer of oxygen vacancies into and out of the interface layer, a band bending of the PCMO bands at the interface was measured for all investigated metals, see chapter 5. The band bending was observed for the metals that form an interface layer (Al and Ta) as well as for the metals that do not form an interface layer. This band bending is expected for metal semiconductor contacts with different work functions χ. A depletion zone at the interface is a result of the band bending. The depletion zone changes with the incorporation of oxygen vacancies into the oxide interface layer or the PCMO. This also changes the resistance of the devices like the incorporation of oxygen vacancies into the oxide layer would change it.

Therefore, the resistance change during switching results from by two different processes, the change of the interface oxide and the change of the depletion zone at the interface. Nevertheless, due to the fact, that no switching was observed for the PCMO/W and PCMO/Mo devices, where at least the PCMO/W device showed a depletion zone in the XPS measurement and it could also be expected for the PCMO/Mo devices, one could conclude that the main part of the switching results from the change of the interface oxide. Another reason for the different switching behaviour of the devices with and without interface oxide could be, that the voltage drop at the interface is different for the different devices. This means that the voltage drop at the interfaces for devices without an oxide interface layer could be too small to move oxygen vacancies or oxygen between the PCMO and the interface layer. Therefore, no change of the interface layer and no change of the depletion zone can take place, meaning that the resistance of the device does not change.

In conclusion, the formation of an oxide interface layer is crucial for the resistive switching of PCMO in combination with an oxidisable metal.

6.3. Resistive switching of PCMO/oxide devices

Parts of this section are published in [1].

After concluding that the interface oxide is crucial for the resistive switching of PCMO, here the resitive switching behaviour of PCMO in combination with a directly deposited oxide on top of the PCMO will be investigated. Starting with PCMO in combination with ALD grown Al_2O_3, the formerly investigated metals, Ta and W, deposited as oxides directly, Ta_2O_5 and WO_3 will be investigated. Additionally, the often used in filamentary switching material HfO_2 will be investigated regarding its switching behaviour in combination with PCMO. In literature, only oxidisable metals in combination with PCMO are investigated and PCMO oxide combinations are not well investigated [1]. Therefore, the above PCMO oxide combinations will be presented in the following. As before, all PCMO layers have a thickness of 20 nm and are grown with the standard parameters on a 25 nm thick Pt layer on a Si/SiO_x wafer with a Ta adhesion layer. All devices are covered with a 20 nm Pt top electrode. In this chapter the Pt top electrode is only used as a contact layer, it does not serve to protect the film from external influences. The devices also have the structure that is mentioned in section 3.2.2.

PCMO/Al_2O_3

After showing that PCMO in combination with Al forms an interface oxide layer and demonstrating the impact of this oxide interface layer, studying PCMO in combination with atomic layer deposition (ALD) grown Al_2O_3 layer could give some more insights about the thickness of the native oxide layer of the PCMO/Al devices. ALD grown Al_2O_3 is well known for high density and highly insulating behaviour. Therefore, devices with 1 nm, 2 nm, and 5 nm Al_2O_3 are investigated, see figure 6.10 a)-c), even if this is thinner than the Al layers that are investigated in section 6.1.2. Nevertheless, the Al_2O_3 is deposited via ALD and therefore it can be assumed that even 1 nm Al_2O_3 produces a fully covering layer on top of the PCMO.

Figure 6.10 a) shows the measured I-V curves for PCMO/(1 nm Al_2O_3) devices. It can be seen that the $100 \times 100\,\mu m^2$ device only shows a small hysteresis in the positive branch and no hysteresis in the negative branch. Furthermore, the resistance of the $100 \times 100\,\mu m^2$ PCMO/(1 nm Al_2O_3) devices is way higher than the resistance of the PCMO/(7 nm Al) devices. For the $50 \times 50\,\mu m^2$ and $20 \times 20\,\mu m^2$ devices, a slight hysteresis can be seen and the resistance is also higher than for the $100 \times 100\,\mu m^2$ devices. Nevertheless, the resistance change between the $50 \times 50\,\mu m^2$ and $20 \times 20\,\mu m^2$ devices is low, compared to the change of resistance when decreasing the device size from $100 \times 100\,\mu m^2$ to $50 \times 50\,\mu m^2$. Furthermore, it can be seen, that the slope of the I-V measurements changes between the $50 \times 50\,\mu m^2$ and $20 \times 20\,\mu m^2$ devices. The resistance at low voltages is about the same for the $50 \times 50\,\mu m^2$ and $20 \times 20\,\mu m^2$ devices. Only for higher voltages, a clear difference can be seen with the smaller devices showing significantly lower currents. Nevertheless, the ON/OFF-ratio, even for the smallest device size, is quite low, therefore, these devices

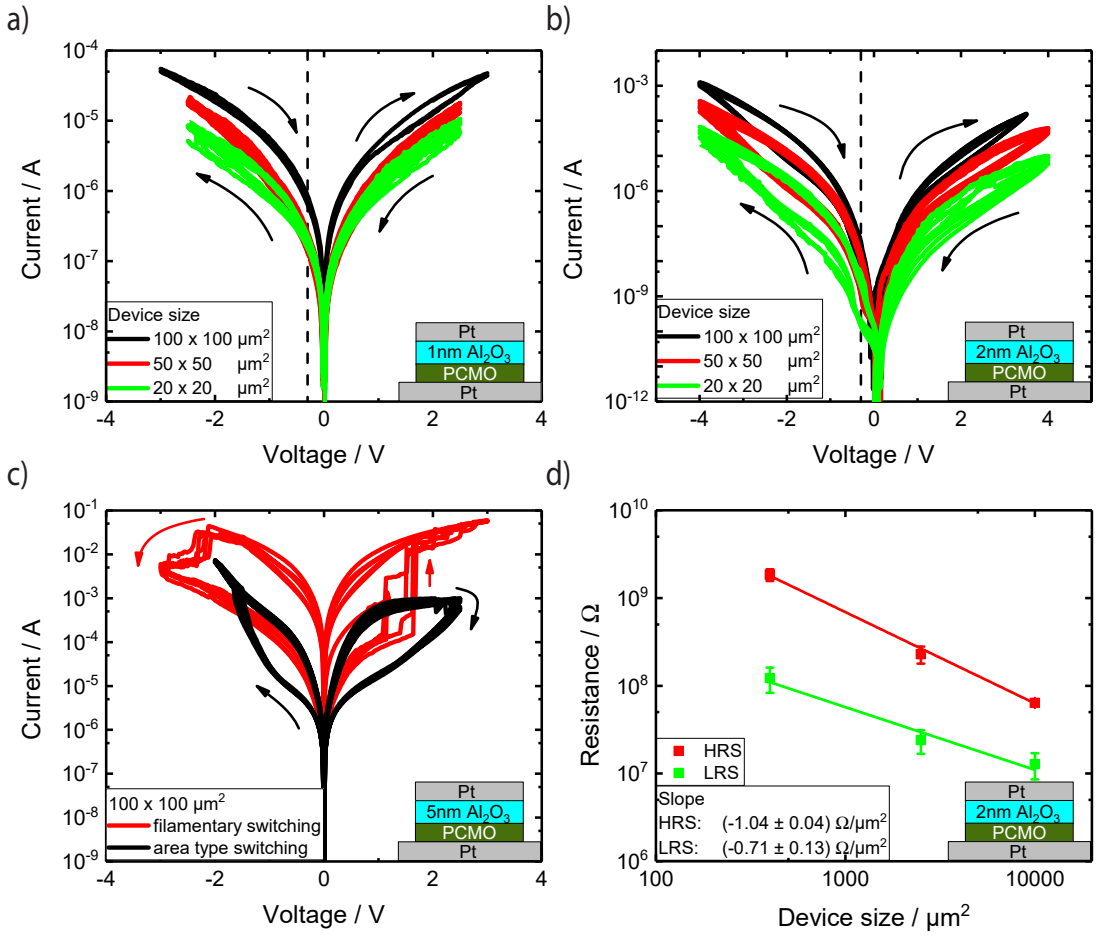

Figure 6.10.: IV measurements of PCMO in combination with ALD grown Al_2O_3 layers of different thickness, a) 1 nm, b) 2 nm, and c) 5 nm. d) Scaling of resistance with device size of PCMO/(2 nm Al_2O_3) devices.

will not be investigated further.

The I-V measurements of a 2 nm Al_2O_3 layer on top of PCMO are shown in figure 6.10 b). It can be seen that for all different device sizes, reproducible switching curves can be measured. Furthermore, the decrease of current/increase of resistance with decreasing device size can be seen in the I-V measurements. The I-V measurements are comparable to the PCMO/(7 nm Al) devices, shown in figure 6.1 c), even if the resistance is around one order of magnitude higher for the 2 nm Al_2O_3 devices. Furthermore, a kink feature can be seen around -1 V and 1 V for the PCMO/(2 nm Al_2O_3) devices. This feature is also not visible in the I-V measurements of the PCMO/(7 nm Al) devices. The kink in the I-V measurement could indicate the change in the conduction mechanism inside the device or the beginning of the resistive switching. Nevertheless, due to the fact that the kink occurs on the positive and negative branch in the HRS and the LRS one can conclude that the kink does not indicate the beginning of the switching inside the device, but the change in the conduction mechanism. This change could be from trap assisted tunneling (Poole-Frenkel-effect) [170] to direct tunneling (Fowler Nordheim tunneling) [171]. The exact reason for this kink in the I-V measurement is not analysed further in this work. The scaling of the resistance with the device size is shown in figure 6.10 d). It can be seen that the resistances of the HRS and the LRS are scaling with the device size. The slopes are $-1.04 \pm 0.04\,\Omega/\mu m^2$ for the HRS and $-0.71 \pm 0.13\,\Omega/\mu m^2$ for the LRS. The reason that the LRS slope shows a large difference to the HRS slope could be that the conduction mechanism in the HRS and the LRS differs. Nevertheless, the value of the resistance change with device size is still close enough to -1 $\Omega/\mu m^2$, that area type resistive switching can be assumed.

The impact of even thicker (5 nm) Al_2O_3 on the resistive switching of PCMO can be seen in figure 6.10 c). Here, the switching curves of the $100 \times 100\,\mu m^2$ devices are shown. It is evident that two different switching mechanisms are present in these type of devices, filamentary (red) and area type resistive switching (black). The area type resistive switching curve shows a hystersis on the positive and negative branch and no abrupt SET on the negative branch. The switching direction of the two switching mechanisms is indicated by the arrows, red for the filamentary switching and black for the area type resistive switching. It can be seen that the switching direction of the filamentary switching is opposite to the switching direction of the area type resistive switching. The appearance of the two switching mechanisms can be controlled by adapting the voltage of the the first cycle. During the first cycle, larger positive voltages lead to an abrupt increase in current. This first abrupt SET is assigned to the filament formation. Afterwards the switching voltage of the SET decreases to vlaues below 2 V. It is noticeable that this SET voltage of the filamentary switching curves is even lower than the SET and RESET voltages of the area type resistive switching devices. Like for the PCMO/Ti devices, both switching mechanisms share one state, the LRS for the area type resistive switching and the HRS for the area type resistive switching. The origin of the two different switching mechanisms determines it immediately, due to the fact, that Al_2O_3 is known to show filamentary resistive switching within the Al_2O_3 [172, 173]. Therefore, it could be possible that the filamentary switching takes place in the Al_2O_3 layer and the area type resistive switching is an interface effect.

In conclusion one can say, that the PCMO/(2 nm Al_2O_3) devices are the ones which

have the most similar switching behaviour compared to the PCMO/(7 nm Al) devices. The 1 nm Al_2O_3 does not show good switching properties, but also no ohmic contact. A reason for this could be that even if 1 nm ALD grown Al_2O_3 should cover the whole sample, the Al_2O_3 layer is too thin and the voltage drop across the interface does not change the device state significantly. The 5 nm Al_2O_3 layer instead showed resistive switching without an abrupt SET, but for these type of devices, filamentary switching was also observed. Therefore, one could conclude only from the switching curves, that the native oxide layer between the PCMO and the Al is between 1 nm and 2 nm. This conclusion neglects the fact, that the ALD grown Al_2O_3 could be much more dense than the oxide formed at the interface to the evaporated Al and therefore, the native oxide could be thicker but lees dense. Additionally, the native oxide could also be present in different oxidation states AlO_x while the ALD oxide is fully oxidised Al_2O_3. Nevertheless, by the shape of the switching curve, and the resistance one can conclude that the native oxide should also be around 2 nm.

PCMO/Ta_2O_5

In section 5.1.2, it was shown, that a native oxide was formed at the interface between the PCMO and the Ta metal. The measured I-V characteristics of these devices are presented above. It was shown, that for these devices, only the $20 \times 20\,\mu m^2$ devices showed resistive switching. The reason why the larger devices do not show resistive switching is not clear. Nevertheless, the impact of a directly deposited Ta_2O_5 layer with different thicknesses, 7 nm and 10 nm, will be presented here. The Ta_2O_5 layer is deposited by sputter deposition. The sputter parameters can be found in section 3.1.3

Figure 6.11 a) shows the I-V measurements of PCMO in combination 7 nm Ta_2O_5. It can be seen, that PCMO/(7 nm Ta_2O_5) devices show resistive switching for devices of different sizes, $100 \times 100\,\mu m^2$, $50 \times 50\,\mu m^2$, and $20 \times 20\,\mu m^2$. The black arrows indicate the switching direction. It is obvious that the hysteresis is way more pronounced on the negative branch. On the positive branch, HRS and LRS are hard to distinguish from each other. This behaviour is the case for all shown device sizes. Furthermore, it can be seen that the difference between HRS and LRS is higher for smaller devices. Also a slight change in slope of the I-V measurement can be seen at around −2 V. The change of the slope can be attributed to the starting of the SET process of the device. The black dashed line indicates −0.3 V, the voltage that is used to read out the devices. Figure 6.11 b) shows the change of the resistance at −0.3 V by changing the device size. The behaviour that was already visible in the switching curves can also be seen here. The HRS and the LRS are scaling with the device size, smaller devices lead to a higher resistance and a smaller current as expected. The slope of the HRS is $-0.95 \pm 0.04\,\Omega/\mu m^2$ and for the LRS the slope is $-0.97 \pm 0.11\,\Omega/\mu m^2$. Therefore, one can conclude that the PCMO in combination with 7 nm Ta_2O_5 shows area type resistive switching.

The impact of even thicker Ta_2O_5 layer on the I-V measurement is presented in figure 6.11 c). Beside the fact that the resistance is increased compared to the 7 nm Ta_2O_5 devices, the shape of the I-V curves differs for all presented device sizes, $100 \times 100\,\mu m^2$, $50 \times 50\,\mu m^2$, and $20 \times 20\,\mu m^2$. The ON/OFF-ratio at the negative branch is way lower and also a slight ON/OFF-ratio is visible on the positive branch of the I-V measurement. A reason for the different ON/OFF-ratio can be the different voltage drop across the

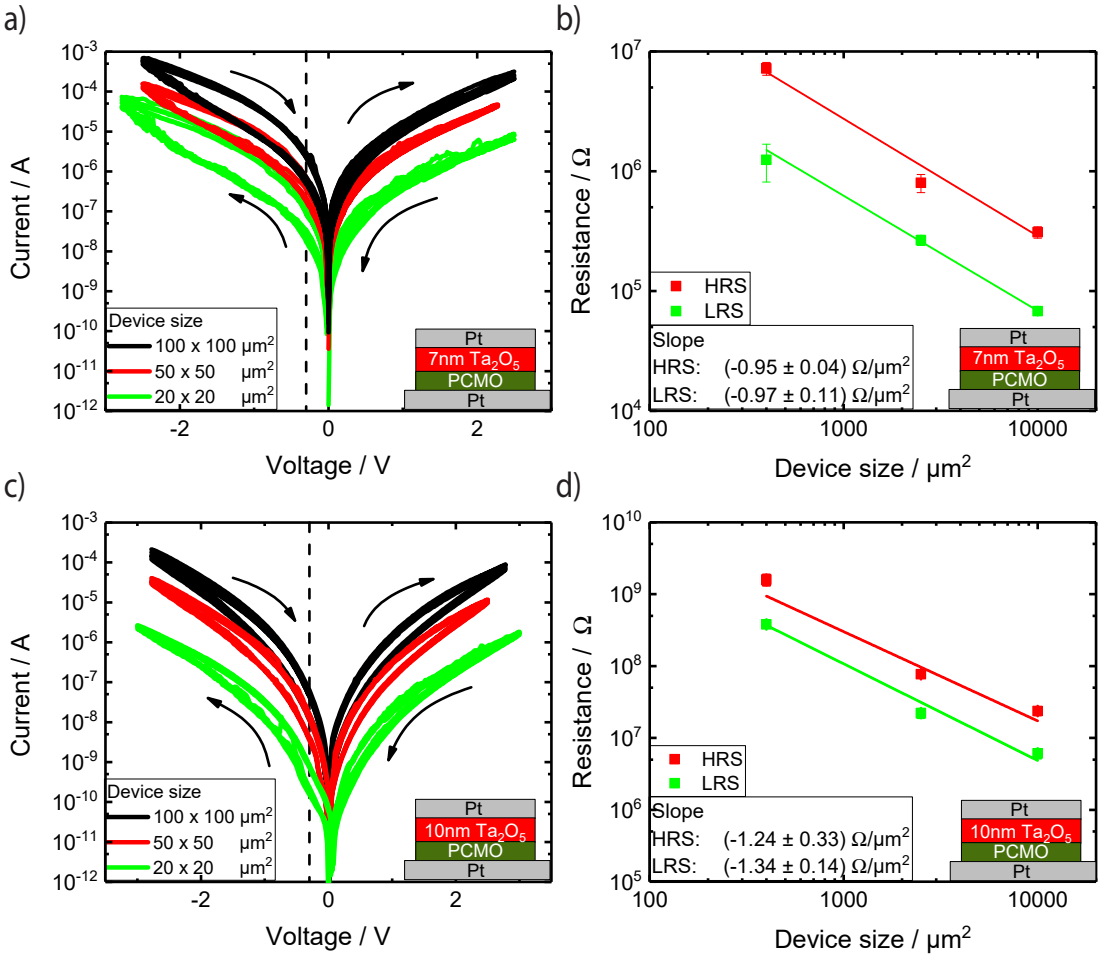

Figure 6.11.: Switching curves and resistance scaling of PCMO in combination with 7 nm and 10 nm sputtered Ta_2O_5. a) I-V measurement of PCMO/(7 nm Ta_2O_5) devices. b) Change of resistance with area for the PCMO/(7 nm Ta_2O_5) devices. c) I-V measurement of PCMO/(10 nm Ta_2O_5) devices. d) Change of resistance with area for the PCMO/(10 nm Ta_2O_5) devices.

device and the interface. Due to the thicker Ta_2O_5 layer, one can expect a larger voltage drop over the oxide layer, due to its higher resistance. Due to the higher voltage drop across the oxide layer, the voltage drop across the interface and the PCMO could be so small, that only a small amount of oxygen vacancies can move between the Ta_2O_5 and the PCMO layer. Therefore, the resistance change could be way lower and also no change in slope that indicates a pronounced SET process is visible for these devices. Increasing the switching voltage further, which could increase the switching behaviour of the devices, led to a breakdown of the shown devices. The black arrows indicate the switching direction of the devices. The black dashed line indicates $-0.3\,\mathrm{V}$, the voltage that is used to read out the devices. In Figure 6.11 d) the change of resistance with changing device size for the PCMO/(10 nm Ta_2O_5) can be seen. It can be seen, that also for the thicker Ta_2O_5 layer, the resistance scales with the device size. The fitted slopes are: $-1.24 \pm 0.33\,\Omega/\mu\mathrm{m}^2$ for the HRS and $-1.34 \pm 0.14\,\Omega/\mu\mathrm{m}^2$ for the LRS. The fitted slopes are slightly steeper than $-1\,\Omega/\mu\mathrm{m}^2$. Nevertheless, both states show the same scaling behaviour. Therefore, one can conclude that the PCMO/(10 nm Ta_2O_5) devices show area type resistive switching.

One can conclude, that the direct deposition of Ta_2O_5 improved the switching behaviour of the PCMO based devices compared to the PCMO/Ta devices. The PCMO/(7 nm Ta_2O_5) show a higher ON/OFF-ratio and a slightly lower resistance, compared to the 10 nm Ta_2O_5. The reason for this could be the different voltage drops across the devices, as described in the section above. Furthermore, the area scaling of the device is closer to $-1\,\Omega/\mu\mathrm{m}^2$ for the 7 nm than for the 10 nm Ta_2O_5 devices. Nevertheless, both different stacks showed indications for area type resistive switching. The only drawback of the 7 nm devices is the absence of a hysteresis on the positive branch. Nevertheless, no hysteresis in the positive branch, but non-volatile switching on the negative branch is reported several times for different area type resistive switching devices.

PCMO/WO_3

In section 6.2 it was shown that PCMO in combination with W metal does not show any switching behaviour. The reason for this was found to be the missing interface oxide that was shown in section 5.1.3. Therefore, the impact of a directly deposited WO_3 layer with different thicknesses, 7 nm and 10 nm, on top of the PCMO layer will be shown. The WO_3 is grown by sputter deposition. The sputter parameters can be found in section 3.1.3.

In figure 6.12 a) the I-V measurement of different sized PCMO/(7 nm WO_3) devices, $100 \times 100\,\mu\mathrm{m}^2$, $50 \times 50\,\mu\mathrm{m}^2$, and $20 \times 20\,\mu\mathrm{m}^2$, can be seen. A clear hysteresis on the positive and the negative voltage branch of the I-V measurement can be seen for all device sizes. It is worth mentioning that the positive and negative branch of the I-V measurement have a quite symmetric shape. The HRS shows a linear current-voltage behaviour in the semi-logarithmic plot of the I-V measurement. Beside this the LRS shows a curvature that is more linear in the logarithmic plot. The black arrows indicate the switching direction of the devices. The On/Off-ratio of these devices is around 1.5 orders of magnitude. In the I-V measurement a scaling of the current with the device size can be seen. The black dashed line indicates the read out voltage $-0.3\,\mathrm{V}$. Figure 6.12 b) shows the change of the device resistance at $-0.3\,\mathrm{V}$ with decreasing device

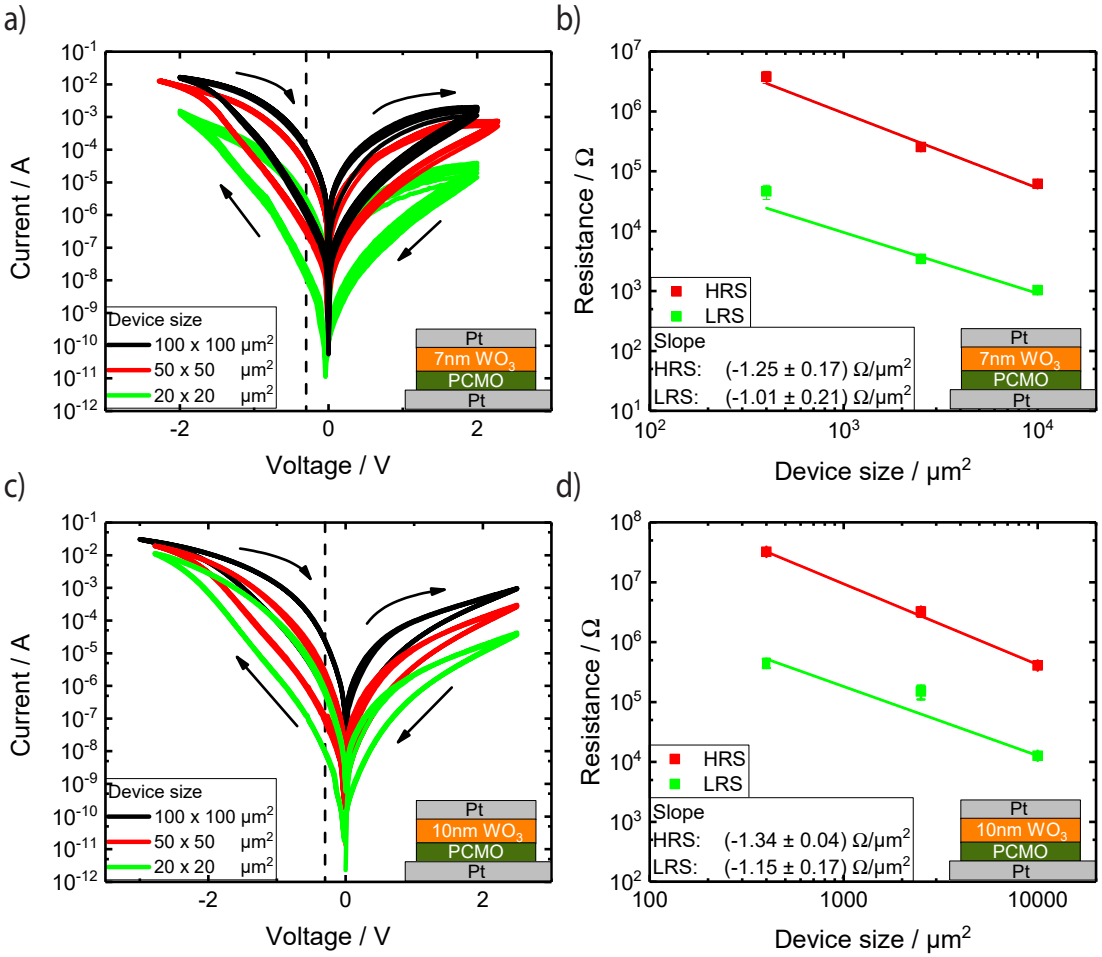

Figure 6.12.: Switching curves and resistance scaling of PCMO in combination with 7 nm and 10 nm sputtered WO_3. a) I-V measurement of PCMO/(7 nm WO_3) devices. b) Change of resistance with area for the PCMO/(7 nm WO_3) devices. c) I-V measurement of PCMO/(10 nm WO_3) devices. d) Change of resistance with area for the PCMO/(10 nm WO_3) devices.

size. It can be seen, that the HRS resistance as well as the LRS resistance is increasing with decreasing device size. The change of the resistance is $-1.25 \pm 0.17\,\Omega/\mu m^2$ for the HRS and $-1.01 \pm 0.21\,\Omega/\mu m^2$ for the LRS. According to the change in resistance with changing device size, one can conclude that the switching takes place across the whole device area and no filamentary switching takes place. Another hint for this is the absence of an abrupt SET process, but a gradual SET process in the I-V measurements.

The impact of a thicker 10 nm WO_3 on the I-V characteristics of the devices can be seen in figure 6.12 c). As for the 7 nm WO_3 devices, a hysteresis on the positive and the negative branch of the I-V measurement can be seen. However, the switching curves of the devices with the 10 nm WO_3 layer are less symmetrical compared to the switching curves of the devices with the 7 nm WO_3 layer. Nevertheless, on the negative branch, the switching curves of the 10 nm WO_3 devices show a similar behaviour as the 7 nm WO_3 devices, a quasi linear behaviour of the HRS in the semi-logarithmic current voltage diagram and a curvature in the LRS. On the positive branch of the I-V measurement of the 10 nm WO_3 devices, the HRS shows also a pronounced curvature as the LRS does and is not as linear as the HRS of the 7 nm WO_3 devices. Also the difference between the HRS and the LRS is lower for the 10 nm WO_3 devices on the positive branch than for the 7 nm WO_3 devices. Beside this differences, a decrease in current with decreasing device size can already be seen in the I-V measurement. The extracted resistance at -0.3 V that shows the scaling of the resistance with device size is plotted in figure 6.12 d). It can be seen, that the HRS as well as the LRS scales with the device area. The change of resistance is $-1.34 \pm 0.04\,\Omega/\mu m^2$ for the HRS and $-1.15 \pm 0.17\,\Omega/\mu m^2$ for the LRS. Even if the change in the HRS and the LRS differs slightly, one can conclude that the PCMO/(10 nm WO_3) devices show area type resistive switching.

A possible explanation for the difference in the measured I-V curves of the 7 nm and 10 nm WO_3 devices could be the different voltage drop across the interface of the device due to the larger voltage drop across the oxide layer for the thicker oxide. This change in voltage drop across the device interface would lead to a smaller driving force of the oxygen vacancies to change the device state. This means that for the thicker WO_3 layer less oxygen vacancies are exchanged between the PCMO and the WO_3 layer. This leads to a smaller ON/OFF-ratio. However, it is not possible to distinguish whether the HRS or the LRS changes in comparison, as the resistance value is higher for the thicker WO_3 layer, as expected. Furthermore, maybe a thinner WO_3 layer would lead to even higher ON/OFF-ratios and could also decrease the switching voltage, due to the shifted voltage drop across the device. Unfortunately, devices with even thinner WO_3 layer does not show any resistive switching behaviour. A reason for this could be, that the WO_3 needs a certain thickness to cover the whole PCMO area due to its roughness because of the sputtering process and shortcuts between the PCMO and the Pt top electrode are possible.

PCMO/HfO_2

HfO_2 is a widely investigated material to show filamentary resistive switching in combination with different materials [174–179]. Nevertheless, HfO_2 is not investigated yet in combination with PCMO. Therefore, the resistive switching behaviour of PCMO in combination with 5 nm and 7 nm HfO_2 will be presented in this section.

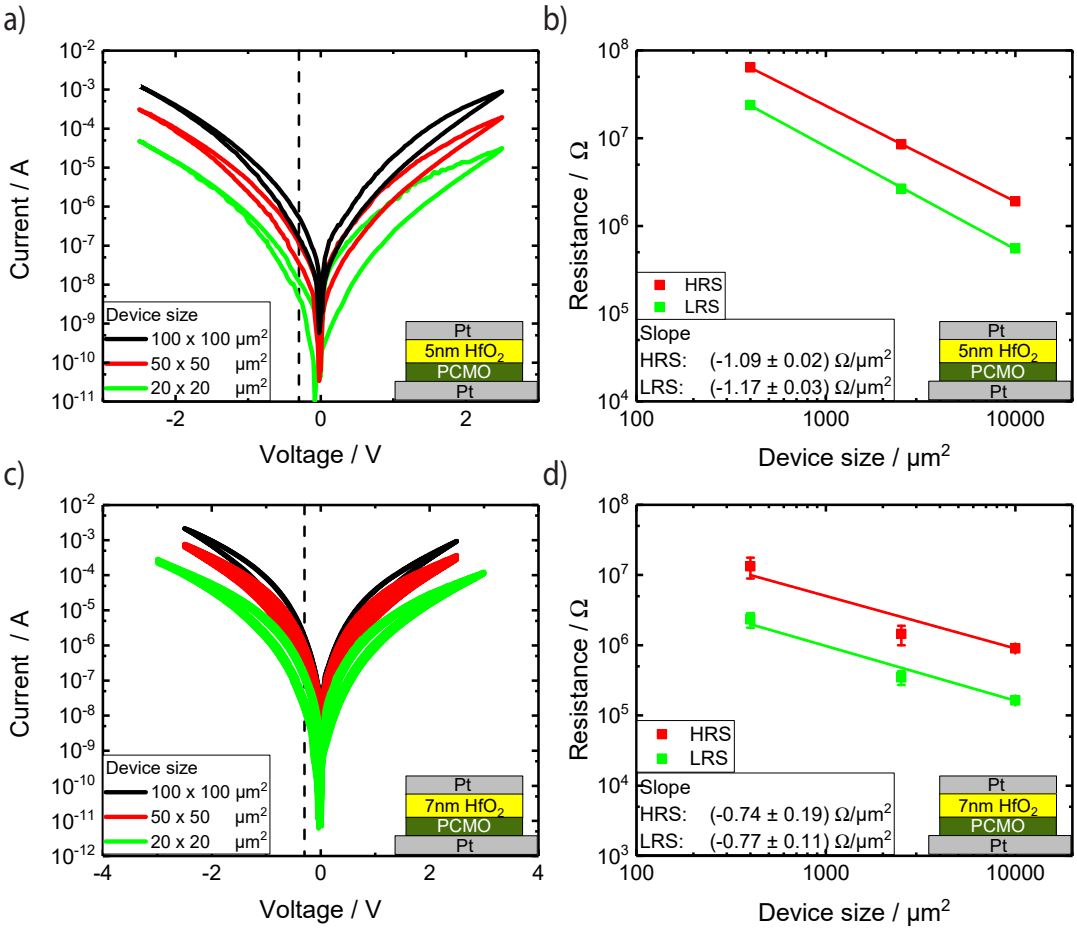

Figure 6.13.: Switching curves and resistance scaling of PCMO in combination with 5 nm and 7 nm sputtered HfO_2. a) I-V measurement of PCMO/(5 nm HfO_2) devices. b) Change of resistance with device area for the PCMO/(5 nm HfO_2) devices. c) I-V measurement of PCMO/(7 nm HfO_2) devices. d) Change of resistance with device area for the PCMO/(7 nm HfO_2) devices.

The I-V measurement of PCMO in combination with 5 nm HfO_2 is shown in figure 6.13 a). The used switching voltage are $-2.5\,V$ and $2.5\,V$ for all different device sizes. For all three investigated device sizes, $100 \times 100\,\mu m^2$, $50 \times 50\,\mu m^2$, and $20 \times 20\,\mu m^2$, a hysteresis on the positive and the negative branch with clear separable HRS and LRS can be seen. It is noticeable that the difference between the HRS and the LRS is larger on the positive branch of the I-V measurement. However, for reasons of consistency, the resistance to determine the area scaling probability of the devices is measured again at $-0.3\,V$. Another interesting characteristic of the I-V measurement is the fact, that the ON/OFF-ratio on the positive voltage branch increases with decreasing device size and on the negative voltage branch, the ON/OFF-ratio decreases. This decreasing behaviour of the ON/OFF-ratio can also be seen in the resistance plot, figure 6.13 b). Nevertheless, the decrease is less pronounced in the negative as in the positive branch and therefore only slightly visible in the resistance plot. The extracted slopes are $-1.09 \pm 0.02\,\Omega/\mu m^2$ for the HRS and $-1.17 \pm 0.03\,\Omega/\mu m^2$ for the LRS. The slopes are both close to -1 $\Omega/\mu m^2$ as one would expect for area type resistive switching. Nevertheless, would one measure the change of resistance on the positive branch the difference between the HRS and LRS would be larger. However, this is not considered further here for reasons of consistency.

Resistive switching of PCMO in combination with 7 nm HfO_2 can be seen in figure 6.13 b). It can be seen, that for all investigated device sizes $100 \times 100\,\mu m^2$, $50 \times 50\,\mu m^2$, and $20 \times 20\,\mu m^2$, a separable HRS and LRS can be seen. Furthermore, the switching curves are more symmetrical on the positive and negative branch than the switching curves of the 5 nm HfO_2 samples. The used switching voltage for the 7 nm HfO_2 devices are $2.5\,V$ and $-2.5\,V$ for the $100 \times 100\,\mu m^2$ and $50 \times 50\,\mu m^2$ devices and $3\,V$ and $-3\,V$ for the $20 \times 20\,\mu m^2$ devices. The resistance, read out at $-0.3\,V$, indicated by the black dashed line in figure 6.13 c), is plotted against the device size in figure 6.13 d). A clear linear trend in the double logarithmic plot can be seen. Nevertheless, the change of resistance with device size is adapted to $-0.74 \pm 0.19\,\Omega/\mu m^2$ for the HRS and $-0.77 \pm 0.11\,\Omega/\mu m^2$ for the LRS. These values a smaller than the expected value of -1 $\Omega/\mu m^2$. An explanation for this behaviour can not be given and also no hint on the reason for this can be seen in the I-V measurements.

6.3.1. Discussion of PCMO/oxide devices

The different PCMO/oxide combinations presented in the section above sll showed resistive switching behaviour, even if the related PCMO/metal combinations, presented in section 6.2, does not show any resistive switching.

Comparing the different switching switching behaviours of the different Al_2O_3, Ta_2O_5, WO_3, and HfO_2 layers in combination with PCMO, one can see, that the 7 nm and 10 nm WO_3 and the 7 nm Ta_2O_5 devices, showed the best switching behaviour. This is concluded from the ON/OFF-ratio, the shape of the switching curve and the area scaling of the resistance. The Al_2O_3, 10 nm Ta_2O_5, and the HfO_2 devices the resistance does not scale properly with the device area or the ON/OFF-ratio is quite small.

Various reasons can lead to different switching behaviour of the various oxides: the activation energy of oxygen vacancies ($V_O^{\bullet\bullet}$) inside the oxide or the difference in work

Material	Al_2O_3	Ta_2O_5	WO_3	HfO_2
$V_O^{\bullet\bullet}$ activation energy	$\sim 1.8\,eV$	$0.74\,eV$ - $1.63\,eV$	$0\,eV$ - $1.8\,eV$	$\sim 2.4\,eV$
Work function	$\sim 4.74\,eV$	$\sim 4.80\,eV$	$\sim 5.05\,eV$	$\sim 4.74\,eV$

Table 6.3.: Activation energies of oxygen vacancies and work function of the different oxides that are used in combination with PCMO, Al_2O_3 [180, 181], Ta_2O_5 [182, 183], WO_3 [184–186], HfO_2 [187, 188]

function between the PCMO and the oxide. Additionally the deposition technique of the oxide could also impact the resistive switching behaviour. Furthermore, all oxides are quite low in resistance. A possible explanation for this behaviour could be an uneven thickness of the oxide layer, where only small areas contribute to the switching behaviour or that the oxide is very rich in defects. In chapter 5 one can see that the deposited oxide is fully oxidised. Nevertheless, it was possible to show for the Ta_2O_5 layer, that the interface between the PCMO and the oxide is reduced. This behaviour was not visible for the WO_3 layer.

The different activation energies of oxygen vacancies are given in table 6.3. It can be seen, that the activation energy for WO_3 and Ta_2O_5 are the lowest. Nevertheless, for these two, the widest range of activation energy is also given in the literature. This range is mainly determined by different deposition methods of the oxide and other post processing steps. Therefore, one can not make a clear statement about the activation energy in the sputtered thin films that are used in this work. This means that the activation energy is also affected by the thin film parameters, for example the defect density or the crystallinity. Nevertheless, the oxygen vacancy activation energies give a first impression of possible explanations for the various switching behaviours. The highest activation energy is given for HfO_2, from which one could can conclude that higher voltages are needed to switch the devices in the same way as the others. For this purpose, the migration energies of oxygen vacancies within the oxide should actually also be considered, but these can also be strongly influenced by the manufacturing processes, the defect density and other factors. Therefore, one can only make simple assumption about the difference in the switching behaviour. Beside the activation energy of oxygen vacancies, the work function of the different oxides is given in table 6.3. The work functions of the different oxides found in literature are only slightly different and no clear trend can be seen. Nevertheless, the effective work function also differs from the given values. Therefore, the different work functions are only a slight hint, how the field drop across the interface could look like and how much field drops across this interface. Unfortunately, neither the difference in work functions, nor the different oxygen vacancy activation energies can describe the different shapes of the I-V curves of the different materials. If one compares Ta_2O_5 with WO_3 the strongest difference is noticeable. While WO_3 exhibits symmetry in the switching curves, Ta_2O_5 has the strongest asymmetry. Unfortunately, an explanation for this behaviour can not be given.
In conclusion, one can say, that all investigated PCMO/oxide combinations showed resistive switching.

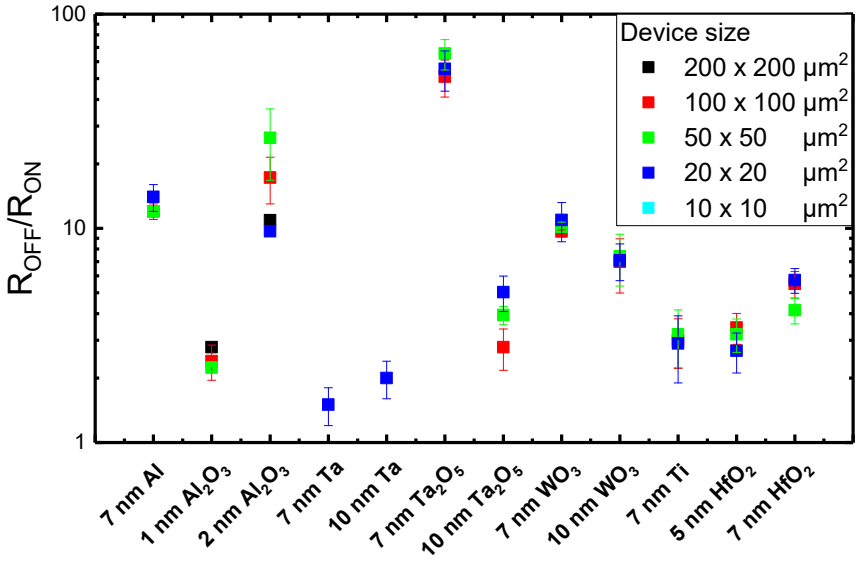

Figure 6.14.: ON/OFF ratio of the different investigated PCMO devices in combination with metals (section 6.2) and oxides (section 6.3). Only switching the ON/OFF ratio of the area type resistive switching devices are given here and not switching devices or filamentary switching devices are neglected.

6.4. Discussion of PCMO devices in combination with different interface layers

The presented and discussed data of the PCMO/metal devices (section 6.2) and the PCMO/oxide devices (section 6.3) shows in combination with chapter 5, a clear trend for factors that are important for area type resistive switching. From chapter 5 one can conclude, that the PCMO/Al and the PCMO/Ta devices form an interface oxide between the PCMO and the deposited metal. This interface oxide could not be shown for the PCMO/W interface. The PCMO/Mo and PCMO/Ti interfaces were not investigated in chapter 5. Nevertheless, from literature it is well known that PCMO in combination with Ti forms an oxide at the interface [47, 163] and for the PCMO/Mo devices the conclusion was made, that no interface layer was formed due to the change of Gibbs free energy. In section 6.2 it was shown, that PCMO in combination with Al, Ta, and Ti showed resistive switching and in combination with W, and Mo showed no resistive switching. However, this does not mean that PCMO in combination with W or Mo cannot show resistive switching. It only means that the deposition and processing methods chosen in this work have not led to the appropriate resistive switching conditions being fulfilled in the device. One can now conclude from the data that is collected in chapter 5 and section 6.2, that the oxide at the interface plays an important role in resistive switching. A possible explanation for the importance of the interface oxide was given with the voltage drop that is necessary to move oxygen/oxygen vacancies between the PCMO and the oxide/metal layer. This movement of oxygen/oxygen vacancies is as explained in chapter 2 for the change in resistive switching. Without a certain voltage drop across the interface/in the right region of the device, no switching occurs.

The afterwards investigated PCMO devices with Al_2O_3, Ta_2O_5, WO_3, and HfO_2 showed all area type resistive switching. Even the larger devices, $100 \times 100\,\mu m^2$ and $50 \times 50\,\mu m^2$, of the Ta_2O_5 and all WO_3 devices showed resistive switching. This was not the case for the Al and W metal. This is an additional hint that the oxide plays an important role during the resistive switching. Nevertheless, in the PCMO/oxide devices, one has to distinguish between PCMO-based resistive switching and switching in the respective oxides, since most of the oxides investigated in this section also show resistive switching in combination with other metals. However, filamentary switching often occurs in the oxide based devices.

Comparing the PCMO/Al and the PCMO/Al_2O_3 devices, the shape of the switching curves of the 2 nm Al_2O_3 devices are comparable to those of the 7 nm Al devices. Therefore, one can conclude, that the native oxide that forms at the interface between the PCMO and the Al metal could be at least 2 nm thick. Nevertheless, the resistance is slightly higher for the Al_2O_3 devices than for the Al devices. This could be explained by the different deposition techniques that are used for the Al (EBE) and the Al_2O_3 (ALD). One could expect that the Al_2O_3 from the ALD is denser as the native oxide that forms at the interface between the PCMO and the Al metal that is deposited. Furthermore, the evaporated Al/Al_2O_3 is expected to have more defects in the thin film. Therefore, the oxide at the interface is expected to be at least 2 nm thick or even thicker.

To compare all switching devices to each other, the ON/OFF ratio of the investigated switching devices is presented in figure 6.14. Beside the different materials, also the different device sizes are plotted there. It can be seen, that On/OFF ratios between 1.5 for the Ta metal and around 100 for the Ta_2O_5 can be reached. ON average the ON/OFF ratio is between 2 and 6 for the area type resistive switching devices. Only the 7 nm Al, 2 nm Al_2O_3, 7 nm Ta_2O_5, and 7 nm WO_3 devices show ON/OFF ratio above 10. The 2 nm Al_2O_3 devices show a wide spread of the ON/OFF ratios for different device sizes while the other devices show a constant ON/OFF ratio for the investigated device sizes. This constant ON/OFF ratio is expected for the area type resistive switching devices as the HRS and the LRS scales with the area. However, the ON/OFF ratio of the 2 nm Al_2O_3 devices does not show any systematic changing.

One can conclude, that PCMO shows area dependent switching in combination with a metal that forms a native interface oxide or an directly deposited oxide. The manufacturing process has an enormous influence on the switching behaviour, and filamentary switching behaviour which can be considered as a failure mechanism can also occur. A clear discussion of the underlying switching mechanism will be given in chapter 7.

6.5. Switching properties of selected device stacks

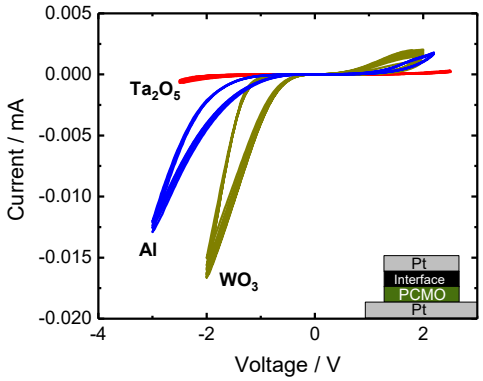

Figure 6.15.: Comparison of I-V measurements of PCMO in combination with Al, Ta_2O_5, and WO_3 interface layer in a non-logarithmic scale.

In section 6.4 the results of the investigation of PCMO in combination with different metals and oxides are discussed. From this discussion, one can conclude that PCMO in combination with 7 nm Al, 7 nm Ta_2O_5, and 7 nm WO_3 shows the best switching behaviour, see comparing figure 6.15.
Therefore, these three different device stacks will be investigated further in the following. Starting with the initialisation of the samples, the investigation of the stability of the HRS and the LRS and the reliability of the samples will be presented. Finally, the effect of the so-called subloops will be discussed. These are meta-stable states that arise during the writing of the LRS and decay within milliseconds. Unless otherwise stated, all measurements are performed with the $20 \times 20\,m^2$ devices.

Initialisation

In filamentary type switching devices, the first cycle is used to form the conductive filament through the oxide layer. This formation changes the device state from a high resistive state into a lower resistive state. During the formation of the filament often higher voltages and currents are needed than for the resistive switching afterwards [189, 190]. The first cycle in filamentary switching devices is therefore often called forming. Due to the fact that no filament has to be formed in area type resistive switching devices, no forming cycle is necessary for these devices. Nevertheless, the first cycle also show a different behaviour compared to the switching cycles. The resistance changes from a low resistive state, lower than the LRS, into a higher resistive state, that can be referred to as the HRS. Therefore, the first cycles of the filamentary switching devices are referred to as an initialisation phase of the device that is needed to bring the device to the necessary initial state for resistive switching. The first cycle is always performed on the positive branch of the resistive switching cycle.

Exemplary initialisation cycles of PCMO in combination with 7 nm Al for different device sizes, $100 \times 100\,\mu m^2$, $50 \times 50\,\mu m^2$, $20 \times 20\,\mu m^2$, and $10 \times 10\,\mu m^2$ can be seen in figure 6.16 a). The initial resistance shows an ohmic behaviour for the different device sizes from the switching curves and between 0.75 V and 2.0 V a significant increase of the resistance occurs. This increase in resistance is either abrupt or gradual. The abrupt as well as the gradual increase occurs for all different device sizes. If one looks more closely at the increase in resistance, one can see an increase of up to two orders of magnitude for the abrupt and gradual increase of resistance during the first switching cycle. Sometimes, the resistance also decreases first and increases afterwards even further, see $50 \times 50\,\mu m^2$ and $10 \times 10\,\mu m^2$ devices. Furthermore, for the $20 \times 20\,\mu m^2$ and $10 \times 10\,\mu m^2$ devices, some of the devices do not show any initialisation in the first cycle and start already in

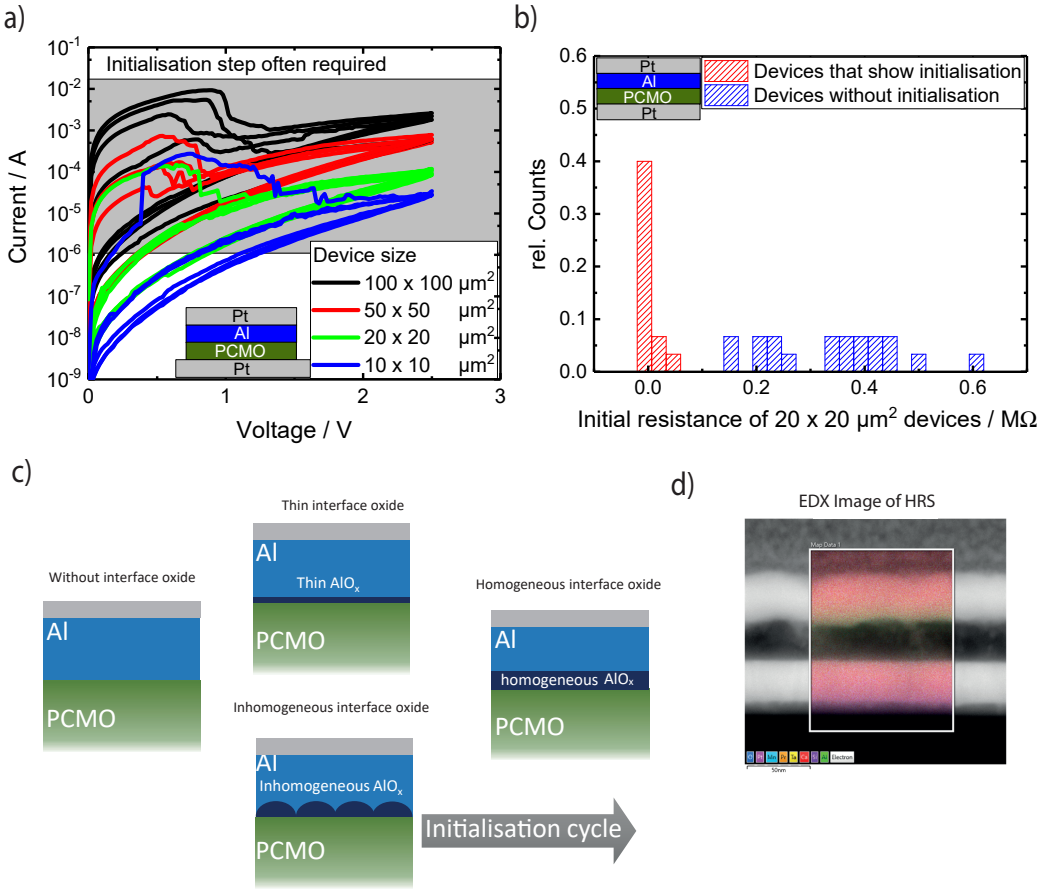

Figure 6.16.: a) Initialisation curves of PCMO in combination with Al. b) Resistance distribution of the $20 \times 20\,\mu m^2$ devices with and without initialisation . c) Schematic representation of the interface without oxide, with native oxide and an oxide the initialisation curve. d) EDX TEM image of HRS after initialisation.

a higher resistive state that can be referred to the LRS. For these devices the abrupt or gradual increase in resistance that can be seen, can be related to the initial resistance of the devices. This can be seen in figure 6.16 b) for the $20 \times 20\,\mu m^2$ devices. Devices with low initial resistance show an initialisation, beside devices with higher initial resistance in the range of the expected LRS do not show any initialisation. Here one can also see that about 50% of the devices show an initialisation and 50% of the devices do not need an initialisation. The reason for this different behaviour, if an initialisation is needed or not, could be the inhomogeneity in the PCMO thin film and the deposited interface layer. Nevertheless, a short explanation of the processes that could happen during the initialisation cycle will be given in the following.

Figure 6.16 c) shows a schematic of the PCMO/Al stack and the interface between the PCMO and the Al. In chapter 5, the interface between the PCMO and Al was investigated and it was seen that a native oxide was formed at the interface during deposition. Nevertheless, the low initial resistance of the devices and the initialisation step could not be explained by a homogeneous and thick interface oxide. It is more likely that the interface oxide is rather inhomogeneous or quite thin. This inhomogeneity of the oxide

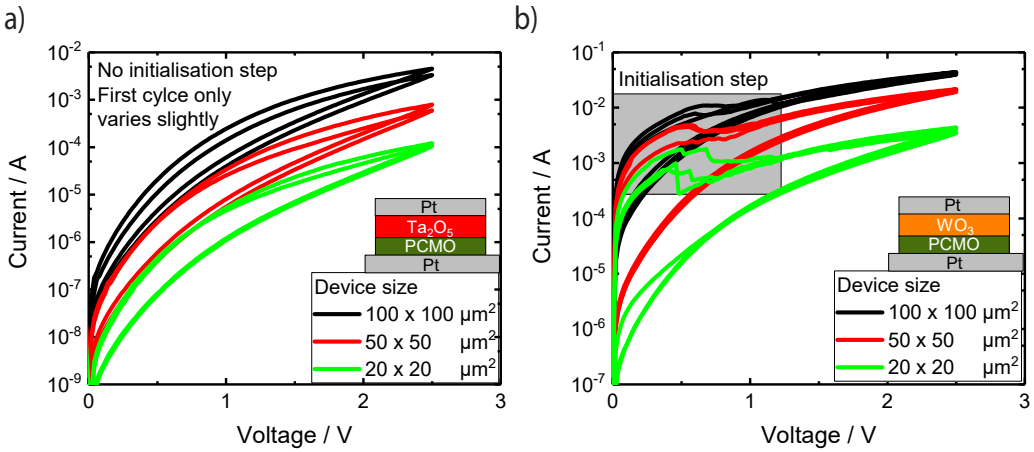

Figure 6.17.: Initialisation curves of a) PCMO/Ta_2O_5 and b) PCMO/WO_3 for devices of different size.

could be further enhanced by the rough PCMO surface. The initialisation sweep then ensures that either a more homogeneous or a thicker oxide forms at the interface. This is due to the movement of oxygen from the PCMO into the Al/AlO_x layer. Unfortunately, no values can be given for the homogeneity or thickness change of the AlO_x due to the initialisation process. Figure 6.16 d) shows an EDX TEM image of the PCMO/Al device in the HRS after the initialisation. As mentioned above, due to the rough PCMO surface, no defined oxide layer can be seen at the interface and therefore, no change in the oxide layer during initialisation can be seen in TEM. Nevertheless, Herpers [33] investigated that for PCMO/Ti devices, the initialisation leads to a formation of TiO_2 at the interface. Therefore, the conclusion appears obvious that the AlO_x layer at the interface oxidises further or becomes more homogeneous during the initialisation. An explanation of the abrupt increase in resistance can be that due to the inhomogeneous interface between the PCMO and the Al/AlO_x conductive paths, where no oxide has been formed, oxidise and the conduction mechanism changes. Nevertheless, no clear answer to this question can be given here. A possible reason could be the same as for the abrupt SET process in filamentary systems. The voltage drop across a serial resistance which is exceeded and the voltage drop across the interface becomes crucial to change the resistance [179] .

Keeping this discussion about the change of the native interface oxide in mind, one can assume that for the PCMO/Ta_2O_5 and PCMO/WO_3 devices, no initialisation is observed. This is due to the fact that the oxide that is deposited at the interface is already fully oxidised and no further homogenisation step should be needed. The first cycle of different PCMO/Ta_2O_5 devices are shown in figure 6.17 a). No abrupt increase of the device resistance as for the PCMO/Al devices during the first cycle can be seen. The slight variation in the first switching cycle can be explained by device to device variations due to the rough interface between the PCMO and the Ta_2O_5. Nevertheless, the resistance increases slightly during the first switching cycles, and the resistive cycles are at slightly higher resistances as the first cycle. A possible explanation for this may be the removal of oxygen from the PCMO, which causes the resistance to increase and a widening of the depletion zone.

For the PCMO/WO_3 devices, on the other hand, an abrupt and a gradual increase in resistance during the initialisation cycle can be seen for all different areas, figure 6.17 b). This increase in resistance is surprising, since fully oxidised WO_3 was deposited and in chapter 5 no reduction of the oxide at the interface was found, unlike in the case of Ta_2O_5. The increase of the resistance is only in the range of half an order of magnitude. This is way lower compared to the PCMO/Al devices. A possible explanation for this behaviour can be the rough surface of the PCMO layer, which leads to an inhomogeneous thickness of the WO_3. This inhomogeneous thickness leads to an inhomogeneous voltage drop across the devices which could lead to an enhanced movement of oxygen at these position. Nevertheless, a clear explanation for this behaviour can not be given here.

In conclusion, all the devices need an initialisation that brings the device into the switching state. A clear explanation for this behaviour can only be given for the PCMO/Al devices with the homogenisation of the native interface oxide. For the PCMO/oxide devices the initialisation can not be explained with the homogenisation/oxide of the interface oxide in the same way as for the PCMO/Al devices. Here the roughness of the PCMO layer could play an important role. Nevertheless, for every sample a first initialisation cycle is necessary that increases the resistance of the device further.

Variability

In the following the variability between different switching cycles and devices of the same stack for the PCMO/Al, PCMO/Ta_2O_5 and PCMO/WO_3 will be presented. Therefore, different devices of each stack are switched several hundred times, to investigate the variability of the devices. For the variability, one has to distinguish between two different aspects, the cycle to cycle and the device to device variability. Cycle to cycle variability refers to the fluctuations of the HRS and LRS resistance of one device during different switching cycles. Device to device variability instead means the difference in resistance for different devices due to slight differences in the processing of the samples or inhomogeneities during the deposition of the thin film. It is important to mention, that the variability measurements are done with voltage pulses. The used pulses always have the same height as the corresponding voltage sweep that is used during the switching. The pulse length is chosen to be 100 ms. The read pulse is always done with a height of -0.3 V, the same read voltage that was used during the I-V measurement. The pulse length of the read pulse was set to 1 ms. The read pulses with this values do not change the resistive state of the device. This will be shown in chapter 8.

In figure 6.18 a) the resistance of 200 switching cycles of the $20 \times 20\,\mu m^2$ PCMO/Al devices are shown. The resistance increases slightly in the beginning and stabilises after 20 cycles. Furthermore, it can be seen, that the relative increase of the HRS resistance is slightly higher than the increase of the LRS resistance. This increase in the resistance can be related to a further oxidation and homogenisation of the native oxide layer at the interface. After this increase, the HRS and the LRS are quite stable with only slight variations. The variability of the HRS is higher than the variability of the LRS. Nevertheless, the HRS and the LRS are clearly separable during the whole measurement with an ON/OFF-ratio of around 5. The Weibull probability of different PCMO/Al devices, each switched several times, can be seen in figure 6.18 b). It can be seen that

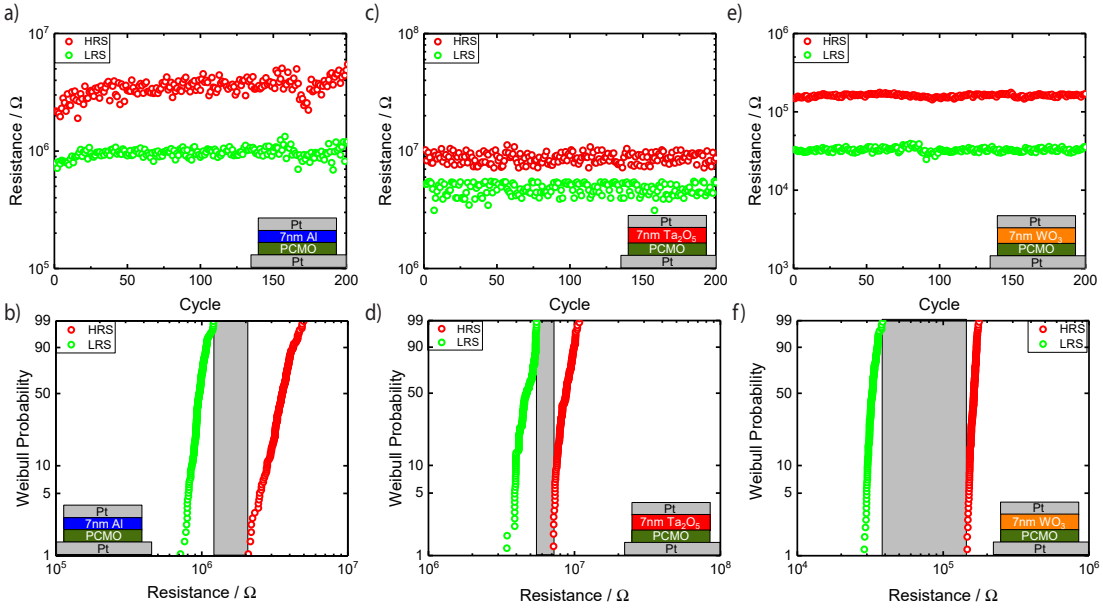

Figure 6.18.: Variability of the switching of the PCMO/Al, PCMO/Ta_2O_5 and PCMO/WO_3 devices. a), c), e) 200 switching cycles of the corresponding $20 \times 20\,\mu m^2$ devices. b), d, f) Combined Weibull probability different $20 \times 20\,\mu m^2$ devices of the corresponding material stacks.

the resistance distribution of the HRS is larger than the resistance distribution of the LRS. A possible reason for these variations can be manufacturing differences over the sample, which cause the interface oxide to form differently, making the resistances of the devices slightly different. Nevertheless, a clear separation of LRS and HRS can be identified, shown in gray. Unfortunately the smallest possible ON/OFF ratio between the 99 % LRS value and the 1 % HRS value is only around 3.

200 switching cycles of PCMO/Ta_2O_5 devices are shown in figure 6.18 c). No increase of the LRS and HRS resistance in the beginning, as seen for the PCMO/Al devices, can be identified, but the LRS as well as the HRS show large variations within the 200 cycles. The variations of the LRS and the HRS are related to the mean value of the relative resistance in the same order of magnitude. Beside the large variations the HRS and the LRS are stable within the shown cycles. The ON/OFF ratio fluctuates due to the large variations in the HRS and the LRS. This leads to a small minimum ON/OFF-ratio of the devices of around 2. Nevertheless, a clear separation between the HRS and the LRS is still visible and no overlapping of states takes place. The Weibull probability of different PCMO/Ta_2O_5 devices combined, is presented in figure 6.18 d). Here it is also visible that the relative variations of the HRS and the LRS are in the same order of magnitude. Furthermore, a clear separation of the HRS and the LRS can be seen, indicated by the gray area. The ON/OFF ratio between the 99 % LRS value and the 1 % HRS value is around 1.5. This is significantly lower than for the I-V measurements. This is even smaller than for the cycles that are shown in figure 6.18 c). One can conclude from this, that the cycle to cycle variability of the PCMO/Ta_2O_5 devices is in the same order of magnitude as the device to device variability.

For the PCMO/WO_3 devices, 200 switching cycles are shown in figure 6.18 e). The HRS

as well as the LRS show a stable switching without large variations. Also no trend, increase or decrease of the resistance during these cycles, can be identified for the HRS and the LRS either. Furthermore, the ON/OFF-ratio is around 10 for the devices and does not have large variations. This stable switching is also visible in the Weibull plot shown in figure 6.18 f). The LRS as well as the HRS show only a slight spread in the resistance. The 1 % and the 99 % value of the LRS have only a difference of around 1000 Ω, a variation of 30 % relative to the median. For the HRS the difference is around 1000 Ω, around 30 % of the meadian as well. The separation between the 99 % value of the LRS and the 1 % value of the HRS are shown in gray. Here an ON/OFF ratio around 8 can be seen. This is slightly lower than for the 200 cycles shown in figure 6.18 e). This is a hint that the device to device variability is slightly larger than the cycle to cycle variability of the PCMO/WO_3 devices.

Comparing all three different device stacks, one can conclude that the PCMO/WO_3 devices show the most stable switching behaviour, for the cycle to cycle variability as well as for the device to device variability. It is worth noting that the device to device variability of the PCMO/WO_3 devices is even smaller than for the PCMO/Al and PCMO/Ta_2O_5 devices. This means, that main reason for the device to device variability is not the inhomogenity of the interface between the PCMO and the metal/oxide. Otherwise, the device to device variability of the PMCO/WO_3 devices should be in the same order of magnitude as the other material stacks. Furthermore, the different deposition methods of the metal and the oxide can also be no reasonable explanation of the difference in the device to device variability, due to the fact that the WO_3 as well as the Ta_2O_5 are sputtered and only the Al layer is evaporated. Unfortunately, no conclusive explanation can be given for this observation.
The cycle to cycle variability is also the smallest for the PCMO/WO_3 devices and the largest for the PCMO/Ta_2O_5. The PCMO/Al devices only show a slight variation for the HRS resistance than for the LRS resistance. Furthermore, the PCMO/Al devices are the only devices that does not show an increase of the resistance for the first switching cycles.

Stability

To use the PCMO based devices as possible non volatile memory cell for future applications the device state has to be stable over time. Therefore, different device are set into the HRS or LRS and are read out after certain periods of time to determine the change in resistance. The HRS and LRS are written in with an I-V sweep on the positive/negative branch, respectively. The read out is done with voltage sweeps up to −0.3 V.

The behaviour of the HRS and the LRS of the PCMO/Al devices over long times is shown in figure 6.19 a). Both, the HRS and the LRS are stable over the investigated time of 1000 h. Slight variations of the resistance values for the HRS and the LRS are measured over time, but no clear trend of an increasing or decreasing resistance can be seen for the HRS and the LRS. Only at the beginning a slight increase within the first measurement interval of the LRS is measured. This increase of the resistance can be referred to electronic states that decay within a few seconds and will be explained in the next section about subloops. If one ignores this increase of the LRS at the beginning, the LRS and HRS are stable over several days. After around 100 h the LRS shows a high

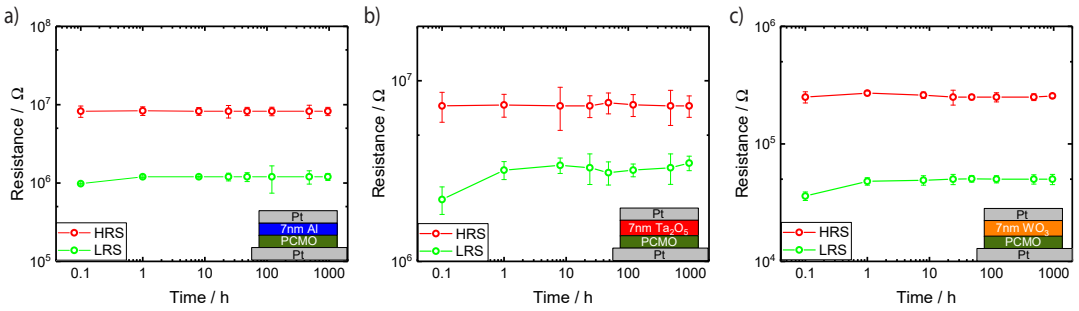

Figure 6.19.: Stability of the HRS and the LRS of the $20 \times 20\,\mu m^2$ a) PCMO/Al, b) PCMO/Ta_2O_5 and c) PCMO/WO_3 devices over a period of several days.

error value. The reason for this variation in the different devices could be explained by contact issues caused by some other material on the contact needle or replacement of the contact needle. Nevertheless, afterwards the variations of the LRS decreases again, which indicates, that the state itself has not changed.

The HRS and the LRS of the PCMO/Ta_2O_5 devices are shown in figure 6.19 b). The HRS is stable over a time period of 1000 h with slight variations around a constant mean value. The LRS, on the other hand shows larger variations and also an increase of the resistance in the beginning. Furthermore, the mean value is less constant for the HRS an shows larger fluctuations. Nevertheless, the LRS seems to be constant with larger variations after a first increase of the resistance. The variations of the HRS and the LRS can not be explained by contact issues but are more likely device to device variations of the PCMO/Ta_2O_5 devices.

An example of the stability of the HRS and LRS of $20 \times 20\,\mu m^2$ PCMO/WO_3 devices is shown in figure 6.19 c). The HRS is stable over the shown time without larger variations. The LRS of the PCMO/WO_3 on the other hand shows a slight increase in the beginning and is stable afterwards. This increase could be explained by a chemical gradient of oxygen inside the device. However, this could not be proven experimentally. The variations are also quite small for the LRS. Also the ON/OFF-ratio is stable over time.

Comparing the different devices, PCMO/Al, PCMO/Ta_2O_5, and PCMO/WO_3, one can see that the PCMO/Al and PCMO/WO_3 devices are more stable than the PCMO/Ta_2O_5 devices. The HRS is stable for all tested material combinations and shows only slight variations. But here too, the PCMO/Ta_2O_5 devices show the largest fluctuations. For the LRS, all devices show an increase of the resistance in the beginning. Furthermore, the variations of the LRS of the PCMO/Ta_2O_5 devices is way larger compared to the variations of the PCMO/Al and PCMO/WO_3 devices. The PCMO/WO_3 has the most stable state for the HRS as well as for the LRS. The reason for the stability of the states can not be explained here.

Subloops

In figure 6.19 a) an increase of the LRS of the PCMO/Al in the beginning of the measured time period can be seen. Therefore, subloop measurements are performed for the PCMO/Al devices to check for volatile phenomena. These subloop measurements are

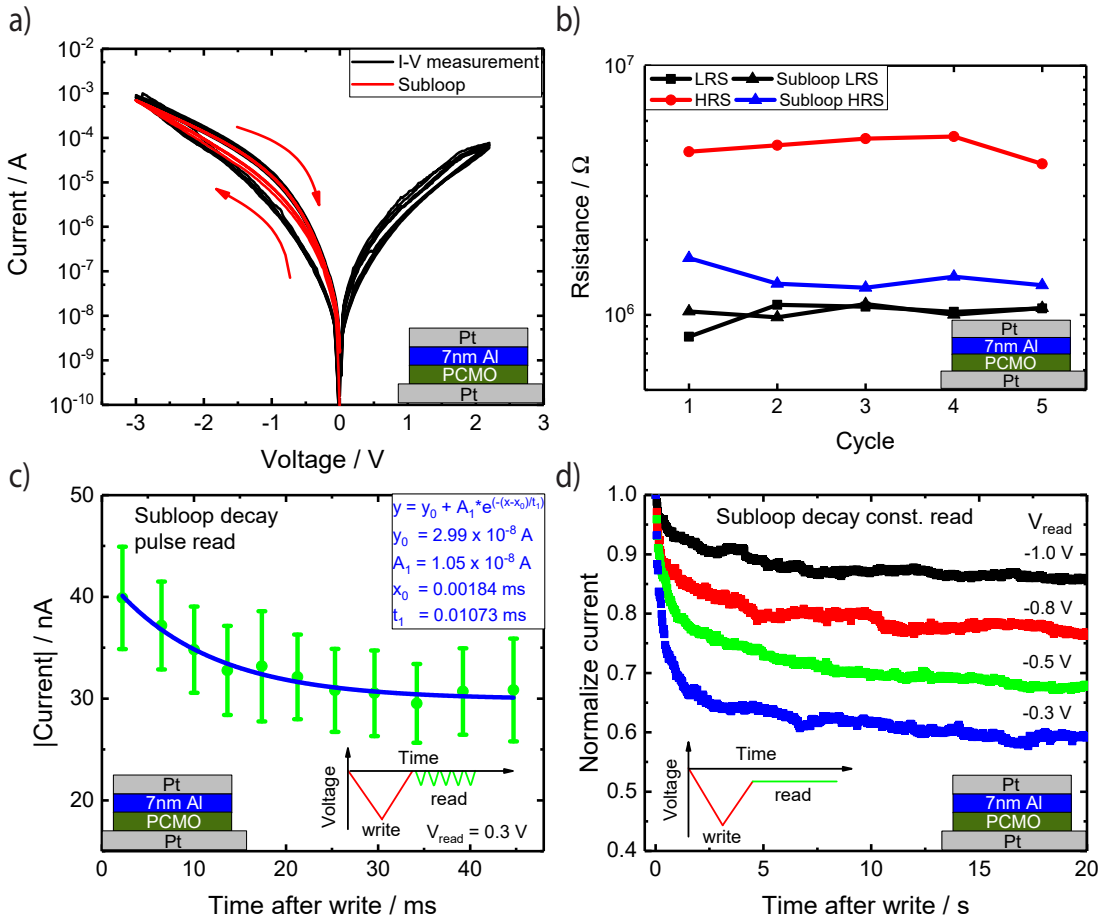

Figure 6.20.: a) PCMO/Al LRS subloop measurement and b) variability of the switching states and the subloop states within a few cycles. c) and d) decay of the subloops with pulsed readout and constant readout, respectively.

Table 6.4.: Fitting values of the exponential decay of the volatile part of the LRS the so called subloops

Parameter	y_0 / A	A_1 / A	x_0 / ms	/ t_1 / ms
Value	2.99×10^{-8}	1.05×10^{-8}	0.00184	0.01073

comparable to I-V measurement with the difference that only one voltage branch is cycled. One would expect that the resistance does not change after one switching cycle and repeated cycling with the same voltage would either have no impact on the device state or lead to an increase/decrease of the resistance of the HRS/LRS, respectively. To investigate the observed increase of the resistance, the negative resistance of the I-V cycle is applied repeatedly.

Figure 6.20 a) shows the subloop measurement of the $20 \times 20\,\mu m^2$ PCMO/Al devices with an additional I-V measurement. The red arrows represent the switching direction of the subloop measurement. It can be seen, that the LRS of the I-V measurement (black) has the same value as the LRS of the subloop measurements (red). After reaching 0 V and starting a new subloop cycle, the resistance is increased slightly. The subloop cycle show a hysteresis with a smaller opening than the normal switching cycles. The switching direction of the subloops are the same as for the I-V measurement. Figure 6.20 b) shows the described behaviour of the switching and the subloop states once again more clearly with respect to different switching cycles. Here it becomes clearer that the LRS of the I-V measurements and the subloops have the same value and the HRS of the subloops is above the LRS values. It has to be mentioned that no RESET happens between the subloop LRS and the HRS. The LRS state decays slightly without a RESET process at 0 V.

This means that the LRS of the PCMO/Al devices have a volatile and a non-volatile part. The non-volatile part is investigated in the section above about the stability of the HRS and the LRS. An explanation for this behaviour will be given later, in section 7.5. In figure 6.20 c), the decay of the volatile part of the LRS is presented. The measurement is done with a voltage sweep that writes in the LRS. Afterwards, the decay is read out with voltages pulses with a length of 100 µs and a height of −0.3 V. These read out pulses are applied after each other with an even spacing, see scheme in figure 6.20 c). It can be seen, that the state decays within a few ms and shows an exponential behaviour. The exponential decay can be fitted by

$$y = y_0 + A_1 e^{-(x-x_0)/t_1}. \tag{6.1}$$

The values of the fit are presented in figure 6.20 c) and in table 6.4. Due to the fast time scales of the decay, it can be assumed that the effect is an electronic effect which is maintained by the applied voltage and decays when the voltage reaches 0 V. Further explanations will be given in section 7.5.

To investigate the decay of the subloop state further, the decay is monitored with different read out voltages that are applied in a constant way, without any time in between. The results of this and the measurement scheme can be seen in figure 6.20 d). Here, the decay over several seconds is monitored. It can be seen that for all investigated read out voltages, −1 V, −0.8 V, −0.5 V and −0.3 V, the decay happens in the beginning of the

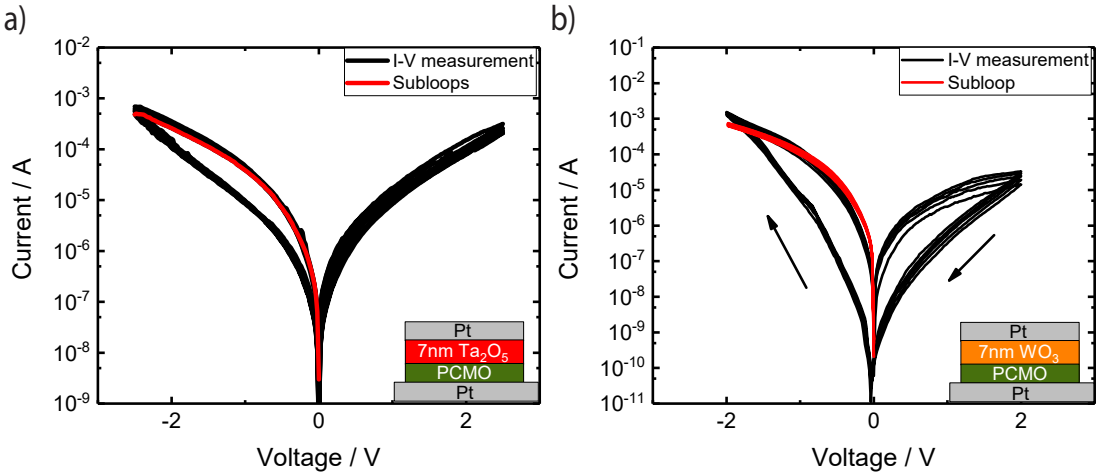

Figure 6.21.: LRS subloop measurements of a) PCMO/Ta_2O_5 and b) PCMO/WO_3 devices.

measurement within the first ms. Nevertheless, it can be seen, that for higher read out voltages, the relative decay is smaller. Nevertheless, even for $-1\,V$ a small decay can be seen within a few seconds. This means, that the electronic state decays slightly even if $-1\,V$ remains applied. This means that the electronic state that is occupied for this effect is above $-1\,V$.

No subloop could be measured for the HRS. The curves are presented in the appendix.

The measurement of the PCMO/Ta_2O_5 and PCMO/WO_3 devices are presented in figure 6.21. It can be seen for the PCMO/Ta_2O_5 devices, figure 6.21 a), as well as for the PCMO/WO_3 devices, figure 6.21 b), that no subloops could be measured for these devices. The negative sweep of the PCMO/Ta_2O_5 is nearly identical with the LRS of the previous IV measurement. The subloop measurement of the PCMO/WO_3 also shows no hysteresis. A possible reason for this behaviour could be the defect density of the native oxide layer and the sputtered oxide. This will be further discussed in section 7.5. Furthermore, no subloop on the positive branch for the HRS could be measured for the PCMO/Ta_2O_5 and PCMO/WO_3 devices.

6.6. Conclusion of switching properties of selected device stacks

It has been shown that the three selected device stacks PCMO/Al, PCMO/Ta_2O_5 , and PCMO/WO_3 show all different switching properties. The first cycle of each device stack was investigated. Here, a clear decrease of the resistance could be seen for the PCMO/Al and the PCMO/WO_3 devices. For the PCMO/Al devices this could be explained by the homogenisation of the AlO_x layer at the interface. For the PCMO/WO_3 device this explanation could not be given. The rough surface could have an impact on the first switching cycle but due to the fact that no initialisation was seen for PCMO/Ta_2O_5 this explanation does not stand up for long. Unfortunately, no conclusive explanation could be given for this behaviour.

During the variability and stability, it could be seen that the PCMO/Al and PCMO/WO_3 devices are much more stable over time and between different measurements compared to the PCMO/Ta_2O_5 devices. For the PCMO/Al devices a small increase in the LRS resistance in the beginning of the variability measurement could be seen. This stabilises within a few pulses. A possible reason for this could be not perfectly chosen voltages.

At the end, the volatile part of the LRS has been investigated for the PCMO/Al devices. Here, it could be shown that this state decays within a few ms.

7. Two Resistor Model

Parts of the experiments shown in this section are performed together with Sebastian Hambsch, as well as parts of the presented model that will be presented. Parts of this chapter are already published in [2].

As described in chapter 2, there is a common agreement that the movement of oxygen vacancies/oxygen is the underlying mechanism for the resistance change in area type resistive switching VCM devices. Nevertheless, the complex material stack with different sublayers that are sensitive for oxygen content makes it difficult to assign the change in resistance to a certain sublayer [48, 146, 149, 191, 192]. This makes a simulation of the switching process complicated. The variety of transport mechanisms that come into play inside the different layers such as Poole-Frenkle emission [193, 194], direct tunneling [195, 196], trap-assisted tunneling [196, 197] as well as polaron hopping [198] make it even more complicated. All of these different processes result in a complex non-linear current voltage dependence during the switching. Therefore, no physical model that can describe the switching dynamics of the PCMO based memristive devices was introduced yet.

In this chapter, the gap of this missing model should be closed by a mathematical model consisting of two serial resistors to describe the current voltage characteristics of the PCMO/Al devices in the I-V measurements of chapter 6. Afterwards, the two resistors will be attributed to a certain layer of the stack by the results of chapter 5 and 6. Furthermore, a physical meaning will be given to the fit parameter. Afterwards, the SET and RESET process will be analysed step by step. At the end, the in chapter 6.5 identified volatile states, the so called subloops and their behaviour will be described by the model.

The empirical model that will be introduced in this chapter consist of two voltage dependent resistors. In the following the resistors will be called R_1 and R_2. R_1 and R_2 are connected in series. The resistance of each resistor can be calculated by

$$\mathrm{R}_{1,2} = \alpha_{1,2} \cdot \exp\left(-V_{1,2} \cdot \beta_{1,2}\right). \tag{7.1}$$

$V_{1,2}$ is the individual voltage drop over R_1 and R_2, respectively, $\alpha_{1,2}$ and $\beta_{1,2}$ are the fit parameters. In section 7.2 the physical meaning of the fit parameters will be discussed. The total applied voltage V can be calculated by the sum of V_1 and V_2.

7.1. Description of I-V measurement with two resistor model

Figure 7.1 a) shows the R-V measurement of the PCMO/Al devices. The information that is shown in this R-V measurement is the same as in the I-V measurement of figure 6.1. The R-V measurement shows a HRS and a LRS branch for $V < 0$ and $V > 0$. It can be seen, that the SET process of the device starts at $-2\,\mathrm{V}$. The RESET process

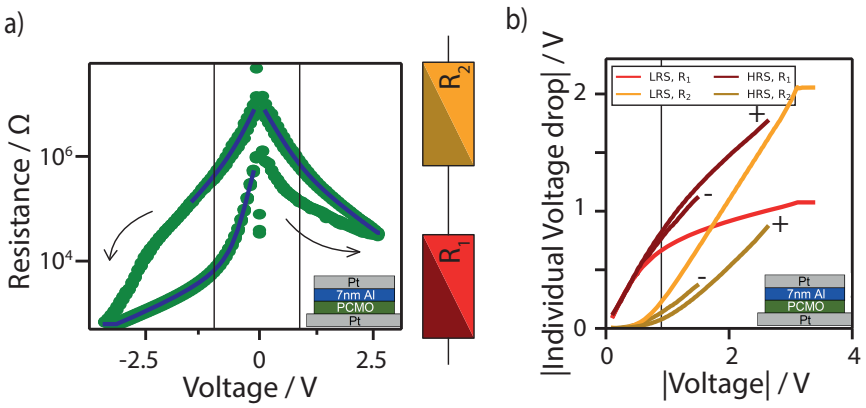

Figure 7.1.: a) R-V Measurement of the PCMO/Al system shown in green with the fits shown in blue, illustration of the two resistors in series. b) Individual voltage drop across the R_1 and R_2. + and - labels the positive and the negative voltage branches that are fitted for the HRS, respectively. The fitted values of $\alpha_{1,2}$ and $\beta_{1,2}$ can be found in table 7.1. Adapted from [2].

Table 7.1.: Fitted parameters of the two resistor model for the R-V measurement shown in figure 7.1. The different parameter sets referrer to the different fitted voltages and resistance values.

Parameter	HRS^+	HRS^-	LRS^-
$\log(\alpha_1)\,/\Omega$	7.0	7.1	6.2
$\log(\alpha_2)\,/\Omega$	4.8	5.1	3.4
$\beta_1\,/\,\mathrm{V}^{-1}$	3.5	4.3	8.2
$\beta_2\,/\,\mathrm{V}^{-1}$	2.1	3.7	0.9

starts already at 0 V, this can be seen later. The switching direction is indicated by the arrows. The slope of the semi-logarithmic plot of the R-V measurement divides every branch into to parts, a region with a steep slope, near zero, and a region with a shallow slope at higher voltages. This is indicated by the black lines.

The two resistor model is used to fit the parts of the R-V measurement where no switching happens. This is due to the fact that the model only describes the electrical transport in the device for a fixed ion distribution. The fitted parts can be seen in blue figure 7.1 a). The optimised fit parameters can be seen in table 7.1.
In figure 7.1 b) it can be seen that the fraction of $V_1/V_2 = R_1/R_2$ changes with the total applied voltage. It can be seen that around 0 V most of the voltage drops over R_1, for higher voltages the voltage drop over R_2 becomes larger.

In summary, the current is limited in these devices by a non-ohmic transport characteristics. Furthermore, the mathematical two resistor model describes the R-V measurement quite well.

7.2. Determination of R_1 and R_2.

The impedance spectroscopy shown in this section was performed by the Institute of Semiconductor Electronics at RWTH Aachen.

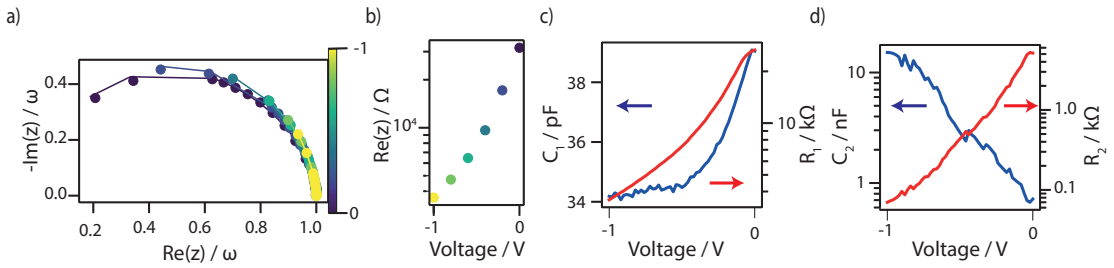

Figure 7.2.: a) Nyquist plot of the HRS of the SC samples. The frequency ranges from 2×10^3 Hz to 3×10^5 Hz. The colour represents the applied voltage from 0 V to −1 V and the nyquist-data for each dc voltage is normalised to the z value at 2×10^3 Hz. b) The real value of Z at 2×10^3 Hz at different applied voltages. c) The capacity and resistance of the first R-C circuit as a function of applied voltage. d) The capacity and resistance of the second R-C circuit as a function of applied voltage. Adapted from [2].

Impedance spectroscopy (IS) is performed to verify the model and to gain information about the possible physical origin of the two resistors. In figure 7.2 a), the Nyquist plots for different applied voltages, normalised with the impedance at 2×10^3 Hz are shown. Figure 7.2 b) shows values used for the normalisation of the Nyquist plot in figure 7.2 a). The used frequencies during the IS ranges from 2×10^3 Hz to 3×10^5 Hz. The used equivalent circuit for the fitting of the SI data consist of two resistor-capacitor (R-C) circuits in series. This is equivalent to the circuit of the two resistor model, with two additional capacitors parallel to the resistors. The equivalent circuit has four fitting parameters: C_1, R_1^{IS}, C_2, and R_2^{IS}. One R-C circuit would lead to a lower accuracy of the fit. Other works support the equivalent circuit with two R-C pairs [199].

The evolution of the fit parameters C_1, R_1^{IS}, C_2, and R_2^{IS} can be seen in figure 7.2 c) and d), respectively. Both resistances decrease with increasing negative voltage. Furthermore, R_1^{IS} is larger than R_2^{IS} as expected from the fitted voltage drop across the two resistors, see figure 7.1 b). The capacitance is dominated by C_1. While C_1 becomes smaller, C_2 becomes larger with increasing voltage. This behaviour will be explained later.

Nevertheless, the IS shows that a two resistor-capacitor circuit describes the IS measurement and the resistance values fit to the values R_1 and R_2 of the two resistor model. This means, that two resistors can generally describe the resistance-voltage dependence in the PCMO/Al devices. The next step is to identify the origin of the two resistances in the devices.

The resistance in figure 7.1 a) and the current in figure 6.1 is limited by a non-ohmic current transport. Therefore, all ohmic junctions inside the device can be neglected, namely PCMO/Pt and Al/Pt. In section 5.1.1 it was shown that the measured Mn $2p$ peak changes after the deposition of the Al layer deposition on top of the PCMO layer, a Mn^{2+} feature occurs, see figure 5.2. Furthermore, the Al $2p$ peak does not only show the metal feature but also an oxide feature, see figure 5.2. This indicates a formation of an interface layer. The Al metal oxidises due to the movement of oxygen ions from the PCMO into the Al with an oxygen deficient region in the PCMO layer. Furthermore,

the shift of the Pr $3d\,5/2$ of around 0.9 eV, see figure 5.3 a), indicates a downwards band bending of the PCMO bands at the interface between the PCMO and the Al/AlO_x layer with a depletion zone inside with increased resistance in the PCMO.

Two regions of increase resistance can be identified with the XPS measurements presented in section 5.1.1, the native AlO_x layer for the Al layer and region of oxygen deficient PCMO for the PCMO layer. The high bandgap AlO_x is expected to have a much higher resistance than the depletion zone of the PCMO layer. It was shown in figure 7.1 b), 7.2 c) and d), and table 7.1 that R_1 is way larger than R_2. Therefore, R_1 can be assigned to the AlO_x layer and R_2 can be assigned to the oxygen deficient layer in the PCMO.

For further validation of the assignment of the two layers of the device stack, the AlO_x and the oxygen deficient layer in the PCMO, to the resistors of the model, the fitted capacitance of the IS measurements will be considered again. A plate capacitor will be assumed to describe the capacitance of the AlO_x. The capacitance can be described with

$$C = \epsilon \cdot \epsilon_r \frac{A}{d}. \tag{7.2}$$

Inserting the values of the AlO_x layer of the device into equation 7.2, $A = 2500\,\mu m^2$ as the device size, $\epsilon_r = 7$, $d = 4$ nm as assumed thickness of the native AlO_x, the capacitance calculates to 37 pF at 0 V. This fits to the values that are fitted in the IS measurement, see figure 7.2 c). The decrease of the capacitance with increasing applied voltage can be easily explained. The current in the AlO_x layer flow through excited, shallow defects [200–202]. Uncharged defects increase the capacitance of the layer while ionised defects lower the capacitance [203]. The ionisation of the defects happens with increasing negative applied voltage. This means that the capacitance of the layer will decrease with increasing voltage. This behaviour was observed during the IS measurement, see figure 7.2 c).

Calculating the capacitance of the PCMO depletion layer with $\epsilon_r = 110$ and $d = 2$ nm, the capacitance is around 1 nF [204]. This capacitance fits to the fitted capacitance from the IS measurement. The assumed thickness of the depletion layer is quite small due to the fact that the PCMO has a lot of free charges due to its the high doping level of 30 %. This screens the internal voltage drop. Applying a negative voltage would lead to a neutralisation of the depletion layer and the capacitance increases, as observed in the IS measurement, see figure 7.2 d).

In conclusion, the combination of the XPS measurement, section 5.1.1, the electrical measurements, chapter 6, and the impedance spectroscopy, figure 7.2 could identify the two resistors of the two resistor model as the native AlO_x layer and the oxygen depletion zone inside the PCMO layer.

7.3. Physical meaning of fit parameters of two resistor model

In the following, the fit parameters α_1, α_2, β_1, and β_2 will be assigned to a physical meaning.

The applied voltage ionises the shallow defects inside the native AlO_x layer, electrons are released to the conduction band and they contribute to the current. This ionisation of a single electron from a trap with a potential that has a $1/r$ behaviour into the conduction band is called Poole-Frenkel effect [205]. The resistance can be described with

$$R \propto \exp\left(\frac{e}{k_B T}\left(\phi_B - 2\sqrt{eV/(4\pi\epsilon d)}\right)\right). \tag{7.3}$$

V is the voltage drop over the AlO_x barrier, e the elementary charge, k_B the Boltzmann-constant, T the temperature, ϵ the permittivity of the barrier, d the thickness of the barrier, and ϕ_B the barrier height at zero applied electric field. Comparing now the two resistor model to the Poole-Frenkel effect it can be approximated that

$$\beta_1 \propto \frac{1}{\sqrt{\epsilon d_s}}. \tag{7.4}$$

d_s indicates that the screening changes the barrier width, therefore, the thickness d was replaced by d_s. ϵ changes with the oxygen vacancy $V_O^{\bullet\bullet}$ concentration. For α_1 it is assumed that every ionised trap adds one free charge carrier to the system. This means for an equally distributed number of traps n_t in the barrier

$$\alpha_1 \propto \frac{1}{n_t}. \tag{7.5}$$

The electric current in PCMO is carried by polarons [33, 54] that can be described by

$$R \propto \frac{V}{n_p e a \omega} \frac{1}{\sinh\left(x(V)\right)} \exp\left(\frac{\Delta W_{ac}}{k_B T}\right) \tag{7.6}$$

with

$$x(V) = \frac{eVa}{2k_B T r}. \tag{7.7}$$

V is the applied voltage, n_p the polaron density, e the elementary charge, a the hopping distance, ω the hopping frequency, ΔW_{ac} the activation energy for hopping, k_B the Boltzmann constant, T the temperature, and r the thickness of the hopping region that is equal to the thickness of the depletion zone due to the fact that the voltage drops mostly over the insulating depletion zone. The distance between two neighbouring Mn ions is 0.4 nm that is equal to the hopping distance a [33]. For small $|x(V)|$ values one can approximate $1/\sinh(x(V))$ with $2 \cdot \exp\left(-x(V)\right)$. Comparing the exponent $x(V)$ to the exponent of the two resistor model one finds

$$\beta_2 \propto \frac{1}{r}. \tag{7.8}$$

With decreasing oxygen content, the mobility of the charge carrier μ in the PCMO drops by one order of magnitude, and the charger carrier concentration n by 10 %. This means that

$$\alpha_2 \propto \frac{1}{\mu n_p}. \tag{7.9}$$

Keeping in mind that a lower concentration of the charge carriers n_p changes the screen-

Fit parameter	Proportional to	Interpretation
α_1	$1/n_t$	Base resistivity of the whole AlO_x barrier.
β_1	$1/(\sqrt{\epsilon d_s})$	Modification of the E-field by screening.
α_2	$1/(\mu n_p)$	Base resistivity of PCMO: The amount of charge carriers and their mobility.
β_2	$1/r$, n_p	Modulation of the E-field in the depletion zone by its width.

Table 7.2.: Summary of the fit parameters, their connection to physical parameters, and their interpretation. Adapted from [2].

ing of the internal field and the width of the depletion zone equation (7.8) can be expanded to

$$\beta_2 \propto n_p. \tag{7.10}$$

Table 7.2 summarises the identification of the fit parameter and their physical meaning.

7.4. Description of resistive switching with two resistor model

As stated in section 7.1 the two resistor model only describes the parts of the IV measurement curve where no switching happens and the overall switching dynamics can not be described by this model. Nevertheless, in section 8.1 and section 9.1 it is shown, that different states in between the HRS and the LRS are possible. This intermediate states can be used to analyse the SET and RESET process. Therefore, the switching cycles will be performed with increasing SET and RESET stop voltages, after every SET or RESET a read out sweep is performed. The SET and RESET stop voltage is increased by 0.1 V with every cycle. This read out sweep is analysed with the two resistor model to gain information about the ion movement during the switching process.

The upper part of figure 7.3 shows the analysis of the SET process and the lower part the analysis of the RESET process. Figure 7.3 a) shows the read out sweeps for different voltages of the switching sweeps during the investigation of the SET process. The data is shown in green and the fitting of the data with the two resistor model is shown in blue. It can be seen, that for different SET stop voltages the read out sweeps show different resistance values. The resistance decreases with increasing SET stop voltage. Nevertheless, for all shown read out sweeps the two resistor model fits the data quite well. Figure 7.3 b) shows the current that was read out during the read out sweeps shown in figure 7.3 a). It can be seen, that the current does not change in the beginning for low SET stop voltages, namely region A. Afterwards the currents starts to increase and shows an exponential behaviour in the semi-logarithmic plot, namely region B. At around -3 V the current shows a kink, the change in current with every voltage step becomes smaller. The evolution of the fit parameters during the stepwise SET process is shown in figure 7.3 c). It can be seen, that for low SET stop voltages, region A, all parameters are constant and show only slight fluctuations. For higher voltages α_1 and α_2 starts to decrease. This means, that after the comparison of section 7.3 the number

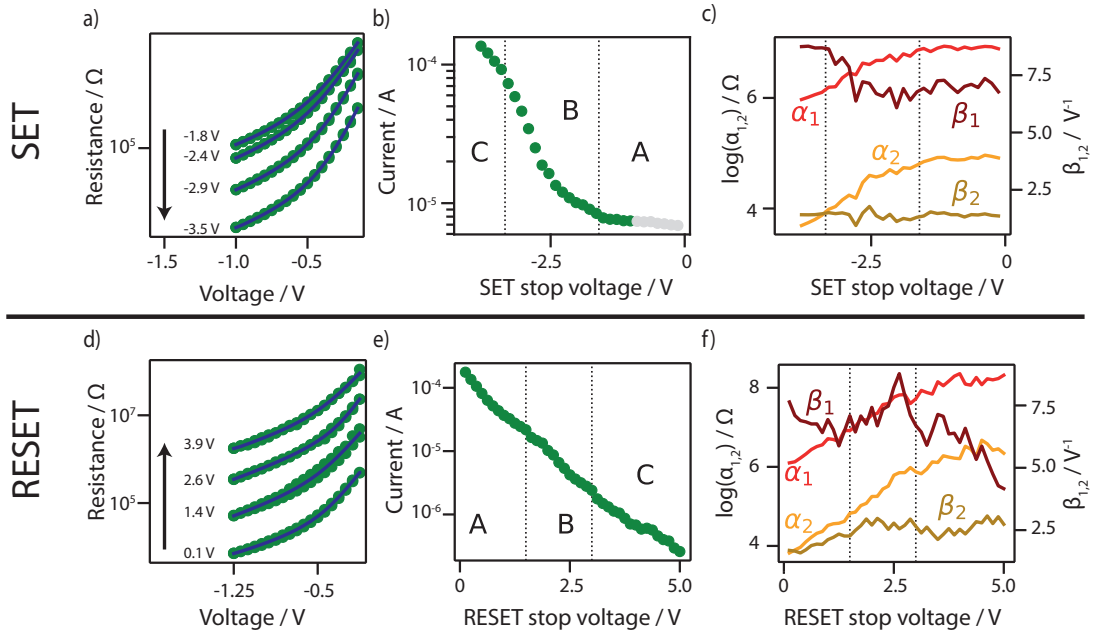

Figure 7.3.: Fitting of SET and RESET process with two resistor model. a)/b)/c) SET Process a) Read out sweeps after different SET sweeps with fitting. b) Evolution of current with different SET voltage stop. c) Evolution of SET fit parameters. d)/e)/f) SET Process d) Read out sweeps after different RESET sweeps with fitting. e) Evolution of current with different RESET voltage stop. f) Evolution of RESET fit parameter.

of traps inside the AlO_x layer increases as well as the mobility and the number of charge carriers inside the PCMO depletion zone. $|V_1|$ ionizes the new traps in the AlO_x layer and ϵ decreases. This leads to an increase of β_1. For higher voltages the SET process shows a saturation, region C, due to amount of oxygen vacancies inside the AlO_x layer. This leads to a quite conductive AlO_x layer and the voltage drop across this layer decreases. Therefore, $|V_1|$ is not sufficient to ionise the additional traps deep inside the AlO_x layer. This provokes the opposite effect of the ionised traps and β_1 stays constant as seen in figure 7.3 c). The constant behaviour of β_2 indicates that during the whole SET process the amount of oxygen vacancies in the interface region stays constant due to the fact that the modulation of the E-field in the depletion zone by its width stays constant.

The described behaviour of the SET process from the analysis of the fit parameters of the two resistor model is schematically drawn in figure 7.4 b). The dashed lines indicates the interface region. It can be seen that the oxygen vacancies move from the PCMO layer inside the AlO_x layer across the interface and into the bulk.

The investigation of the RESET process is shown in the lower part of figure 7.3. It can be seen in figure 7.3 d) that with increasing RESET stop voltage the resistance of the current increases. Again the fit, shown in blue, fits the data of the read out sweep, shown in green quite well. The RESET stop voltage is again increased by 0.1 V with every cycle. The evolution of the read out current with increasing RESET stop can be seen in figure 7.3 e). It can be seen that the current decreases with increasing RESET stop voltage. The RESET already starts at low voltage and the current change is linear

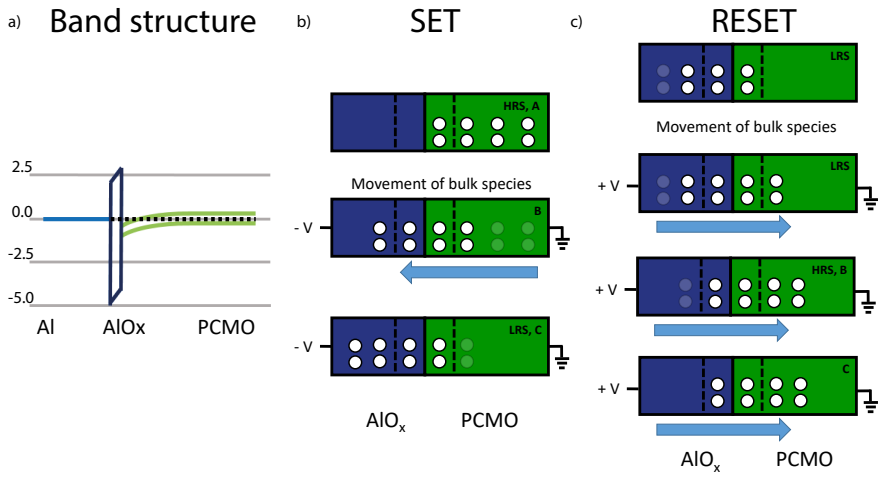

Figure 7.4.: Schematic drawing of a) the band structure of the PCMO/Al devices and the b) SET and c) RESET process.

in the semi logarithmic plot. This behaviour is the same as expected from section 8.1. Furthermore, no saturation or kink in the course of the current can be seen. The evolution of the fit parameters during the invetsigation of the RESET process is shown in figure 7.3 f). It can be clearly seen, that the α_1 and α_2 parameter starts to increase directly. This shows, as already described for the SET process, that oxygen vacancies start to move from the AlO_x layer into the PCMO layer. This leads to an decrease of traps inside the AlO_x layer and α_1 increases. Additionally, the additional oxygen vacancies inside the PCMO layer increases the resistance of the PCMO layer and α_2. For higher voltages only the interface region of the AlO_x layer contains oxygen vacancies and the continued movement of oxygen vacancies increases the resistance of the AlO_x and the PCMO layer and α_1 and α_2 even further. The change in β_1 that can be seen in figure 7.3 f) can be explained by two different effects. First the increase in resistance leads to a higher voltage drop V_1. This higher voltage drop leads to a higher number of ionised traps that decreases ϵ and increases β_1. This is the case at the beginning of region B. Afterwards, the number of ionised oxygen vacancies in the AlO_x decreases due to the decreasing number of oxygen vacancies inside the AlO_x layer. The lack of ionised oxygen vacancies in the AlO_x increases ϵ and decreases β_1. This effect happens in the second half of region B. β_2 stays constant because of the constant amount of oxygen vacancies in the depletion zone. For even higher voltages, region C, α_1 and α_2 saturates. This means that the oxygen vacancy concentration has already reached its final value and the resistivity of AlO_x and the PCMO saturates.

The analysed movement of oxygen vacancies for the RESET process is schematically shown in figure 7.4 c). It can be seen, that the oxygen vacancies move between the PCMO and the AlO_x across the interface layer and the fit parameter describe this movement quite well.

In summary, the SET and RESET process could be analysed with the help of the two resistor model. The evolution of the fit parameters gives insight into the oxygen vacancy movement within the different regions of the stack during SET and RESET.

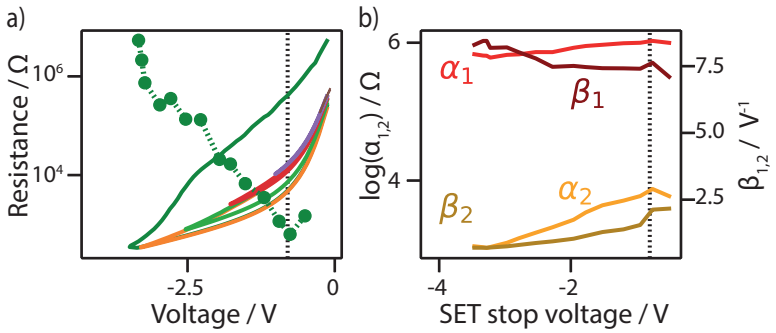

Figure 7.5.: a) Negative branch of the R-V measurement with a switching cycle and different subloops with different SET stop voltages. b) Evolution of fit parameters of the two resistor model.

7.5. Subloops

In section 6.5 it was shown that the LRS contains of a volatile and a non volatile state. It was shown in figure 6.20 c) and d) that this volatile state decays without an applied voltage within a few ms. This decay time can be prolonged by the continuous application of a voltage. This is a first hint that the underlying mechanism of the subloops is not only given by the movement of ions but also electronic effects come into play. In the following, the two resistor model will be used to identify the subloops and describe the origin of the subloops.

Figure 7.5 a) shows the negative branch of the R-V measurement. In green the SET process is shown, the other colours show subloop measurement with different SET stop voltages. The green dots indicate the area of the hysteresis of the subloop measurement with different SET stop voltages. It can be seen, that the area of the hysteresis of the subloops increases for SET stop voltages higher as $-0.8\,\mathrm{V}$. For lower voltages, no hysteresis is visible in the R-V measurement. The evolution of the fit parameters α_1, α_2, β_1, and β_2 is shown in figure 7.5 b). The fit parameters start to change at around $-0.8\,\mathrm{V}$. While the α_1 parameter stays more or less constant with only a slight decrease, β_1 increases, α_2 and β_2 decrease.

A similar behaviour of switching with subloops was observed by La Torre et al. [206] in Ta_2O_5 devices. The main difference is that the subloops in the Ta_2O_5 devices were observed in the HRS. The origin of the volatile states in these devices was attributed to a charging of trap states. Nevertheless, no details of the position or the origin of these traps was given by La Torre et al. [206]. In this work, the subloops were observed in the LRS but they will also be assigned to the ionisation of trap states in the AlO_x layer.

First one can assume to have two types of states inside the AlO_x layer, the one that are connected to the Poole-Frenkel effects and the traps that will be connected to the subloops. The traps that contribute to the Poole-Frenkel effect are shallow traps that lie close to the conduction or valence band. Beside this, the traps that lead to the subloops are deep inside the band gap of the AlO_x barrier. In addition one can assume that the barrier is further oxidised in the LRS at the interface between the PCMO and the Al, concluding from the discussion of the SET process in section 7.4. Furthermore, the

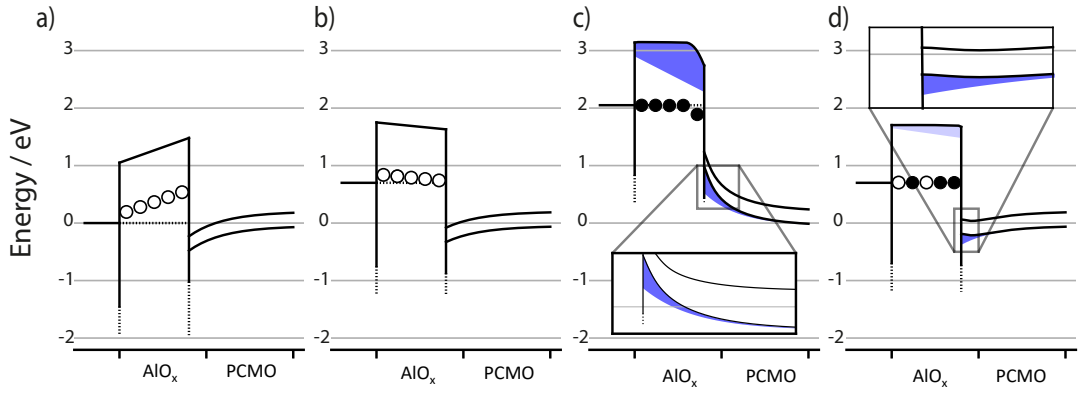

Figure 7.6.: Band diagram of the PCMO/Al devices to show the impact of trap states on the band structure to explain the volatile LRS state. a) LRS state with empty trap states inside the AlO_x layer. b) LRS state with applied voltage V_f that lifts the Fermi level on the level of the Fermi energy. c) LRS state at higher voltages V_m. Trap states are filled and effect the band bending of the PCMO depletion zone can be seen. d) Going back to V_f leaves the trap states partly ionised and the PCMO band shows an upwards bending. This reduces the resistance of the device stack.

degree of oxidation of the AlO_x layer decreases with distance to the PCMO interface. This means, that the AlO_x layer has an unknown, unequal oxidation state with a high trap density inside its band gap.

The band structure with the trap states deep in the AlO_x band at different applied voltages can be seen in figure 7.6. Empty traps are represented by empty circles and ionised traps are represented by filled circles. Figure 7.6 a) shows the system at 0 V. All traps are empty and not ionised. By applying a voltage to the system V_f, the Fermi-level in the Al aligns with the traps. The electrons can tunnel into trap states and start to charge them, see figure 7.6 b). The traps are placed 1.8 eV below the conduction band. This is in good agreement with traps in amorphous AlO_x [207, 208]. By increasing the voltage further to the SET voltage V_{SET} all traps are ionised inside the AlO_x. An electric potential in the AlO_x is generated by the ionised traps. This potential moves the traps upwards until they are reaching the threshold voltage. Furthermore, the generated potential reaches into the PCMO and bends the PCMO bands upwards. This leads to a partly neutralisation of the depletion zone and a decrease of α_2 as it can be seen in figure 7.5 a). Additionally, with increasing voltage V a higher fraction of the traps is ionised and β_2 decreases. For PCMO in contact with a metal and without a depletion zone, the contact should be approximately ohmic and β_2 should be $0\,V^{-1}$ [33].

While V_f was not sufficient to ionise the traps, decreasing the voltage again to V_f some of the traps remain ionised, see figure 7.6. The change in the resistance that was observed in figure 6.20 a) and 7.5 a) can be explained by the remaining ionised traps. The ionised traps decrease the resistance of the PCMO more than the resistance of the AlO_x layer. Furthermore, the depletion zone width depends on the state of the traps and charged traps contribute to the screening of the applied electronic potential.

This lead to the conclusion that the subloops and the volatile part of the LRS result

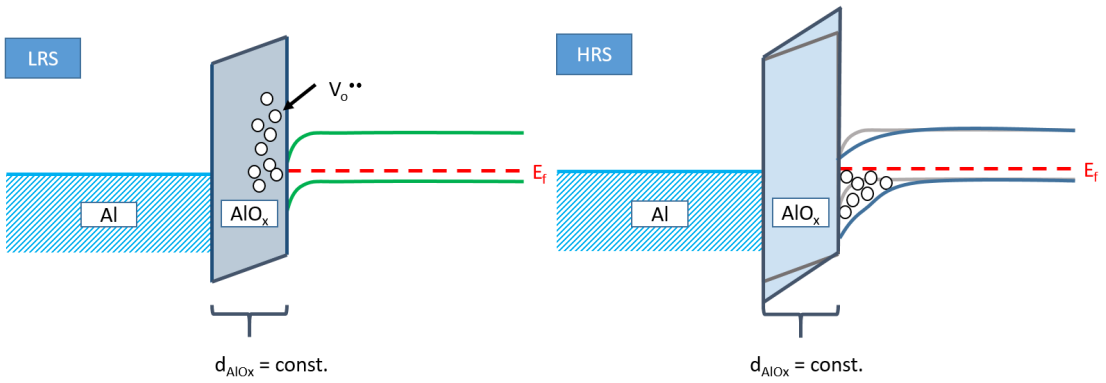

Figure 7.7.: Schematic band diagram of the PCMO/Al devices with an oxide at the interface for the LRS and the HRS. This schematic drawing represents only gives a brief overview of the oxygen vacancy distribution and in no way reflects the exact heights of the bands.

from electrons ionising trap states deep inside the AlO_x band gap.

7.6. Conclusion of two resistor model

The purely mathematical two resistor model introduced in this chapter is able to describe the R-V measurement of the PCMO/AlO_x devices from chapter 6 for the parts of the R-V measurement in which no switching takes place. Furthermore, the individual voltage drop across the two resistors could be calculated. With the help of impedance spectroscopy the assumed resistors could be confirmed. Additionally, the impedance spectroscopy and the results of section 5.1.1 have led to the identification that the two resistors are the interface AlO_x layer and a depletion zone inside the PCMO at the interface to the AlO_x layer. This shows that the interface oxide is crucial for resistive switching in these type of devices by comparing the results of the model and the switching devices of chapter 6.

By analysing the conduction mechanisms inside the AlO_x and the PCMO, namely the Poole-Frenkel effect and Polaron hopping, a physical meaning could be given to the fit parameters of the two resistor model. α_1 and α_2 represent the base resistivity of the AlO_x and the depletion zone of the PCMO, respectively. β_1 represents the modification of the electronic field inside the AlO_x by screening and β_2 represents the modulation of the electronic field in the depletion zone of the PCMO by its width. The proportionalities of the fit parameter to physical values can be found in table 7.2.

Afterwards, the two resistor model was used to analyse the SET and RESET process and provides insights into the ion movement in the PCMO and the AlO_x. Due to the fact that the two resistor model can only fit the parts of the R-V measurement in which no switching takes place, the SET and RESET process are analysed by a step-wise SET and RESET. The change in resistance could be attributed to the exchange of oxygen/oxygen vacancies between the PCMO and the AlO_x layer. The movement of oxygen vacancies is represented in figure 7.4. Figure 7.7 shows a representative of the band diagram of the HRS and the LRS which is derived from the model. It can be seen, that the oxygen vacancies change the band bending and the barrier height at the interface.

Beside the switching, the volatile states of the LRS that was observed in section 6.5 could be explained with the help of the two resistor model. The change in resistance could be attributed to the ionisation of traps deep inside the AlO_x band gap.

In conclusion the model gives insights into the physical processes that dominate the switching process and to simulate the dynamics of the resistance change of PCMO/Al devices. In future this model could be used as input for circuit design in the field of neuromorphic computing or to design further devices simulations of area type resistive devices.

8. Switching Kinetics of PCMO

In this chapter the switching kinetics of PCMO in combination with 7 nm Al, 7 nm Ta_2O_5 and 7 nm WO_3 will be presented. Starting with the Al device kinetics, the kinetics of the devices with the other materials will be presented separately. Afterwards, the kinetics will be compared to each other. At the end of this chapter, the PCMO based device kinetics will be compared to filamentary switching devices like STO or Ta_2O_5 [3, 174, 210].
The kinetics measurements are performed with a *Keithley 4200A-SCS* measurement setup. The properties of the measurements setup are described in section 3.4.2.

These measurements are important for further applications in circuits and for neuromorphic applications to define the dynamics of the PCMO based resistive switching devices.

A schematic representation of the measurement scheme that is used for the kinetic measurements for all devices is shown in figure 8.1 a). First, the devices are set into a predefined resistive state with the help of a preparation cycle. This state is either the high resistive state (HRS) or the low resistive state (LRS) for the SET or the RESET kinetics, respectively. Afterwards the device state is read out again, to determine the device state before a given SET/RESET pulse. Afterwards, a voltage pulse with a given height and length is applied to the device. This pulse changes the device state. The device state is read out with another read out pulse. The read out before and after the defined switching pulse define the change in resistive state, presented by the ON/OFF-ration. The used read out pulses have a height of $-0.3\,\mathrm{V}$ and a length of 0.1 ms. It is important to notice, that the read out pulse does not change the device state. Afterwards, the device is brought back into the predefined state by applying another preparation cycle and the switching pulse is either increased in voltage or time. This is done until a certain voltage and time is reached and the measurement ends.

The calculated SET kinetics based on different acceleration cases of the oxygen ions for filamentary switching devices published by Menzel et al. [209] and can be seen in figure 8.1 b). Additionally, measurement data of STO based switching devices is presented there. It can be seen that the main driving force during the SET kinetics of filamentary type resistive switching devices is the temperature in the disc region of the device. [209]. Furthermore, in 2018 Menzel et al. stated that heating is not crucial for the switching dynamics and the ion movement in area type resistive switching devices [42]. In this devices the operation is only accelerated by the electric field [42]. Nevertheless, the simulated stack is not the same stack as used in this work, therefore one can only make limited statements.

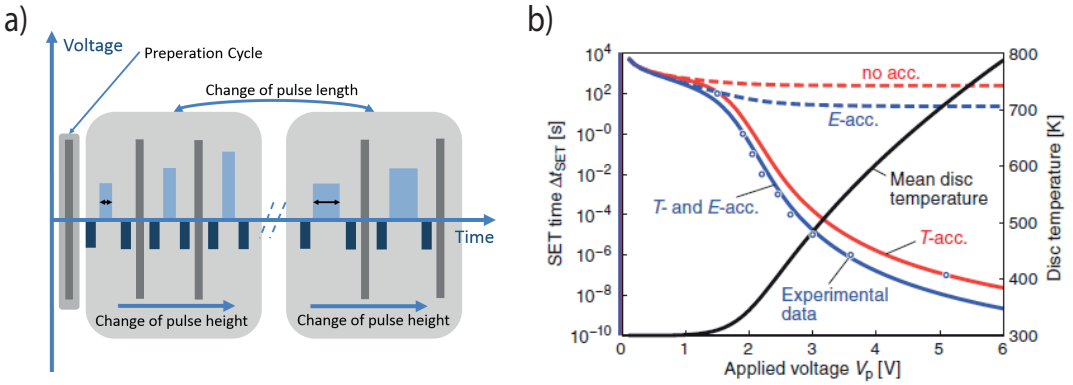

Figure 8.1.: a) Measurement scheme of the kinetic measurements. First, the device is set into a predefined resistance state with a preparation cycle. Afterwards the device state is read out, a defined voltage pulse is applied and the device state after this voltage pulse is read out. Afterwards, the device is set back into the predefined state and the pulse voltage/pulse height is increased. b) Calculated SET time for filamentary switching devices based on four different acceleration cases with data for STO kinetics, taken from [209]

8.1. PCMO/Al switching kinetics

In this section the switching kinetics of the $20 \times 20\,\mu m^2$ PCMO/Al devices will be presented.

Exemplary current transients of read out pulses that are used to determine the change in the ON/OFF-ratio during the SET and RESET kinetic measurements are shown in figure 8.2. As already stated in the beginning of this section, the read out pulses regardless of whether a SET or RESET kinetic is measured, have an length of 1 ms and a height of $-0.3\,V$. Read out pulses after SET pulses with different voltages and before them can be seen in figure 8.2 a). All of the shown SET pulse examples to change the device state here have a length of 0.1 ms. It can be seen, that the read current increases with increasing pulse voltage. This is the current representation of the effect one have already seen in the heatmap of the SET kinetic measurement. Figure 8.2 b) shows the current transients of read out pulses of the LRS and after a RESET pulse with different voltages. All of the used RESET pulses to change the device state here have a length of 0.1 ms. A clear trend of decreasing current with increasing pulse height can be seen in the current transients. The change in the device state, ON/OFF-ratio is calculated with the measured currents of the read out pulses. Repeating this measurements with different pulse lengths and different pulse voltages reveals the kinetics of the device.

Figure 8.3 shows the measured ON/OFF-ratios, indicated by colour, for the SET and RESET process for different pulse voltages and pulse times. Figure 8.3 a) and b) shows the SET and RESET kinetic with an colour scale between 1 and 4, respectively. The pulse voltage for the SET process is varied between $-1\,V$ and $-4\,V$. For the RESET process the pulse voltage is varied between 1 V and 3 V. The pulse length is varied for the SET and the RESET process between 100 ms and 1 µs. In figure 8.3 c) the RESET process between 2 V and 3 V is presented with an adapted colour scale. The ON/OFF-ratio here is between 1 an 10.

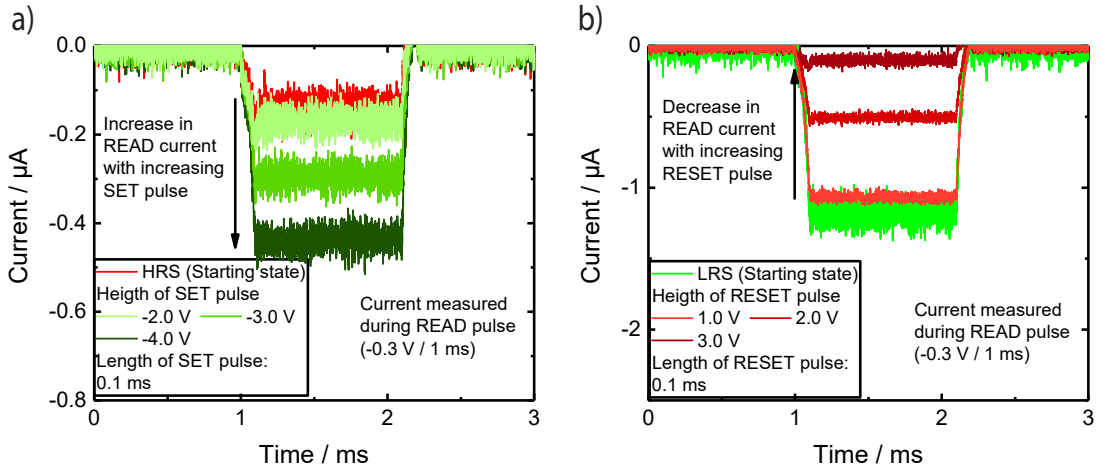

Figure 8.2.: Current transients of read out pulses with a length of 1 ms and a height of −0.3 V. a) Current transients of read out pulses during the SET kinetic measurement for different SET pulse voltages. b) Current transients of read out pulses during the RESET kinetic measurement for different RESET pulse voltages.

For the SET process, figure 8.3 a), it can be seen, that the ON/OFF-ratio increases with increasing pulse voltage and pulse length. The SET process starts for pulses with a length of 100 ms at around 1.5 V. For pulses with a length of 1 µs at around 3.5 V. For lower voltages, no change in the resistive state could be measured for this pulse lengths. This means that a switching voltage change by 2 V changes the needed pulse length by five orders of magnitude for to achieve the same change in resistance. For a given pulse length, the ON/OFF-ratio increases by 1 every volt the pulse height is increased. This is not quite correct, because the increase in the ON/OFF-ratio with increasing voltage diminishes slightly for higher voltages. This can be explained by the decrease of the voltage drop over the device with decreasing resistance. If the device starts to SET and the resistance starts to decrease, the voltage drop over the device becomes smaller. Therefore, the driving force of the ions inside the devices becomes smaller and higher voltages are needed to reach the same change of the resistance. Additionally, the ON/OFF-ratio also increases by one every 1.5 orders of magnitude if the pulse length is increased for high pulse voltages around −4 V. For small voltages this behaviour can not be concluded.

The RESET process is depicted in in figure 8.3 b). Here it can also be seen that the ON/OFF-ratio increases with increasing pulse voltage and pulse length. The RESET process already starts at way lower voltages as the SET process. For the 100 ms pulse length, the ON/OFF-ratio is already 2 at −1 V. For short pulses, 1 µs, an ON/OFF-ratio of 2 is already reached at 2 V. This mean that the switching voltage changes only by 1 V for a 5 orders of magnitude change in pulse length. For the RESET process the change in ON/OFF-ratio for a given pulse length with changing pulse voltages is not constant over the whole voltage range. For higher voltages, the change in the ON/OFF-ratio for a given voltage step is higher than for lower voltages. This can be explained in the same manner as for the SET process. The gradual increase of the device resistance during the application of the pulse leads to an increase of the voltage drop over the device and therefore the field inside the device increases. Due to the fact, that the field is the main driving force for the ion movement inside the devices, the ion movement is increased.

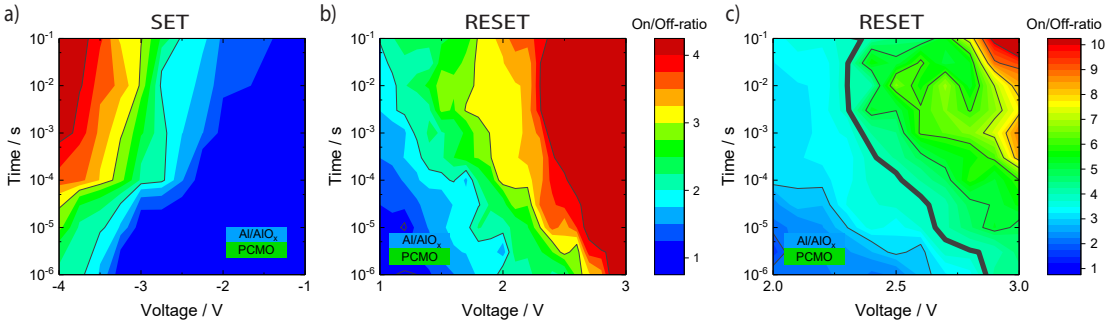

Figure 8.3.: Measurement of the SET (a)) and RESET (b)) kinetics of PCMO/Al resistive switching devices. c) shows the RESET kinetics with an adapted colour scale to shows the possibilities of higher ON/OFF-ratios.

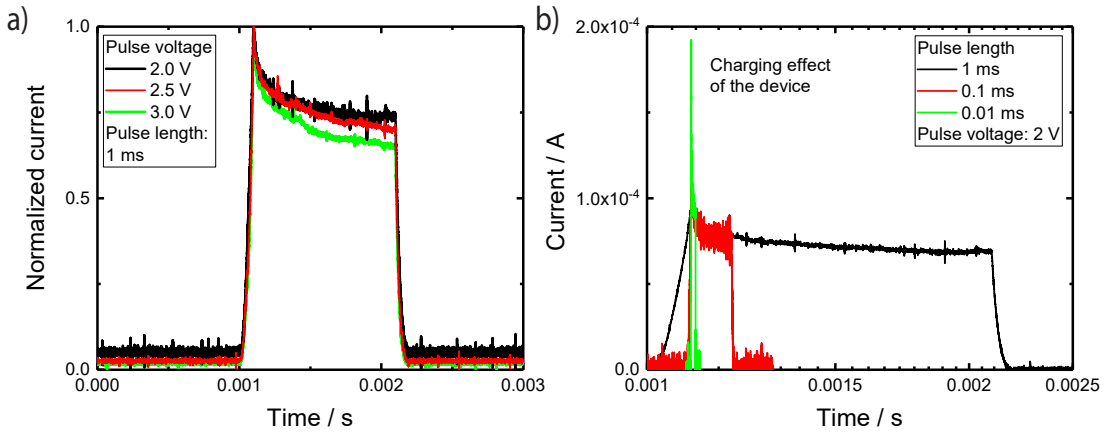

Figure 8.4.: Current transients of the RESET kinetic measurements to visualize the change of the current for different the pulse heights a) and the pulse lengths b) during the switching.

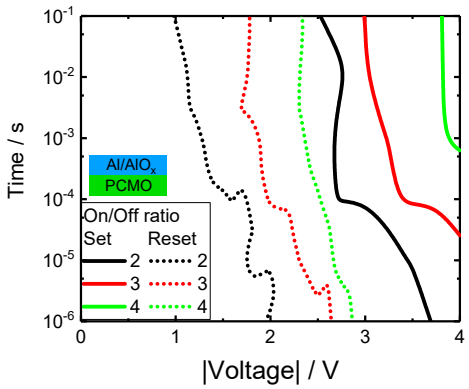

Figure 8.5.: Extracted contour lines of the heatmap, figure 8.3, of PCMO/Al devices. for ON/OFF-ratios of 2, 3 and 4.

Additionally, the change in ON/OFF-ratio with changing pulse length is around two orders or magnitude for a change of 1 in the ON/OFF-ratio.
The RESET kinetics with an adapted ON/OFF-ratio indication, colour scale, up to an ON/OFF-ratio of 10 for the regime between 2 V and 3 V shown in figure 8.3 c). It can be seen that for long pulses with high voltages even an ON/OFF-ratio of 10 could be reached. The previously described acceleration of the change in resistance with increasing voltage is also clearly visible. The thick line indicates an ON/OFF-ratio of 4, the highest ON/OFF-ratio indicated in figure 8.3 b).

The increase in ON/OFF-ratio with increasing pulse voltage and pulse length, can not only be seen in the current transients of the read out pulses, figure 8.2, or in the heatmap measurements, figure 8.3, but it can also be seen directly in the current transients during the switching, see figure 8.4. Figure 8.4 a) shows the normalized current response of the devices during the RESET process for different pulse voltages, 2.0 V, 2.5 V and 3.0 V at a given pulse length of 1 ms. It can be seen that the decrease in current during the switching increases with voltages. This is consistent with the observations of the device state measurements before and after the SET and RESET pulse, like it is done in figure 8.3. In figure 8.4 b) the current transients of RESET pulse with a given voltage, 2 V, but different pulse lengths, 1 ms, 0.1 ms and 0.001 ms is shown. It can be seen that the current for all three measurements matches for the given times quite well. The different states after the applied pulses only occur due to the different times the voltage is applied. This is an important difference to filamentary switching devices what will be discussed later. This behaviour is also reflected in the kinetic measurements and can be observed for the SET current transients of all samples.

To make the differences between the SET and RESET process clearer, the extracted contour lines of the different ON/OFF-ratios are plotted in figure 8.5. A clear difference in voltage for the SET and RESET process for a given pulse length can be seen. The voltage needed for the SET process is around 1.5 V higher as the voltage needed for the RESET process. Also the before described change in the spacing of the ON/OFF-ratio change can be divined. On the other hand the slope of the ON/OFF-ratio seems to be constant for all the different devices. This difference in the ON/OFF-ratio kinetics for

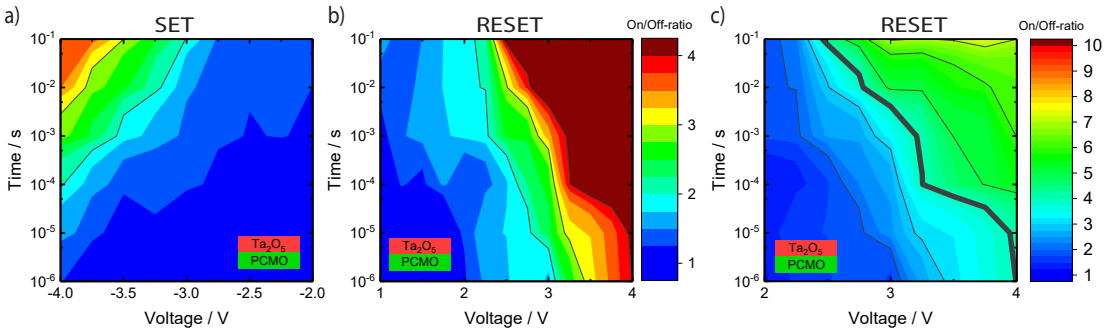

Figure 8.6.: Measurement of the SET (a) and RESET (b) kinetics of PCMO/Ta_2O_5 resistive switching devices. c) shows the RESET kinetics with an adapted colour scale to shows the possibilities of higher ON/OFF-ratios

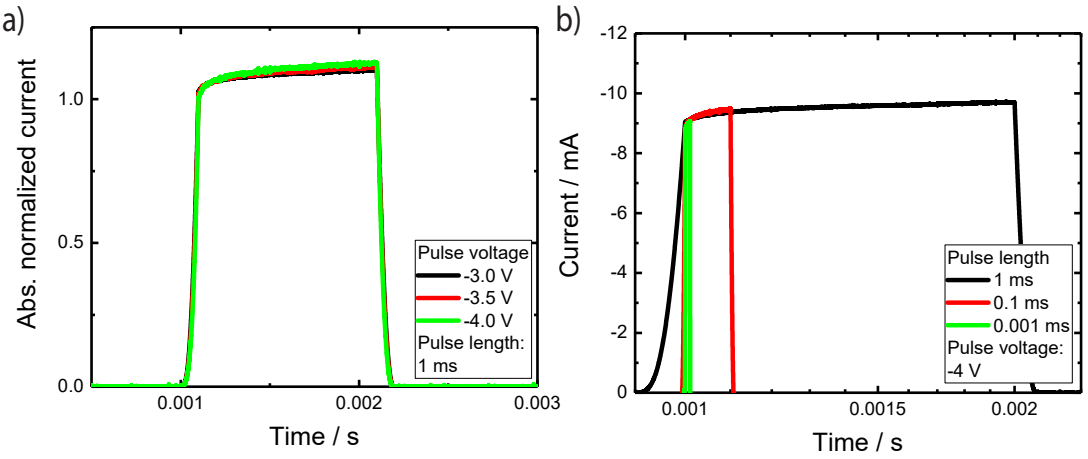

Figure 8.7.: Exemplary SET pulses of the PCMO/Ta_2O_5 kinetics. a) SET pulses with a length of 1 ms and pulse voltages of −3 V, −3.5 V and −4 V. b) SET pulses with a height of −4 V and lengths of 1 ms, 0.1 ms and 0.001 ms.

SET and RESET can partly be understood with the change of the Gibbs free energy as explained in chapter 5. The incorporation of oxygen inside the barrier layer is energetically favourable until a certain chemical gradient is reached. Therefore, the RESET process can be performed with lower voltages.

8.2. PCMO/Ta_2O_5 switching kinetics

In this section the kinetic measurements of $20 \times 20\,\mu m^2$ PCMO/Ta_2O_5 devices will be presented.
Figure 8.6 shows the measured ON/OFF-ratios for the PCMO/Ta_2O_5 devices with respect to the applied pulse voltage and pulse length. The ON/OFF-ratio is indicated by different colours.

The SET kinetics of the PCMO/Ta_2O_5 samples are measured for pulses between −2 V and −4 V and pulse lengths between 1 µs and 100 ms. The RESET kinetics are measured with pulses between 1 V and 4 V and pulse lengths between 1 µs and 100 ms

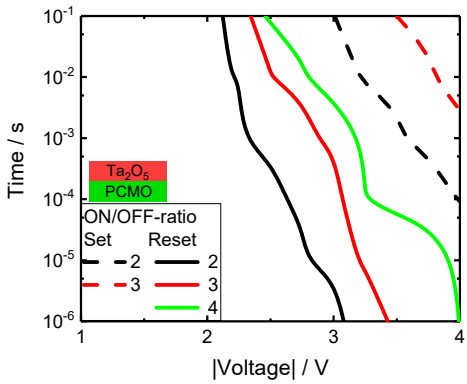

Figure 8.8.: Extracted contour lines of the heatmap, figure 8.6, of PCMO/Ta_2O_5 devices for ON/OFF-ratios of 2, 3 and 4.

The SET process, presented in figure 8.6 a) starts at around 3 V for pulses with a length of 100 ms. For short pulses around 1 µs no change in the resistance state could be observed for the investigated voltage range up to 4 V. Extrapolating the kinetic behaviour up to higher voltages, one could expect a first change in the resistive state for pulses of 1 µs around −4.6 V. Nevertheless, the devices cannot withstand such high voltages and would break.
For a given pulse length, the ON/OFF-ratio increases roughly by one by increasing the voltage by one volt. No clear trend that this change is dependent on the resistance state of the device, like it was observed for the PCMO/Al devices, can be observed for the PCMO/Ta_2O_5 devices. This behaviour can also be observed in the current transients, like it was shown for the PCMO/Al devices.
At −4 V the ON/OFF-ratio changes by 1 with every 1.5 order of magnitude change in pulse length. Figure 8.7 shows exemplary the current transients of the applied SET pulses for different pulse voltages a) and different pulse lengths b). Like for the exemplary RESET pulses of the PCMO/Al devices, see section 8.1, a clear trend can be seen. For the different pulse voltages, figure 8.7 a), the increase in the absolute normalised current is higher for higher voltages. The currents are normalised on the current value at the beginning of the SET pulse. Therefore, the normalised current is higher than 1 at the end of the SET pulse. All pulses have a length of 1 ms. The impact of the pulse time during the SET pulse can be seen in figure 8.7 b). Pulses with a length of 1 ms, 0.1 ms and 0.01 ms have been applied. It can be seen, that the current transients overlap for the given pulse length. This behaviour is also reflected in the kinetic measurements and can be observed for the SET current transients of all samples.

The RESET kinetics measured for the PCMO/Ta_2O_5 devices are shown in Figure 8.6 b). The RESET for these devices already starts at 2 V for pulses with a length of 100 ms, this is around 1 V lower compared to the SET process. For short pulses with a length of 1 µs, the RESET starts at around 3 V. This increase of the switching voltage is due to a decrease in pulse length of 5 orders of magnitude. This increase is comparable to the PCMO/Al devices. In contrast, the increase in ON/OFF-ratio with increasing applied voltage is lower for the SET process as for the RESET process for the PCMO/Ta_2O_5

devices. Figure 8.6 c) shows the RESET kinetics of the PCMO/T_2O_5 with the original colour scale up to an ON/OFF-ratio of 10. The thick line indicates an ON/OFF-ratio of 4, the former upper limit of the ON/OFF-ratio colour scale. It can be seen, that the max. reached ON/Off-ratio at 4 V with a pulse length of 100 ms is 7. The ON/OFF-ratio decreases by one with ever 1.5 order of magnitude decrease of the pulse time at 4 V. Furthermore, even for high ON/OFF-ratio the measured curves have the same slope.

The extracted contour lines are of the heatmap plot of the SET and RESET process are presented in figure 8.8. Here the absolute voltage is plotted on the x-axis. Therefore, the SET and RESET kinetics could be better compared to each other. It can be clearly seen, that the RESET process can reach higher ON/OFF-ratios at lower voltages and shorter pulses compared to the SET process. The difference between the SET and RESET process is around 1 V at an ON/OFF-ratio of 2. This difference increases with increasing ON/OFF-ratio. The difference of an ON/OFF-ratio of 3 occurs already around 1.3 V. This change in difference can be understood by the before described voltage drop difference for the SET and RESET process. While the resistance decreases during the SET process and thus the relative voltage drop across the device decreases, it increases during the RESET process, which causes the RESET process to accelerate itself.
Even stronger is the impact of the difference in pulse length. For an ON/OFF-ratio of 2 and 3, the time difference at the same voltage, 3 V and 3.5 V, is around 5 orders or magnitude in time. This is the whole presented time range. Nevertheless, the slope of the ON/OFF-ratio lines in the kinetic measurements is similar. Assuming, that the amount of oxygen vacancies that has to be moved between the PCMO and the Ta_2O_5 barrier to achieve a certain change in the ON/OFF-ratio is the same during SET and RESET and the overall voltage drop over the device is smaller in the LRS than in the HRS, there has to be another reason for the faster RESET kinetics. This reason could be a chemical gradient and the change in Gibbs free energy for the oxidation of the material. In principle this oxidation at the interface could be excluded due to the fact, that fully oxidised Ta_2O_5 is deposited on the PCMO. Nevertheless, we have seen in chapter 5 that the Ta_2O_5 seems to be slightly reduced at the interface of the PCMO. Therefore, the change in Gibbs free energy and a chemical gradient could be a possible explanation for the faster RESET kinetics.

8.3. PCMO/WO_3 switching kinetics

In this section, the kinetic measurements of PCMO/WO_3 devices will be presented. Figure 8.9 shows the measured ON/OFF-ratio of the PCMO/WO_3 devices with respect to the applied pulse voltage and pulse length.

The SET kinetics of the PCMO/WO_3 samples are measured for pulses between -1 V and -4.5 V and pulse lengths between 1 µs and 100 ms. The RESET kinetics are measured with pulses between 1 V and 4 V and pulse lengths between 1 µs and 100 ms

The SET process starts for pulses with a length of 100 ms at -3 V. For short pulses, 1 µs, the ON/OFF-ratio starts to change at -4 V. A change of 5 orders of magnitude in pulse time changes the switching voltage by 1 V. However, one must make a restriction here: This is only the case for an ON/OFF-ratio of 2. For higher ON/OFF-ratios the voltages seems to increase faster. For example for an ON/OFF-ratio of 3, the the voltage

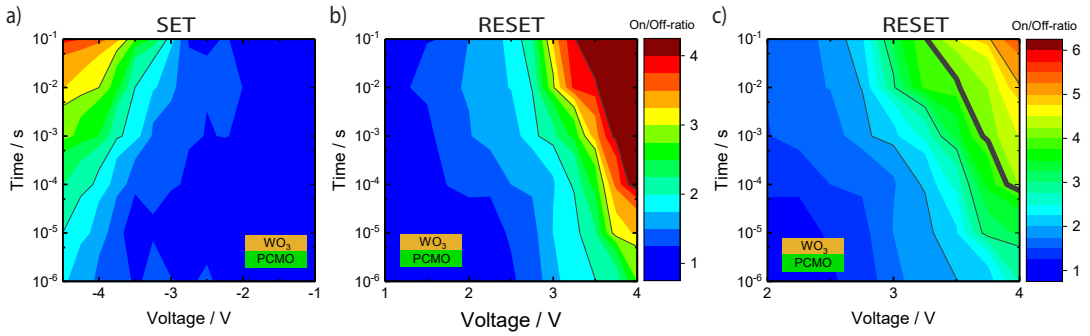

Figure 8.9.: Measurement of the SET (a) and RESET (b) kinetics of PCMO/WO_3 resistive switching devices. c) shows the RESET kinetics with an adapted colour scale to shows the possibilities of higher ON/OFF-ratios

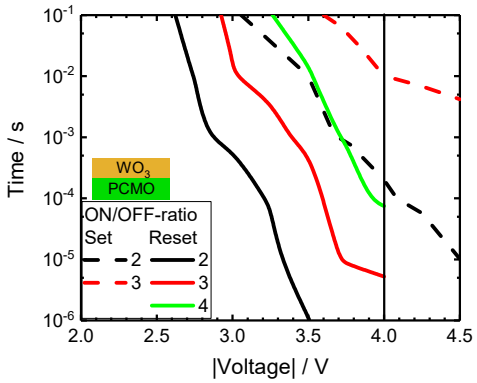

Figure 8.10.: Extracted contour lines of the heatmap, figure 8.9, of PCMO/WO_3 devices for ON/OFF-ratios of 2, 3 and 4.

increases by 1 for a change of 1.5 orders of magnitude in pulse length. Nevertheless, due to the limited voltage range that is measured, no generally statement for the increase of voltage by shortening the pulse length can be made. Also no visible trend that the change in ON/OFF-ratio with increasing voltages changes dependent on the ON/OFF-ratio could be seen.

The RESET process starts at 2.5 V for pulses with a length of 100 ms. This can be seen in figure 8.9 b). For shorter pulses this voltage increases up to 3 V. Nevertheless, an ON/OFF-ratio of 2 is reached at 2.6 V, 3.5 V for 100 ms,1 µs pulses, respectively. Higher ON/OFF-ratios during the RESET, 3 or 4, can already by reached at slightly higher voltages, 2.9 V or 3.3 V, respectively. Changing the pulse length, the ON/OFF-ratio decreases by 1 for every 1.5 order of magnitude time change in pulse length. Figure 8.9 c) shows the RESET kinetics of the PCMO/WO_3 devices between 2 V and 4 V with an adapted colour scale up to an ON/OFF-ratio of 6. It can be seen, that the max reachable ON/OFF-ratio at 4 V and a pulse length of 100 ms is around 5.5. The thick line represents an ON/OFF-ratio of 4. This was the upper limit of the colour scale in figure 8.9 b) for a better comparison of the kinetics.

The extracted ON/OFF-ratio contour lines of the kinetic measurements for the SET and

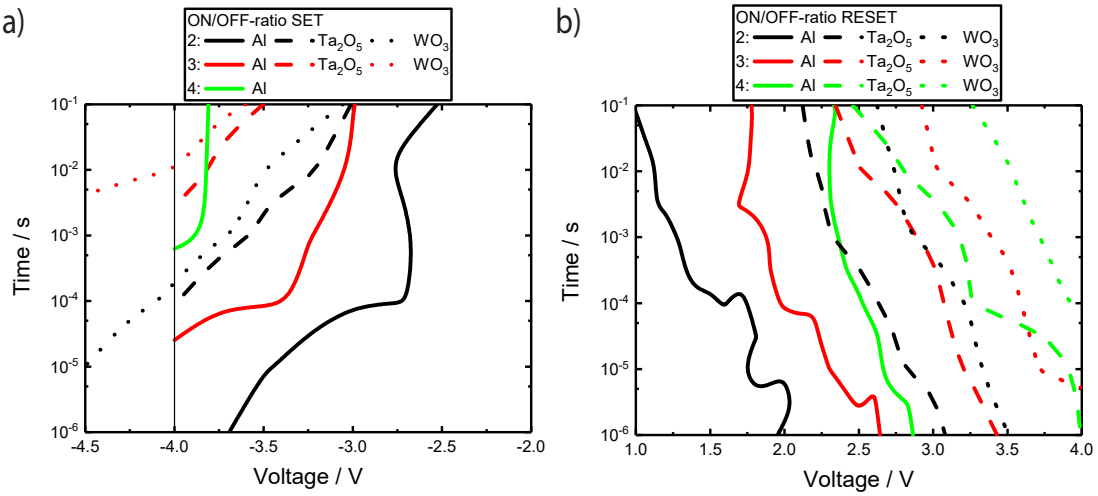

Figure 8.11.: Extracted contour lines of all three devices, PCMO/Al, PCMO/Ta_2O_5 and PCMO/WO_3.

RESET process of the PCMO/WO_3 devices can be seen in figure 8.10. The voltage/time behaviour of the SET process for different ON/OFF-ratios is the same and the extracted lines are parallel to each other. Nevertheless, the RESET process and the SET process show a different slope in the extracted ON/OFF-ratio lines. This can be clearly seen at an ON/OFF-ratio of two. For the RESET process it starts at 2.6 V for pulses of 100 ms and for the SET at −3.1 V for pulses of 100 ms. For pulses of 10 µs an ON/OFF-ratio of 2 can be reached at 3.4 V for the RESET process and at −4.5 V for the SET process. The voltage increase for the RESET process is around 0.8 V and for the SET process around 1.4 V. This is a difference of 0.6 V within 4 orders of magnitude in time. Furthermore, the spacing between the ON/OFF-ratio lines is also different for the SET and RESET process. The voltage difference between an ON/OFF-ratio of 2 and 3 is around 0.3 V for the RESET process and 0.6 V for the SET process at a pulse length of 100 ms.

8.4. Discussion of kinetics

In this section the SET and RESET kinetics of the PCMO devices will be discussed. First the kinetics of the PMCO devices in combination with Al, Ta_2O_5 and WO_3 will be compared to each other and the differences and similarities will be discussed. Additionally, the kinetics will be compared to kinetics of single crystalline PCMO devices in combination with YSZ. Afterwards, the switching kinetics of PCMO/Al devices as exemplary system will be compared to the switching kinetics of other resistive switching materials. During this, filamentary and area type resistive switching devices are taken into account.

8.4.1. Comparison of PCMO kinetics

Comparison of polycrystalline PCMO devices with different interface layer

In this section the kinetics of PCMO in combination with three different materials, Al, Ta_2O_5 and WO_3 will be compared to each other and discussed. Figure 8.11 shows the extracted ON/OFF-ratios of the SET and the RESET kinetic measurement for all three

Table 8.1.: Slopes of extracted ON/OFF-ratio lines of measured SET and RESET kinetics of PCMO/Al, PCMO/Ta_2O_5 and PCMO/WO_3 devices for different ON/OFF-ratios.

ON/OFF-ratio	PCMO/Al	PCMO/Ta_2O_5	PCMO/WO_3
SET			
2	3.3 (s/v)	2.8 (s/v)	2.9 (s/v)
3	3.3 (s/v)	2.9 (s/v)	2.6 (s/v)
RESET			
2	-3.9 (s/v)	-4.6 (s/v)	-5.1 (s/v)
3	-4.0 (s/v)	-4.4 (s/v)	-4.8 (s/v)
4	-7.1 (s/v)	-3.3 (s/v)	-4.8 (s/v)

devices. The solid lines represent the PCMO/Al devices, the dashed lines represent the PCMO/Ta_2O_5 devices and the dotted lines represent the PCMO/WO_3 devices. The different colours represents the different ON/OFF-ratios, 2 (black), 3 (red) and 4 (green).

Figure 8.11 a) shows the SET kinetics for the different devices. It can be seen, that the SET of the PCMO/Al devices starts at lowest voltage at $-2.5\,\mathrm{V}$ for pulses with a length of 100 ms and an ON/OFF-ratio of 4 can be reached for high voltages. This is not the case for both PCMO/oxide devices, Ta_2O_5 and WO_3. Even for high voltages no ON/OFF-ratio of 4 can be reached for this devices. The SET process also starts later compared to the PCMO/Al devices, at around $-3\,\mathrm{V}$ for an ON/OFF-ratio of 2. Nevertheless, it is worth mentioning that the difference between the PCMO/Ta_2O_5 and PCMO/WO_3 is small and also the extracted lines are parallel to each other. This means that the overall SET kinetic between these two devices are very similar. The SET voltages for the PCMO/WO_3 devices are slightly higher as the SET voltages for the PCMO/Ta_2O_5 devices. The slope of the PCMO/Al SET kinetics are very different from the PCMO/oxide devices. The increase of voltage for these devices is lower for decreasing pulse length. This can also be seen in in the fitted slopes of the extracted ON/OFF-ratios. The fitted slopes of the SET process are presented in table 8.1. The previously mentioned difference in slope between the PCMO/Al and the PCMO/Ta_2O_5, PCMO/WO_3 is also visible in the fitted slopes. The difference in slope is around $0.4\,s/v$.

The extracted ON/OFF-ratios for the RESET process for all three PCMO based devices in combination with Al, Ta_2O_5 and WO_3 can be seen in figure 8.11 b). Here, too, it is noticeable that the RESET of the PCMO/Al devices starts first. An ON/OFF-ratio of 2 during the RESET of the PCMO/Al for pulses of a length of 100 ms can be reached at 1 V. For the PCMO/Ta_2O_5 devices, this can only be reached at around 2.5 V. At this voltage, the PCMO/Al devices have already reached an ON/OFF-ratio of 4. Unlike the SET process, the spacing between the PCMO/Ta_2O_5 devices and the PCMO/WO_3 devices for a defined ON/OFF-ratio is around 1 V for all presented ON/OFF-ratios. The PCMO/WO_3 needs higher voltages than the other devices. Nevertheless, the RESET voltages of the PCMO/WO_3 devices are still around 0.5 V lower as for the SET process. Beside this, the change of voltage with changing pulse length is also worth mention here. In contrast to the SET process, the slope of the different devices is around 4 for all devices, see lower part of table 8.1. Moreover, the slope of the PCMO/WO_3 is on average the largest. This means, that the voltage changes the least for the change in

pulse length, if one disregards an ON/OFF-ratio of 4 of the PCMO/Al devices. Here the slope is even higher.

Regarding to Menzel et al. [211], the voltage increment ΔV_{10x} that is needed to accelerate the switching process by a factor 10 in time can be given by

$$\Delta V_{10x} = -\frac{1}{m} \ln(10) \tag{8.1}$$

with m equals the slope of the switching kinetics. For ion migration m_{mig} was derived from the Mott-Gurney law for ion hopping:

$$j_{hop} = 2zecaf \exp\left(-\frac{\Delta W_{hop,0}}{k_B T}\right) \sinh\left(\frac{aze}{2k_B T} E\right). \tag{8.2}$$

From this Menzel et al. [211] extracted the slope m_{mig} to

$$m_{\mathrm{mig}} = -\frac{aze}{2k_B T w} \tag{8.3}$$

with a the hopping distance of the ions, z the charge number, e the elementary charge, k_{B} the Boltzmann constant, T the temperature and w the distance of the electric field drop, $E = {}^{V}/_{w}$. The typical values of the hopping distance a are 0.2 nm-0.5 nm [211]. The hopping distance is assumed to 0.4 nm. From the before determined slopes, table 8.1 and equation 8.3, the field drop distance w can be calculated. The calculated field drop distance can be found in table 8.2. One has to mention, that this field drop distance is only based on the assumption that the switching process is only based field driven ion movement and no thermal acceleration or other effects. Furthermore, the thickness that is calculated is always a combination of the field drop across the oxide layer and the PCMO layer. For the PCMO/Al devices, the depletion zone has also be taken into account. Nevertheless, one can use this field drop distance to make further assumptions. For the PCMO/Al devices, the field drop distance is calculated to $\sim$4.8 nm and $\sim$4.1 nm for the SET and the RESET, respectively. In literature, the thickness of a native Al_2O_3 layer on Al is determined between 2 nm - 5 nm [212, 213]. Most of these studies are done in atmosphere and not in combination with PCMO. Therefore, one can estimate that the native Al_2O_3 layer is expected to be thinner. Unfortunately, a clear statement about the thickness of the native Al_2O_3 layer cannot be made here. The field drop distance for the PCMO/Ta_2O_5 devices is calculated to $\sim$5.6 nm and $\sim$3.9 nm for the SET and the RESET, respectively. For the PCMO/WO_3 devices it is calculated to $\sim$5.6 nm and $\sim$3.9 nm for the SET and RESET, respectively. It is noticeable that field drop distances for the PCMO/Ta_2O_5 and the PCMO/WO_3 devices is smaller than the thickness of the respective oxide layer. Furthermore, does the field drop distance change significantly between the SET and RESET process for these devices while for PCMO/Al it is relatively constant. A possible explanation for the change in the field drop distance could be that the oxidation state of the oxide layer changes during the SET and RESET process and the main field drop happens over the more oxidised part of the layer. Nevertheless, this change can only be partly understood.

To discuss the kinetics of the different devices even further, one has to think about the limiting process of the kinetics. Due to the fact, that the resistive change is induced by the exchange of oxygen vacancies/oxygen between the PCMO and the metal/oxide

Table 8.2.: Field drop distance inside the devices, calculated from the SET and RESET kinetic slopes, table 8.1 and equation 8.3.

Field drop distance w		
Al	Ta_2O_3	WO_3
SET		
$\sim 4.8\,nm$	$\sim 5.6\,nm$	$\sim 5.6\,nm$
RESET		
$\sim 4.1\,nm$	$\sim 3.9\,nm$	$\sim 3.2\,nm$

layer, one can think about two limiting processes, the movement of oxygen inside the metal/oxide layer, and the exchange of oxygen/oxygen vacancies between the PCMO and the metal/oxide layer. Comparing the diffusion coefficients of oxygen of the three different oxides, Al_2O_3 [214, 215], Ta_2O_5 [215], and WO_3 [216], one can see, that the diffusion coefficient of oxygen is the lowest for the Al_2O_3, two orders of magnitude lower compared to the Ta_2O_5 [215]. This would lead to the conclusion, if the movement of oxygen inside the metal/oxide layer would be the limiting process of the kinetics, that the PCMO/Al devices, should have the slowest kinetics. However, the data show exactly the opposite trend. The PCMO/Al devices shows the fastest kinetics compared to the PCMO/Ta_2O_5 and the PCMO/WO_3 devices. This is a hint, that the movement of oxygen inside the interface layer is not the limiting process of the shown kinetics.
The second possible process for limiting the switching kinetics is the exchange of oxygen/oxygen vacancies between the PCMO and the oxide layer across the interface. Unfortunately, only consideration on the different exchange properties can be made at this point. Due to the fact, that the Al_2O_3 is a native oxide at the interface, one can consider, that it is less dense and has a lower barrier height at the interface compared to the directly deposited oxides Ta_2O_5 and WO_3. Comparing the work functions of Al_2O_3 [136], Ta_2O_5 [183], and WO_3 [217], it can be seen, that all the work functions are in the same order of magnitude around 5 eV for directly deposited oxides. Furthermore, it has to be taken into account that the native AlO_x is way thinner than the Ta_2O_5 and the WO_3 layer. This means that the field inside the AlO_x is larger as the field in the other oxides. this leads to the faster switching dynamics. What has not been taken into account here, however, is the additional depletion zone in the PCMO. This depletion zone also influences the switching kinetics. Nevertheless, these are simple considerations and have not been experimentally proven yet.

In conclusion one can say, that the PCMO/Al devices show the fastest switching behaviour and also need the smallest voltages during the SET and RESET process compared to the PCMO/Ta_2O_5 and the PCMO/WO_3 devices. Additionally, the PCMO/Al devices show the highest ON/OFF-ratio during the SET and RESET kinetics for the investigated time and voltage range. Therefore, the PCMO/Al devices will be used as examples for a comparison of the polycrystalline PCMO devices to single crystalline PCMO devices. They will also be used in the following to compare the PCMO kinetics to switching kinetics of different materials and also to filamentary switching systems.

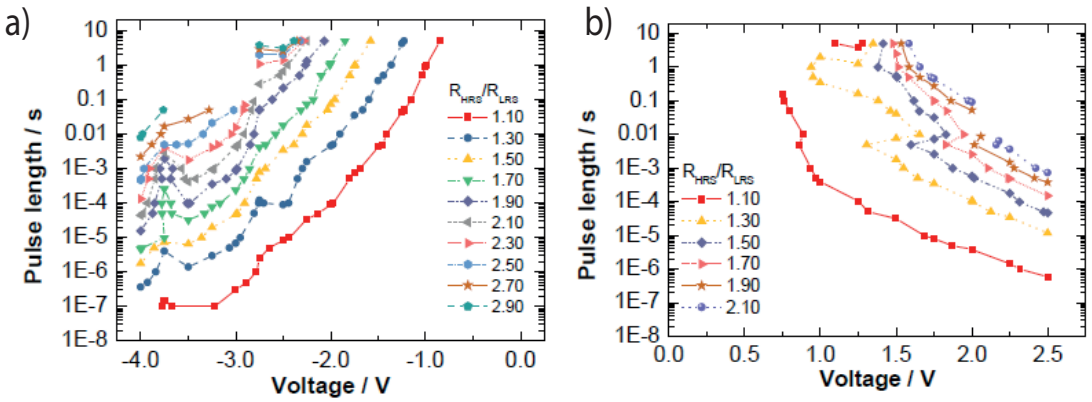

Figure 8.12.: Measurement of SET a) and RESET b) kinetics of single crystalline PCMO devices grown on SRO in combination with 2.4 nm YSZ. Taken and adapted from [34]

Comparison of single- and polycrystalline PCMO devices

This is work is focusing on the resistive switching properties of polycrystalline PMCO resistive switching devices. For a better understanding and classification of the switching kinetics of the polycrystalline devices, these are now compared with the kinetics of single crystalline PCMO devices, measured by Arndt et al [34]. These PCMO devices have the following device stack: STO/SRO/PCMO/YZS/Rh. Additonall information regarding the growth of single crystalline PCMO devices can be found elsewhere [34].

Figure 8.12 shows the extracted ON/OFF-ratio contour lines of the SET and RESET kinetics measured by Aarndt et al. [34]. The ON/OFF-ratios of the SET process are presented in figure 8.12 a). The lines present an ON/OFF-ratio between 1.10 an 2.90 in steps of 0.2. It can be seen, comparing the 2.1 line of the single crystalline sample to the measured ON/OFF-ratios of the polycrystalline PCMO/Al devices, see figure 8.5, that the starting voltage of the change in ON/OFF-ratio differs. For the 100 ms pulses the RESET for the single crystalline devices reaches an ON/OFF-ratio of 2 at around 3 V. Beside this the polycrystalline PCMO/Al samples reaches an ON/OFF-ratio of 2 at −2.5 V. This is 0.5 V lower. But more worth mentioning is the different change of voltage with changing pulse length. The single crystalline PCMO devices do not reach an ON/OFF-ratio of 2.1 for pulses of a length of 1 µs for the investigated voltage range of Arndt et al. [34]. The PCMO/Al devices on the other hand reach an ON/OFF-ratio of 2 at −3.7 V for pulses with a length of 1 µs. Additionally the maximal reachable ON/OFF-ratio during the SET process of the single crystalline PCMO devices shown by Arndt et al. [34], is 2.9 for long and high pulses. For example at a pulse length of around 100 ms, a voltage of −3.75 V is needed to reach this ON/OFF-ratio. This voltages and the voltage time dependence differ strongly from the PCMO/Al devices as described above, but compared to the PCMO/Ta_2O_5 and PCMO/WO_3 devices, the voltages and also the voltage time dependence of the single crystalline PCMO devices is in the same order of magnitude. A possible explanation of this is the fact, that YSZ is also an directly deposited oxide like Ta_2O_5 and WO_3.

The RESET process of the single crystalline PCMO/YSZ devices measured by Arndt et al. [34] can be seen in figure 8.12 b). The measured voltage regime is between 0.75 V and

2.5 V. The plotted ON/OFF-ratio is between 1.10 and 2.10 in steps of 0.2. Comparing again the 2.10 ON/OFF-ratio of the single crystalline devices with the 2.0 ON/OFF-ratio of the polycrystalline PCMO devices. The ON/OFF-ratio of 2.1 of the single crystalline PCMO devices is reached with pulses of 100 ms at 2.0 V. This is around 1 V higher compared to the PCMO/Al devices but in the same voltage range like the PCMO/Ta_2O_5 devices and even around 0.5 V lower compared to the PCMO/WO_3, compare figure 8.12 b) and figure 8.11 b). At 2.5 V, the highest investigated voltage by Arndt et al. [34], an ON/OFF-ratio of 2.1 can be reached with pulses of a length of 1 ms. At this pulse length a pulse height of around 1.7 V for the PCMO/Al devices is needed. The PCMO/Ta_2O_5 devices need again a comparable voltage of 2.3 V for the required ON/OFF-ratio of 2 for the pulse length of 1 ms as the single crystaline PCMO devices. The PCMO/WO_3 devices need even higher voltages for the RESET process. An ON/OFF-ratio of two can be reached for the PCMO/WO_3 devices for pulses of 100 ms with voltages of 2.6 V. This is even higher than the investigated voltage range of Arndt et al. [34] for the single crystalline PCMO devices.

In conclusion one can say, that the single and polycrystalline SET and RESET kinetics are not very different. The SET and RESET process of the single crystalline PCMO/YSZ devices is comparable to the SET and RESET process of the polycrystalline PCMO/Ta_2O_5. Therefore, no statement can be made about the influence of the crystallinity of the PCMO layer on the device kinetics yet.

8.4.2. PCMO kinetics in comparison with other systems

To get a better overview of the kinetics of different materials, the recorded PCMO/Al kinetic data will now be compared with other materials.

A detailed explanation of the SET kinetic measurement of the filamentary switching devices will not be given here. This explanation can be found elsewhere [3, 221]. Only a brief explanation of the main differences will be given here. Due to the fact, that the SET of filamentary switching systems occurs with an abrupt change in the current no real gradual change of the resistance an the ON/OFF-ratio can be observed. Furthermore, due to the heating of the device during the SET process, the SET time is defined as time until a current jump in the current transient occurs. For most filamentary switching systems, the SET kinetics are defined as a specific ON/OFF-ratio and the voltage that is at least needed for a specific pulse length to reach this ON/OFF-ratio. Due to the stochastic SET process of theses devices, due to different heating and filament growth. Furthermore, the SET kinetics of filamentary switching systems show a non-linear behaviour due to the heating of the filament [29, 174].

In figure 8.13 kinetic measurements of different resistive switching devices with different materials and different switching behaviours, namely filamentary and area type, are shown. Different filamentary switching systems are shown like: STO/Al [3], STO/PT [218], STO/HfO_2 [218], Ta/TaO_x [219] and TiO_x/Al_2O_3 [220]. Beside this two different area type resistive switching materials are shown, the PCMO/Al devices and TiO_x/Al_2O_3 [220] devices. It can be seen, that the different materials all switch at different voltages. The Ta/TaO_x [219] devices already switch at very low voltages below 1 V, followed by the filamentary switching TiO_x/Al_2O_3 [220] devices. Comparing all filamentary switch-

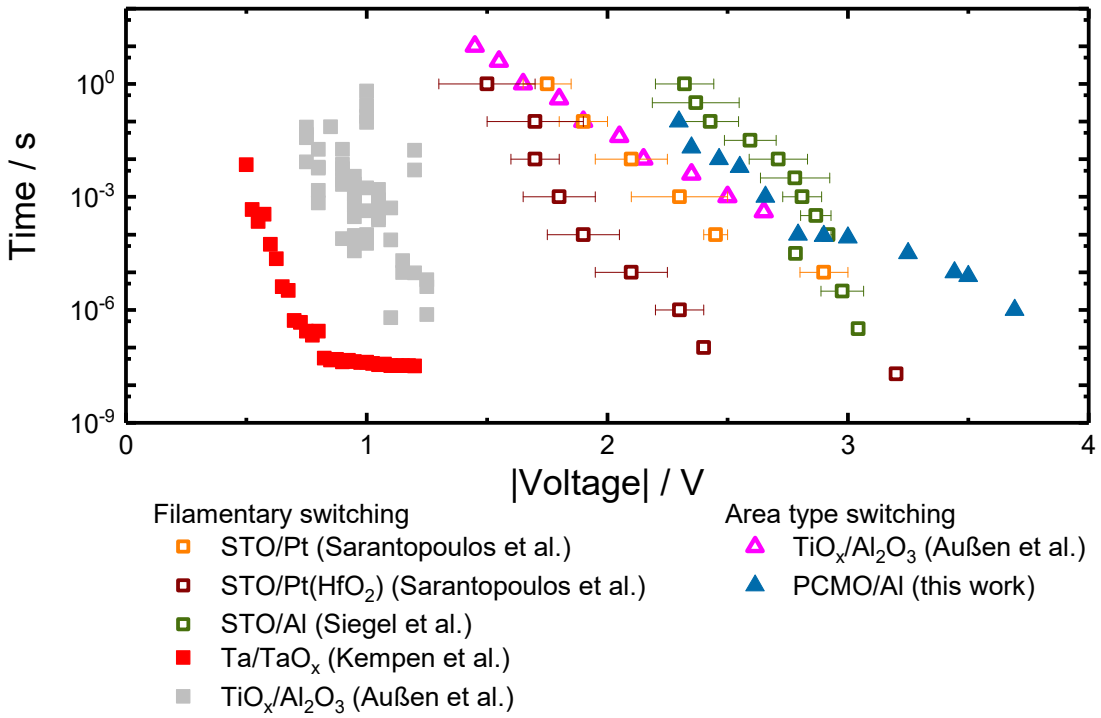

Figure 8.13.: SET kinetic comparison of different materials and switching types to place the SET kinetics of PCMO/Al and other PCMO based devices in an overall picture. STO/Al [3], STO/Pt [218], STO/HfO_2 [218], Ta/TaO_x [219], TiO_x/Al_2O_3 [220].

ing devices to each other, it can be seen, that they all have the same slope for longer pulses down to a pulse length of 1 µs. For even slower pulses the increase in voltages with decreasing pulse length increases. This can be clear seen for the Ta/TaO_x [219] and STO/HfO_2 [218] devices.

For the area type resistive switching SET kinetic measurements, it can be seen, that the switching voltages of the PCMO/Al devices of this work are slightly higher for given pulse lengths as the TiO_x/Al_2O_3 [220] devices. Nevertheless, the slope is the same for both devices. This becomes particularly clear in the area where the two measurement series overlap.

Comparing now the area type resistive switching devices and the filamentary switching devices, it can be seen that the switching voltage of the area type resistive switching devices is not necessarily larger compared to the filamentary switching devices as can be seen for the STO devices. Industrial used filamentary switching devices such as the Ta/Ta_2O_5 or the HfO_2 switch at way lower voltages and shorter pulse times. Also, the change of the voltage with changing pulse length is lower for filamentary switching systems compared to area type resistive switching systems. This could be correlated by the lack of Joule heating of the devices, which Menzel et al. [42] simulated for the area type resistive switching devices.

In conclusion one can say, that the area type resistive switching devices compared to filamentary type resistive switching devices need higher voltages . The slope of the

switching kinetics of these devices is also lower compared to typical filamentary switching systems as the Ta/Ta_2O_5 or the HfO_2.

8.5. Conclusion of switching kinetics

In summary, the PCMO/Al devices shows the fastest switching kinetics compared to the investigated PCMO/Ta_2O_5 and PCMO/WO_3 devices. In order to achieve the same result, lower voltages and lower pulse times were required in these devices. It is worth mentioning that the SET kinetics of the PCMO/Ta_2O_5 and PCMO/WO_3 devices have a similar behaviour, this means similar pulse voltages and pulse lengths result in a similar change in the device state. However, they differ greatly in the RESET process. Here, the PCMO/Ta_2O_5 devices were much faster and switched at much lower voltages. The analysis of the change of pulse length with changing voltage/ the slope of the kinetics, lead to the point, that field drop distance is the smallest for the Al during the SET process, but the largest during the RESET process. The field drop distance of the PCMO/Al devices changes the less compared to the other investigated devices. This investigation only considers the field driven ion migration and neglects heating or other effects that influences the switching. Therefore, this result can only be an indication for the field drop distance.
Beside this, the limiting process of the kinetics was discussed and it was concluded that the exchange of oxygen vacancies between the PCMO and the metal oxide layer should be the limiting process.

Comparing the polycrystalline PCMO samples to single crystalline PCMO samples in combination with YSZ from [34] one can see, that the switching of the polycrystalline PCMO sample in combination with Al shows a faster switching kinetic. A conclusive explaination for this behaviour can not be given here.

Lastly, the PCMO/Al kinetic behaviour was compared with the switching behaviour of various area type and filamentary switching devices. It could be seen, that the slope of the kinetic of the area type switching devices is lower compared to the filamentary switching devices. This behaviour was assigned to the Joule heating that happens in the filamentary switching devices. Typical filamentary switching devices also switch at lower voltages as the area type switching systems.

9. Neuromorphic Applications

In chapter 8 it was shown, that the resistance change of the PCMO based memristive devices depends on the applied pulse, height and length. Before it was already shown that multilevel switching is possible for these devices. To prove that the devices are suitable for neuromorphic computing applications Long Term Potentiation (LTP) and Long Term Depression (LTD) as well as Spike Timing Dependent Plasticity (STDP) measurements are performed and shown in this chapter. Furthermore, the LTP and LTD measurements are used as input for the synaptic weight change for a neural network simulations to investigate a possible use of the devices as weights in artificial neural networks (ANN). *The simulations are perforemd by Sebastian Siegel.*

9.1. Long Term Potentiation / Depression

Parts of this section are published in [1].

During Long Term Potentiation (LTP)/Long Term Depression (LTD) measurements, the device state is changed gradually by the multiple application of a single pulse without bringing the device back into a predefined state. For LTP/LTD it is important to choose the voltage of the pulse such that it does not change the device state completely within one single pulse between the HRS and the LRS. After every switching pulse, that changes the device state slightly, a read out pulse with $-0.3\,\mathrm{V}$ and $1\,\mathrm{ms}$ is done. At this voltage, the device state is not changed by the pulse. Different voltages are used for PCMO/Al, PCMO/Ta_2O_5 , and PCMO/WO_3 devices. All used switching pulses have a length of $100\,\mu\mathrm{s}$.

Figure 9.1 a) shows the LTP/LTD measurement of the PCMO/Al devices for different potentiation and depression voltages. Here, the resistance of the device is plotted against the number of the applied switching pulse. The LTP pulses are ordered in the

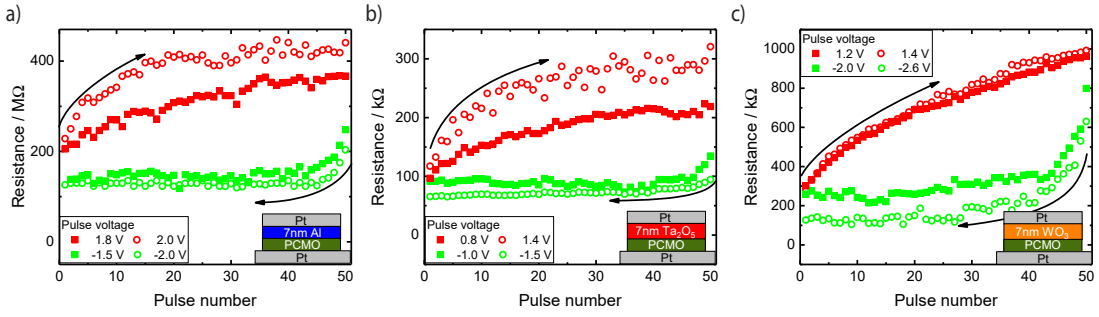

Figure 9.1.: Long Term Potentiation (LTP) and Long Term Depression (LTD) measurement of PCMO in combination with a) Al, b) Ta_2O_5 , and c) WO_3 for different potentiation and depression voltages. Adapted from [1].

opposite direction pulse number 50 is the first pulse that is applied to the device and pulse number one the last one this is the case for all different devices. The black arrow indicates the measurement direction. The depression of the PCMO/Al devices is done with 1.8 V and 2.0 V. For the potentiation −1.5 V and −2.0 V are used. For the depression it can be seen, that the resistance increases with increasing pulse number in a gradual manner. Furthermore, it can be seen, that for the higher depression voltage the increase is larger compared to the smaller depression voltage. This is especially visible within the first depression pulses. The depression measurements with higher depression voltage 2.0 V saturates at around 25 pulses and increases only slightly afterwards. The increase of resistance of the depression measurements with the lower depression voltages of 1.8 V saturates at higher pulse numbers and at lower resistance values. The potentiation measurement shows a similar behaviour. For the higher potentiation voltage −2.0 V the decrease of the resistance is also larger for the first pulses of the LTP measurement than for the lower potentiation voltage −1.5 V. Unlike for the LTD measurement, no difference for the resistance after 50 pulses can be seen with the LTP measurement. The resistance after 50 pulses is the same for −1.5 V and −2.0 V. Furthermore, it can be seen that the decrease of the resistance within the first pulses is larger as the increase of the resistance within the first pulses of the LTD measurements.

The LTP/LTD measurements of the PCMO/Ta_2O_5 devices is shown in figure 9.1 b). The depression measurement behaves in a similar way as the LTD measurement of the PCMO/Al devices. The increase of the resistance for the first pulses is larger for higher voltages as well as the resistance change at the end of the measurement. Furthermore, a start of a saturation process for both voltages, 0.8 V and 1.4 V Additionally a slight offset happens. Nevertheless, a slight increase of the resistance of the device can also be seen after 50 pulses. The LTP measurements are performed with −1 V and −1.5 V. The largest decrease in resistance occurs at the beginning of the measurement. Larger voltages also lead to a larger decrease of the resistance. The resistance saturates within the first few pulses for the lower and the higher pulses. Afterwards, the resistance is stable and no further changes occur.

The PCMO/WO_3 devices are presented in figure 9.1 c). Here also the gradual increase of the resistance during the depression can be seen. The depression is performed with 1.2 V and 1.4 V. The increase of the resistance within the measured number of pulses is the same for both investigated depression voltages. Furthermore, no larger difference in the resistance change between two measurement points comparing the beginning and the end of the measurement like it was observed for the PCMO/Al and PCMO/Ta_2O_5 devices. This means that the resistance change is constant over the whole measurement range and the resistance increases almost linearly. The potentiation measurements shows a slightly different behaviour than the depression measurement. The decrease of resistance is larger in the beginning of the measurement and its seems to saturate after several pulses. Furthermore, higher voltages lead to a lower resistance value. Additionally, the resistance curve is less linear than in the depression measurement.

Comparing all three different devices, PCMO/Al, PCMO/Ta_2O_5 , and PCMO/WO_3 devices, one can see, that for all devices, higher pulse voltages lead to a larger resistance change within one pulse and within the whole measurement. For the PCMO/Al and the PCMO/Ta_2O_5 devices, the increase in resistance at the beginning of the depression

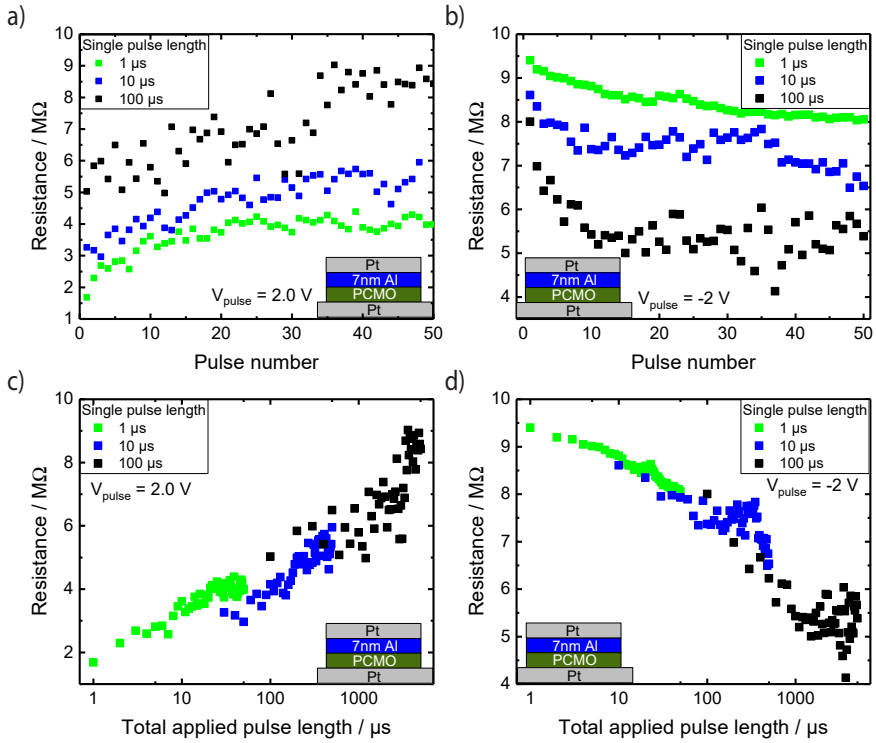

Figure 9.2.: Time dependence of resistance change of PCMO/Al devices. a) LTD and b) LTP measurement with 2.0 V pulses and pulse lengths of 100 µs, 10 µs, and 1 µs. Resistance of the c) LTP measurement and d) LTD measurement plotted against the total applied pulse length for pulses of different length.

measurement is the larger than the increase at the end of the measurement. The situation is different for PCMO/WO_3 devices. The change in resistance is almost linear for the whole measurement range. The linearity is favourable for devices used in ANNs due to the fact that a single pulse would always lead to the same resistance change. With non-linear resistance pulse curves, different pulses would lead to different resistance changes, which would have to be compensated for by the network. Furthermore, the resistance saturates for the PCMO/Al and PCMO/Ta_2O_5 devices and not for the PCMO/WO_3 devices. For the LTP measurement, the decrease of resistance is for all three investigated device stacks is the largest for the first few pulses. Afterwards, the resistance saturates for all three device stack. Furthermore, the difference for the different investigated voltages during the LTP measurements is smaller than the impact of different voltages for the LTD measurements.

9.1.1. Resistance-Time-Dependence

In section 9.1 it is shown that the increase/decrease in resistance during the LTP/LTD measurement depends on the applied voltages. On the other hand, in chapter 8 it is demonstrated that the resistance change within a pulse is not only dependent on the pulse voltage but also on the pulse length. Therefore, the impact of the pulse length on the LTP/LTD measurement will be investigated in the following.

Figure 9.2 a) shows the LTD measurement of the PCMO/Al devices with pulses of 2.0 V

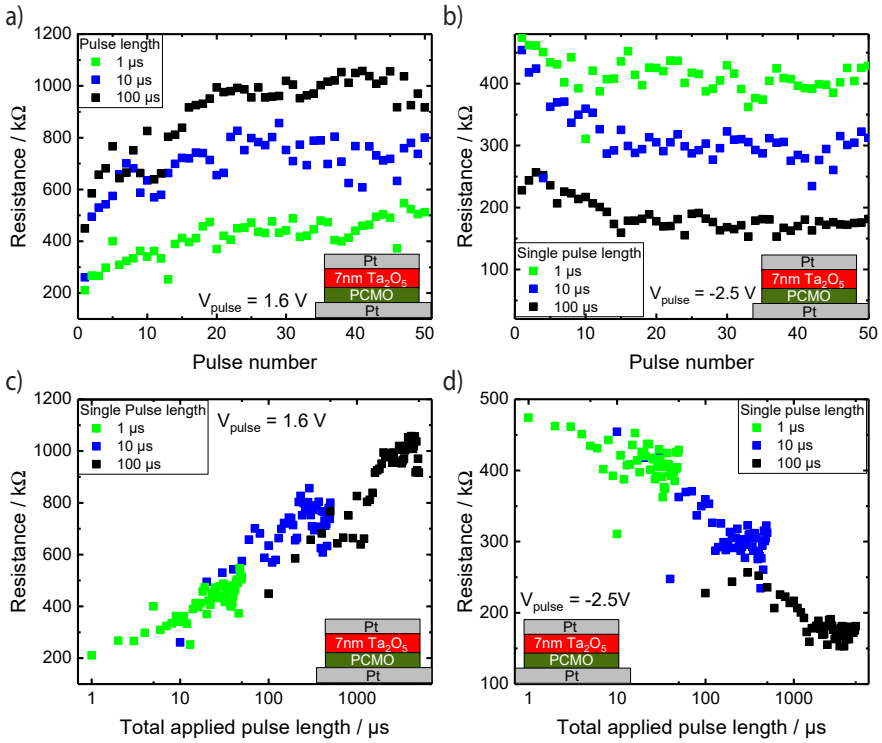

Figure 9.3.: Time dependence of resistance change of PCMO/Ta_2O_5 devices. a) LTD and b) LTP measurement with 1.6 V/−2.5 V pulses and pulse lengths of 100 µs, 10 µs, and 1 µs. Resistance of the c) LTP measurement and d) LTD measurement plotted against the total applied pulse length for pulses of different length.

and different pulse lengths, 100 µs, 10 µs, and 1 µs. The increase of the resistance is larger for longer pulses, as expected from the switching kinetics in chapter 8. For the higher pulse voltages, the increase of the resistance is the largest within the first cycles and the saturation value differs. Moreover, the variation of the resistance increases with increasing pulse length. The LTP measurement of the PCMO/Al devices with a pulse voltage of −2.0 V and 100 µs, 10 µs, and 1 µs pulse length is shown in figure 9.2 b). As for the LTD measurement, the resistance change within one pulse is larger for the longer pulses and the resistance after the LTP measurement also depends on the pulse length. The resistance is lower at the end for longer pulses. Furthermore, a saturation of the resistance occurs during the LTP measurement. Figure 9.2 c) and d) shows the resistance of the the LTP/LTD measurement plotted against the total applied pulse length, respectively. The x-axis shows the accumulated pulse length of already applied pulses. For the LTP as well as for the LTD measurement the resistance changes linearly with the total applied pulse length in the semi-logarithmic plot. This means that the application of pulses is cumulative with respect to the total pulse length. For example, the applications of 10 1 µs pulses changes the resistance of the PCMO/Al devices in the same way as the application of a single 10 µs pulse. This is true for both the LTP and LTD measurements.

The time dependence of the LTD measurement of the PCMO/Ta_2O_5 devices with pulses of 1.6 V and pulse lengths of 100 µs, 10 µs, and 1 µs is presented in figure 9.3 a). The increase in resistance is larger for longer pulses. Additionally, the resistance at which the resistance saturates is higher for longer pulses. Furthermore, the main increase of

the resistance happens within the first cycles. Unlike the PCMO/Al samples, no larger variability with longer pulses can be observed. The same behaviour shows the LTD measurement with −2.5 V and pulse lengths of 100 µs, 10 µs, and 1 µs, shown in figure 9.3 b). The decrease of the resistance happens for all pulse lengths within the first few pulses. For the 1 µs and 10 µs pulses it can be seen clearly that the increase of the resistance in the beginning differs and the saturation of the LTP measurement happens at a higher pulse number. The 100 µs LTP measurement shows a saturation at even higher pulse numbers. The resistance does not change further after 20 pulses and stays constant within the next 30 pulses. This can be explained by the fact that the minimum resistance of the LRS has been reached and no further reduction of the resistance is possible. Plotting the resistance of the LTP/LTD measurement against the total applied pulse length, it can be seen that the resistance change is linear for the LTP/LTD measurement within the total applied pulse length in the semi-logarithmic plot, figure 9.3 c) and d), respectively. This means, that for the PCMO/Ta_2O_5 devices the resistance change is also cumulative with respect to the pulse length as it was observed for the PCMO/Al devices.

One can conclude that the resistance change of the PCMO/Al and the PCMO/Ta_2O_5 devices within the LTP/LTD measurement depends not only on the voltage of the applied pulse but also on the pulse length as already shown for single pulses in chapter 8. The fact that the change in resistance depends for the different pulse lengths only on the total applied pulse length and not on the number of the in advance applied pulses makes the devices even more suitable for neuromorphic applications. This is due to the fact that a defined resistance change can be achieved not only by different pulse voltages, but also by the application of a different pulse length. This offers the opportunity to tune the applied pulse in voltage and length to the given resistance value and the expected resistance change.

9.2. Spike Timing Dependent Plasticity

Parts of this section are published in [1].

As already mention in chapter 2, spiking neural networks uses the spike timing of pulses to update the values of the network, namely spike timing dependent plasticity (STDP). Therefore, the time difference between two spikes, the pre- and post-synaptic spike, is crucial. The PCMO devices represent the synapses. Two pulses are applied, one to the top and one to the bottom electrode of the device with a certain time difference. The pulse that is applied to the top electrode will be referred to as the pre-synaptic spike and the pulse that is applied to the bottom electrode will be referred to as the post-synaptic spike. These pulses overlap at the device and depending on the time difference the voltage drop across the device is different and changes the resistance in a different way. Figure 9.4 a) shows a sketch of the applied pulses on the top (blue) and on the bottom electrode (red). The measurements are performed with the *ArC ONE* from *ArC INSTRUMENTS*.

The change of conductance of the PCMO/Al device plotted against the time delay between pre- and the pos-synaptic spike can be seen in figure 9.4 b). The change in conductance is largest for small time delays between the pre- and the post-synaptic spike

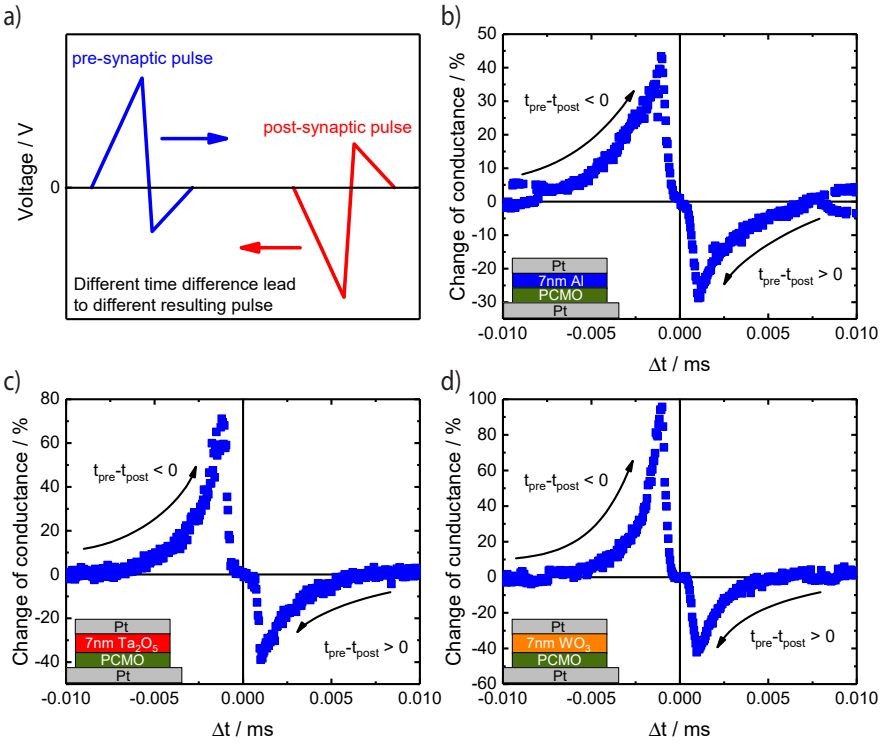

Figure 9.4.: a) Schematic of the applied pulses on the top and bottom electrode. b), c), and d) Change of conductance plotted against the time difference between the pre- and the post-synaptic spike for the PCMO/Al, PCMO/Ta_2O_5 , and PCMO/WO_3 , respectively.

and decreases with increasing time delay (Δt). Furthermore, it is important which pulse comes first. It can be seen that if the pre-synaptic spike reaches the device before the post-synaptic spike ($\Delta t < 0$) the conductance change is positive and if the pre-synaptic spike reaches device after the post-synaptic spike ($\Delta t > 0$) the conductance change is negative. Furthermore, it can be seen the maximum increase in conductance is around twice as high as the maximum decrease in conductance.

The STDP measurement of the PCMO/Ta_2O_5 and the PCMO/WO_3 devices can be in figure 9.4 c) and d). The increase/decrease of conductance is the largest for small time delays between the pre- and the post-synaptic spike and decreases with increasing time delay (Δt). Also, if the pre-synaptic spike reaches the device before the post-synaptic spike ($\Delta t < 0$) the conductance change is positive and if the pre-synaptic spike reaches device after the post-synaptic spike ($\Delta t > 0$) the conductance change is negative for the PCMO/Ta_2O_5 and PCMO/WO_3 devices as for the PCMO/Al devices. Furthermore, the increase of conductance is also twice as high as the decrease of conductance for the PCMO/Ta_2O_5 and the PCMO/WO_3 devices.

Comparing all three devices, PCMO/Al, PCMO/Ta_2O_5 , and PCMO/WO_3 devices, it can be seen that the overall behaviour for all three devices during the STDP measurement is the same. Nevertheless, the STDP curve of the PCMO/Al devices is more symmetric comparing the increase and decrease in conductance than for the PCMO/Ta_2O_5 and the PCMO/WO_3 devices. The PCMO/WO_3 devices show a clear asymmetry between the

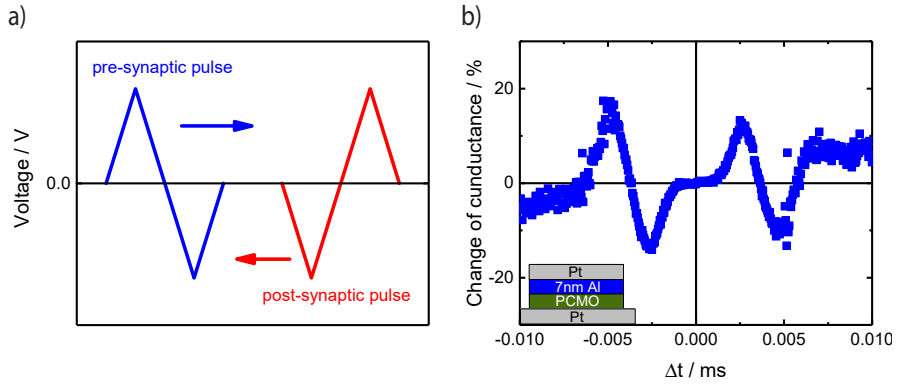

Figure 9.5.: Impact of different pulse shape on the device response during a STDP measurement. a) Pulse scheme that is used during the STDP measurement. b) Change of conducatance depending on the time difference of the two pulses shown in a).

increase and decrease of the conductance.

Furthermore, the impact of the applied pulse shape was investigated with the PCMO/Al devices. figure 9.5 a) shows a schematic of a different applied pulse shape. Figure 9.5 b) shows the resulting change in the conductance for the used pulses during the STDP measurement. The single peak, that was seen at around $\Delta t = 0$ in figure 9.4 b) is not visible anymore. Two peaks can be seen instead. These two peaks are shifted into the positive and the negative delay (Δt) region. This symmetry of the response of the device during the STDP measurement can be understood by the symmetry of the pulses that are applied to the device. They add up and the maximum voltage is not reached around zero time delay but at a time delay of half the pulse length.

In conclusion, the pulse shape can be used to tune the device response during a certain time delay. This makes the devices even more flexible and the pulse shape can be used if it is for example not possible to apply the post-synaptic pulse before the pre-synaptic pulse, due to some circuit requirements. Strictly speaking, the STDP measurements shown here are not real STDP measurements, as there are no pulses separated in time, but the superposition of the pulses is used to generate a corresponding change in the resistance of the devices.

9.3. MNIST pattern recognition

The simulations presented in this section are performed by Sebastian Siegel based on the data shown above. The presentation of the simulation results serves to complete the data of the properties of the PCMO-based memory cells for a neural network. Therefore, only the results of the network simulation and a brief introduction will be given here. A detailed explanation of the simulation, the fitting and the results can be found at [1].

9.3.1. Description of network and algorithm

To investigate the possibility to use the PCMO based devices as synapses in a multilayer perceptron network and to investigate the influences of different pulse voltages and pulse lengths, the evolution of the resistance of the PCMO/Al, PCMO/Ta_2O_5 ,

and PCMO/WO_3 devices is fitted mathematically and integrated into a neural network training framework.. Therefore, the logistic function

$$y(n) = \frac{\acute{y}}{1 + \exp\left(\alpha \times n - c\right)} \tag{9.1}$$

with y is the fitted resistance/conductance for the LTD/LTP curve, respectively. $\acute{y}$ is the maximum value at which the function saturates, and α and c determine the steepness of the increase. This is similar to other approaches e.g. in [222]. This function is used to describe the change of the resistance within one SET or RESET pulse during the LTP and LTD measurements. For the LTP measurement, not the resistance but the conductance is fitted with equation 9.1. Beside fitting the resistance, a common approach for a behavioural model is to fit the resistance change [222]. This approach showed the same fitting accuracy but a lower computational performance in the TensorFlow environment.

$\acute{y}_{\mathrm{pot}}$ and $\acute{y}_{\mathrm{dep}}$ correspond to the saturation values of the LTP and LTD measurements. With this parameters the ON/OFF-ratio of a pair of potentiation and depression pulse parameters can be calculated. The PCMO/WO_3 devices show the highest ON/OFF-ratio and the PCMO/Ta_2O_5 devices the lowest. In general, higher SET and RESET voltages lead to higher ON/OFF-ratios. α resembles the steepness of the initial change of the resistance. For α no clear dependency on the SET and RESET pulse voltage can be seen.

The fitted LTP/LTD measurements are used as input for the weight change in an artificial neural network (ANN) due to its gradual resistance change during training with the Stochastic Gradient Descent algorithm. Therefore, simulations of a multilevel perceptron network are conducted in a TensorFlow environment in Python [223]. The simulated perceptron network consist of four layers of neurons, two hidden layers, one input and one output layer. The input layer consist of 784 neurons, the first hidden layer of 250 neurons, the second hidden layer of 125 neurons, and the output layer of 10 neurons. The weights between two neurons are assumed to be arranged in a matrix layer consisting out of PCMO-based memristive devices. For initialisation, the weights are randomly drawn from a uniform distribution in the given resistance range of the investigated LTP and LTD measurements. Gradient descent learning using a back propagation algorithm is used to determine the gradient for each weight. Depending on the sign of the gradient either a SET or a RESET pulse should be applied.
During the forward pass, an MNIST sample image is presented to the input layer. Each pixel is converted into an input voltage acoording to its gray scale value and this input vector is transformed by the memristive weight matrix into a vector of output currents. With a Rectified Linear Unit (ReLU) function, the input voltage to the next weight layer is determined from the currents.
From the backward pass of the total network error E, the gradient for the gradient-descent algorithm $\delta \mathrm{E}/\delta g_{i,j}$ is calculated. All gradients are accumulated for every weight within each epoch. Every training epoch consist of a subset of 60000 samples from the MNIST data set.
During the update operation either a SET, RESET, or no pulse are applied to the PCMO-based device that acts as weight. Due to the fact that the SET and the RESET pulses are fixed, only the sign of the accumulated gradient is deciding for the update polarity. This means that small gradients would have the same effect as large gradients. Therefore, it is decided that only the largest positive and the smallest negative gradient

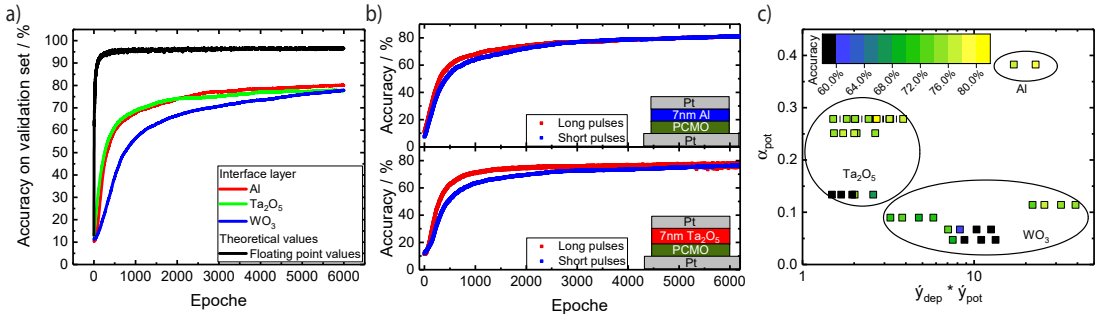

Figure 9.6.: a) Results of the best LTP and LTD combination of the PCMO/Al, PCMO/Ta_2O_5 and PCMO/WO_3 devices for 6000 epochs and the benchmark test of the network layer with floating points values. b) Impact of pulse length on the convergence rate and the maximum accuracy of the simulations for the PCMO/Al and the PCMO/Ta_2O_5 devices. c) Recognition accuracy for all fitted LTP/LTD combination depending on the fitted ON/OFF-ratio and the steepness of the LTP curve α_{pot}.

in every layer will be updated. This leads to a large number of epochs to reach the maximum pattern recognition accuracy.

10000 validation samples from the MNIST data set are used after each learning epoch to validate the learning. The fraction of correctly recognised images is calculated as the pattern recognition accuracy. A benchmark test with floating point weights is performed to demonstrate the networks maximum possible recognition accuracy. This maximum recognition accuracy was determined to 96.7 %.

9.3.2. Results of simulations

6000 learning epochs as described above are performed for every possible LTP and LTD combination of the PCMO/Al, PCMO/Ta_2O_5 , and PCMO/WO_3 devices.

In figure 9.6 a) the best results LTP/LTD combination after every epoch of the 6000 applied epochs are shown. Here, the convergence rate of the different devices and the maximum accuracy can be seen. Furthermore, the maximum accuracy and the convergence rate of the benchmark test is presented in the same figure. Comparing the PCMO/Al, PCMO/Ta_2O_5 , and PCMO/WO_3 , it can be seen that the convergence rate of the PCMO/Ta_2O_5 is the largest but comparable with the convergence rate of the PCMO/Al devices. The convergence rate of the PCMO/WO_3 devices is the lowest. Nevertheless, even if the convergence rate of the PCMO/Al devices is slightly lower than the the convergence rate of the PCMO/Ta_2O_5 devices, after around 2000 epochs the recognition accuracy of the PCMO/Al devices becomes larger than the PCMO/Ta_2O_5 devices. After 6000 epochs the PCMO/Al devices reaches 82 % recognition accuracy. The PCMO/Ta_2O_5 devices reaches 76 % recognition accuracy as well as the PCMO/WO_3 devices, even if the PCMO/WO_3 devices show an even smaller convergence rate compared to both other devices. Comparing all three different device stacks to the benchmark test with the floating point values, shown in black, it can be seen that the maximum recognition accuracy of the same network with floating-point weights is around 14 % higher namely at 96.7 %.

The impact of the pulse length for the PCMO/Al and the PCMO/Ta_2O_5 devices on the convergence rate and the reachable recognition accuracy is shown in figure 9.6 b). It can be seen, that for the PCMO/Al as well as for the PCMO/Ta_2O_5 devices, shorter pulses leads to a lower convergence rate. This is more pronounced for the PCMO/Ta_2O_5 devices than for the PCMO/Al devices. After around 3000 epochs, the recognition accuracy of the simulation of the PCMO/Al and PCMO/Ta_2O_5 devices is the same for the short and the longer pulses. Afterwards, the convergence rate does not differ and the maximum recognition accuracy after 6000 epochs is the same for short and long pulses. This difference in convergence rate that reaches the same recognition accuracy can be understood quite well by the results of section 9.1.1, figure 9.2 and figure 9.3. There it was shown, that the resistance change is only dependent on the total applied pulse time and not on the number of pulses that has to be applied to reach this total applied pulse time. Therefore, the resistance change of one weight is smaller for shorter pulses. This means that more pulses are needed to change the weight in the same way with shorter pulses than with longer pulses. Therefore, the convergence rate is lower for the shorter pulses than for longer pulses. The pulse length therefore can be regarded as an intermediary of an adjustable convergence rate.

The reachable accuracy after 6000 epochs for all possible LTP/LTD combinations for the PCMO/Al, PCMO/Ta_2O_5 , and PCMO/WO_3 devices is presented in figure 9.6 c). On the x-axis the maximum ON/OFF ratio of the fits is shown and on the y-axis the steepness of the LTP curve α_{LTP} is shown. The different devices PMCO/Al, PCMO/Ta_2O_5 , and PCMO/WO_3 forms clusters. Each device stack exhibits a unique combination of steepness and ON/OFF ratio. Furthermore, a higher steepness and a higher ON/OFF-ratios leads to a higher recognition accuracy. For the higher ON/OFF-ratio this can be understood easily because more states can be distinguished from each other and the resistance difference between the weights is higher. On the other hand, the increasing accuracy with increasing steepness of the LTP curve α_{LTP} can not be understood directly, because it appears contrary to the observation that a more linear behaviour of the resistance and an equal resistance change between two pulses is preferable for the recognition accuracy [224]. This is attributed to the non-reversible weight update followed from a strong non-linearity [59]. Nevertheless, due to the different update rule of the network and the large batch size and sparse update matrix, one device is mostly updated in the same direction. Update pulses with different polarities occur only rarely on the same device.

In conclusion PCMO/Al, PCMO/Ta_2O_5 and PCMO/WO_3 devices can be used as weights in ANN learning. For the different device stacks different recognition accuracy could be achieved. The PCMO/Al devices showed the highest recognition accuracy with 82 %. Optimising different parameters showed that the maximum reachable accuracy depends on the shape of the evolution of the resistance during the LTP/LTD measurement and the ON/OFF-ratio of the devices. Furthermore, it was shown that different convergence rates could be achieved by different pulse lengths. This difference in convergence rate did not effect the maximum recognition accuracy.

9.4. Conclusion of neuromorphic applications

For the PCMO/Al, PCMO/Ta_2O_5 and PCMO/WO_3 devices, LTP and LTD measurements are performed. During the LTP/LTD measurement the resistance change within one applied pulse increases with the pulse voltage. Additionally, the saturation resistance increases with larger pulse voltages. Larger voltages lead to a higher HRS and a lower LRS value after 50 cycles. Furthermore, it was seen that the PCMO/WO_3 devices show the most linear increase in resistance during the LTD measurement. The decrease of resistance during the LTP measurement happened for all device stacks PCMO/Al, PCMO/Ta_2O_5 , and PCMO/WO_3 within the first few pulses. Afterwards, the resistance remains stable.

A dependence of the pulse time was shown for the PCMO/Al and PCMO/Ta_2O_5 devices. Beside the fact that longer pulses lead to a larger resistance change within one pulse, the pulse times are cumulative. This means that the same resistance change occurs for ten 1 µs pulses as well as for one single 10 µs pulse. This gives the devices an even broader application range, due to the better tunability of the resistance with the pulse length and height.

Furthermore, it could be shown that the PCMO/Al, PCMO/Ta_2O_5 and PCMO/WO_3 devices show an STDP like behaviour. For this purpose, two overlapping pulses are applied to the devices as pre- and post-synaptic spikes. The time difference between the two spikes is crucial for the resistance change of the device. Additionally the change of the PCMO/Al device response with a different pulse shape of the pre- and post-synaptic spike was shown. This gives the devices the opportunity to respond in a given way to given circuit requirements.

Finally, the possibility to use the PCMO/Al, PCMO/Ta_2O_5 and PCMO/WO_3 devices as weights in ANN was shown. A recognition accuracies between 82 % for the PCMO/Al devices and 76 % for the PCMO/WO_3 devices could be achieved. With a new compensation method Siegel et al. now achieves floating point accuracy with these devices [225].

10. Conclusion & Outlook

10.1. Conclusion

The aim of this work was to gain further knowledge about the switching mechanism of area type resistive switching device by analysing polycrystalline PCMO based memristive devices. Furthermore, the suitability of these devices for beyond "von-Neuammn"-computing should be demonstrated.

Starting with the deposition of the PCMO thin film, different PLD growth and post-processing parameters and their impact on the thin film properties were analysed. By analysing the laser energy it could be seen that for 27 mJ and 30 mJ the stoichiometry of the thin films fits best to the expected stoichiometry of $Pr_{0.7}Ca_{0.3}MnO_3$. Therefore, all thin films that are later analysed are grown at a laser energy of 27 mJ. The impact of the thickness of the PCMO thin film on its morphology is shown in section 4.3.2. Thinner films, 15 nm and 20 nm, show a flatter surface than thicker thin films, 25 nm, 30 nm and 50 nm. The 10 nm thin film did not show a fully covered surface. Additionally, it was shown that lower pressure during the growth of the PCMO leads to a smoother surface, section 4.3.3. The RMS value of the PCMO thin film increases by a factor 6, 0.25 nm to 1.5 nm, within a change of two orders of magnitude of the process pressure, 0.001 33 mbar to 0.133 mbar O_2. Furthermore, it was shown that the density of the PCMO increases within decreasing process pressure. Changing the oxygen partial pressure and keeping the pressure inside the PLD chamber with Ar gas constant does not change the overall thin film morphology significantly.

The post processing of the PCMO thin film after the growth by RTA was analysed. The rapid thermal annealing in this work was done at 650° in N_2 for 2 min. It could be shown that the thin film roughness decreases by 25 %. Within the change of the roughness, the thickness of the thin film decreases by around 42 % during the RTA process. This behaviour was explained by the change of the thin film from amorphous to polycrystalline that was shown with GIXRD. Furthermore, the stoichiometry of the thin film changes slightly during the RTA process from $Pr_{0.68\pm0.02}Ca_{0.318\pm0.012}MnO_3$ to $Pr_{0.73\pm0.02}Ca_{0.27\pm0.03}MnO_3$, measured by ICPMS. This indicates that the amount of Ca changes in the thin film during the RTA. It is not clear whether what happens with the Ca during the annealing. Different annealing temperatures and gases have been investigated in the previous work [123].

The resistive switching devices that were presented in chapter 6 all consist out of the PCMO films optimised in chapter 4 in combination with different metals and oxides. The interface between the PCMO and Al, Ta, W, Ta_2O_5, and WO_3 have been investigated in chapter 5. For the PCMO/Al and the PCMO/Ta an interface oxide between the PCMO and the respective metal could be observed by XPS. This was on the one hand seen in the Al $2p$/Ta $4f$ spectra by the appearance of an oxide peak and on the other hand by the

appearance of a Mn^{2+} in the Mn $2p$ spectrum feature due to the loss of oxygen inside the PCMO thin film. The formation of this oxide could be explained by the change in Gibbs free energy during the formation of interface oxide. Furthermore, the peak position of the Pr $3d$ peaks shifts around 0.9 eV/0.6 eV to higher binding energies after the deposition of the Al/Ta layer. This shift could be attributed to a downwards band bending of the PCMO bands. TEM analysis that have been performed on the PCMO/Al devices could not reveal the AlO_x layer at the interface. It was not even possible to narrow down the Al exactly due to the rough interface. For the PCMO/W interface neither an oxide peak, nor a Mn^{2+} feature could be observed in the XPS measurement after the deposition of the W layer. For the W layer only a surface oxide and no interface oxide could be measured. Only a slight peak shift of the Pr $3d$ peak of around 0.2 V was observed. This leads to the conclusion that even if no oxide is formed at the interface a slight downward band bending occurs. Nevertheless, despite the optimisation of growth, the roughness of PCMO thin films is very high, which often means that no systematic trends are discernible.

The interface of the PCMO/metal combinations, namely PCMO/Ta_2O_5 and WO_3 that were investigated in chapter 5 did not show any Mn^{2+} feature in the Mn $2p$ spectra. Therefore no change of the oxidation state of the PCMO could be observed after the oxide deposition. Nevertheless, a slight shift of the Pr $3d$ peak was observed. The PCMO/Ta_2O_5 devices showed a shift of around 0.4 eV and the PCMO/WO_3 devices showed a shift of around 0.6 eV. This indicates a downwards band bending of the PCMO bands at the interface between the PCMO and the oxides.

At the beginning of chapter 6 the effect of different PCMO properties in combination with Al metal on the resistive switching properties were presented. The focus here was mainly on different PCMO and Al thicknesses, see section 6.1. It could be seen, that the resistance of the high and the low resistive state increases with increasing PCMO and Al thickness. Due to the fact that the resistance of the area type resistive switching devices increases further for smaller devices, a lower resistance value for the large devices was preferable. For the 10 nm and 15 nm PCMO devices, no reproducible resistive switching could be observed. Additionally the change of resistance with the device size was not equal for the HRS and the LRS of the 15 nm PCMO device. The reason for this was that the PCMO layer was not completely closed as discussed in section 6.1.1. The 20 nm PCMO devices showed the best switching behaviour with a high ON/OFF-ratio of around 7, resistance values in the MΩ range and a changing of the HRS/LRS within the area of $-1.11 \pm 0.04\,\Omega/\mu m^2 / -1.12 \pm 0.05\,\Omega/\mu m^2$, respectively. The impact of different Al metal thicknesses was investigated in section 6.1.2. For thin Al thicknesses, no switching could be observed. This was explained by the rough PCMO surface that lead to shortcuts without a certain thickness of the Al layer. The best fitting Al thickness was determined to 7 nm.

Afterwards, different metals, Ta, W, Mo, and Ti, and oxides, Al_2O_3, Ta_2O_5, WO_3, and HfO_2 in combination with 20 nm PCMO have been investigated. For the investigated metals it could be seen that only the PCMO/Ta and PCMO/Ti devices showed resistive switching, section 6.2. Combining these results with the results from chapter 5, it was concluded that the formation of an oxide interface layer is crucial for the resistive switching of the PCMO based devices. The oxide interface layer in PCMO/Ti devices

was already investigated in [33]. The investigated oxides all showed resistive switching, see section 6.3.

Comparing all the results from section 6.2 and section 6.3, the PCMO/Al, PCMO/Ta_2O_5, and PCMO/WO_3 devices were identified as the best candidates for future memory devices and investigated further. The initialisation, variability, stability and volatile states of these devices have been investigated. The first cycle of the PCMO/Al and PCMO/WO_3 devices showed an increase in the resistance of the device. This increase was higher for the PCMO/Al devices. This behaviour was explained in section 6.5 by the homogenisation of the oxide interface layer that has been seen in chapter 5 for the PCMO/Al devices. For the PCMO/WO_3 devices the lowest variability and largest resistance window could be observed. All three devices were stable over several days without large changes in the resistance. For the PCMO/Al devices in addition a volatile part of the LRS could be observed. This volatile part of the LRS could be attributed to charged defects states in the native AlO_x layer. The decay of these states happens within a few ns. An explanation for this was given in section 7.5.
Additionally, the SET and RESET kinetics of these devices have been investigated in chapter 8. It could be seen that the SET and RESET process of the PCMO/Al devices happen at the lower voltages than for the PCMO/Ta_2O_5 and PCMO/WO_3 devices. Furthermore, the change of voltage with changing pulse time was the lowest for the PCMO/Al devices. The SET process of the PCMO/Ta_2O_5 and the PCMO/WO_3 devices happen nearly at the same voltages and same pulse times. For the RESET process, the PCMO/Ta_2O_5 devices switch at lower voltages than the PCMO/WO_3 devices.
The slopes that were extracted from the kinetic measurement were used to calculate the field drop distance during the SET and the RESET process for all three devices. The field drop distance was calculated for the PCMO/Al to $\sim$4.8 nm/$\sim$4.1 nm, for the PCMO/Ta_2O_5 to $\sim$5.6 nm/$\sim$4.9 nm, and for the PCMO/WO_3 to $\sim$5.6 nm/$\sim$3.2 nm, for the SET/RESET process, respectively. The calculated field drop distance for the PCMO/Al devices fits well to the thickness of the AlO_x layer used in chapter 7 to calculate the theoretical capacitance. Furthermore, it could be concluded that the kinetics are only limited by the field driven motion of oxygen vacancies and no heat acceleration occurs.

For a better understanding of the underlying switching mechanism in the PCMO based devices and to describe the I-V curves, a purely mathematical two resistor model was introduced in chapter 7. The model consist out of two voltage dependent resistors in series. The resistors are described by $R_{1,2} = \alpha_{1,2} \cdot \exp(-V_{1,2} \cdot \beta_{1,2})$. This simple model was able to describe the I-V measurements for the PCMO/Al devices from chapter 6. By combining the results of chapter 6, chapter 5 and additional impedance spectroscopy measurements, the two resistors could be attributed to the interface oxide layer, R_1, and a oxygen depletion zone in the PCMO layer, R_2. Furthermore, physical meaning could be given to the fit parameters by analysing the transport mechanism in the AlO_x layer and the PCMO layer, namely Poole-Frenkle effect and Polaron hopping. α_1 represents the base resistivity of the AlO_x barrier, β_1 the modification of the E-field by screening, α_2 the base resistivity of the PCMO layer, and β_2 the modulation of the E-field in the depletion zone. The proportionalities of the fit parameters can be found in table 7.2. The disadvantage of the two resistor model is that it can only describe parts of the I-V measurement in which no switching happens. Therefore, the two resistor model was not

able to describe the switching process during the switching. Nevertheless, by cutting the SET and the RESET process into smaller pieces and changing the resistance value gradually. Investigating the read out sweeps after small resistance changes with the two resistor model and analysing the evolution of the fit parameters gave new insights into the movement of oxygen vacancies in the area type resistive switching devices. It was shown, that the exchange of oxygen vacancies between the PCMO layer and the native AlO_x is the reason for the change in resistance. Here, the change in resistance in the AlO_x is much larger than the change in resistance in the PCMO.
Furthermore, the volatile part of the LRS could be described by the two resistor model. It could be seen that the main change happens inside the AlO_x and the PCMO, $\beta_{1,2}$, and the resistivity of the PCMO, α_2, while the base resistivity of the AlO_x, α_1, stays quite constant. Therefore, the subloops could be explained by the charging and discharging of deep trap states in the band gap of the AlO_x. The trap states that are responsible for the volatile state of the LRS are deep states inside the AlO_x band gap. Meanwhile, the traps that contribute to the Poole-Frenkel effect are shallow traps.

In chapter 9 the use of PCMO device for neuromorphic applications of the PCMO/Al, PCMO/Ta_2O_5 , and PCMO/WO_3 have been investigated. It was shown the repeated application of a single pulse leads to a gradual change in resistance. This LTP/LTD measurements were used as inputs as weight updates in a multi-layer perceptron for MNIST pattern recognition. A maximal recognition accuracy of 82 % for the PCMO/Al devices could be reached. The other devices, PCMO/Ta_2O_5 and PCMO/WO_3 , have achieved an accuracy of 76 %. Furthermore the impact of different pulse voltages and pulse lengths on the pattern recognition accuracy were studied. It could be seen that a higher ON/OFF-ratio leads to a higher recognition accuracy. Furthermore, it was shown in section 9.1.1 that the pulse length of the applied voltages pulses is accumulative.

The invented two resistor model, together with the results of the interface investigation, the switching curves, and the kinetic measurement contributes to a better understanding of the area type switching memristive device. Beside an easy model to describe the switching curves, the switching dynamics could be analysed by this model and gave insights into the ion movement during switching. This insights in the movement of oxygen vacancies together with the results regarding the structure of the devices gave new insights into the underlying mechanism. Furthermore, the results of the switching of the different device stacks, the kinetic measurement, and the neuromorphic applications gave insights that PCMO based memristive devices are suitable to solve modern computing problems. Additionally, neuromorphic applications are possible with these devices.

10.2. Outlook

The shown device characteristics in chapter 6, 8, and 9 gave a broad overview about the switching characteristics of the PCMO based resistive devices. Nevertheless, most of the measurements measurements are performed with µm size single devices. For circuit integration at least a cross point structure is needed. Therefore, the devices has to be integrated into a cross point or a cross bar structure. Furthermore, the device size has to be shrunken further. This shrinking of the devices would lead to an increase of the LRS and HRS resistance that could have the advantage that the power consumption of the devices would decrease. Nevertheless, a higher LRS resistance could also be an opportu-

nity due to the fact that the influence of the surrounding circuit on the resistance could be neglected. Additionally, the increase of the resistance must also not become too large so that the current can still be read out. Here, the different materials that have been investigated in this work can be expanded and possibly a better material combination or material processing can be developed. For a CMOS integration of these devices, the processing of the PCMO films must also be improved. Currently, the PCMO layers are annealed at 650 °C. This temperature would degrade the CMOS transistors during back-end-of line integration. The annealing temperature must be lowered to a maximum of 450 °C. Such an improvement of the PCMO based resistive switching devices could lead to a new area of memory devices that are based on the change on the resistance state.

The two resistor model introduced in this work is a first step towards a better understanding of area type resistive switching devices. This model could be used as input for circuit and device simulations to gain information about circuit and device requirements for future computing techniques. Nevertheless, the two resistor model only represents a clear simplification of reality. Furthermore, the model can not describe the switching parts of the I-V measurements and is only a static model.
An improvement of this model, that can describe the switching part of the I-V measurement would provide further insights into the ion movement during the switching process. Additionally, the underlying transport mechanisms of the model focuses only on one transport mechanism for each layer. This might need to be extended to other effects in the layers. Furthermore, the exchange process of the oxygen during the switching process can not be described with this model. Nevertheless, describing the exchange of oxygen vacancies with an additional model would lead to further understanding of interface effects in this devices. These additions of the the simple two resistor model and introducing another model that can describe the exchange of oxygen during the switching has the chance to further contribute to the understanding of area type resistive switching devices.

A. Appendix

A.1. Additional information on PCMO thickness determination

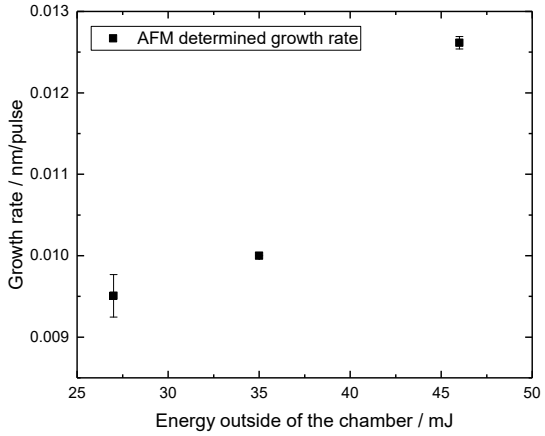

Figure A.1.: Growth rate of the PCMO plotted against the laser energies.

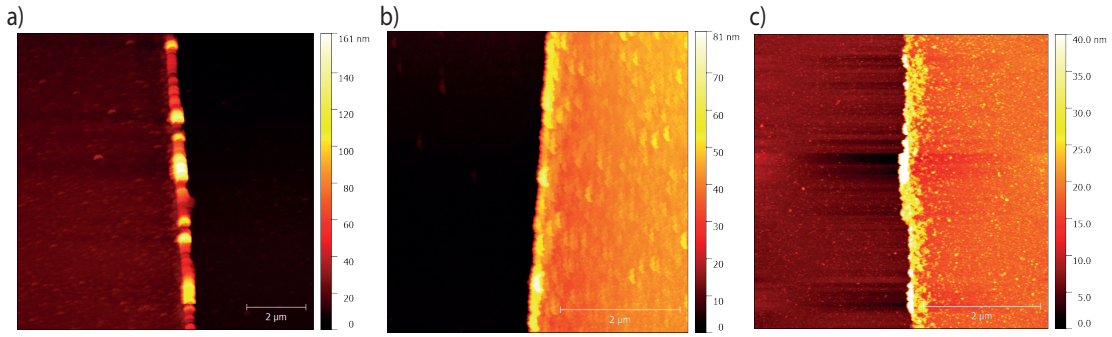

Figure A.2.: Exemplary AFM images from the edges, which were used to determine the layer thickness.

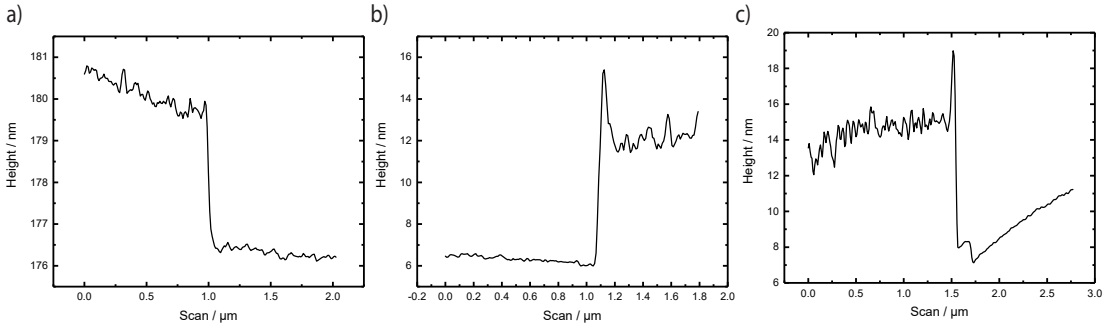

Figure A.3.: Extracted line scans across the edge in the AFM images.

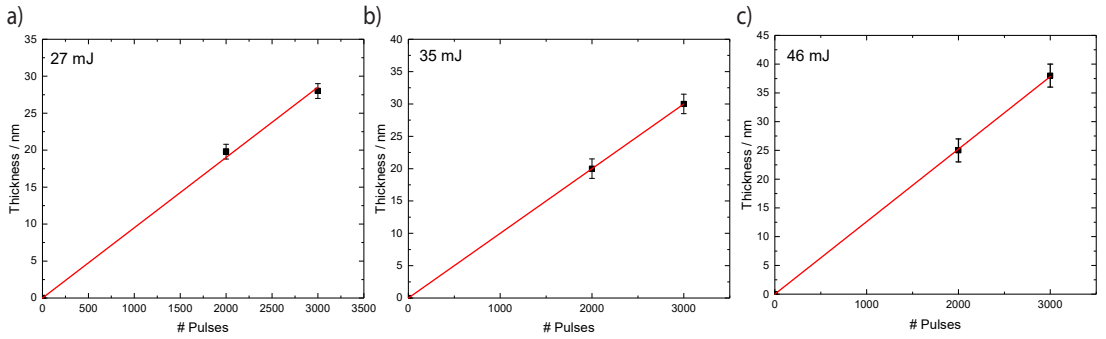

Figure A.4.: Determination of the growth rate of the PCMO for different laser energies.

A.2. Temperature during EBE process

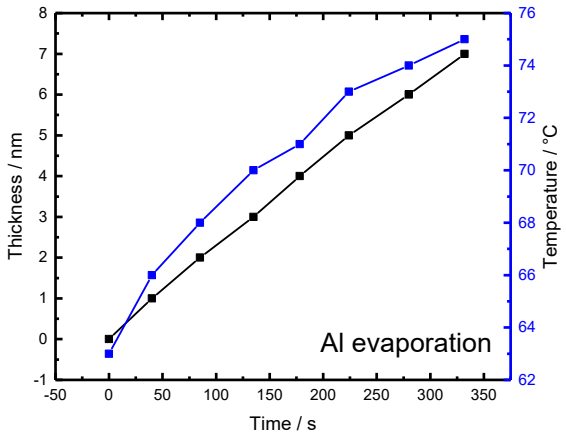

Figure A.5.: Temperature increase during the Al evaporation in the EBE.

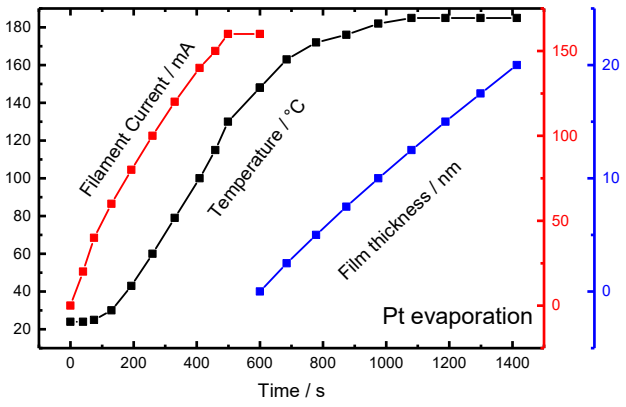

Figure A.6.: Temperature increase during the Pt evaporation in the EBE.

List of Figures

1.1. Race to future solutions of today's computing architecture problems. Taken from [13] . . . 3
1.2. a) Illustration of today's computing architecture with the exchange of date between the computing unit and data storage. b) Illustartion of in-memory computing without data exchange. Taken from [14] . . . 4

2.1. Schematic I-V curves of resistive switching devices with the two basic operation principles unipolar (a) and bipolar (b) switching. Adapted from [27]. . . . 7
2.2. a) Filamentary type resistive switching: A conductive filament is formed through the insulating oxide. (b) Homogeneous area type switching: The entire interface takes part in the switching process. Taken from [25] . . . 9
2.3. Scheme of area type resistive switching devices. The amount of oxygen/oxygen vacancies inside the material determines the resistance state. The resistance is change by the exchange of oxygen/oxygen vacancies. Taken from [25] . . . 9
2.4. Different perovskite Structure of mixed-valence magnates and orbit splitting of 5d-orbitals. . . . 11
2.5. a) A schematic of the organisational principles of the brain with its neurons and synapses. b) A schematic of a multi layer network performing object recognition. c) A schematic of a state-of-the-art silicon based computing system. Taken from [58]. . . . 14

3.1. Schematic of PLD chamber manufactured by *TSST*. Laser hitting the target material and creates the plasma plume onto the heated substrate. Different gas inlets and pressure gauges control the growth environment. . 18
3.2. a) Schematic drawing of the EBE process. b) Schematic drawing of a sputter chamber. Both drawings are taken from [34]. . . . 19
3.3. Schematic drawing of the different steps that has to be performed during Lithography. . . . 22
3.4. Schmatic of Bragg-Brentano geometry for XRD measurement with reflection at the lattice planes. Redrawn from [34]. . . . 23
3.5. Measurement scheme of the XRR geometry with reflection of at the interfaces. Redrawn from [34] . . . 24
3.6. Scheme of XPS measurement to determine the material. Redrawn from [34] 25
3.7. Quadrant diagram of the Keithley 2611A with the different measurement regimes, taken from [119]. . . . 27
3.8. Image of the ArcONE measurement system from *ArC Instruments*. . . . 29

4.1. AFM scans of (a) Pt grown on Si and (b) 20 nm PCMO thin film grown at room temperature with a energy of 27 mJ, a frequency of 5 Hz and a O_2-pressure of 0.133 mBar . . . 31

4.2. XPS,XRR and GIXRD measurement of standard PCMO thin film. (a) XPS measurement of Mn $2p$ peak to determine the Pr/Ca-ratio of the thin film. The result is $Pr_{0.69\pm0.03}Ca_{0.31\pm0.02}MnO_3$. (b) XRR measurement of as grown PCMO thin film to determine the thickness to 20 nm. (c) GIXRD measurement of as grown PCMO thin film. 32

4.3. GIXRD measurement of a 50 nm thick PCMO thin film before (a) and after (b) RTA at 650 °C for 2 minutes in N_2-atmosphere. The crystallization of the thin film in different crytsal phases can be seen. The lattice planes of the main diffraction peaks can be seen in the lower part of the figure. 33

4.4. AFM images of PCMO thin film before RTA a) and after RTA b)/c). A decrease of around 25 % in the overall roughness of the PCMO thin film can be observed after the RTA process at 650 °C for 2 min 34

4.5. Increase of grain size during the RTA process. Taken from [123] 34

4.6. Change of PCMO thickness during RTA process for 2000 and 3000 pulses for different laser energy in absolute and relative values. An overall change in thickness of around 42 % can be observed. 35

4.7. XRR measurements before and after RTA process. Changes in oscillation can be seen. 35

4.8. XPS spectra and analysis of PCMO thin films grown at different laser energies. a) Pr $3d$ peaks of PCMO thin films grown with different laser energies. b) Ca $2p$ peaks of PCMO thin films grown with different laser energies. c) Mn $2p$ peaks of PMCO thin films grown with different laser energies. d) Analysis of $^{Mn^{3+}}/_{Mn^{4+}}$ ratio of PCMO thin films grown at different laser energies. 36

4.9. XRR measurements of 10 nm, 15 nm, 25 nm, 30 nm and 50 nm thick PCMO thin films. It can be seen, that the oscillations of the 10 nm PCMO thin film do not match the oscillation of the thicker PCMO thin films. 38

4.10. $1 \times 1\,\mu m^2$ AFM scans of 10 nm, 15 nm, 25 nm, 30 nm and 50 nm thick PCMO thin films after RTA process. Additionally an $5 \times 5\,\mu m^2$ AFM scan of the 10 nm thin film is given, to show the island formation across the whole sample surface. The AFM image of the 20 nm can be found in figure 4.4. 39

4.11. Roughness parameters of the 10 nm, 15 nm, 25 nm, 30 nm and 50 nm PCMO thin film. a) RMS, b) max. height and c) median height values extracted from the AFM scans given in figure 4.10 40

4.12. XPS measurement of the Mn $2\,p\,3$ peak for different O_2 pressure during PCMO growth. No increase of the Mn^{2+} shake up and satelite feature can be seen. This means that the ambient pressure has no effect on the oxidation state of the PCMO layer. 40

4.13. $1 \times 1\,\mu m^2$ AFM images of 20 nm PCMO thin films grown 0.133 mbar, 0.065 mbar, 0.0133 mbar, 0.065 mbar and 0.001 33 mbar O_2 pressures after RTA process. The colour scales is fixed between zero and 12 for all images. A decrease of average height and roughness can be seen for decreasing O_2 pressure. 41

4.14. Roughness parameters of 20 nm thick PCMO grown at 0.133 mbar, 0.065 mbar, 0.0133 mbar, 0.065 mbar and 0.001 33 mbar O_2 pressure in the chamber. a) RMS, b) max. height and c) median height values extracted from the AFM scans given in figure 4.13. The roughness of the sample decreases with decreasing O_2-pressure. An error of 10 % is assumed for all measured values. 42
4.15. a) XRR measurements of 20 nm PCMO thin films grown at different O_2 pressure inside the PLD chamber An increase of the total reflection angle of the XRR measurement with decreasing O_2 pressure can be seen. b) Angle with max. counts plotted against the O_2 pressure during growth. A clear increase of the max. cps / total reflection angle with decreasing pressure can be seen. 42
4.16. AFM images of PCMO thin films grown at different 0.133 mbar with 50 % and 10 % O_2 partial pressure. 43
4.17. Roughness parameters of 20 nm PCMO grown at 0.133 mbar with 50 % and 10 % O_2 partial pressure. a) RMS, b) max. height and c) median height values extracted from the AFM scans given in figure 4.16. The roughness of the sample decreases with decreasing O_2 partial pressure. An error of 10 % is assumed for all measured values. 43
4.18. XRR (a)) and XPS (b)) measurements of the PCMO thin film grown at different O_2 partial pressure. No change in the total reflection angle of the XRR measurement or the Mn oxidation state can be seen. 44
4.19. a)-d) AFM images of PCMO grown with PLD targets of different stoichiometries. The stochiometry of the target is indicated by the inlet in the AFM images. e)-g) Height values extracted from the AFM images for the different stoichiometries. e) RMS, f) Max. height and g) Median height. 45
4.20. a) Mn $2p$ peak of PCMO60 thin film with the fitted peaks, Mn^{3+} and Mn^{4+}. b) Percentage of Mn^{3+} and Mn^{4+} in the PCMO thin films grown with targets of different stoichiometry determined by the Mn $2p$ peak. . . 46
4.21. a)-c) $1 \times 1\,\mu m^2$ AFM scans of PCMO thin films annealed at different temperature, 350 °C, 450 °C and 550 °C respectively. d) RMS values, e) max. height and f) median height of the AFM scans a)-c). Additionally the values of the 650 °C thin film are added to d)-f). 47
4.22. GIXRD scans of PCMO thin films annealed for 2 min in N_2-atmosphere at 350 °C, 450 °C and 550 °C with an incident angle of 0.4°. 47

5.1. Ellingham diagram of the oxidisable metals used in this chapter as interface materials: Al, Ta, and W. It shows the temperature dependence of the stability of the thermodynamically stable compounds likely to appear in the samples. It can be seen that the Al is more likely to form an oxide than Ta and W. Additionally, the work function and the change of Gibbs free energy is plotted for the different materials. [136, 137] 52
5.2. XPS measurements of PCMO in combination with an Al interface layer. a) Al spectrum at different angles, 30° and 80°. A clear increase of the AlO_x feature at higher angles can be seen. This indicates an increase of the oxidation state deeper inside the PCMO. b) Mn $2p$ spectrum of PCMO without and with Al layer. A Mn^{2+} satellite feature can be seen for the PCMO thin film with the Al layer. 53

5.3. a) XPS measurement of Pr $3d$ spectrum without (black) and with (red) Al layer. A slight shift to higher binding energies of the Pr $3d$ $^5/_2$peak can be seen. b) Reconstructed band diagram of the PCMO, AlO_x, Al junction. 54

5.4. a), b) TEM measurement of the PCMO/Al devices with a magnification of 300k. c), d) STEM measurement of the PCMO/Al devices. 55

5.5. EDX measurements of the PCMO/Al devices and interface. a) EDX map of the whole device stack with all investigated elements. b) EDX line scans across the device. c) EDX line scans along the PCMO layer. 56

5.6. Ta $4f$ spectra of Ta metal deposited on PCMO. a) Ta $4f$ spectrum of 3 nm Ta deposited on PCMO at different angles, 30° and 80°. b) Fitting of the Ta $4f$ spectrum of 3 nm Ta on PCMO. c) Ta metal reference spectrum. d) Fitting of Ta $4f$ spectrum of 5 nm Ta deposited on PCMO. 57

5.7. a) Mn $2p$ spectrum of PCMO without (black) and with (red) 3 nm Ta on top. b) Pr $3d$ spectrum of PCMO without (black) and with (red) 3 nm Ta on top. 58

5.8. Reconstructed band structure of the Ta/PCMO interface from the XPS measurements shown in figure 5.6 and figure 5.7. 59

5.9. XPS measurements of PCMO without and with W on top. a) Measurement of the W $4f$ spectrum at different take-off angles, 30° and 80°. b) Fitting of the W $4f$ XPS data with a metallic and two different oxidation states at 45° take off angle. c) Mn $2p$ spectrum of PCMO without and with W. Pr $3d$ spectrum of PCMO without and with W. d) Pr $3d$ spectrum of the PCMO with and without W metal on top. 60

5.10. Visualisation of the bands at the interface between W and PCMO without a WO_2/WO_3 layer at the interface. Only a slight band bending of the PCMO is expected due to figure 5.9 d). 61

5.11. Ta $4f$ spectra of Ta_2O_5 in combination with PCMO. a) Ta $4f$ spectrum of Ta_2O_5 in combination with PCMO at different angles, 30° (black) and 80° (red). A slight metal feature can be seen for both angles. b) Fitting of the Ta $4f$ with a Ta^{5+} and a Ta metal feature. c) Fitting of a Ta $4f$ reference spectrum grown on SiO_2 with the same growth parameters as for the growth on PCMO. d) Proportion of the Ta^{5+} area of the whole Ta $4f$ peak area. Decreasing Ta^{5+} proportion with increasing profiling depth. . . 62

5.12. XPS measurements of a) Mn $2p$ and b) Pr $3d$ peak without and with Ta_2O_5 on top of the PCMO thin film. a) No clear change of the Mn $2p$ spectrum can be seen. b) A slight shift of 0.4 eV of the Pr $3d$ peak can be seen. . . . 63

5.13. XPS spectra of the PCMO in combination with WO_3. a) W $4f$ sepctra at different take of angles, 30° (black) and 80° (red). b) Fitting of the W $4f$ spectra with a W^{6+} doublet. Additionally a WO_3 loss feature can be seen. c) Mn $2p$ of PCMO without and with WO_3. No additional Mn^{2+} feature and also no change in peak shape. d) Pr $3d$ peak of PCMO without (black) and with (red) WO_3. A slight peak shift of 0.6 eV can be seen. . . 65

6.1. Resistive switching curves and linear scaling of resistance with device size for devices with different PCMO thicknesses, 15 nm a) and b), 20 nm c) and d), 30 nm e) and f), 50 nm g) and h). 69

6.2. a) Slope of the resistance change with changing device size for different PCMO thicknesses. b) HRS, LRS and ON/OFF-ratio value of the $20 \times 20\,\mu m^2$ devices for devices with different PCMO thickness. 71
6.3. a)-c) IV curves of PCMO based resistive switching devices with Al layers of different thicknesses, 5 nm a), 10 nm b), and 15 nm c). d) HRS and LRS dependence on the device size for the 10 nm and 15 nm thick Al layer. 72
6.4. a) Slope of the resistance change with changing device size for different Al thicknesses with 20 nm PCMO thickness. b) HRS, LRS and ON/OFF-ratio value of the $20 \times 20\,\mu m^2$ devices for devices with different Al thickness with 20 nm PCMO thickness. 73
6.5. a) Switching curves of PCMO in combination with 7 nm Ta metal of different device sizes. b) Switching curves of PCMO in combination with 7 nm Ta metal of $20 \times 20\,\mu m^2$ devices. c) Resistance value of $20 \times 20\,\mu m^2$ devices at -0.3 V. 76
6.6. a) Switching curves of PCMO in combination with 10 nm Ta metal of different device sizes. b) Switching curves of PCMO in combination with 10 nm Ta metal of $20 \times 20\,\mu m^2$ devices. c) Resistance value of $20 \times 20\,\mu m^2$ devices at -0.3 V. 76
6.7. Switching curves of PCMO in combination with a) 7 nm and b) 10 nm W of $100 \times 100\,\mu m^2$, $50 \times 50\,\mu m^2$, and $20 \times 20\,\mu m^2$ devices. 77
6.8. a) I-V measurement of PCMO in combination with 7 nm Mo of devices with different sizes, $100 \times 100\,\mu m^2$, $50 \times 50\,\mu m^2$, and $20 \times 20\,\mu m^2$. b) I-V measurements of $20 \times 20\,\mu m^2$ PCMO devices in combination with 7 nm and 10 nm Mo. 78
6.9. a) I-V measurements of a $100 \times 100\,\mu m^2$ PCMO in combination with 7 nm Ti that shows filamentary switching (red) and area type resistive switching (blue). b) Area scaling of the area type resistive switching curve of the PCMO/Ti devices. 79
6.10. IV measurements of PCMO in combination with ALD grown Al_2O_3 layers of different thickness, a) 1 nm, b) 2 nm, and c) 5 nm. d) Scaling of resistance with device size of PCMO/(2 nm Al_2O_3) devices. 82
6.11. Switching curves and resistance scaling of PCMO in combination with 7 nm and 10 nm sputtered Ta_2O_5 85
6.12. Resistive switching curves and area scaling of PCMO in combination with WO_3 87
6.13. Resistive switching curves and area scaling of PCMO in combination with HfO_2 89
6.14. ON/OFF ratio of the different investigated PCMO devices in combination with metals (section 6.2) and oxides (section 6.3). Only switching the ON/OFF ratio of the area type resistive switching devices are given here and not switching devices or filamentary switching devices are neglected. . 92
6.15. Comparison of I-V measurements of PCMO in combination with Al, Ta_2O_5, and WO_3 interface layer in a non-logarithmic scale. 94
6.16. a) Initialisation curves of PCMO in combination with Al. b) Resistance distribution of the $20 \times 20\,\mu m^2$ devices with and without initialisation . c) Schematic representation of the interface without oxide, with native oxide and an oxide the initialisation curve. d) EDX TEM image of HRS after initialisation. 95

6.17. Initialisation curves of a) PCMO/Ta_2O_5 and b) PCMO/WO_3 for devices of different size. 96

6.18. Variability of the switching of the PCMO/Al, PCMO/Ta_2O_5 and PCMO/WO_3 devices. a), c), e) 200 switching cycles of the corresponding $20 \times 20\,\mu m^2$ devices. b), d, f) Combined Weibull probability different $20 \times 20\,\mu m^2$ devices of the corresponding material stacks. 98

6.19. Stability of the HRS and the LRS of the $20 \times 20\,\mu m^2$ a) PCMO/Al, b) PCMO/Ta_2O_5 and c) PCMO/WO_3 devices over a period of several days. 100

6.20. a) PCMO/Al LRS subloop measurement and b) variability of the switching states and the subloop states within a few cycles. c) and d) decay of the subloops with pulsed readout and constant readout, respectively. . . . 101

6.21. LRS subloop measurements of a) PCMO/Ta_2O_5 and b) PCMO/WO_3 devices. 103

7.1. a) R-V Measurement of the PCMO/Al system shown in green with the fits shown in blue, illustration of the two resistors in series. b) Individual voltage drop across the R_1 and R_2. + and - labels the positive and the negative voltage branches that are fitted for the HRS, respectively. The fitted values of $\alpha_{1,2}$ and $\beta_{1,2}$ can be found in table 7.1. Adapted from [2]. 106

7.2. a) Nyquist plot of the HRS of the SC samples. The frequency ranges from 2×10^3 Hz to 3×10^5 Hz. The colour represents the applied voltage from 0 V to −1 V and the nyquist-data for each dc voltage is normalised to the z value at 2×10^3 Hz. b) The real value of Z at 2×10^3 Hz at different applied voltages. c) The capacity and resistance of the first R-C circuit as a function of applied voltage. d) The capacity and resistance of the second R-C circuit as a function of applied voltage. Adapted from [2]. . . 107

7.3. Fitting of SET and RESET process with two resistor model. 111

7.4. Schematic drawing of a) the band structure of the PCMO/Al devices and the b) SET and c) RESET process. 112

7.5. a) Negative branch of the R-V measurement with a switching cycle and different subloops with different SET stop voltages. b) Evolution of fit parameters of the two resistor model. 113

7.6. Band diagram of the PCMO/Al devices to show the impact of trap states on the band structure to explain the volatile LRS state. a) LRS state with empty trap states inside the AlO_x layer. b) LRS state with applied voltage V_f that lifts the Fermi level on the level of the Fermi energy. c) LRS state at higher voltages V_m. Trap states are filled and effect the band bending of the PCMO depletion zone can be seen. d) Going back to V_f leaves the trap states partly ionised and the PCMO band shows an upwards bending. This reduces the resistance of the device stack. 114

7.7. Schematic band diagram of the PCMO/Al devices with an oxide at the interface for the LRS and the HRS. This schematic drawing represents only gives a brief overview of the oxygen vacancy distribution and in no way reflects the exact heights of the bands. 115

8.1. Measurement scheme of the kinetic measurements. 118

8.2. Current transients of read out pulses with a length of 1 ms and a height of −0.3 V. a) Current transients of read out pulses during the SET kinetic measurement for different SET pulse voltages. b) Current transients of read out pulses during the RESET kinetic measurement for different RESET pulse voltages. 119
8.3. Measurement of the SET and RESET kinetics for PCMO/Al devices . . . 120
8.4. Current transients of the RESET kinetic measurements to visualize the change of the current for different the pulse heights a) and the pulse lengths b) during the switching. 120
8.5. Extracted contour lines of the heatmap, figure 8.3, of PCMO/Al devices. for ON/OFF-ratios of 2, 3 and 4. 121
8.6. Measurement of the SET (a) and RESET (b) kinetics of PCMO/Ta_2O_5 resistive switching devices. c) shows the RESET kinetics with an adapted colour scale to shows the possibilities of higher ON/OFF-ratios 122
8.7. Exemplary SET pulses of the PCMO/Ta_2O_5 kinetics. a) SET pulses with a length of 1 ms and pulse voltages of −3 V, −3.5 V and −4 V. b) SET pulses with a height of −4 V and lengths of 1 ms, 0.1 ms and 0.001 ms. . . 122
8.8. Extracted contour lines of the heatmap, figure 8.6, of PCMO/Ta_2O_5 devices for ON/OFF-ratios of 2, 3 and 4. 123
8.9. Measurement of the SET (a) and RESET (b) kinetics of PCMO/WO_3 resistive switching devices. c) shows the RESET kinetics with an adapted colour scale to shows the possibilities of higher ON/OFF-ratios 125
8.10. Extracted contour lines of the heatmap, figure 8.9, of PCMO/WO_3 devices for ON/OFF-ratios of 2, 3 and 4. 125
8.11. Extracted contour lines of all three devices, PCMO/Al, PCMO/Ta_2O_5 and PCMO/WO_3. 126
8.12. Measurement of SET a) and RESET b) kinetics of single crystalline PCMO devices grown on SRO in combination with 2.4 nm YSZ. Taken and adapted from [34] 130
8.13. SET kinetic comparison of different materials and switching types to place the SET kinetics of PCMO/Al and other PCMO based devices in an overall picture. STO/Al [3], STO/Pt [218], STO/HfO_2 [218], Ta/TaO_x [219], TiO_x/Al_2O_3 [220]. 132

9.1. Long Term Potentiation (LTP) and Long Term Depression (LTD) measurement of PCMO in combination with a) Al, b) Ta_2O_5 , and c) WO_3 for different potentiation and depression voltages. Adapted from [1]. . . . 135
9.2. Time dependence of resistance change of PCMO/Al devices. a) LTD and b) LTP measurement with 2.0 V pulses and pulse lengths of 100 µs, 10 µs, and 1 µs. Resistance of the c) LTP measurement and d) LTD measurement plotted against the total applied pulse length for pulses of different length. 137
9.3. Time dependence of resistance change of PCMO/Ta_2O_5 devices. a) LTD and b) LTP measurement with 1.6 V/−2.5 V pulses and pulse lengths of 100 µs, 10 µs, and 1 µs. Resistance of the c) LTP measurement and d) LTD measurement plotted against the total applied pulse length for pulses of different length. 138

9.4. a) Schematic of the applied pulses on the top and bottom electrode. b), c), and d) Change of conductance plotted against the time difference between the pre- and the post-synaptic spike for the PCMO/Al, PCMO/Ta_2O_5 , and PCMO/WO_3 , respectively. 140
9.5. Impact of different pulse shape on the device response during a STDP measurement. a) Pulse scheme that is used during the STDP measurement. b) Change of conducatance depending on the time difference of the two pulses shown in a). 141
9.6. a) Results of the best LTP and LTD combination of the PCMO/Al, PCMO/Ta_2O_5 and PCMO/WO_3 devices for 6000 epochs and the benchmark test of the network layer with floating points values. b) Impact of pulse length on the convergence rate and the maximum accuracy of the simulations for the PCMO/Al and the PCMO/Ta_2O_5 devices. c) Recognition accuracy for all fitted LTP/LTD combination depending on the fitted ON/OFF-ratio and the steepness of the LTP curve α_{pot}. 143

List of Tables

3.1. General PLD parameters of PCMO growth. These parameters are used unless otherwise stated. 18
3.2. Sputter parameters of the different materials used in this work. 20
3.3. Intensity ratios of spin-orbit coupling [115]. 26
3.4. Measurements ranges of the Keithley 4200-SCS. Taken from [120]. 28

4.1. Parameters of the highest peaks that are measured in Figure 4.3 (b). . . . 33

5.1. Proportion of the different fitted peak areas in the total area of the peak. 58

6.1. Extracted change of resistance with devices size of PCMO/Al devices with different PCMO thicknesses from figure 6. 71
6.2. Extracted resistance change of the LRS and HRS with device size for 20 nm PCMO in combination with different Al thicknesses from figure 6.3 and figure 6.1. 73
6.3. Activation energies of oxygen vacancies and work function of the different oxides that are used in combination with PCMO, Al_2O_3 [180, 181], Ta_2O_5 [182, 183], WO_3 [184–186], HfO_2 [187, 188] 91
6.4. Fitting values of the exponential decay of the volatile part of the LRS the so called subloops 102

7.1. Fitted parameters of the two resistor model for the R-V measurement shown in figure 7.1. The different parameter sets referrer to the different fitted voltages and resistance values. 106
7.2. Summary of the fit parameters, their connection to physical parameters, and their interpretation. Adapted from [2]. 110

8.1. Slopes of extracted ON/OFF-ratio lines of measured SET and RESET kinetics of PCMO/Al, PCMO/Ta_2O_5 and PCMO/WO_3 devices for different ON/OFF-ratios. 127
8.2. Field drop distance inside the devices, calculated from the SET and RESET kinetic slopes, table 8.1 and equation 8.3. 129

Bibliography

[1] Alexander Gutsche et al. “Exploring Area-Dependent $Pr_{0.7}Ca_{0.3}MnO_3$-Based Memristive Devices as Synapses in Spiking and Artificial Neural Networks”. In: *Frontiers in Neuroscience* 15 (2021). ISSN: 1662-453X. DOI: 10.3389/fnins.2021.661261.

[2] Alexander Gutsche et al. “Disentangling ionic and electronic contributions to the switching dynamics of memristive $Pr_{0.7}Ca_{0.3}MnO_3$/Al devices by employing a two-resistor model”. In: *Physical Review Materials* 005000 (2022), pp. 1–14. DOI: 10.1103/PhysRevMaterials.00.005000.

[3] Sebastian Siegel et al. “Trade-Off Between Data Retention and Switching Speed in Resistive Switching ReRAM Devices”. In: *Advanced Electronic Materials* 7 (Nov. 2020), p. 2000815. DOI: 10.1002/aelm.202000815.

[4] Thomas Heisig et al. “Chemical Structure of Conductive Filaments in Tantalum Oxide Memristive Devices and Its Implications for the Formation Mechanism”. In: *Advanced Electronic Materials* (2022), p. 2100936.

[5] Antonio M. Ortiz et al. “The Cluster Between Internet of Things and Social Networks: Review and Research Challenges”. In: *IEEE Internet of Things Journal* 1.3 (2014), pp. 206–215. DOI: 10.1109/JIOT.2014.2318835.

[6] Kiat Seng Yeo et al. “Internet of Things: Trends, challenges and applications”. In: *2014 International Symposium on Integrated Circuits (ISIC)*. 2014, pp. 568–571. DOI: 10.1109/ISICIR.2014.7029523.

[7] Pradyumna Gokhale, Omkar Bhat, and Sagar Bhat. “Introduction to IOT”. In: *International Advanced Research Journal in Science, Engineering and Technology* 5.1 (2018), pp. 41–44.

[8] Shancang Li, Li Da Xu, and Shanshan Zhao. “The internet of things: a survey”. In: *Information Systems Frontiers* 17.2 (Apr. 2015), pp. 243–259. DOI: 10.1007/s10796-014-9492-7.

[9] Yen-Kuang Chen. “Challenges and opportunities of internet of things”. In: *17th Asia and South Pacific Design Automation Conference*. 2012, pp. 383–388. DOI: 10.1109/ASPDAC.2012.6164978.

[10] Dennis V Christensen et al. “2022 roadmap on neuromorphic computing and engineering”. In: *Neuromorphic Computing and Engineering* 2.2 (May 2022), p. 022501. DOI: 10.1088/2634-4386/ac4a83.

[11] John Vidal. “Tsunami of data’could consume one fifth of global electricity by 2025”. In: *Climate Home News* 11 (2017), p. 12.

[12] H. Thimbleby. “Modes, WYSIWYG and the von Neumann bottleneck”. In: *IEE Colloquium on Formal Methods and Human-Computer Interaction: II*. 1988, pp. 4/1–4/5.

[13] M. A. et al. Zidan. “The future of electronics based on memristive systems”. In: *Nature Electronics* 1 (2018), pp. 22–29. DOI: 10.1038/s41928-017-0006-8.

[14] Abu Sebastian et al. “Memory devices and applications for in-memory computing”. In: *Nature Nanotechnology* 15.7 (2020), pp. 529–544. DOI: 10.1038/s41565-020-0655-z.

[15] Gordon E. Moore. “Cramming more components onto integrated circuits”. In: *Electronics* 38 (1965), 114 ff.

[16] Hassan N. Khan, David A. Hounshell, and Erica R. H. Fuchs. “Science and research policy at the end of Moore’s law”. In: *Nature Electronics* (Jan. 2018), pp. 14–21. DOI: 10.1038/s41928-017-0005-9.

[17] S. E. Thompson and S. Parthasarathy. “Moore’s law: the future of Si microelectronics”. In: *Materials today* 9 (2006), 20–25.

[18] Paulo Cappelletti et al. *Flash memories*. Springer Science & Business Media, 2013.

[19] Chih-Yuan Lu, Kuang-Yeu Hsieh, and Rich Liu. “Future challenges of flash memory technologies”. In: *Microelectronic Engineering* 86.3 (2009). The Fourth IEEE International Symposium on Advanced Gate Stack Technoiogy (ISAGST 2007), pp. 283–286. DOI: 10.1016/j.mee.2008.08.007.

[20] Seung Soo Kim et al. “Review of Semiconductor Flash Memory Devices for Material and Process Issues”. In: *Advanced Materials* (), p. 2200659. DOI: 10.1002/adma.202200659.

[21] Naveen Verma et al. “In-Memory Computing: Advances and Prospects”. In: *IEEE Solid-State Circuits Magazine* 11.3 (2019), pp. 43–55. DOI: 10.1109/MSSC.2019.2922889.

[22] Daniele Ielmini and H.-S. Philip Wong. “In-memory computing with resistive switching devices”. In: *Nature Electronics* 1.6 (June 2018), pp. 333–343. DOI: 10.1038/s41928-018-0092-2.

[23] Arpan Kumar Kar. “Bio inspired computing – A review of algorithms and scope of applications”. In: *Expert Systems with Applications* 59 (2016), pp. 20–32. DOI: 10.1016/j.eswa.2016.04.018.

[24] Yifan Chen et al. “Editorial: Biologically Inspired Computing and Networking”. In: *Mobile Networks and Applications* 26.3 (June 2021), pp. 1344–1346. DOI: 10.1007/s11036-021-01768-8.

[25] Akihito Sawa. “Resistive switching in transition metal oxides”. In: *Materialstoday* 11.6 (2009), pp. 28–36. DOI: 10.1088/0957-4484/20/21/215201.

[26] Mario Lanza. “A Review on Resistive Switching in High-k Dielectrics: A Nanoscale Point of View Using Conductive Atomic Force Microscope”. In: *Materials* 7.3 (Mar. 2014), pp. 2155–2182. DOI: 10.3390/ma7032155.

[27] Rainer Waser et al. “Redox-based resistive switching memories nanoionic mechanisms, prospects, and challenges”. In: *Advanced Materials* 21.25-26 (2009), pp. 2632–2663. DOI: 10.1002/adma.200900375.

[28] Rainer Waser and Masakazu Aono. “Nanoionics-based resistive switching memories”. In: *Nature Materials* 6.11 (Nov. 2007), pp. 833–840. DOI: 10.1038/nmat2023.

[29] R. Dittmann, S. Menzel, and R. Waser. "Nanoionic memristive phenomena in metal oxides: the Valence Change Mechanism". In: *Adv. Phys.* (2022).

[30] Christoph Baeumer et al. "Quantifying redox-induced Schottky barrier variations in memristive devices via in operando spectromicroscopy with graphene electrodes". In: *Nature Communications* 7.1 (Aug. 2016), p. 12398. ISSN: 2041-1723. DOI: 10.1038/ncomms12398.

[31] Qi Liu et al. "Real-time observation on dynamic growth/dissolution of conductive filaments in oxide-electrolyte-based ReRAM". In: *Advanced Materials* 24.14 (2012), pp. 1844–1849.

[32] R. Waser, R. Bruchhaus, and S. Menzel. "Redox-based Resistive Switching Memories". In: *Nanoelectronics and Information Technology (3rd ed.)* Ed. by R. Waser. Wiley-VCH, 2012, pp. 683–710.

[33] Anja Herpers. "Electrical characterization of manganite and titanate heterostructures". RWTH Aachen, Diss., 2014. Dr. RWTH Aachen, 2014, p. 150. ISBN: 978-3-89336-948-5.

[34] Benedikt Arndt. "Resistive Switching in $Pr_1-xCa_xMnO_3$/YSZ: Conclusive Model and Switching Kinetics". PhD thesis. 2022.

[35] S. Lashkare, S. Subramoney, and U. Ganguly. "Nanoscale Side-Contact Enabled Three Terminal Pr0.7Ca0.3MnO3Resistive Random Access Memory for In-Memory Computing". In: *IEEE Electron Device Letters* 41.9 (2020), pp. 1344–1347. ISSN: 15580563. DOI: 10.1109/LED.2020.3010858.

[36] Sandip Lashkare, Vivek Saraswat, and Udayan Ganguly. "Understanding the Region of Resistance Change in Pr0.7Ca0.3MnO3RRAM". In: *ACS Applied Electronic Materials* 2.7 (2020), pp. 2026–2031. ISSN: 26376113. DOI: 10.1021/acsaelm.0c00297.

[37] Jinwon Go et al. "W/WO3-x based three-terminal synapse device with linear conductance change and high on/off ratio for neuromorphic application". In: *Applied Physics Express* 12.2 (Feb. 2019), p. 026503. ISSN: 18820786. DOI: 10.7567/1882-0786/aafc74.

[38] JG Simmons and RR Verderber. "Phenomena in thin insulating films new conduction and reversible memory". In: *Proc. Roy. Soc. A* 301 (1967), pp. 77–102.

[39] A Sawa et al. "Interface resistance switching at a few nanometer thick perovskite manganite active layers". In: *Applied physics letters* 88.23 (2006), p. 232112.

[40] A Asamitsu et al. "Current switching of resistive states in magnetoresistive manganites". In: *Nature* 388.6637 (1997), pp. 50–52.

[41] Ch Jooss et al. "Polaron melting and ordering as key mechanisms for colossal resistance effects in manganites". In: *Proceedings of the National Academy of Sciences* 104.34 (2007), pp. 13597–13602.

[42] S. Menzel et al. "The ultimate switching speed limit of redox-based restive switching devices". In: *Faraday Discuss.* 213 (2019), pp. 197–213.

[43] Napolean A et al. "Review on role of nanoscale HfO_2 switching material in resistive random access memory device". In: *Emergent Materials* 5.2 (Apr. 2022), pp. 489–508.

[44] Chenxi Wang, Huimin Qiao, and Yunseok Kim. “Perspective on the switching behavior of HfO_2-based ferroelectrics”. In: *Journal of Applied Physics* 129.1 (2021), p. 010902.

[45] Christian Lenser et al. “Formation and Movement of Cationic Defects During Forming and Resistive Switching in $SrTiO_3$ Thin Film Devices”. In: *Advanced Functional Materials* 25.40 (2015), pp. 6360–6368. DOI: adfm.201500851.

[46] Dong-Jun Seong et al. “Resistive-Switching Characteristics of $Al/Pr_{0.7}Ca_{0.3}MnO_3$ for Nonvolatile Memory Applications”. In: *IEEE electron device letters* 30.9 (2009), pp. 919–921.

[47] Anja Herpers et al. “Spectroscopic Proof of the Correlation between Redox-State and Charge-Carrier Transport at the Interface of Resistively Switching Ti/PCMO Devices”. In: *Advanced Materials* 26.17 (2014), pp. 2730–2735. DOI: 10.1002/adma.201304054.

[48] Benedikt Arndt et al. “Spectroscopic Indications of Tunnel Barrier Charging as the Switching Mechanism in Memristive Devices”. In: *Advanced Functional Materials* 27.45 (2017). DOI: 10.1002/adfm.201702282.

[49] Kibong Moon et al. “Bidirectional non-filamentary RRAM as an analog neuromorphic synapse, Part I: $Al/Mo/Pr_{0.7}Ca_{0.3}MnO_3$ material improvements and device measurements”. In: *IEEE Journal of the Electron Devices Society* 6 (2017), pp. 146–155.

[50] Kyungjoon Baek et al. “In situ TEM observation on the interface-type resistive switching by electrochemical redox reactions at a TiN/PCMO interface”. In: *Nanoscale* 9.2 (2017), pp. 582–593.

[51] Oskar Janik. “In-situ Charakterisierung des remanenten Widerstandsschaltens von PCMO-Edelmetall Sandwichstrukturen mit hochauflösender Transmissionselektronenmikroskopie”. Master Thesis. Universität Göttingen, 2014.

[52] V. M. Goldschmidt. “Die Gesetze der Krystallochemie”. In: *Naturwissenschaften* 14 (May 1926), pp. 477–485. DOI: 10.1007/BF01507527.

[53] J. M. D. Coey, M. Viret, and S. von Molnár. “Mixed-valence manganites”. In: *Advances in Physics* 48.2 (1999), pp. 167–293. DOI: 10.1080/000187399243455.

[54] S Schramm, J Hoffmann, and Ch Jooss. “Transport and ordering of polarons in CER manganites PrCaMnO”. In: *Journal of Physics: Condensed Matter* 20.39 (Sept. 2008), p. 395231. DOI: 10.1088/0953-8984/20/39/395231.

[55] J Appel. “Polarons”. In: *Solid State Physics*. Vol. 21. Elsevier, 1968, pp. 193–391.

[56] J. Kübler H. Böttger V. V. Bryksin and K.-H. Höck. *Hopping Conduction in Solids, VCH-Verlagsgesellschaft, Weinheim, Deerfield Beach-Florida 1985.* DOI: 10.1002/bbpc.19870910117.

[57] David Silver et al. “Mastering the game of go without human knowledge”. In: *nature* 550.7676 (2017), pp. 354–359.

[58] Kaushik Roy, Akhilesh Jaiswal, and Priyadarshini Panda. “Towards spike-based machine intelligence with neuromorphic computing”. In: *Nature* 575.7784 (Nov. 2019), pp. 607–617. ISSN: 1476-4687. DOI: 10.1038/s41586-019-1677-2.

[59] Geoffrey W. Burr et al. “Neuromorphic computing using non-volatile memory”. In: *Advances in Physics: X* 2.1 (2017), pp. 89–124. DOI: 10.1080/23746149.2016.1259585.

[60] Maxim Milakov. *Deep Learning With GPUs*. https://www.nvidia.co.uk/docs/IO/147844/Deep-Learning-With-GPUs-MaximMilakov-NVIDIA.pdf. Online; accessed 05-January-2023. 2014.

[61] M. Prezioso; F. Merrikh Bayat; B. Hokins; K. Likharev; D. Strukov. “Self-Adaptive Spike-Time-Dependent Plasticity of Metal-Oxide memristors”. In: *Scientific Reports* 6 (21331 2016). DOI: 10.1038/srep21331.

[62] David Daniel Cox and Thomas Dean. “Neural networks and neuroscience-inspired computer vision”. In: *Current Biology* 24.18 (2014), R921–R929.

[63] Alex Krizhevsky, Ilya Sutskever, and Geoffrey E Hinton. “Imagenet classification with deep convolutional neural networks”. In: *Communications of the ACM* 60.6 (2017), pp. 84–90.

[64] S Agatonovic-Kustrin and R Beresford. “Basic concepts of artificial neural network (ANN) modeling and its application in pharmaceutical research”. In: *Journal of Pharmaceutical and Biomedical Analysis* 22.5 (2000), pp. 717–727. ISSN: 0731-7085. DOI: 10.1016/S0731-7085(99)00272-1.

[65] Jacek Zurada. *Introduction to artificial neural systems*. West Publishing Co., 1992.

[66] Pádraig Cunningham, Matthieu Cord, and Sarah Jane Delany. “Supervised Learning”. In: *Machine Learning Techniques for Multimedia: Case Studies on Organization and Retrieval*. Ed. by Matthieu Cord and Pádraig Cunningham. Berlin, Heidelberg: Springer Berlin Heidelberg, 2008, pp. 21–49. ISBN: 978-3-540-75171-7. DOI: 10.1007/978-3-540-75171-7_2.

[67] Jesper E Van Engelen and Holger H Hoos. “A survey on semi-supervised learning”. In: *Machine Learning* 109.2 (2020), pp. 373–440.

[68] Happiness Ugochi Dike et al. “Unsupervised learning based on artificial neural network: A review”. In: *2018 IEEE International Conference on Cyborg and Bionic Systems (CBS)*. IEEE. 2018, pp. 322–327.

[69] Tannu Chauhan et al. “Supervised and Unsupervised Machine Learning based Review on Diabetes Care”. In: *2021 7th International Conference on Advanced Computing and Communication Systems (ICACCS)*. Vol. 1. 2021, pp. 581–585. DOI: 10.1109/ICACCS51430.2021.9442021.

[70] Kai Arulkumaran et al. “Deep reinforcement learning: A brief survey”. In: *IEEE Signal Processing Magazine* 34.6 (2017), pp. 26–38.

[71] Richard S Sutton and Andrew G Barto. *Reinforcement learning: An introduction*. MIT press, 2018.

[72] David E Rumelhart, Geoffrey E Hinton, and Ronald J Williams. “Learning representations by back-propagating errors”. In: *nature* 323.6088 (1986), pp. 533–536.

[73] David E Rumelhart et al. “Backpropagation: The basic theory”. In: *Backpropagation: Theory, architectures and applications* (1995), pp. 1–34.

[74] Logan G. Wright et al. “Deep physical neural networks trained with backpropagation”. In: *Nature* 601.7894 (Jan. 2022), pp. 549–555. DOI: 10.1038/s41586-021-04223-6.

[75] Timothy P Lillicrap et al. “Backpropagation and the brain”. In: *Nature Reviews Neuroscience* 21.6 (2020), pp. 335–346.

[76] Henry Markram, Wulfram Gerstner, and Per Jesper Sjöström. “A history of spike-timing-dependent plasticity”. In: *Frontiers in synaptic neuroscience* 3 (2011), p. 4.

[77] Abigail Morrison, Markus Diesmann, and Wulfram Gerstner. “Phenomenological models of synaptic plasticity based on spike timing”. In: *Biological cybernetics* 98.6 (2008), pp. 459–478.

[78] D. O. Hebb. *The Organization of Behavior*. Wiley & Sons, New York, NY, 1949.

[79] Robert Eason. *Pulser Laser Depoisition of Thin Films: Aplications-Led Growth of Functional Materials*. John Wiley & Sons, 2006. ISBN: 978-0-471-44709-2.

[80] Michael J Aziz. “Film growth mechanisms in pulsed laser deposition”. In: *Applied Physics A* 93.3 (2008), pp. 579–587.

[81] Dave HA Blank, Matthijn Dekkers, and Guus Rijnders. “Pulsed laser deposition in Twente: from research tool towards industrial deposition”. In: *Journal of physics D: applied physics* 47.3 (2013), p. 034006.

[82] James A Greer. “History and current status of commercial pulsed laser deposition equipment”. In: *Journal of Physics D: Applied Physics* 47.3 (2013), p. 034005.

[83] S. Wicklein et al. “Pulsed laser ablation of complex oxides: The role of congruent ablation and preferential scattering for the film stoichiometry”. In: *Applied Physics Letters* 101.13 (2012), p. 131601. DOI: 10.1063/1.4754112.

[84] Jeff Cheung and Jim Horwitz. “Pulsed laser deposition history and laser-target interactions”. In: *MRS bulletin* 17.2 (1992), pp. 30–36.

[85] Guus JHM Rijnders et al. “In-situ growth monitoring during PLD of oxides using RHEED at high oxygen pressure”. In: *Materials Science and Engineering: B* 56.2-3 (1998), pp. 223–227.

[86] Zhongping Wang and Zengming Zhang. “Electron beam evaporation deposition”. In: *Advanced Nanodeposition Methods; Chen, X., Lin, Y., Eds* (2016).

[87] Donald M Mattox. *Handbook of physical vapor deposition (PVD) processing*. William Andrew, 2010.

[88] S. M. Rossnagel. “Thin film deposition with physical vapor deposition and related technologies”. In: *Journal of Vacuum Science & Technology A* 21.5 (2003), S74–S87. DOI: 10.1116/1.1600450.

[89] Kiyotaka Wasa and Shigeru Hayakawa. “Handbook of sputter deposition technology”. In: (1992).

[90] Diederik Depla, Stijn Mahieu, and JE Greene. “Sputter deposition processes”. In: *Handbook of deposition technologies for films and coatings*. Elsevier, 2010, pp. 253–296.

[91] Hehe Zhang. “Resistive switching phenomena in stacks of binary transition metal oxides grown by atomic layer deposition”. In: (2019).

[92] Peter Ozaveshe Oviroh et al. “New development of atomic layer deposition: processes, methods and applications”. In: *Science and Technology of Advanced Materials* 20.1 (2019), pp. 465–496. ISSN: 18785514. DOI: 10.1080/14686996.2019.1599694.

[93] AT Fiory. “Recent developments in rapid thermal processing”. In: *Journal of electronic materials* 31.10 (2002), pp. 981–987.

[94] Richard B Fair. *Rapid thermal processing: science and technology*. Academic Press, 2012.

[95] MicroChemicals GmbH. *Basics of Microstruturing*.

[96] C. Lenser. “Investigation of Resistive Switching in Fe-doped $SrTiO_3$ by Advanced Spectroscopy”. PhD thesis. RWTH Aachen, Germany, 2013.

[97] Harry J Levinson. *Principles of lithography*. Vol. 146. SPIE press, 2005.

[98] Takashi Ito and Shinji Okazaki. “Pushing the limits of lithography”. In: *Nature* 406.6799 (2000), pp. 1027–1031.

[99] Christian Wagner and Noreen Harned. “Lithography gets extreme”. In: *Nature Photonics* 4.1 (2010), pp. 24–26.

[100] Per G. Glöersen. “Ionbeam etching”. In: *Journal of Vacuum Science and Technology* 12.1 (1975), pp. 28–35. DOI: 10.1116/1.568767.

[101] PJ Revell and GF Goldspink. “A review of reactive ion beam etching for production”. In: *Vacuum* 34.3-4 (1984), pp. 455–462.

[102] GA Vawter. “Ion beam etching of compound semiconductors”. In: *Handbook of Advanced Plasma Processing Techniques* (2000), pp. 507–547.

[103] Bert Voigtländer. *Scanning probe microscopy: Atomic force microscopy and scanning tunneling microscopy*. Springer, 2015.

[104] Nicholas A Geisse. “AFM and combined optical techniques”. In: *Materials today* 12.7-8 (2009), pp. 40–45.

[105] Peter Eaton and Paul West. *Atomic force microscopy*. Oxford university press, 2010.

[106] M.K. Khan, Q.Y. Wang, and M.E. Fitzpatrick. “1 - Atomic force microscopy (AFM) for materials characterization”. In: *Materials Characterization Using Nondestructive Evaluation (NDE) Methods*. Ed. by Gerhard Hübschen et al. Woodhead Publishing, 2016, pp. 1–16. ISBN: 978-0-08-100040-3. DOI: 10.1016/B978-0-08-100040-3.00001-8.

[107] Yoshio Waseda, Eiichiro Matsubara, and Kozo Shinoda. *X-ray diffraction crystallography: introduction, examples and solved problems*. Springer Science & Business Media, 2011.

[108] ES Ameh. “A review of basic crystallography and x-ray diffraction applications”. In: *The international journal of advanced manufacturing technology* 105.7 (2019), pp. 3289–3302.

[109] André Guinier. *X-ray diffraction in crystals, imperfect crystals, and amorphous bodies*. Courier Corporation, 1994.

[110] Akhilesh Pandey et al. “Structural characterization of polycrystalline thin films by X-ray diffraction techniques”. In: *Journal of Materials Science: Materials in Electronics* 32.2 (Jan. 2021), pp. 1341–1368. DOI: 10.1007/s10854-020-04998-w.

[111] Paolo Colombi et al. “Glancing-incidence X-ray diffraction for depth profiling of polycrystalline layers”. In: *Journal of Applied Crystallography* 39.2 (Apr. 2006), pp. 176–179. DOI: 10.1107/S0021889805042779.

[112] Lothar Spieß et al. *Moderne röntgenbeugung*. Vol. 2. Springer, 2009.

[113] Jürgen Bauch and Rüdiger Rosenkranz. “XRR - Röntgenreflektometrie”. In: *Physikalische Werkstoffdiagnostik: Ein Kompendium wichtiger Analytikmethoden für Ingenieure und Physiker*. Berlin, Heidelberg: Springer Berlin Heidelberg, 2017, pp. 50–51. ISBN: 978-3-662-53952-1. DOI: 10.1007/978-3-662-53952-1_25.

[114] Fred A. Stevie and Carrie L. Donley. “Introduction to x-ray photoelectron spectroscopy”. In: *Journal of Vacuum Science & Technology A* 38.6 (2020), p. 063204. ISSN: 0734-2101. DOI: 10.1116/6.0000412.

[115] Siegfried Hofmann. *Auger- and X-Ray Photoelectron Spectroscopy in Materials Science: A User-Oriented Guide*. 2013, p. 528. ISBN: 9783642273803. DOI: 10.1007/978-3-642-27381-0.

[116] J.F. Moulder and J. Chastain. *Handbook of X-ray Photoelectron Spectroscopy: A Reference Book of Standard Spectra for Identification and Interpretation of XPS Data*. Physical Electronics Division, Perkin-Elmer Corporation, 1992. ISBN: 9780962702624.

[117] Brent Fultz and James M Howe. *Transmission electron microscopy and diffractometry of materials*. Springer Science & Business Media, 2012.

[118] Ludwig Reimer. *Transmission electron microscopy: physics of image formation and microanalysis*. Vol. 36. Springer, 2013.

[119] Keithley Instruments Inc. “Series 2600A Datasheet”. In: (2013).

[120] Tektronix. *4200A-SCS Parameter Analyzer Datsheet*, pp. 1–42.

[121] ArC Instruments Ltd. “ArC ONE Memristor Characterisation Plattform”. In: (2019).

[122] O. Yu Gorbenko et al. “Solid solutions $La_{1-x}Ag_yMnO_3 + \delta$: Evidence for silver doping, structure and properties”. In: *Materials Science and Engineering B: Solid-State Materials for Advanced Technology* 116.1 (2005), pp. 64–70. ISSN: 09215107. DOI: 10.1016/j.mseb.2004.09.013.

[123] Alexander Gutsche. “Master Thesis: Resistive Switching in Polycrystalline $Pr_{1-x}Ca_xMnO_3$/Al-Hetero Structures”. 2018.

[124] Holger Borchert et al. “Electronic and chemical properties of nanostructured cerium dioxide doped with praseodymium”. In: *The journal of physical chemistry. B* 109.12 (Mar. 2005), pp. 5728–5738. DOI: 10.1021/jp045828c.

[125] H. Ogasawara et al. “Praseodymium 3d- and 4d-core photoemission spectra of Pr_2O_3”. In: *Phys. Rev. B* 44 (11 1991), pp. 5465–5469. DOI: 10.1103/PhysRevB.44.5465.

[126] S. Lütkehoff, M. Neumann, and A. Ślebarski. “3d and 4d x-ray-photoelectron spectra of Pr under gradual oxidation”. In: *Phys. Rev. B* 52 (19 1995), pp. 13808–13811. DOI: 10.1103/PhysRevB.52.13808.

[127] C. K. Narula et al. "Single-Phase PrO_yZrO_2 Materials and Their Oxygen Storage Capacity: A Comparison with Single-Phase eO_2ZrO_2, PrO_yCeO_2, and $PrO_yCeO_2ZrO_2$ Materials". In: *The Journal of Physical Chemistry B* 103.18 (1999), pp. 3634–3639. DOI: 10.1021/jp984383n.

[128] Novica Paunović et al. "Suppression of inherent ferromagnetism in Pr-doped CeO_2 nanocrystals". In: *Nanoscale* 4.17 (2012), pp. 5469–5476. DOI: 10.1039/c2nr30799e.

[129] Ahmed Almamoori et al. "Improving Adsorptive Performance of CaO for High Temperature CO_2 Capture through Fe and Ga Doping". In: *Energy Fuels* 33 (Jan. 2019). DOI: 10.1021/acs.energyfuels.8b03996.

[130] H. Van Doveren and J.A.T.H. Verhoeven. "XPS spectra of Ca, Sr, Ba and their oxides". In: *Journal of Electron Spectroscopy and Related Phenomena* 21.3 (1980), pp. 265–273. DOI: 10.1016/0368-2048(80)85055-9.

[131] G. Chiarello et al. "An XPS study of SO_2 ON A CaO surface derived from $Ca(OH)_2$". In: *Journal of Electron Spectroscopy and Related Phenomena* 50.2 (1990), pp. 229–237. ISSN: 0368-2048. DOI: 10.1016/0368-2048(90)87067-X.

[132] H.W. Nesbitt and D. Banerjee. "Interpretation of XPS Mn(2p) spectra of Mn oxyhydroxides and constraints on the mechanism of MnO_2 precipitation". In: *American Mineralogist* 83.3-4 (1998), pp. 305–315. DOI: 10.2138/am-1998-3-414.

[133] Haruna D. Aliyu et al. "Surface Ferromagnetism in $Pr_{0.5}Ca_{0.5}MnO_3$ Nanoparticles as a Consequence of Local Imbalance in $^{Mn^{3+}}/_{Mn^{4+}}$ Ratio". In: *Chemistry of Materials* 30.20 (2018), pp. 7138–7145. DOI: 10.1021/acs.chemmater.8b03070.

[134] M. Nyman et al. "Epitaxially Textured $Pr_0 \cdot {}_6Ca_{0.4}MnO_3$ Thin Films Under Considerably Low Substrate Temperature". In: vol. 75. Dec. 2015. DOI: 10.1016/j.phpro.2015.12.180.

[135] Joonghoe Dho et al. "Two ferromagnetic transitions in $Pr_0 \cdot {}_8Ca_{0.2}MnO_3$". In: *Solid State Communications* 123.10 (2002), pp. 441–444. DOI: 10.1016/S0038-1098(02)00375-7.

[136] Pauline Cornette, Dominique Costa, and Philippe Marcus. "Relation between Surface Composition and Electronic Properties of Native Oxide Films on an Aluminium-Copper Alloy Studied by DFT". In: *Journal of The Electrochemical Society* 167 (Nov. 2020), p. 161501. DOI: 10.1149/1945-7111/abc9a1.

[137] Mark T. Greiner et al. "Transition Metal Oxide Work Functions: The Influence of Cation Oxidation State and Oxygen Vacancies". In: *Advanced Functional Materials* 22.21 (), pp. 4557–4568. DOI: 10.1002/adfm.201200615.

[138] P. van der Heide. *X-ray Photoelectron Spectroscopy: An introduction to Principles and Practices*. WILEY, 2011. ISBN: 978-1-118-06253-1.

[139] Eugene S. Ilton et al. "XPS determination of Mn oxidation states in Mn (hydr)oxides". In: *Applied Surface Science* 366 (2016), pp. 475–485. ISSN: 0169-4332. DOI: 10.1016/j.apsusc.2015.12.159.

[140] Shutaro Asanuma et al. "Relationship between resistive switching characteristics and band diagrams of $Ti/Pr_{1x}Ca_xMnO_3$ junctions". In: *Physical Review B* 80 (Dec. 2009). DOI: 10.1103/PhysRevB.80.235113.

[141] Elena O. Filatova and Aleksei S. Konashuk. "Interpretation of the Changing the Band Gap of Al_2O_3 Depending on Its Crystalline Form: Connection with Different Local Symmetries". In: *The Journal of Physical Chemistry C* 119.35 (2015), pp. 20755–20761. DOI: 10.1021/acs.jpcc.5b06843.

[142] Elena Atanassova and Dencho Spassov. "Thin Ta_2O_5 Films on Si by XPS". In: *Surface Science Spectra* 7.2 (2000), pp. 143–149. DOI: 10.1116/1.1323656.

[143] Robin Simpson et al. "XPS Investigation of Monatomic and Cluster Argon Ion Sputtering of Tantalum Pentoxide". In: *Applied Surface Science* 405 (Feb. 2017). DOI: 10.1016/j.apsusc.2017.02.006.

[144] N. Alov. "Determination of the States of Oxidation of Metals in Thin Oxide Films by X-Ray Photoelectron Spectroscopy". In: *Journal of Analytical Chemistry* 60 (May 2005), pp. 431–435. DOI: 10.1007/s10809-005-0114-x.

[145] Maria Vasilopoulou et al. "Hydrogenated under-stoichiometric tungsten oxide anode interlayers for efficient and stable organic photovoltaics". In: *Journal of Materials Chemistry A* 2 (Feb. 2014), pp. 1738–1749. DOI: 10.1039/C3TA13975A.

[146] Dong-jun Seong et al. "Effect of Oxygen Migration and Interface Engineering on Resistance Switching Behavior of Reactive Metal/Polycrystalline $Pr_{0.7}Ca_{0.3}MnO_3$ Device for Nonvolatile Memory Applications". In: *Electron Devices Meeting (IEDM), 2009 IEEE International* (2009), pp. 101–104. DOI: 10.1109/IEDM.2009.5424410.

[147] Hiroyasu Kawano et al. "Enhancement of switching capability on bipolar resistance switching device with $Ta/Pr_{0.7}Ca_{0.3}MnO_3/Pt$ structure". In: *Applied Physics Express* 1.10 (2008), pp. 1019011–1019013. ISSN: 18820778. DOI: 10.1143/APEX.1.101901.

[148] Keiji Shono et al. "Origin of Negative Differential Resistance Observed on Bipolar Resistance Switching Device with $Ti/Pr_{0.7}Ca_{0.3}MnO_3/Pt$ Structure". In: *Applied Physics Express* 1 (Apr. 2008), p. 055002. DOI: 10.1143/apex.1.055002.

[149] Kibong Moon et al. "Bidirectional non-filamentary RRAM as an analog neuromorphic synapse, Part I: $Al/Mo/Pr_{0.7}Ca_{0.3}MnO_3$ material improvements and device measurements". In: *IEEE Journal of the Electron Devices Society* 6.1 (2018), pp. 146–155. ISSN: 21686734. DOI: 10.1109/JEDS.2017.2780275.

[150] Kibong Moon et al. "NbO 2 IMT oscillator neuron". In: *IEDM* (2015), pp. 463–466.

[151] Xinjun Liu et al. "Low programming voltage resistive switching in reactive metal/polycrystalline $Pr_{0.7}Ca_{0.3}MnO_3$ devices". In: *Solid State Communications* 150.45 (2010), pp. 2231–2235. ISSN: 0038-1098. DOI: 10.1016/j.ssc.2010.09.036.

[152] Vivek Saraswat et al. "Reaction-Drift Model for Switching Transients in $Pr_{0.7}Ca_{0.3}MnO_3$-Based Resistive RAM". In: *IEEE Transactions on Electron Devices* 67.9 (2020), pp. 3610–3617. ISSN: 0018-9383. DOI: 10.1109/ted.2020.3011387.

[153] P. Kumbhare et al. "Memory Performance of a Simple $Pr_{0.7}Ca_{0.3}MnO_3$-Based Selectorless RRAM". In: *IEEE Transactions on Electron Devices* 64.9 (2017), pp. 3967–3970. DOI: 10.1109/TED.2017.2725900.

[154] S. Lashkare et al. "PCMO RRAM for Integrate-and-Fire Neuron in Spiking Neural Networks". In: *IEEE Electron Device Letters* 39.4 (2018), pp. 484–487. DOI: 10.1109/LED.2018.2805822.

[155] Anakha V. Babu et al. “Stochastic learning in deep neural networks based on nanoscale PCMO device characteristics”. In: *Neurocomputing* 321 (2018), pp. 227–236. ISSN: 18728286. DOI: 10.1016/j.neucom.2018.09.019.

[156] S Lashkare et al. “PCMO-Based RRAM and NPN Bipolar Selector as Synapse for Energy Efficient STDP”. In: *IEEE Electron Device Letters* 38.9 (Sept. 2017), pp. 1212–1215. DOI: 10.1109/LED.2017.2723503.

[157] Aditya Shukla et al. “A case for multiple and parallel RRAMs as synaptic model for training SNNs”. In: *arXiv* (2018).

[158] Alessandro Fumarola et al. “Bidirectional Non-Filamentary RRAM as an Analog Neuromorphic Synapse, Part II: Impact of Al/Mo/$Pr_{0.7}Ca_{0.3}MnO_3$ Device Characteristics on Neural Network Training Accuracy”. In: *IEEE Journal of the Electron Devices Society* 6.1 (2018), pp. 169–178. DOI: 10.1109/JEDS.2017.2782184.

[159] M Chase. *NIST-JANAF Thermochemical Tables, 4th Edition*. en. American Institute of Physics, -1, 1998-08-01 1998.

[160] Zhi Luo et al. “Resistive Switching in Perovskite-Oxide Capacitor-Type Devices”. In: *IEEE Transactions on Magnetics* 50.7 (2014), pp. 1–4. DOI: 10.1109/TMAG.2013.2297408.

[161] Naoki Kanegami, Yusuke Nishi, and Tsunenobu Kimoto. “Unique resistive switching phenomena exhibiting both filament-type and interface-type switching in Ti/$Pr_{0.7}Ca_{0.3}MnO$/Pt ReRAM cells”. In: *Applied Physics Letters* 116.1 (2020), p. 013501. DOI: 10.1063/1.5131090.

[162] Z. L. Liao et al. “Categorization of resistive switching of metal-$Pr_{0.7}Ca_{0.3}MnO_3$-metal devices”. In: *Applied Physics Letters* 94.25 (2009), p. 253503. DOI: 10.1063/1.3159471.

[163] Seungjae Jung et al. “Thermally-assisted Ti/$Pr_{0.7}Ca_{0.3}MnO_3$ ReRAM with excellent switching speed and retention characteristics”. In: *2011 International Electron Devices Meeting*. 2011, pp. 3.6.1–3.6.4. DOI: 10.1109/IEDM.2011.6131483.

[164] Jubong Park et al. “Resistive switching characteristics of ultra-thin TiO_x”. In: *Microelectronic Engineering* 88.7 (2011). Proceedings of the 17th Biennial International Insulating Films on Semiconductor Conference, pp. 1136–1139. ISSN: 0167-9317. DOI: 10.1016/j.mee.2011.03.050.

[165] Tamkeen Farooq. “Study of Resistive Switching in Titanium Dioxide (TiO_2) Thin Film for the Application of Non-Volatile Memory: A Review”. In: *International Journal for Research in Applied Science and Engineering Technology* 7.4 (2019), pp. 3030–3037. DOI: 10.22214/ijraset.2019.4508.

[166] Jiun-Jia Huang et al. “Transition of stable rectification to resistive-switching in Ti/TiO_2/Pt oxide diode”. In: *Applied Physics Letters* 96.26 (2010), p. 262901. DOI: 10.1063/1.3457866.

[167] Ruofei Hu et al. “Investigation of Resistive Switching Mechanisms in Ti/TiO_x/Pd-Based RRAM Devices”. In: *Advanced Electronic Materials* 8.8 (2022), p. 2100827. DOI: 10.1002/aelm.202100827.

[168] Kyung Min Kim, Byung Joon Choi, and Cheol Seong Hwang. “Localized switching mechanism in resistive switching of atomic-layer-deposited TiO2 thin films”. In: *Applied Physics Letters* 90.24 (2007), p. 242906. DOI: 10.1063/1.2748312.

[169] Kenji Itaka et al. “Direct Carbothermic Silica Reduction from Purified Silica to Solar-Grade Silicon”. In: *Journal of Physics: Conference Series* 596 (Apr. 2015), p. 012015. DOI: 10.1088/1742-6596/596/1/012015.

[170] J. Frenkel. “On Pre-Breakdown Phenomena in Insulators and Electronic Semi-Conductors”. In: *Phys. Rev.* 54 (8 Oct. 1938), pp. 647–648. DOI: 10.1103/PhysRev.54.647.

[171] Ralph Howard Fowler and L. Nordheim. “Electron emission in intense electric fields”. In: *Proceedings of the Royal Society of London. Series A, Containing Papers of a Mathematical and Physical Character* 119.781 (1928), pp. 173–181. DOI: 10.1098/rspa.1928.0091.

[172] Chih-Yang Lin et al. “Bistable Resistive Switching in Al_2O_3 Memory Thin Films”. In: *Journal of The Electrochemical Society* 154.9 (2007), G189. ISSN: 00134651. DOI: 10.1149/1.2750450.

[173] Sujaya Kumar Vishwanath, Hyunsuk Woo, and Sanghun Jeon. “Enhancement of resistive switching properties in Al_2O_3 bilayer-based atomic switches: multilevel resistive switching”. In: *Nanotechnology* 29.23 (Apr. 2018), p. 235202. DOI: 10.1088/1361-6528/aab6a3.

[174] F. Cüppers et al. “Exploiting the switching dynamics of HfO_2-based ReRAM devices for reliable analog memristive behaviour”. In: *APL Materials* 7.9 (2019), p. 091105. DOI: 10.1063/1.5108654.

[175] Kuan-Liang Lin et al. “Electrode dependence of filament formation in HfO_2 resistive-switching memory”. In: *Journal of Applied Physics* 109.8 (2011), p. 084104. DOI: 10.1063/1.3567915.

[176] M. Lanza et al. “Grain boundaries as preferential sites for resistive switching in the HfO2 resistive random access memory structures”. In: *Applied Physics Letters* 100.12 (2012), p. 123508. DOI: 10.1063/1.3697648.

[177] S. U. Sharath et al. “Towards forming-free resistive switching in oxygen engineered HfO2x”. In: *Applied Physics Letters* 104.6 (2014), p. 063502. DOI: 10.1063/1.4864653.

[178] S. Privitera et al. “Microscopy study of the conductive filament in HfO2 resistive switching memory devices”. In: *Microelectronic Engineering* 109 (2013). Insulating Films on Semiconductors 2013, pp. 75–78. DOI: 10.1016/j.mee.2013.03.145.

[179] Alexander Hardtdegen, Hehe Zhang, and Susanne Hoffmann-Eifert. “Tuning the Performance of $Pt/HfO_2/Ti/Pt$ ReRAM Devices Obtained from Plasma-Enhanced Atomic Layer Deposition for HfO2 Thin Films”. In: *ECS Transactions* 75.6 (Aug. 2016), p. 177. DOI: 10.1149/07506.0177ecst.

[180] D. Liu, S. J. Clark, and J. Robertson. “Oxygen vacancy levels and electron transport in Al_2O_3”. In: *Applied Physics Letters* 96.3 (2010), p. 032905. DOI: 10.1063/1.3293440.

[181] Michael Serhan et al. “In situ study of the electronic structure of atomic layer deposited oxide ultrathin films upon oxygen adsorption using ambient pressure XPS”. In: *AIChE Annual Meeting, Conference Proceedings* 2019-Novem (2019), pp. 1–3. DOI: 10.1039/x0xx00000x.

[182] Ji Hyun Hur. "The origin of the exceptionally low activation energy of oxygen vacancy in tantalum pentoxide based resistive memory". In: *Scientific Reports* 9.1 (2019), pp. 1–9. DOI: 10.1038/s41598-019-53498-3.

[183] Victor Yiqian Zhuo et al. "Band alignment between Ta_2O_5 and metals for resistive random access memory electrodes engineering". In: *Applied Physics Letters* 102 (Feb. 2013). DOI: 10.1063/1.4792274.

[184] M. Gillet et al. "The structure and electrical conductivity of vacuum-annealed WO_3 thin films". In: *Thin Solid Films* 467.1 (2004), pp. 239–246. DOI: 10.1016/j.tsf.2004.04.018.

[185] Seungchan Han et al. "Improving performance of organic solar cells using amorphous tungsten oxides as an interfacial buffer layer on transparent anodes". In: *Organic Electronics* 10.5 (2009), pp. 791–797. DOI: 10.1016/j.orgel.2009.03.016.

[186] G. Halek et al. "Work function analysis of gas sensitive WO_3 layers with Pt doping". In: *Sensors and Actuators B: Chemical* 187 (2013). Selected Papers from the 14th International Meeting on Chemical Sensors, pp. 379–385. DOI: 10.1016/j.snb.2012.12.062.

[187] Nathalie Capron, Peter Broqvist, and Alfredo Pasquarello. "Migration of oxygen vacancy in HfO_2 and across the HfO_2/SiO_2 interface: A first-principles investigation". In: *Applied Physics Letters* 91.19 (2007), p. 192905. DOI: 10.1063/1.2807282.

[188] Kehua Zhong et al. "Work function change of Ni, HfO_2 films and Ni/HfO_2 interfaces as a function of external electric field". In: *International Journal of Modern Physics B* 29.23 (2015), p. 1550168. DOI: 10.1142/S0217979215501684.

[189] Katharina Skaja et al. "Reduction of the forming voltage through tailored oxygen non-stoichiometry in tantalum oxide ReRAM devices". In: *Scientific reports* 8.1 (2018), pp. 1–7.

[190] Wonjoo Kim et al. "Lowering forming voltage and forming-free behavior of Ta2O5 ReRAM devices". In: *2016 46th European Solid-State Device Research Conference (ESSDERC)*. 2016, pp. 164–167. DOI: 10.1109/ESSDERC.2016.7599612.

[191] A. Sawa et al. "Hysteretic current–voltage characteristics and resistance switching at a rectifying $Ti/Pr_{0.7}Ca_{0.3}MnO_3$ interface". In: *Applied Physics Letters* 85.18 (2004), pp. 4073–4075. DOI: 10.1063/1.1812580.

[192] Dong-Jun Seong et al. "Resistive-Switching Characteristics of $Al/Pr_{0.7}Ca_{0.3}MnO_3$ for Nonvolatile Memory Applications". In: *IEEE Electron Device Letters* 30.9 (2009), pp. 919–921. DOI: 10.1109/LED.2009.2025896.

[193] W. S. Lau. "An Extended Unified Schottky-Poole-Frenkel Theory to Explain the Current-Voltage Characteristics of Thin Film Metal-Insulator-Metal Capacitors with Examples for Various High-k Dielectric Materials". In: *ECS Journal of Solid State Science and Technology*, 1.6 (2012), pp. 139–148.

[194] S. D. Ganichev et al. "Distinction between the Poole-Frenkel and tunneling models of electric-field-stimulated carrier emission from deep levels in semiconductors". In: *Phys. Rev. B: Condens. Matter* 61.15 (2000).

[195] Y. Takeuti and H. Funada. "Theory of Electron Tunneling in Semiconductors". In: *J. Phys. Soc. Jpn.* 20.10 (1965), pp. 1854–1865.

[196] F. Jimenez-Molinos et al. “Direct and trap-assisted elastic tunneling through ultrathin gate oxides”. In: *J. Appl. Phys.* 91.8 (2002), pp. 5116–5124.

[197] F. Jimenez-Molinos et al. “Physical model for trap-assisted inelastic tunneling in metal-oxide-semiconductor structures”. In: *J. Appl. Phys.* 90.7 (2001).

[198] C. C. Wang and L. W. Zhang. “Polaron relaxation related to localized charge carriers in $Pr_{1-x}Ca_xMnO_3$”. In: *New J. Phys* 9.210 (2007).

[199] Toshihiro Nakamura, Kohei Homma, and Kunihide Tachibana. “Thin film deposition of metal oxides in resistance switching devices: electrode material dependence of resistance switching in manganite films”. In: *Nanoscale Research Letters* 8.1 (Feb. 2013), p. 76. DOI: 10.1186/1556-276X-8-76.

[200] D. Deger, Kemal Ulutas, and Sahin Yakut. “AC CONDUCTIVITY AND DIELECTRIC PROPERTIES OF Al2O3 THIN FILMS”. In: *Journal of Ovonic Research* 8 (Nov. 2012), pp. 179–188.

[201] Holger Spahr et al. “Conduction mechanisms in thin atomic layer deposited Al2O3 layers”. In: *Journal of Applied Physics* 114.18 (2013), p. 183714. DOI: 10.1063/1.4829910.

[202] K.S. Chari and B. Mathur. “The conduction properties of anodic Al_2O_3 films”. In: *Thin Solid Films* 75.2 (1981), pp. 157–166. DOI: 10.1016/0040-6090(81)90452-1.

[203] Eric Cockayne. “Influence of oxygen vacancies on the dielectric properties of hafnia: First-principles calculations”. In: *Phys. Rev. B* 75 (9 Mar. 2007), p. 094103. DOI: 10.1103/PhysRevB.75.094103.

[204] Francesco Borgatti et al. “Chemical insight into electroforming of resistive switching manganite heterostructures”. In: *Nanoscale* 5 (9 2013), pp. 3954–3960. DOI: 10.1039/C3NR00106G.

[205] J. Frenkel. “On Pre-Breakdown Phenomena in Insulators and Electronic Semi-Conductors”. In: *Phys. Rev.* 54 (8 Oct. 1938), pp. 647–648. DOI: 10.1103/PhysRev.54.647.

[206] Camilla La Torre et al. “Volatile HRS asymmetry and subloops in resistive switching oxides”. In: *Nanoscale* 9 (38 2017), pp. 14414–14422. DOI: 10.1039/C7NR04896C.

[207] M.B. Zahid et al. “Applying Complementary Trap Characterization Technique to Crystalline γ-Phase-Al_2O_3 for Improved Understanding of Nonvolatile Memory Operation and Reliability”. In: *Electron Devices, IEEE Transactions on* 57 (Dec. 2010), pp. 2907–2916. DOI: 10.1109/TED.2010.2071071.

[208] Oliver A Dicks et al. “The origin of negative charging in amorphous Al_2O_3 films: the role of native defects”. In: *Nanotechnology* 30.20 (Mar. 2019), p. 205201. DOI: 10.1088/1361-6528/ab0450.

[209] S. Menzel et al. “Origin of the Ultra-nonlinear Switching Kinetics in Oxide-Based Resistive Switches”. In: *Adv. Funct. Mater.* 21.23 (2011), pp. 4487–4492.

[210] Halid Mulaosmanovic et al. “Switching Kinetics in Nanoscale Hafnium Oxide Based Ferroelectric Field-Effect Transistors”. In: *ACS Applied Materials & Interfaces* 9.4 (2017), pp. 3792–3798. DOI: 10.1021/acsami.6b13866.

[211] S. Menzel et al. “Physics of the Switching Kinetics in Resistive Memories”. In: *Adv. Funct. Mater.* 25.40 (2015), pp. 6306–6325.

[212] “The thickness of native oxides on aluminum alloys and single crystals”. In: *Applied Surface Science* 349 (2015), pp. 826–832. ISSN: 0169-4332. DOI: 10.1016/j.apsusc.2015.05.043.

[213] M. T.A. Saif et al. “Effect of native Al_2O_3 on the elastic response of nanoscale Al films”. In: *Acta Materialia* 50.11 (2002), pp. 2779–2786. DOI: 10.1016/S1359-6454(02)00089-7.

[214] A.H. Heuer. “Oxygen and aluminum diffusion in α-Al2O3: How much do we really understand?” In: *Journal of the European Ceramic Society* 28.7 (2008). Developments in Ceramic Science and Engineering: the last 50 years. A meeting in celebration of Professor Sir Richard Brook’s 70th Birthday, pp. 1495–1507. DOI: 10.1016/j.jeurceramsoc.2007.12.020.

[215] R. Nakamura et al. “Diffusion of oxygen in amorphous Al2O3, Ta2O5, and Nb2O5”. In: *Journal of Applied Physics* 116.3 (2014), p. 033504. DOI: 10.1063/1.4889800.

[216] V.K. Sikka and C.J. Rosa. “The oxidation kinetics of tungsten and the determination of oxygen diffusion coefficient in tungsten trioxide”. In: *Corrosion Science* 20.11 (1980), pp. 1201–1219. DOI: 10.1016/0010-938X(80)90092-X.

[217] Chen Tao et al. “Role of tungsten oxide in inverted polymer solar cells”. In: *Applied Physics Letters* 94.4 (2009), pp. 2–4. DOI: 10.1063/1.3076134.

[218] A. Sarantopoulos et al. “Manuscript in preparation”.

[219] T. Kempen et al. “Manuscript in preparation”.

[220] Stephan Aussen et al. “Direct Comparison of the SET Kinetics of a TiO_x/Al_2O_3-based Memristive Cell in Filamentary- and Area-Mode”. In: *IEEE Nano* (2022). accepted.

[221] Moritz von Witzleben et al. “Investigation of the Impact of High Temperatures on the Switching Kinetics of Redox-Based Resistive Switching Cells using a High-Speed Nanoheater”. In: *Advanced Electronic Materials* 3.12 (2017), p. 1700294. DOI: 10.1002/aelm.201700294.

[222] Manan Suri et al. “Neuromorphic hybrid RRAM-CMOS RBM architecture”. In: *2015 15th Non-Volatile Memory Technology Symposium (NVMTS)*. 2015, pp. 1–6. DOI: 10.1109/NVMTS.2015.7457484.

[223] Martın Abadi et al. “TensorFlow: A System for Large-Scale Machine Learning”. In: *12th USENIX Symposium on Operating Systems Design and Implementation (OSDI 16)*. Savannah, GA: USENIX Association, Nov. 2016, pp. 265–283. ISBN: 978-1-931971-33-1.

[224] Fuxi Cai et al. “A fully integrated reprogrammable memristor–CMOS system for efficient multiply–accumulate operations”. In: *Nature Electronics* 2.7 (July 2019), pp. 290–299. DOI: 10.1038/s41928-019-0270-x.

[225] S. Siegel et al. “Manuscript in preparation”.

Acknowledgements

First of all, I would like to thank Prof. Regina Dittmann for giving me the chance to write my thesis in her group. Her tremendous knowledge about resistive switching and oxide thin film growth and all the discussions were a great help for this thesis. Furthermore, her way of leading the group and encouraging discussion among the group members provided a fruitful research environment. I would also like to thank her for the many opportunities she has opened up for me. These included, above all, the beam times in various places, which I always enjoyed very much.

Secondly, I would like to thank Prof. John Paul Strachan for agreeing to be the second examiner of this thesis.

I would like to thank Prof. Rainer Waser for giving me the opportunity to continue my studies in his institutes after this thesis.

A very special thank you goes to Sebastian Hambsch. First of all, I always enjoyed the time we shared the office. Secondly, with his great knowledge about resistive switching and ideas for measurements, he was always a helping hand. Also worth mentioning is the crime dinner that took place at his place.

For correcting the first draft of the thesis I would like to thank my office mate Kalle Goß.Additionally, we always had a good time sharing the office. Beside this I want to thank Dr. Moritz Weber for sharing the office since my first day in the institute. Even if we are not working on the same topic, it was always helpful to discuss about PLD problems.

Furthermore, I would like to thank Max Buczek, Zoe Fiedler and Dr. Jacqueline Börgers for the fruitful discussions about manganates, area dependent resistive switching and the growth using PLD.

I would like Sebastian Siegel to thank for providing the insights into the network simulations and the results he provided for this thesis.

Of course I am also grateful to the technical staff. For their support in the cleanroom, I would like to thank René Borowski, Mirca Grates, Grigory Potemkin and Clemens Wiedenhöfft. I thank Marcel Gerst for help with the electronic setups for device characterisation and any other computer problems. Georg Pickartz, who kept the laser up and running, taking care of the vacuum and for the one or other nice conversation. Jochen Friedrich for helping with all the electronic problems. Stephan Maßberg for his tireless commitment to wanting to help immediately, even with small things. Furthermore I would like to thank Maria Garcia for taking care of all the administrative stuff.

I want to thank the "Telefonmeeting-group": Felix Cüppers, Stephan Außen, Niclas Schmidt and Solomon Chekol for all the fun we had besides work and all the "Telefonmeetings" we had. Felix Cüppers I would like to thank in addition for the discussions about neuromorphic measurements and Stephan Außen for providing the Si/Pt substrates and developing the process of the membrane samples.

At this point I would like to thank many colleagues and friends with whom I have shared coffee breaks or working session as well as some after work gatherings. A few names I would like to mention: Dr. Vikas Rana, Dr. Stephan Menzel, Dr. Carsten Funck, Dr. Felix Gunkel, Anton Kaus, Lisa Heymann, Dr. Thomas Heisig, Dr. Felix Hensling, Johannes Hellwig, Luisa Bayer, Tim Kempen, Tom, Kristoffer Schnieders, Zhaodong Wang, Jinchao Zhang and many more. I would like to thank Judith Knabe, who, at the end of my doctoral studies, shared and took over most of my teaching related responsibilities. I would like to thank Marcus Wohlgemuth for sharing some rides to Jülich and for all the "gym-talk". Furthermore, I would like to thank Helen Schneider for motivating me every Thursday.

Last but not least, I would like to thank my parents, Marion and Roland Gutsche, my brothers, my family and my friends who supported me during writing this thesis.